TECHNISCHE
UNIVERSITÄT
WIEN

DISSERTATION

Synthesis and Characterization of Novel Inorganic-Organic Hybrids for Photocatalytic H_2 Evolution and Photovoltaic Applications

ausgeführt zum Zwecke der Erlangung des akademischen Grades einer Doktorin
der Naturwissenschaften unter der Leitung von

Prof. Dr. Dominik Eder

E165
Institut für Materialchemie
Eingereicht an der Technischen Universität Wien
Fakultät für Technische Chemie

von

Jia Wang

01528763

Getreidemarkt 09/ BC02 A20, 1060 Wien

Wien, am

Dedicated to

献给三十岁的王佳

勇往直前，开启新的征程

多点勇敢，少点遗憾

Done it, been there.

Abstract

My PhD project focused on the development of advanced materials for solar energy conversion. Compared with their component materials, hybrid materials additionally offer synergistic effects, such as efficient charge separation, and thus have attracted great interest. In this thesis, I investigated two types of organic-inorganic hybrid materials, i.e. metal-organic frameworks (MOFs) and hybrid organic inorganic perovskites (HOIP), for photocatalytic hydrogen production and photovoltaic electricity generation.

The first part of my thesis investigated the influence of the organic ligand in MOFs on the materials structure, functional properties and photocatalytic performance. In particular, I designed mixed-ligand Ti-based MOFs, $MIL_{1-x}(NH_2\text{-}MIL)_x$-125-Ti with varying ligand composition. The MOFs were characterized with a wide range of state-of-the-art techniques, including XRD, SEM, DRS, FT-IR, TGA, physisorption. The results show that the different ligands were homogeneously distributed over the entire framework, affected the pore width, but did not alter the crystal structure. Photocatalytic studies demonstrate that the hydrogen evolution rate of the mixed-ligand MOFs decreased with increasing amount of NH_2-ligand. Photoluminescence and absorption spectroscopies revealed that this can be attributed to a higher charge recombination probability in presence of NH_2-ligand. Furthermore, I observed that methanol constitutes the better hole scavenger for Ti-MIL, while triethanolamine is preferable for NH_2-containing MOFs. Another highlight of this work was the discovery that the reduced Ti-species (Ti^{3+}) in the Ti-MIL can be preserved in oxygen-free aqueous solution for up to at least 45 minutes and utilized for water/alcohol reduction on demand upon the addition of hexachloro-platinic acid. This unprecedented behavior of essentially a "conceptual light battery" will stimulate great interest in the community.

In the second part I studied the thermal stability of MOFs and their conversion into nanostructured metal oxides. This barely investigated calcination process has yielded highly-porous, defect-rich TiO_{2-x} particles with large specific surface areas, which demonstrated greatly enhanced photocatalytic properties when compared to the benchmark P25-TiO_2.

The third part of this thesis dealt with the photovoltaic performance of HOIP in perovskite solar cells (PSCs). I modified the PSC fabrication process and investigated different solar cells configurations and preparation routes of perovskite, in particular I developed a two-step process to anneal the photoactive film (i.e. ‘curing’) that led to fewer defects/grain boundaries and improved power conversion efficiencies. Moreover, the work with the collaborators was among the first to prepare Bi-based PSCs that manifest a superior air-stability and moisture stability, albeit with rather low power conversion efficiencies.

Zusammenfassung

Das Thema meiner Dissertation beschäftigte sich mit der Entwicklung neuartiger Materialien für die solare Energieumwandlung. Von großem Interesse sind dabei Hybridmaterialien, die im Vergleich zu ihren Komponenten, zusätzliche synergistische Effekte, wie z.B. eine effiziente Ladungstrennung, zeigen. In dieser Arbeit habe ich für die photokatalytische Wasserstofferzeugung und die photovoltaische Stromerzeugung zwei Arten von organisch-anorganischen Hybridmaterialien untersucht, und zwar metallorganische Gerüstverbindungen (MOFs) und hybride organische anorganische Perovskite (HOIP).

Der erste Teil meiner Arbeit konzentriert sich auf den Einfluss des organischen Liganden in MOFs auf die Materialstruktur, die funktionellen Eigenschaften und die photokatalytische Leistung. Insbesondere wurden Ti-basierte Mischliganden MOFs ($MIL_{1-x}(NH_2\text{-}MIL)_x$-125-Ti) mit unterschiedlichen Liganden Zusammensetzungen entwickelt. Die hergestellten MOFs wurden mit einer breiten Reihe an modernsten Techniken charakterisiert, einschließlich XRD, SEM, DRS, FT-IR, TGA und Stickstoffadsorption. Die Ergebnisse zeigen, dass die verschiedenen Liganden homogen über das gesamte Gerüst verteilt sind und die Porengröße beeinflussen, jedoch die Kristallstruktur nicht verändern. Die photokatalytischen Studien zeigen, dass die Wasserstoffentwicklungsrate der Mischliganden-MOFs mit zunehmendem Gehalt an NH_2-Liganden abnahm. Photolumineszenz- und Absorptionsspektroskopien konnten zeigen, dass dies auf eine höhere Wahrscheinlichkeit der Ladungsrekombination in Gegenwart des NH_2-Liganden zurückzuführen ist. Außerdem konnte ich feststellen, dass Methanol einen besseren „Lochfänger“ für Ti-MIL darstellt, während Triethanolamin für NH_2-haltige MOFs vorzuziehen ist. Ein weiterer Höhepunkt dieser Arbeit ist die Entdeckung der Stabilität (bis zu mindestens 50 Minuten) der reduzierten Ti-Arten (Ti^{3+}) in Ti-MIL in sauerstofffreien wässrigen Lösungen. Bei Bedarf können diese unter Zusatz von Hexachlorplatinsäure zur Wasser-/Alkoholreduktion eingesetzt werden. Dieses beispiellose Verhalten einer im Wesentlichen "konzeptionellen Lichtbatterie" wird ein großes Interesse in der Community wecken.

Im zweiten Teil der Arbeit untersuchte ich die thermische Stabilität von MOFs und deren Umwandlung in nanostrukturierte Metalloxide. Dieser kaum untersuchte Kalzinierungs-prozess führte zu hochporösen, defektreichen TiO_{2-x}-Partikeln mit großer spezifischer Oberfläche, die im Vergleich zum Benchmark P25-TiO_2 deutlich verbesserte photokatalytische Eigenschaften zeigen.

Der dritte Teil dieser Arbeit beschäftigte sich mit der photovoltaischen Leistung von HOIP in Perovskitsolarzellen (PSCs). Ich habe dafür den PSC-Herstellungsprozess modifiziert und verschiedene Solarzellenkonfigurationen und Präparationswege von Perovskiten erforscht. Vor allem habe ich ein zweistufiges Verfahren zum Glühen der photoaktiven Folie entwickelt (d.h. "Härten"), das zu weniger Defekten/Korngrenzen und verbesserten Wirkungsgraden bei der Energieumwandlung führte. Zudem konnte ich mit Hilfe von Kooperationspartnern Bi-basierte PSCs entwickeln, die eine hervorragende Luft- und Feuchtigkeitsstabilität aufwiesen, wenn auch mit geringeren Wirkungsgraden.

Table of Contents

Table of Figures

1 Introduction

This chapter provides an overview on the topic of this thesis as well as on the state-of-the-art including the scientific background of the research field.

1.1 Energy Issue

As the basis for living, we human beings need energy in the form of food and heat. Besides that, energy also plays an undebatable, important role in modern society, related to economy, security and environments. The energy sources can be classified as renewable energy and non-renewable energy. Non-renewable energy sources, also known as conventional energy, refer to energy obtained from fuels (coal, natural gas, diesel and oil) which are exhaustible sooner or later with time. Renewable energy refers to the energy acquired from plentiful sources available in nature. There are five commonly used renewable energy sources: biomass, tidal energy, geothermal, wind and solar energy.

When rating the merit of energy source, not only the abundance needs to be considered, but also its sustainability and environmental impact. Fossil fuel has become the main energy source in civilized society. For the past couple of centuries, the energy supply has come to rely more and more on fossil fuels. However, the fossil fuel as an energy source is neither renewable nor sustainable. As the demand for fossil fuels has increased, the cost of using them has also increased and each year we find ourselves with larger and larger energy bills. Another big issue of the fossil fuels is the energy consumption related emissions. Burning coal, petroleum and other fossil fuels is the primary mean by which we produce electricity, but it leads to high air, water pollution and global warming.

The concern about environment as well as the rapidly rising energy-demand have motivated the exploitation of renewable, clean energy. Recent years have seen the dramatic growth of renewable energy and the decreasing energy share of oil and coal (Figure 1-1).

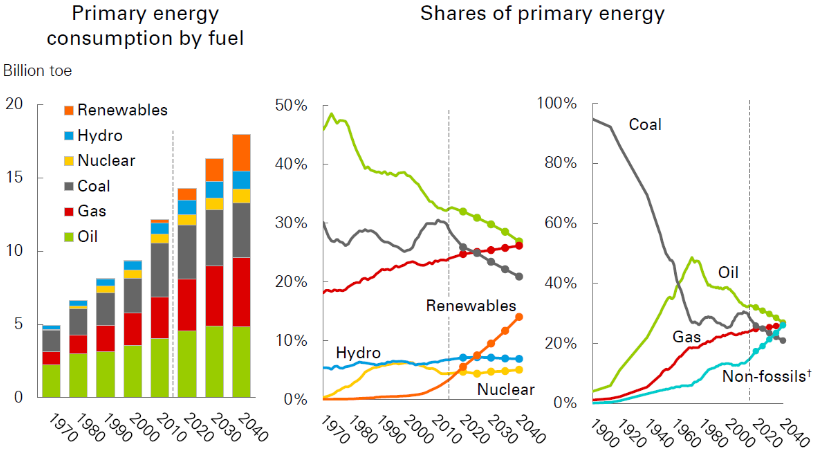

Figure 1-1 Overview of energy supply and demand from 1970-2040(BP Energy Outlook 2018) Non-fossils includes renewables, nuclear and hydro.*

The Sun provides Earth with a staggering amount of energy (Figure 1-2). For example, in 2007, the amount of energy that humans consume annually is 4.6 x 1020 joules,[1] which equals the energy that the sun delivers to the Earth within one hour. Since solar energy system also has the minimal impact on the environment, the conversion of solar energy has become a hot topic in recent years.

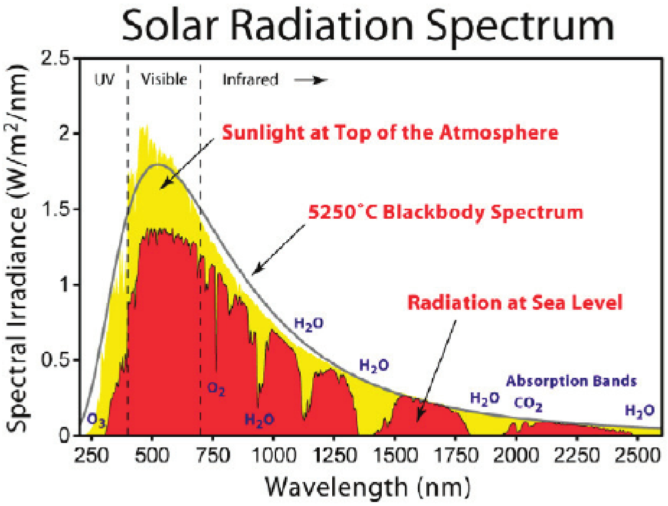

Figure 1-2 Solar spectrum (Data from American Society for Testing and Materials (ASTM) G-173-03 reference spectra) ref[2]

Actually, ever since Earth was born, solar energy has been providing energy for almost all living organisms. Over time, with the development of technology, devices have been applied to collect the solar energy more efficiently as well as to convert it into other forms (Figure 1-3). For example, the solar thermal systems can turn sunlight into heat, which help residents to reduce their carbon footprint efficiently; with photovoltaic devices, sunlight can be converted into electricity and the commercial crystalline silicon solar cell has a relative stable efficiency at around 22%.[3] Moreover, inspired by nature, another attractive approach is to store solar energy in the form of chemical bonds as plants do; therefore, photosynthesis and photocatalysis have raised great research interest.

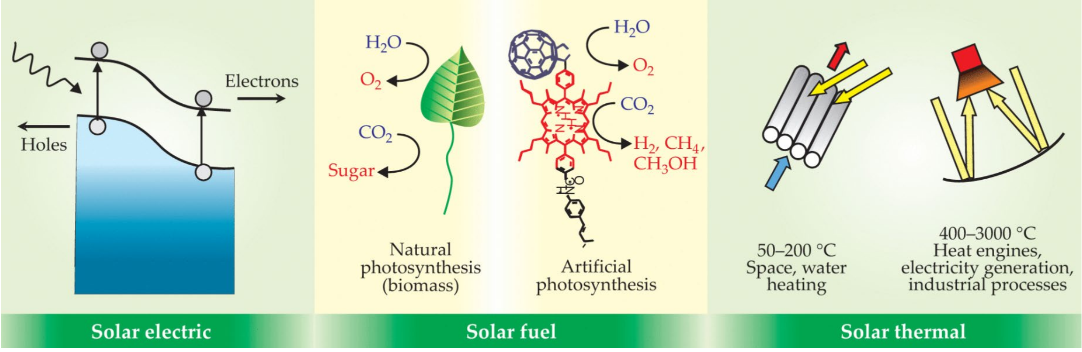

Figure 1-3 Illustration of solar energy application[4]

1.2 Photocatalysis

Catalysis was defined by Berzelius in 1835[5] and refers to the phenomena that a reaction can be accelerated through reduction of kinetic barriers in the reaction process. The chemicals used to reduce the barriers are called catalyst.[6]

Photocatalysis is in the category of catalysis, in which, light in the form of photons is consumed instead of thermal energy to activate the catalytic process. In 1972, Honda and Fujishima[7] demonstrated the first photo-assisted electrochemical splitting of water. Ever since, the interest in photocatalysis has been boosted, also as a consequence of the increasing social concern about energy supply and environmental issues. The applications of photocatalysis are numerous, including environment purification, health protection, energy conversion, chemicals refinery, photocatalytic organic synthesis etc. In addition, the conversion and storage of the energy of photons into chemical bonds, such as into hydrogen (e.g. via water splitting) or hydrocarbons (e.g. via CO_2 reduction) have become prevalent.

1.2.1 Photocatalytic Water Splitting based on Inorganic Semiconductors

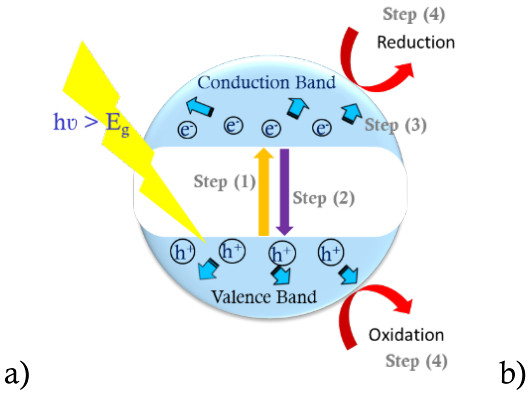

Figure 1-4 Major processes involved in a classic photocatalysis system based on semiconductor

Photocatalysis can be divided into homogeneous and heterogeneous catalysis. In heterogeneous photocatalysis, the catalyst and the reactants exist in different phases. This thesis focuses on heterogeneous photocatalysis based on semiconductor photocatalysts.

Inorganic semiconductors (such as TiO_2,[8-11] Fe_2O_3[12-14]) are the most widely used and investigated photocatalysts. Figure 1-4(a) displays the major processes in a classic photocatalysis system based on inorganic semiconductor.

1) Step 1: light absorption and charge generation – Photons with energy (hυ) equal to or higher than the band gap (E_g) of the semiconductor can be absorbed and produce excitons. In inorganic semiconductors, the energy required to dissociate the excitons into free charge carriers is quite small. At room temperature exciton dissociation (charge separation) can be achieved. As a result, the electron in the valence band (VB) jumps to the unoccupied conduction band (CB), leaving the hole in the valence band.

2) Step 2: charge recombination – Accompanied by the charge generation process, there is the charge recombination, in which the e^- and h^+ annihilate each other, non-radiatively or radiatively, dissipating the excess energy as heat or photon, respectively. Figure 1-4 illustrates only the band-to-band recombination model. In reality, there are also trap-assisted recombination, Auger recombination, surface recombination etc.[15] Charge recombination is usually the efficiency-limiting factor in photocatalysis system; one strategy to supress this process is the utilisation of cocatalysts, charge scavengers or an electric field.

3) Step 3: charge transport and transfer – Photogenerated charge carriers diffuse to the surface of the catalysts and transfer to the adsorbates. The competition of charge transfer and charge loss dictates the photocatalytic efficiency.

4) Step 4: redox reaction – charge carriers react with electron acceptors or donors adsorbed on the surface of the photocatalyst to induce reduction or oxidation reactions, repectively. In addition, one needs to consider the kinetics regarding the diffusion of the reactants to catalytic sites, adsorption and surface diffusion of intermediates and product desorption.

As discussed before, H_2 is another sustainable energy fuel. The advantage of using hydrogen as an energy carrier is that when reacting with oxygen and producing electricity, the only byproducts are water and heat, no greenhouse gas emissions. In addition, the energy density of H_2 is about 61,100 BTUs per pound, three-times higher than that of gasoline (i.e. 20,900 BTUs per pound).[16] Moreover, hydrogen can be produced from various sources, such as from methane, gasoline, biomass, coal or water.[17] Especially, if hydrogen is produced from water, then a sustainable production cycle is formed. Therefore, photocatalytic hydrogen generation from water fulfills the criteria of a sustainable and clean energy development and has become the research focus of this thesis.

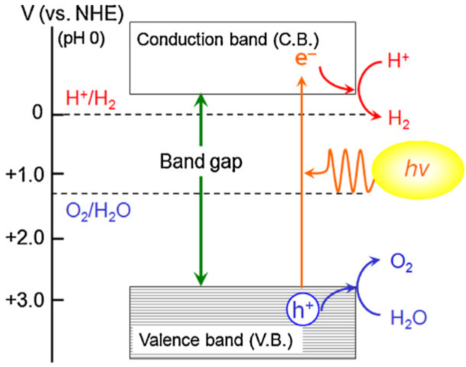

Figure 1-5 Photocatalytic H_2 evolution based on semiconductor. Band potential based on NHE, pH=0.[18]

In a typical photocatalytic water splitting system, the semiconductor usually acts as both the light absorber and the catalyst. As illustrated in Figure 1-5, after light absorption, the electrons in the CB reduce H^+ to H_2, while the holes left in the VB participate in the O_2 generation. The overall photocatalytic water splitting reaction is written as below:

Overall Reaction $2H_2O + hv = O_2 + 2H_2$ 1-1

Reduction (HER) $2H^+ + 2e^- = H_2$

Oxidation (OER) $H_2O + 2h^+ = 2H^+ + 2{\bullet}OH$

$2{\bullet}OH + 2h^+ = O_2 + 2H^+$

The prerequisite for the occurrence of a photocatalytic redox reaction is the band structure alignment between the catalyst and the reactants; for instance, in water splitting, the CB level of the semiconductor needs to be more negative than the H^+ reduction potential and its VB level should be more positive than the H_2O oxidation potential. Importantly, the overall water splitting reaction is a thermodynamically uphill reaction with a large positive change in Gibbs free energy[19], 237 kJ/mol. Therefore, a minimum band gap of 1.23 eV is required. In practice, over-potentials are required to overcome additional barriers induced by charge transfer and reactant adsorption, thus semiconductors with band gaps above 1.8 eV are preferred.

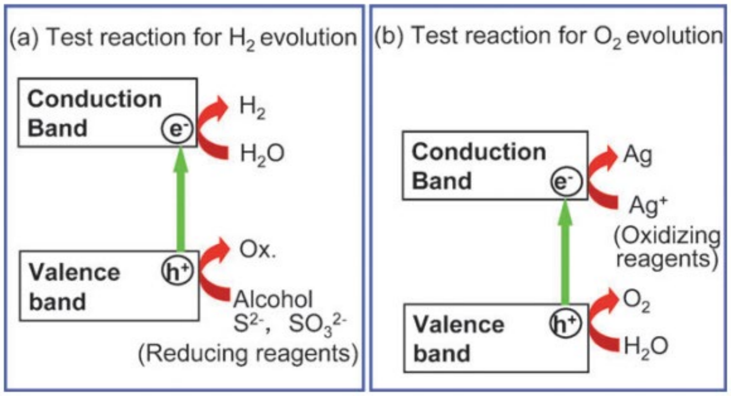

Figure 1-6 H_2 or O_2 evolution in the presence of sacrificial reagents - half reactions of water splitting[20]

The overall reaction of water splitting can be divided into two half reactions: water oxidation to oxygen and water reduction to hydrogen. Noticeable, oxygen evolution is kinetically more challenging, because HER requires two electrons per molecule of generated hydrogen, while OER needs four holes (electron-hole pairs) per molecule of generated oxygen (Equ. 1-1). Another essential factor for the overall performance of the water splitting reaction is the inhibition of back reaction, i.e. water formation.

Because the overall water splitting is a very complicated process, therefore, photocatalytic reactions, with the assistance of sacrificial agent, focusing either on hydrogen evolution or on oxygen evolution have become popular. As water splitting means to split water into H_2 and O_2 in a stoichiometric amount in the absence of sacrificial reagents,[20] the reactions illustrated in Figure 1-6) should be referred to as hydrogen evolution reaction (HER) and oxygen evolution reaction (OER), respectively, the so-called half reactions.

1.2.2 Strategies to Improve the Photocatalytic Efficiency

Below are examples of the developed strategies to improve the efficiency of photocatalysts with respects to the working principles:

- Enhancement of light absorption process: the electronic band structure of the photocatalyst determines the light absorption and subsequent the photocharge generation process. Various methodologies have been investigated to optimize the light absorption process, including band gap tuning (the introduction of defects and dopants into inorganic semiconductor) as well as the tuning of chromophores in organic semiconductors. For example, the hot topic of ‘black’/‘colorful’ TiO_2 is within this scheme.[21-23]
- Improvement of charge transfer/diffusion & inhibition of charge recombination: from the materials point of view, the methods to improve charge transfer/diffusion can be further divided by:
    - morphology control: for instance, the anisotropic morphology, such as 2D or 1D (nanorods or nanotublar) which can facilitate charge transfer or diffusion along certain direction;
    - defects control in the material, including the control of the grain boundaries, dislocation, vacancies etc., as they can be the active sites for recombination.
    - nanosized materials, aiming at reducing the diffusion length from the bulk to the surface, thus lowering the charge recombination probability.

  - shape/facet control: different crystal facets possess different reactive activity, for example, the (101) of anatase $TiO_2$was reported to be more active than other facets.[24]
- to increase the number of available active sites:
  - mono-dispersed nanoparticles or open meso/micro-porous materials, which possess higher surface area and promote the ad/desorption of reacting species as well. For example, gyroidal Ta_2O_5;[25] metal-organic frameworks (MOFs)[26]

In this thesis, I focused on organic-inorganic hybrid materials, i.e. metal organic frameworks (MOFs), as a novel type of catalyst for photocatalytic HER.

1.3 Metal Organic Framework

MOFs have unique properties that differentiate them from both conventional inorganic and organic semiconductors; the investigation of MOFs in the photocatalysis field is comparatively new. Therefore, a brief introduction to the material's historical development, unique structures and properties, synthesis strategies and the status as photocatalysts is presented.

First, what is a MOF?

1.3.1 Historical Development of MOFs

The concept of MOFs was first proposed by Yaghi and Li in 1995[27]. Inspired by microporous inorganic materials, such as zeolites, they designed the first 3D metal-organic framework. This new type of material was composed of metal-carboxylate (MC) layers and organic spacer unit (U) layers, as illustrated in Figure 1-7. For the first MOF, cobalt carboxylate was selected as the 'MC unit' and pyridine as the 'U unit'. In this structure, the MC layer is based on the metal-carboxyl bonding between neighbouring MC units forming a 2D structure. At the same time, the nitrogen of pyridine is bonding two Co atoms of two different MC layers via Co-N dative bond. The anchored pyridine ligands are positioned perpendicular to the MC layers, and the mutual π-stacking interaction between the pyridines further help to hold these layers tightly together. The distance between pyridines is 4-6 Å, which introduces voids/pores into this network, contributing to the final porous structure.

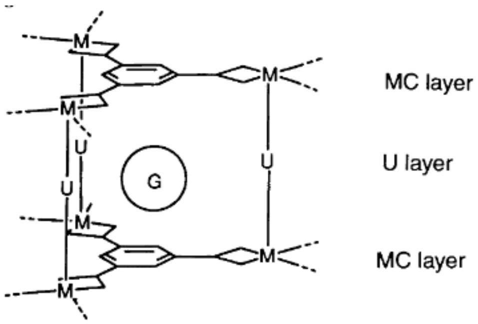

Figure 1-7 Schematic illustration of building units in the first MOF. MC unit is cobalt carboxylate; U unit is pyridine; G represents the guest molecules adsorbed into the pores of the framework. [7]

Beside those pyridine linkers that constitute the network, there are also guest pyridines, which usually occupy the pores between MC layers. Upon heating or solvent exchange, different molecules can be adsorbed inside these channels, but mainly aromatic compounds due to favorable π interactions.

Another early example of the construction of cavity-containing frameworks was reported by MacGillivray et al.[28] The authors took advantage of hydrogen bonding and π–π interactions between the grids to obtain the ordered alignment of transition metal-ion layers ($[M(4,4'\text{-bipy})(pyca)(H_2O)_2]^{+1}$ (where M = Co(II) or Cd(II)). These interconnected rectangular microchannels were able to accommodate both charged and neutral guest molecules.

Due to the functional characteristics and the structure resembling a 3D network with open channels, MOFs have become immediately popular after their invention. However, many early MOFs were limited by low thermal and chemical stability. Without guest solvents, the porosity often could not be retained, thus the pores collapsed. It was not until 1999 that the problem of stability was solved when the strategy of metal carboxylate cluster chemistry was applied.[29] Organic dicarboxylate linkers were introduced to coordinate metal tetrahedron clusters, and the rigid and divergent character of the added linker allowed the articulation of the clusters into a three-dimensional framework structure.

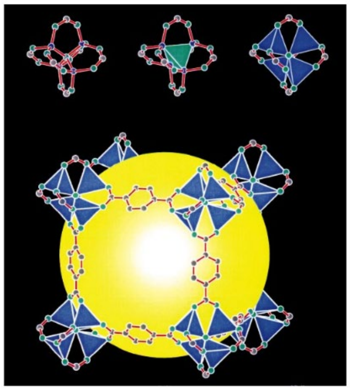

Figure 1-8 Schematic Illustration of Zn-based MOF: MOF-5. In the left ball and stick model, Zn: blue; O: green; C: grey. In the bottom, the ZnO_4 tetrahedra was indicated in blue. One of the cavities in the $Zn_4(O)(BDC)_3$ was indicated by a yellow sphere.[29]

MOF-5, as an early and successful example of MOFs constructed with the coordination chemistry, is discussed here to elaborate the assembly process of MOF in more detail (Figure 1-8). The tetranuclear supertetrahedral cluster motif (i.e., the Zn^{2+} and the appropriate carboxylic acid), yields the oxide-centered cluster as a distinct and well-defined unit. The core of the cluster is a single O atom bonded to 4 Zn atoms, forming a O-centered Zn_4O tetrahedron. Then each Zn forms its own tetrahedron, and the 4 Zn-centered tetrahedrons are connected via Zn-O-C-O-Zn, as shown in the top of Figure 1-8. The resulting cluster possesses a chemical composition of $Zn_4(O)(CO_2)_6$ and can be seen as a secondary building unit (SBU). The organic linker is terephthalic acid, which contains two terminal carboxylate units, each coordinating to one SBU. Consequently, the SBUs sharing the same organic linker are connected to each other, further expanding into a 3-D network. Therefore, SBU clusters may serve as the vertices of the framework, and linkers as the edges/struts. Depending on the radii of the atoms, the volume percentage of unoccupied space (yellow ball in Figure 1-8) can be as high as 80%, which is the reason that MOFs can accommodate a large number of solvent molecules as well as other guest molecules.

It is interesting to compare the similarity between the network of MOF-5 with inorganic zinc phosphates, in which P atoms, instead of C atoms, form PO_4 tetrahedra. Thus, the link between Zn-oxo clusters is O_2-P-O_2 phosphate instead of O_2-C-C_6H_4-C-O_2. However, the surface area of MOFs, which is in the range of thousands of m^2/g, is much larger than that of most purely inorganic materials[30].

Since then a lot of new MOF structures have been synthesized, with a large variation of clusters and ligands.

1.3.2 Synthesis and Characterization of MOFs

The key to a successful MOF synthesis lies in the formation of well-ordered 3D network built with metal-oxo clusters and organic ligands, via intra-molecular interactions. These interactions may include coordinative bonding, π-stacking, hydrogen bonding etc. Stronger interactions are favorable for the framework's stability; therefore, most MOFs are currently built with coordination bonding.

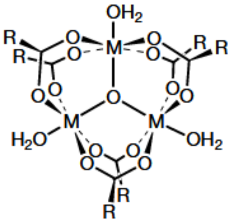

Figure 1-9 Oxo-bridged trinuclear metal carboxylates $[M_3(\mu_3\text{-}O)(O_2CR)_6(H_2O)_3]^{n+}$ *(M= divalent or trivalent transition metal ions,* O_2CR*= organic carboxylate anions)*[14]

The choices of both metal and organic linker are of vital importance to obtain a robust inorganic-organic framework. Apart from the aforementioned tetranuclear clusters, one popular SBU category is oxo-bridged trinuclear metal carboxylates (often known as 'basic' carboxylates) $[M_3(\mu_3\text{-}O)(O_2CR)_6(H_2O)_3]^{n+}$ (M = divalent or trivalent transition metal ions; O_2CR = organic carboxylate anions) (Figure 1-9). They are commonly found in transition metal coordination chemistry and readily assembled from metal ions and carboxylates[31]. For example, Seo and co-workers[31] used a rigid chiral organic molecule with a carboxylic group at one end and a pyridyl group at the other to form trinuclear units (SBUs) (Figure 1-10). These SBUs further generate 2D infinite layers with large 1D chiral channels alongside the c axis, endowing the materials with unique characteristics such as enantioselective catalytic activity[31].

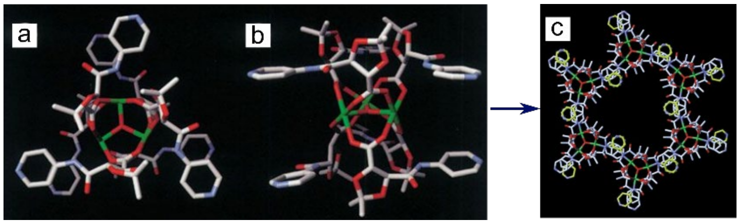

Figure 1-10 a) and b): top and side view of the trinuclear SBUs; c): the hexagonal framework with large pores that is formed with trinuclear SBUs. Zn atoms are shown in green, O in red, N in blue and C in white.[14]

Various preparation strategies have been implemented to synthesize MOFs, including solvothermal synthesis, microwave synthesis, vapor diffusion, gel crystallization, solventless synthesis, sonochemical and electrochemical synthesis. Each strategy has its own advantages as well as disadvantages. For instance, hydrothermal synthesis is a simple approach with high reproducibility and scalability that can yield large crystals[32]. However, its limits include the extensive reaction time and the reliance on toxic solvents. Correspondingly, solventless synthesis is a rapid, non-toxic strategy, but quite demanding when it comes to the precursors. As the focus of this thesis does not lie on the comparison between different synthesis strategies, all the MOF preparations in this work has been accomplished by the most versatile solvothermal synthesis[33].

One appealing characteristic of MOFs is their high structural tunability. Both the inorganic nodes and the organic linkers can be modified easily. In addition to single-metal-oxo cluster, multi-metal as well as tetra- and octamers clusters have been investigated[34]. Yaghi et al have obtained 3-D open-framework solids with tetrahedral cluster $Ge_4S_{10}^{4-}$ and rod-like ligand 4,4'-bipyridine. After copolymerization reactions with metal (II) ions such as Mn, Fe, Co, Cu, and Zn, the final product $M_xCo_{1-x}Ge_4S_{10}\cdot 2(CH_3)_4N$ ($x = 0.86$, M = Mn; $x = 1$, M = Mn, Fe, Co, and Zn) still retained a porous, crystalline structure.

The functionalization of the organic ligands has become another feasible and promising strategy to tailor the structure and, hence, the properties of MOFs. For example, replacing $-SO_3H$ group of the organic linker with -OH group has enabled a new MOF with higher selectivity for adsorption towards CO_2 vs CH_4 as well as a higher NH_3 uptake capacity[35]. Another example is the post-synthetic functionalization of the organic ligand with –NH_2 group, which has shifted the light absorption edge of the parent MOF from 450 nm to almost 700 nm[36].

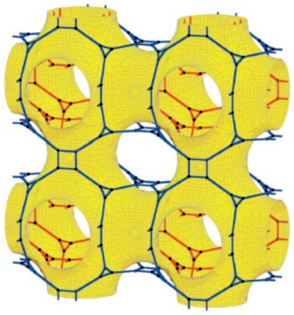

Figure 1-11 Two MOF-14 frameworks (blue and red) interwoven about a P-minimal surface without intersecting the surface.[37]

Beside the SBU and organic ligand tuning, single MOFs can build into more complex structures. A self-hierarchical structure of MOF (Figure 1-11) has been prepared via an interweaving procedure. Interweaving (i.e. catenation) allows mutual reinforcement of the exceptionally large moieties fabricated with 4,4’,4"-benzene-1,3,5-triyl-tribenzoic acid, which alone is expected to be insufficiently rigid to sustain an open framework.[37] This reinforcement has enabled the structure to be more stable in both air and most solvents.

Instead of a trial-and-error strategy, the rational development of new MOFs is increasingly supported by theory, as the computational methodologies for MOFs have greatly developed over the recent years and cover methodologies ranging from atomic-partial charge calculation, force field simulation to density-functional theory (DFT).[38] For instance, Snurr et al. investigated the interaction between NH_3 and surface functional groups in MOFs and predicted the ammonium adsorption behaviour in different MOFs[39], providing guidelines for MOF design for certain application purposes[40].

In recent years, the characterization of MOFs has matured, now involving a range of techniques, such as X-ray diffraction (XRD), physisorption, infrared spectra (IR), solid state nuclear magnetic resonance (NMR), thermal gravimetric analysis (TGA) etc. Notably, these techniques can probe not only the pristine MOFs, but also their sorption properties regarding guest molecules. For instance, IR records the molecular vibrational signals and is thus sensitive to the binding and coordination situation of both, the linker and guest molecules.

1.3.3 Application of MOFs

MOFs' versatile applications stem from their highly porous structure and multi-functionality of the metal-oxo cluster and organic component.

As mentioned before, the pore volume fraction in MOFs can reach as much as 80% and the pore sizes are in the order of angstroms. As a result, the specific surface areas can reach values as high as 7000 m^2/g, such as reported for two Cu-based MOFs[41]. In comparison, the surface areas of inorganic porous materials, e.g. zeolites, are significantly lower, i.e. typically in the range of several hundred m^2/g[42]. In addition, zeolites possess a rigid pore structure, while the presence of organic ligand in MOF allows for a flexible one that is of particular interest for applications such as in molecular sieving. Moreover, zeolites behave more like an apolar adsorbent, while the polarity in MOFs can be tuned via ligand chemistry and introduction of unsaturated coordination sites[43]. Therefore, the porosity-based properties of MOFs differ greatly from those of conventional inorganic porous materials and have thus attracted enormous research enthusiasm since.

In this respect, typical applications of MOFs benefit from guest molecule interactions and thus include gas storage, liquid separation, sensing, drug delivery and chemical purification. Due to the high pore volume, MOFs have been first exploited as gas storage materials for H_2, CO_2, CH_4 etc., showing their excellent gas storage capacity. Later, their application diversified as researchers discovered that the adsorption properties of MOFs follow a commensurate adsorption type[44]. Consequently, MOFs show selective adsorption capabilities, thus offering great potential for selective gas adsorption and separation[45-47].

Furthermore, the pores/channels in MOFs can be positively or negatively charged, which lays the basis for ion exchange as well as selective incorporation of charged metal complexes and organic species (eg., xylene isomers, organic dyes[48-49]) in liquid phase[50]. Hence, MOFs extend their applications to waste purification[51,52-53].

Recently, MOFs have also demonstrated potential in the medical field, i.e. for controllable drug release[54] and slow release of metal ions such as Ag^+ for anti-bacteria treatment[55]. Moreover, MOFs have been used as 'reaction cages' for the degradation of toxicants, such as 2-chloroethyl ethyl sulfide and 2-chloroethylphenyl sulfide, nerve and blister agents.[56]

Another appealing application is the utilization of MOFs as catalysts, for example, in the degradation of sulphur mustard[57]. Due to their selective adsorption character, some MOFs have shown selective catalytic properties in the oxidation of organic species - selective oxidation of benzyl alcohol into benzaldehyde[58], selective oxidation of amines to imines[59]. Moreover, after removing guest species from the pores of the MOF, the unsaturated metal sites me become accessible and thus can act as active catalytic sites during a reaction[60]. Recently, MOFs have become popular in the field of photocatalysis, especially for CO_2 reduction and photocatalytic water splitting[61].

1.3.4 Prospects of MOFs for Photocatalysis

1.3.4.1 Different Roles of MOFs in Photocatalysis

MOFs possess various advantages in photocatalytic applications; their potential roles in a photoredox system are summarized in Figure 1-12.

a) MOFs as the photosensitizer: the MOF is responsible for efficient light absorption and charge generation/separation, thus increasing both, the number and lifetime of charge carriers. The absorption likely happens within the organic linker, while the redox reaction takes place on the surface of an added catalytically active species (e.g. metal oxide nanocluster,[62] polyoxometalates[63-64]).

b) MOFs as the catalyst: in this case, the charge generation is accomplished by an added photosensitizer (e.g. quantum dot, organic dye[65]). The photogenerated charges then transfer to the MOF, specifically, into the metal-oxo nodes, where the redox reaction can proceed.

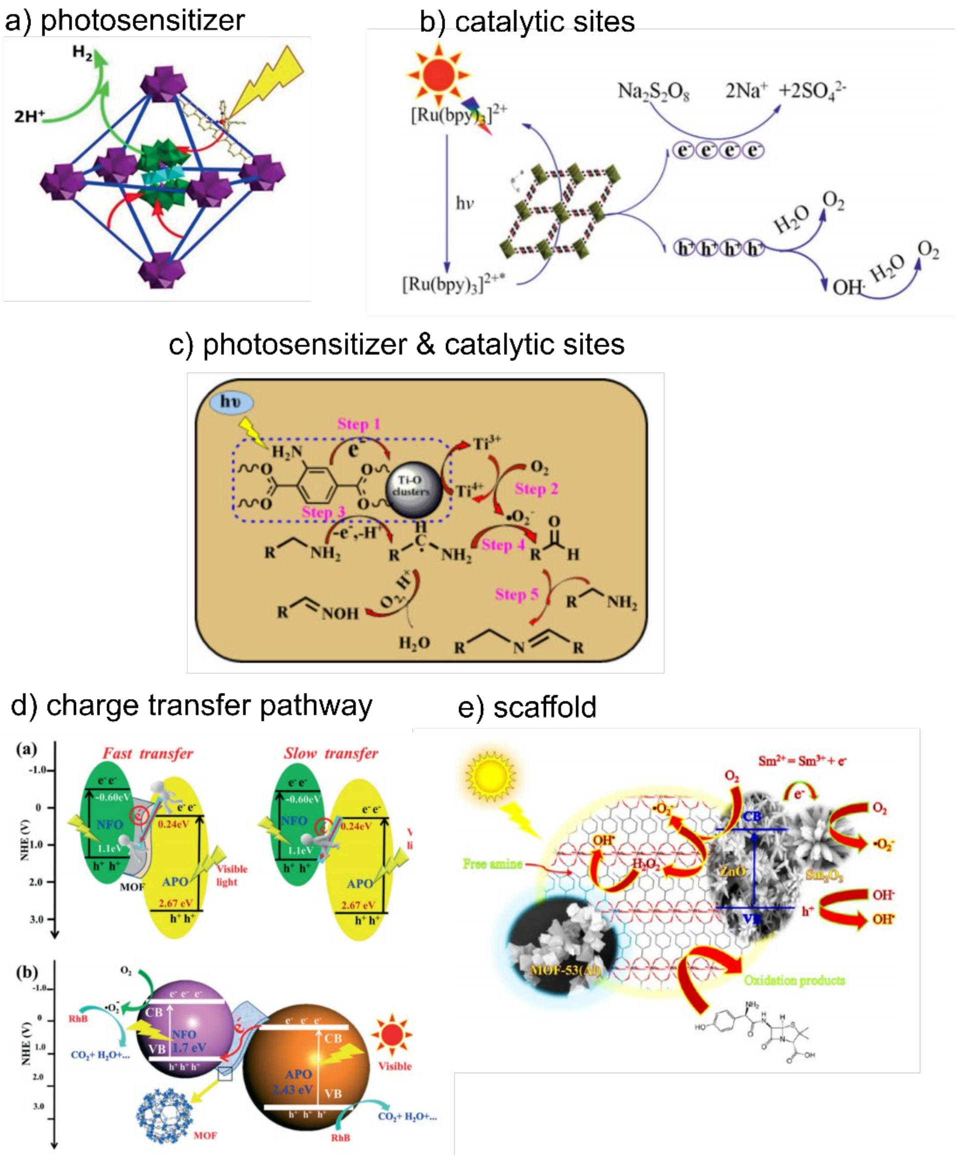
a) photosensitizer

b) catalytic sites

c) photosensitizer & catalytic sites

d) charge transfer pathway

e) scaffold

Figure 1-12 Different roles of MOFs in photocatalysis system: a) as photosensitizer[56];) as catalytic sites[59]; c) as both photosensitizer and catalytic sites[53]; d) as charge transfer pathway[66]; e) as scaffold to support other materials[67].

c) MOFs as the true photocatalyst: herein, the MOF combines both roles as photosensitizer and catalyst. In a typical reaction system, the organic linker absorbs light to produce photogenerated charge carriers, which then transfer to the meal-oxo clusters and induce subsequent photoredox reactions.[59]

d) MOFs as the charge-transporting channel: the MOF works neither as photosensitizer nor as catalytic site. Instead, the MOF offers an active component that facilitates the charge separation and the charge transfer between the photosensitizer and the catalyst in a heterogeneous system.[66]

e) MOFs as a scaffold or host: the open porous structure in MOFs enables the accommodation of photocatalytic species, while, at the same time, the reactants can diffuse into the pores freely. Such systems typically show an enhanced photocatalytic performance due to the spatial separation of the (typically molecular) active species (i.e. by preventing their agglomeration).[67]

The above examples highlight the different roles of MOFs, however, the real photocatalysis system often includes more than one scheme and the roles of MOFs vary accordingly.

1.3.4.2 Charge Generation and Separation in MOFs

Similar to a conventional semiconductor, the major photocatalytic processes in a MOF can be divided into light absorption, charge generation/separation, charge transfer and redox reaction on the surface (Figure 1-4). However, owning to the unique organic-inorganic hybrid structure, the mechanism of charge generation and separation in MOFs is different from that of the inorganic semiconductors.

If we take a closer look at the configuration of the band structure of MOFs, we will see that it resembles a molecular heterojunction, consisting of the organic component and the metal-oxo cluster. The light absorption can thus occur either in the organic linker or in the inorganic SBUs:

(1) within the organic linker, the electron promotion happens between the HOMO (highest occupied molecular orbital) and LUMO (lowest unoccupied molecular orbital);

(2) within the metal-oxo cluster, the electron advances from the 2p orbital of oxygen to the unoccupied d or f orbital of the metal ions.

The alignment of different energy levels determines the subsequent charge separation and energy transfer. Figure 1-13 illustrates the possible photon absorption as well as charge transfer schemes within MOFs.

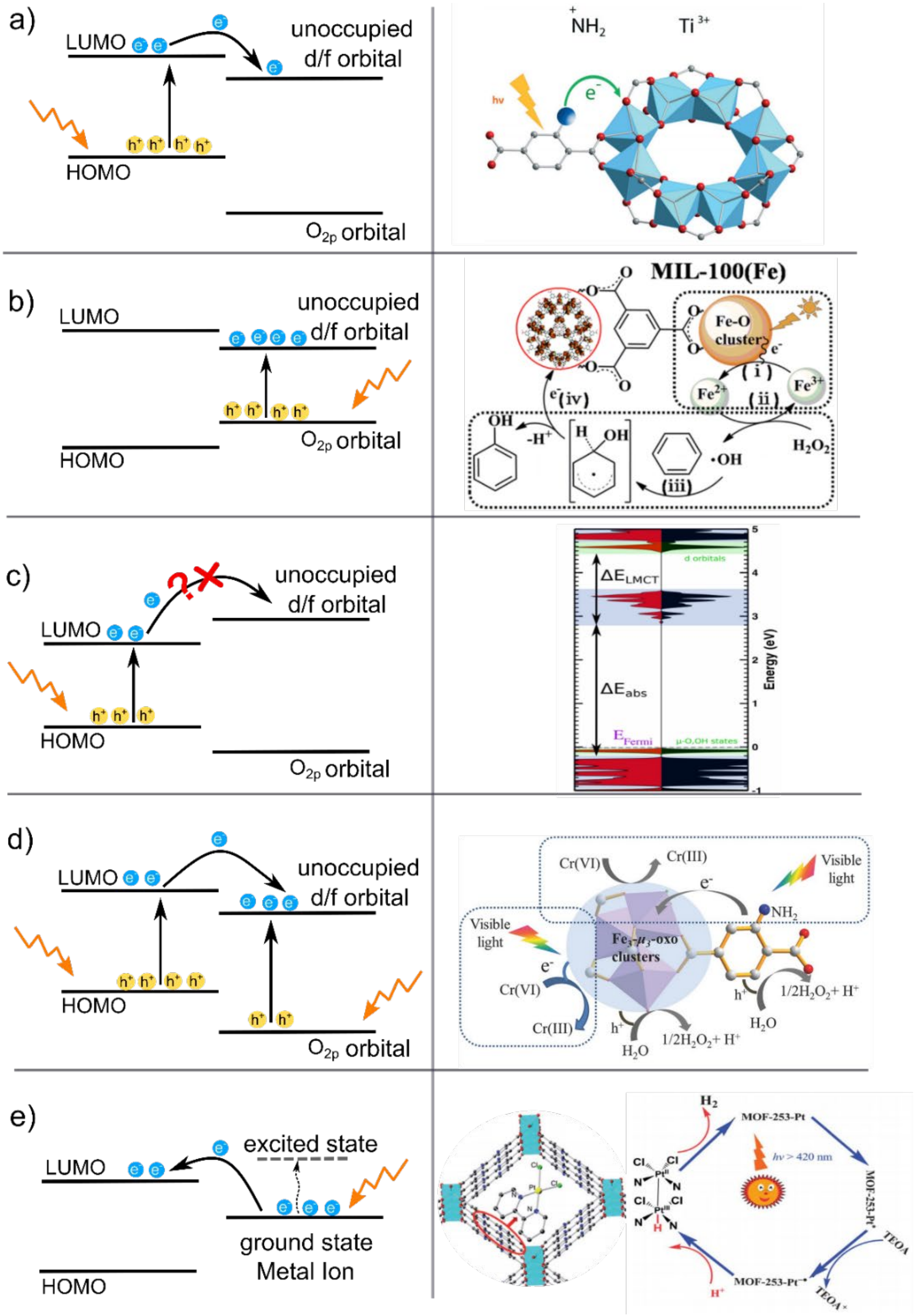

Figure 1-13 Major charge transfer mechanisms in MOFs: a) ligand to metal charge transfer; b) charge generation within metal cluster; c) charge generation within ligand; d) charge generation within both ligand and metal cluster; e) metal to ligand charge transfer. (the right column are reprinted from references 70,71,73,18,76)

a) ***L**igand to **M**etal **C**harge **T**ransfer (LMCT):*

The organic ligand of the MOF can absorb light and yields electron-hole pairs. The photogenerated electrons are then injected into the metal-oxo cluster, leaving a hole on the organic moiety.

Let us take NH_2-MIL-125-Ti as an example (Figure 1-13(a)): upon irradiation, the organic ligand (NH_2-BDC) gets excited – the electrons in the HOMO level absorb the energy of photons and get promoted to the LUMO level – via a n-π^* electron transition.[26, 68] Then, due to the overlap of d orbital of Ti^{4+} and the π^* orbital, the electron further transfers from the organic ligand to the unoccupied Ti d^0 orbital, completing a ligand-metal charge transfer, therefore reducing Ti^{4+} to Ti^{3+}.[69] The hole (h^+) is left on the organic component. EPR has detected the presence of Ti^{3+} upon light irradiation, confirming the LMCT mechanism.[70]

In the LMCT mechanism, photogenerated electrons and holes reside in different components of a MOF, which facilitates the separation of the electron-hole pairs and contributes to a longer lifetime of charge carriers[61]. Therefore, LMCT is the most common charge generation and separation process in active MOF photocatalysts.

b) ***C**harge **G**eneration within **M**etal **C**luster:*

Alternatively, when the energy of incident light is not high enough to excite the organic linker, but sufficient for the metal-oxo cluster, the charge generation occurs within the inorganic SBUs.

A typical example is the MIL-100 (Fe)[71] (Figure 1-13 (b)), in which charge carriers get excited exclusively in the Fe-oxo cluster and are separated by the transfer of electrons from O^{2-} to Fe^{3+} leading to Fe^{3+} to Fe^{2+} reduction. The subsequent redox reaction then regenerates the photoexcited MOF to its original state.

c) ***L**igand to **L**igand **C**harge **T**ransfer (LLCT):*

Due to the band mismatch between the organic and inorganic component, the photogenerated charge carriers in the organic linker may not be allowed to transfer to the metal-oxo cluster. This can be seen in Figure 1-13(c), with the example of Zr-based MOF UiO-66[72]. ΔE_{abs} corresponds to the energy required to excite the linker; ΔE_{LMCT}

corresponds to the energy needed to transfer the excited electron to the node's unoccupied d orbitals. In the case of UiO-66(Zr), there is no overlap between the unoccupied d orbitals (green shade) and the excited linker states (blue shade), consequently, the charge transfer from the ligand to the metal cluster is restricted by the existence of ΔE_{LMCT}.[73] In other words, the photogenerated charges are constrained in the organic ligand, which is unfavorable for the photocatalytic reaction of the sole MOF.

d) ***D****ual* ***E****xcitation* ***P****athways*:

In contrast to the aforementioned cases, the dual excitation mode describes systems, where the light absorption occurs both in the organic linker and in the inorganic cluster.

NH_2-MIL-88B(Fe) is an example to illustrate such a process (Figure 1-13(d)). Under light irradiation, both the amine-functionalized organic linker and the Fe_3-μ_3-oxo clusters get excited. The electrons from the excited organic linker further transfer to the Fe_3-μ_3-oxo clusters and, together with the photogenerated electrons from the Fe_3-μ_3-oxo clusters, conduct the redox reaction[74-75].

e) ***M****etal to* ***L****igand* ***C****harge* ***T****ransfer* (MLCT):

There is another frequently mentioned charge transfer pathway related to photoactive MOFs, metal-ligand-charge-transfer (MLCT) (Figure 1-13(e)), namely after charge generation, the photogenerated electrons from metal-oxo cluster migrate to the organic moieties. However, MLCT is not common in sole MOF, as in most cases, metal nodes tend to 'collect' the photogenerated electrons and act as the photocatalytic sites. MLCT has been reported more in heterogeneous system, for example, post-modification of MOF structure with light- or catalysis active species.[18]

Xu et al[76] immobilized a platinum complex in the 2,2-bipyridine-based microporous MOF-253 via a post-synthetic modification and the Pt complex was covalently bonded to the organic linker of pristine MOF, bipyridine (Figure 1-13 e). A new visible absorption band appears in the obtained Pt-MOF-253. The low-energy absorption in Pt-MOF-253 is attributed to the metal-to-ligand ($Pt^{II} \rightarrow$ bipyridine π^*) charge transfer (MLCT) transition.[76]

It can be concluded from Figure 1-13 that the organic component generally plays an important role in the charge generation and separation process, contributing to the final electronic band structure of MOFs. The terms HOMO and LUMO are used to describe the band structure of photoactive MOFs, instead of VB and CB. The final composition of HOMO and LUMO depends on the relative potential level of different energy bands. For example, in LMCT model, LUMO and HOMO is attributed from metal-oxo cluster and organic linker, respectively.

1.3.4.3 Advantages and Disadvantages of MOFs over Inorganic Semiconductor

MOFs should be considered as an array of self-assembled molecular catalysts rather than as classical semiconductors,[77] as the hybrid nature of organic and inorganic components endows MOFs as catalysts with distinct characteristics, which advantages over both molecular catalyst and classical semiconductors. The potential of MOFs as a new promising type of photocatalysts is demonstrated with respect to the fundamental processes (discussed in 1.2.1) that occur in a photocatalysis system:

Advantages:

1) Light absorption: In most cases, both the organic linker and the inorganic cluster participate in the light absorption process in MOF, as discussed in 1.3.4.2. This unique photoexcitation process enables the light absorption of MOFs with great tunability, via the tuning of chromophore units either in the organic linker, or in the inorganic SBUs, or hybridizing with a light sensitizer.[78]

2) Efficient charge separation: in most cases, the organic linker and metal-oxo cluster constitute the LUMO and HOMO, or the other way around, which means MOFs can be considered as an intrinsic hetero-junction. This spatially separated electronic band structure in MOFs favours the charge separation and simultaneously, hinders charge recombination, as the electron needs to 'travel back' to recombine with the hole – in brief, contributing to a longer carrier lifetime.

3) High surface area and alternating MC/linker sites: the high surface area indicates more exposed catalytic sites as well as larger platform for reactants adsorption, thus more reaction sites for surface reaction and hence a higher turnover rate. The alternating

MC/linker sites facilitate the adsorption process as the reactants can interact with either the organic linker or the neighboring MC.

4) Open microporous structure: the high porosity of MOFs may suppress the classical bulk recombination of holes and electrons; it further shortens the mean pathway of charge carriers to the 'surface'[61]. However, it may restrict reactant diffusion to the active sites, even allowing only small molecules to enter and react within the pore network.

5) Incorporation of hetero species: the additional benefit of porosity is the ability to accommodate small molecules that allows to integrate both light-harvesting and catalytic components with a uniform spatial distribution.

6) Great flexibility of the structure and composition, a general attribute of MOFs: both the metal nodes and the organic linker can be tuned and thus obtained new structure is endowed with specific property that can benefit certain process, such as light absorption, reactants adsorption, diffusion for redox reactions etc.. Therefore, compared with 'rigid' inorganic semiconductors, the properties of MOFs is more tailorable.

7) For fundamental research: MOFs can offer a platform to investigate both short and long range energy transfer, as the distance and the orientation between chromophores can be adjusted, e.g. via ligand tuning. Therefore, mechanistic insights for energy transfer process in photocatalysis can be obtained.

Challenges:

Despite the many potential advantages offered by the MOFs structure with regard to photocatalytic applications as compared to standard solid-state semiconductors, there are several limitations and challenges yet to be addressed.

1) The stability when exposed to heat (thermal), chemicals (oxidation, pH, solvent), and light. Over the last couple of years, the solvent stability of Zr-, Ti- based MOFs has been improved to a certain extent, and many reported MOFs perform well in short photocatalytic tests. However, the long-term stability is rarely attempted or reported and needs more detailed investigation. In addition to the solvent stability, as a photocatalyst, the light stability of MOFs also needs to be taken care of. The good news is that MOFs' stability can be improved from the aspect of material design, either by the selection of

robust components that can withstand the external stimuli or by the formation of stronger coordination bonding between the organic linker and inorganic cluster – but this has yet to be attempted.

2) The electrical conductivity of many MOFs is typically lower than that of inorganic semiconductors, which can limit the charge transfer process along the 3D matrix. However, this may be mitigated by the fact that a) the charge transfer paths are very short, and b) the intrinsic ligand transfer/mobility can be tuned. Thus, dedicated studies are needed to identify optimum diffusion length based on charge mobility, vice versa.

3) The extremely small pore size can restrict the diffusion of the reactants and products, especially in liquid phase reactions. Moreover, the inner surface of the pores can act as defects and recombination centers, which can be detrimental to the photocatalytic properties. First attempts to selectively remove ligands have been investigated in this thesis, aiming at the optimization of diffusion process limited by pore diameters.

4) Finally, from a synthetic point of view, the major challenges involve the scale-up and environmentally friendly MOFs production with the required purity and uniformity. Several newly developed synthesis strategies, such as microthermal synthesis and solvent-free synthesis are promising to resolve this problem.

1.3.5 Project Motivation

Since the first work on MOF-based photocatalysis in 2009[79], a wealth of efforts has been devoted to this field with an exponential growth of publications. To achieve a higher photocatalytic activity, the typical strategies involve the synthesis of new MOF structures and their chemical modification. As a result, the research has yielded a considerably large amount of MOF structures (e.g. Zr-, Cu-, Fe-, Ti-, Co-, Mn-…based MOFs) and tested a variety of applications (e.g. CO_2 reduction, H_2 production, organic dyes degradation), yet often in a “trial-and-error” approach.

1.3.5.1 Choice of MOFs

Among the many studied MOFs, Ti-based MOFs have drawn attention in the field of photocatalytsis attributing to the following merits: the small ionic radius of Ti^{4+} renders a strong Ti-O bond, contributing to a high chemical stability; the high coordination number increases the structural diversity; the transition between Ti^{4+}/Ti^{3+} under excitation enables the Ti-based MOFs redox active. Ti-based MOFs are UV or visible light active and the photo-excited Ti-based MOFs are capable of conducting H^+/H_2 reaction owing to their appropriate LUMO level. In addition, as stated in 1.3.4.1, MOFs can serve as templates to obtain porous metal oxides via calcination, Ti-based MOFs hence gain more credits owning to their photocatalytically active calcination product, TiO_2. Therefore, I chose Ti-based MOFs for this thesis, specifically, MIL-125-Ti and NH_2-MIL-125-Ti.

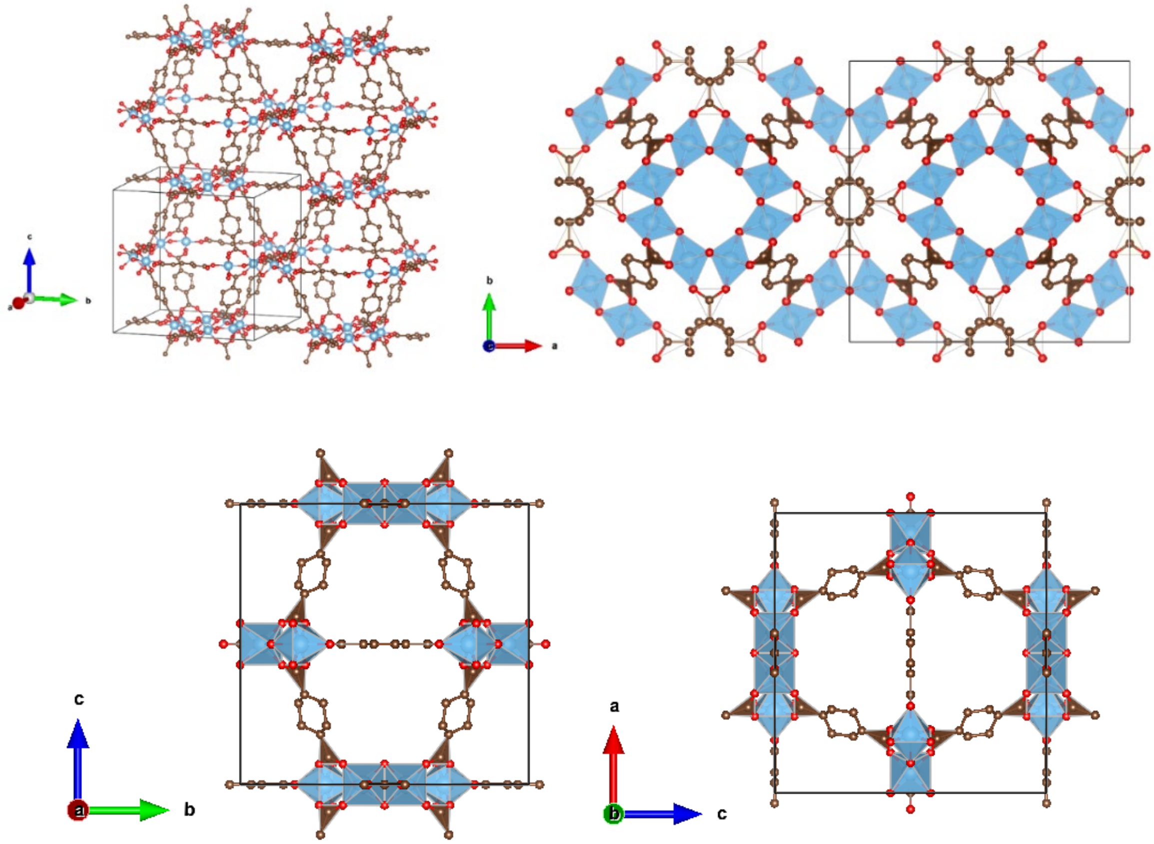

Figure 1-14 Simulated crystal structure of MIL-125-Ti. Red: oxygen, Blue: titanium, Grey: Carbon. Hydrogen has been omitted. Drawn with software-Vesta.

MIL-125-Ti (MIL is the acronym for Material from Institute Lavoiser) was reported in 2009 as the first crystalline and porous carboxylate-based Ti-MOF[80], while its analogous structure NH_2-MIL-125-Ti was reported in 2011[81]. The crystal structures of MIL-125-Ti and NH_2-MIL-125 are isostructural; the difference of these two MOFs lies in the composition of the organic ligands that constitute the framework structure: the former is based on the terephthalic acid (H_2BDC) and the latter on 2-amino terephathalic acid (NH_2-BDC). The theoretical formula of MIL- and NH_2-MIL-125 are $Ti_8O_8(OH)_4$-(O_2C-C_6H_4-CO_2)$_6$ (1587.56 g/mol) and $Ti_8O_8(OH)_4$-(O_2C-C_6H_5N-CO_2)$_6$ (1653.74 g/mol), respectively. In both MOFs, the SBU is a cyclic octamer, constructed with 8 corner- or edge-sharing octahedral titanium units[79]. One SBU then connects to 12 other SBUs through organic linkers, leading to a three-dimensional porous network (Figure 1-14).

The crystal structures of MIL-125-Ti and NH_2-MIL-125-Ti are both tetragonal and belong to the space group of I4/mmm[80]. According to literature,[47] the lattice parameters are: in MIL-125-Ti, a=b=18.6540 Å, and c=18.1440 Å; in NH_2-MIL-125-Ti, a=b=18.6730 Å, and c=18.1380 Å.

There are two types of pores in the framework, typical for the tetragonal crystal structure. In MIL-125-Ti, the calculated size of the pores are 12.5 Å and 6.1 Å, respectively; while in NH_2-MIL-125-Ti, the presence of amino group leads to an expected reduction in pore size, 10.7 Å and 4.7 Å, respectively.[47, 82]

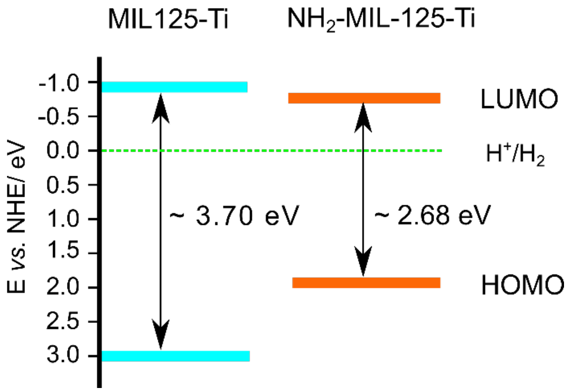

Figure 1-15 LUMO and HOMO level in MIL-125-Ti and NH_2-MIL-125-Ti

Based on the reported values, the edge positions of HOMO and LUMO with respect to the NHE energy level are depicted Figure 1-15. It can be concluded that the photoexcitation in the MIL-125-Ti can only be triggered by the UV light, while NH_2-MIL-125-Ti can potentially absorb visible light as well.

1.3.5.2 State-of-the-Art

Table 1-1 Photocatalytic Applications of MIL-125-Ti and its derivatives (modified from Reference [83])

Strategies	details	MOF	Applications	Light Source
Decoration of Linker	-NH$_2$	MIL-125-Ti	CO$_2$, Cr$_{(VI)}$ reduction	Vis
	-NH$_2$	MIL-125-Ti	Amines oxidation	Vis
	-NH$_2$	MIL-125-Ti	Alcohols oxidation	Vis
	-NH$_2$	MIL-125-Ti	N-hydroxy-carbamates	UV-Vis
	-NH$_2$	MIL-125-Ti	PCVG	UV
	-AM-Eu	NH$_2$-MIL-125-Ti	Alcohols oxidation	UV-Vis
	NHMe/Et/Pr	NH$_2$-MIL-125-Ti	CO$_2$ reduction	Vis
Combination with Semiconductors	g-C$_3$N$_4$	MIL-125-Ti	RhB degradation	Vis
	g-C$_3$N$_4$	Ag/MIL-125-Ti	Nitrobenzene reduction alcohols oxidation	Vis
	g-C$_3$N$_4$	NiPD/MIL-125-	H$_2$ production	Vis
	CFB	NH$_2$-MIL-125-Ti	H$_2$ production	Vis
	In$_2$S$_3$	MIL-125-Ti	Tetracycline degradation	Vis
	BiOBr	NH$_2$-MIL-125-Ti	RhB degradation	Vis
	PHIK	NH$_2$-MIL-125-Ti	RhB degradation	Vis
	TiO$_2$	MIL-125-Ti	Solar Cell	Solar Light
	CdS	MIL-125-Ti	H$_2$ production	UV
	TiO$_2$	NH$_2$-MIL-125-Ti	Photoelectrochemical sensor	Vis
MNPs Loading	Pt, Au	MIL-125-Ti	H$_2$, formate production	Vis
	Au, Pd, Pt	MIL-125-Ti	H$_2$ production, alcohols oxidation	UV- Vis
	Ag	MIL-125-Ti	RhB degradation	Vis
	Ag	RGO/MIL-125-	RhB degradation	Vis
	Ni	NH$_2$-MIL-125-Ti	H$_2$ production	UV
	Ag	MIL-125-Ti-AC	MB degradation	Vis
	Pt	NH$_2$-MIL-125-Ti	Photocathode, H$_2$ production	Vis
	Ni	NH$_2$-MIL-125-Ti	Alcohols oxidation	Vis
Metal Complex Loading	Co-complex	NH$_2$-MIL-125-Ti	H$_2$ production	Vis
	Cr^{3+} complex	NH$_2$-MIL-125-Ti	MB degradation	Vis
	Ni^{2+} species	NH$_2$-MIL-125-Ti	H$_2$ production	UV

MIL-125-Ti and NH$_2$-MIL-125-Ti have been investigated as photocatalysts for a range of applications, including CO$_2$ reduction, alcohols oxidation, H$_2$ production as well as dye degradation (Table 1-1)[58, 84-86]. Moreover, various strategies have been developed to achieve a higher photocatalytic efficiency, including functionalization of the ligand, combination with semiconductors, noble metal nanoparticles and metal complexes (Table 1-1).

The majority of the community has focused on testing the performance of the MOFs with little effort being dedicated to the fundamental aspects. As more MOFs being developed as photocatalysts, the understanding of key processes, mechanisms and limitations engaged in MOF photocatalysis requires a more systematic and targeted research.

Next, although increasing the light absorption through ligand tuning has become a feasible strategy to prepare visible-light active MOF photocatalysts, little attention has been paid to the overall influence of the ligand tuning. For instance, NH_2-MIL-125-Ti has been as a successful representative of ligand tuning of MIL-125-Ti. NH_2-MIL-125-Ti has the advantage over MIL-125-Ti in light absorption, whether it is also superior in other aspects, such as charge-separation and charge-transfer, unfortunately, I could not identify a rigorous study that addresses this issue (Table 1-1).

1.3.5.3 Project Aims

The first aim of this work is to investigate the photocatalytic process of MOF, including the role of hole sacrificial agent and cocatalyst, the key factor for the photocatalytic activity, which is expected to provide guidelines for further materials modification and design.

Another aim of this work is to evaluate the overall effect of ligand tuning on the materials' properties, including charge separation ability and catalytic performance, which shall increase our knowledge about the photocatalysis process of MOFs and further provide guidelines for designing advanced MOF-based photocatalysts.

Furthermore, MOFs can evolve into corresponding metal oxides upon calcination, and the obtained oxides usually inherit a porous structure from the parent MOFs, which is beneficial for the applications limited by diffusion process and surface area. In this work, the thermal decomposition process of MOFs into oxides will be investigated and the photocatalytic potential of the obtained metal oxides will be evaluated.

2 Characterization

2.1 Characterization Techniques

Various characterization methods have been applied in this thesis, in order to reveal the nature of the materials, for instance, the crystal structure, the morphology, the thermal stability, and the electrochemical properties.

2.1.1 Electron microscopy (EM)

EM refers to a diversity of characterization techniques, which use the electron beam as the source of illumination.

According to the Abbe equation (2-1), the resolution of a diffraction-based technique in a perfect optical system depends greatly on the wavelength of the irradiation particles:

$$d = \frac{0.61\lambda}{n\ sin\alpha} \quad \text{2-1}$$

Where d is the resolution; λ is the wavelength of incident particle; n is the refractive index relative to the free space; and α is the semi-angle in radians.

The wave-particle dualism, postulated by *L. de Broglie*, proposed that all moving matter has wave properties and elaborated the relationship between the wavelength λ and the matter's momentum p. This theory is of vital importance for electron microscopy, as it indicates that the accelerated electrons can be treated as waves, and the wavelength is related to the acceleration voltage U. Based on Equ. 2-1, Table 2-1 compares the obtained magnifications when blue light and electrons (U=~20 kV) are used as the stimulation source. The resolution in the case of electrons reaches nanometer range; moreover, it can reach the limit of atom with increased acceleration voltage. EM enables researchers to gain insights into the structure, morphology and composition of the material in the nanoscale, thus it has been very helpful and necessary for materials characterization.

Table 2-1 Relation of Irradiation Wavelength and Magnification

Microscopy	λ (nm)	n sinα	Magnification
Light	400	200	1000
Electron	0.003	0.015	500000

When a focused electron beam is directed onto a sample, it can be scattered, absorbed or transmitted, generating a multitude of signals (Figure 2-1). There are corresponding techniques based on the various interaction of the incident electrons with the specimen. In the following section, the electron microscopy applied in this thesis will be discussed in more detail.

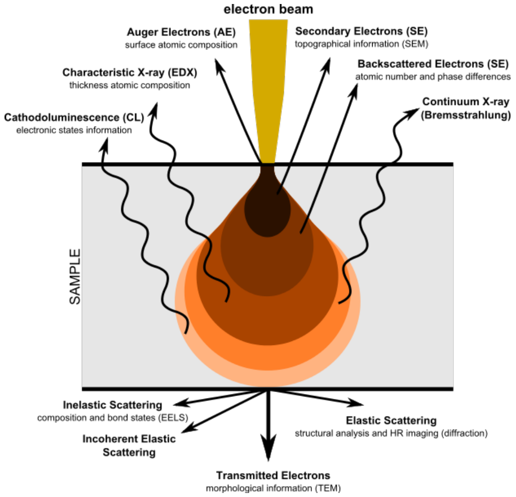

Figure 2-1 Electron Interaction with Matter[87]

2.1.1.1 Scanning Electron Microscopy (SEM)

SEM can analyze and observe the surface structure of the material. The working process of SEM, as a representative for electron microscopy, is depicted in Figure 2-2. First, a beam of electron, either thermoionically emitted or filed emitted, is directed and accelerated with the help of the anode. Then the beam is focused with condenser lenses and coils. The attachments below the electron gun are lenses. There are different lenses for the adjustment of the electron beam to produce a finely focused electron beam. Finally, the beam reaches and interacts with the sample, whereby various detector collect the corresponding signals.

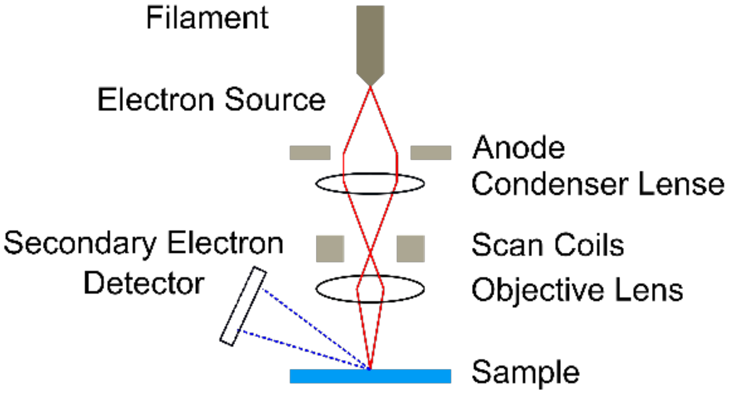

Figure 2-2 SEM equipment

SEM utilizes the signal of secondary electrons (SE) and/or sometimes back-scattered electrons (BSE). The generation of SE and BSE is illustrated in Figure 2-3. The sample absorbs an incident electron, and then releases another electron; a new electron is ejected from the material by the incident electron. Those released electrons are called SE, while the incident electrons are called primary electrons. If the primary electrons are only scattered and reflected back from the sample, then the electrons coming out of the sample are called BSE. Usually there are different detectors in the SEM machine for the SE and the BSE. SEs are the product of inelastic scattering, so its energy is quite low; only those signals generated from the near-surface area can escape and be detected. After signal processing, black-and-white SEM images are obtained. The number of SEs escaped from the observed area determines the brightness and the contrast of the image. With SEM, researchers can obtain a surface profile of materials.

To avoid the loss of signals caused by collision with air molecules, SEM was designed with a high vacuum operating system. However, in recent years, environmental SEM with low vacuum level for biological samples has been developed. In this thesis, SEM measurements were conducted with FEGSEM Quanta 200 (USTEM, TUWien) and the signals being collected were SE, under high vacuum level (10^{-6} torr). Both film and powders SEM samples were prepared by first attaching to the conducting carbon tape and then to the sample holder. To avoid surface charging and improve the resolution, for some samples AuPd or Pt (~15 nm) was sputtered onto less conductive materials; nonetheless, the sputtering may hide surface features to a certain extent.

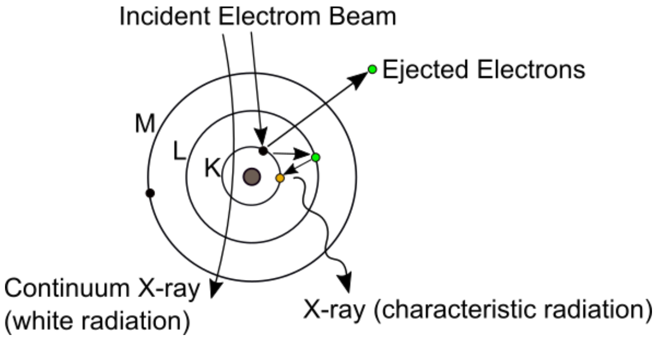

Figure 2-3 Schematic illustration of various signals generated during SEM measurement

2.1.1.2 Energy-dispersive X-ray Spectroscopy (EDX)

EDX is an element analytic technique. During the SE generation process, it is also possible to generate X-rays (Figure 2-3). As the escape of a SE leaves a hole behind, the electron from the outer shell can jump into the inner shell. The energy difference between the two shells can be released in the form of X-rays. Therefore, the energy of these X-rays is determined by the atomic structure and characteristics of the emitting element. In EDX measurements, there is an energy-dispersive spectrometer that collects the X-rays emitted by the specimen and outputs an EDX spectrum. As the number of emitted X-rays is related to the concentration of the certain element in the sample, EDX is both qualitative and quantitative.

In this work, EDX was measured with FEGSEM Quanta 200. The sample preparation was the same as for SEM.

2.1.1.3 Transmission Electron Microscopy (TEM)

When an electron beam passes through an ultrathin specimen (often less than 100 nm thick), part of the incident electron beam can be transmitted through the sample and lose a negligible amount of energy. These electrons can be divided into unscattered transmitted electrons and elastically scattered electrons (Figure 2-1). TEM is an EM technique, which exploits the signals of above electrons and reveals the contour as well as the internal structure of a thin sample.

A typical set-up of a transmission electron microscope consists of the electron gun, the condenser system, the objective lens, the diffraction/intermediate lens, the projective lenses, the image observation and the vacuum system. There are usually two observation modes in TEM—imaging mode and diffraction mode. Figure 2-4 compares the working principles of these two modes. In both cases, the incident electron beam is first shaped with a series of condenser lenses and condenser apertures before the interaction with specimen, same as in SEM. Then the position of the aperture (Figure 2-4, red) decides which transmitted signal is selected and thus determines the final observation mode. In imaging mode, an objective aperture is placed at the back focal plane. Further image magnification is completed with the intermediate lens and the projector lens. The electron beam in TEM has a very high acceleration voltage, typically 100 KeV to 300 KeV, which contributes to the extremely small de Broglie wavelength of the electrons. As a result, the imaging resolution of TEM can reach a column of atoms.

The diffraction mode characterizes the electron diffraction (ED) behavior of incident electrons. Considering the wave nature of electrons, the periodic structure of a crystalline solid can be treated as a diffraction grating. When the incident beam interacts with the specimen, the electrons are scattered in a predictable manner. Tracing back from the observed diffraction pattern, researchers are able to deduce the crystal structure of the specimen. For example, the ED pattern of a polycrystalline solid consists of a set of rings; while in the case of single crystalline sample it is a set of separate dots and each dot represents a crystal facet. In fact, diffraction pattern and image are present simultaneously in the TEM (Figure 2-4). Different from the imaging mode, in the diffraction mode a SAED aperture is inserted in the first intermediate image position. Then the strength difference of intermediate lens decides that the diffraction pattern, instead of the image, is focused in the plane of the second intermediate image. After further magnification by the projective lens system, the diffraction pattern is obtained with a fluorescent screen, recorded on photographic film, on imaging plates or using a CCD (charge-coupled detector) camera. ED has become a very informative technique and is frequently used to reveal the lattice details of crystals.

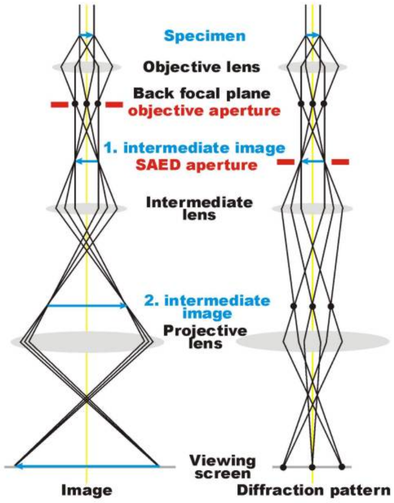

Figure 2-4 TEM and ED principle illustration[88] *http://www.microscopy.ethz.ch/TEMED.htm*

In this work, TEM images and ED pattern were obtained with FEI Tecnai G20 and FEI Technai F20 (Thermo Fischer Scientific, USTEM Center, TUWien). TEM samples were prepared by the deposition of diluted sample (usually, ethanoic solution) onto cupper grids (partially covered with carbon film).

2.1.2 Spectroscopy

Spectroscopy studies the interaction of electromagnetic radiation/light with the matter. Spectroscopy can be further categorized based on the stimulation source (X-ray, Ultraviolet, Infrared, etc.) as well as the type of interaction (absorption, scattering, transmission, etc.).

2.1.2.1 X-ray photoelectron spectroscopy (XPS)

XPS is among the most powerful techniques to analyze the chemical composition and the chemical state of solid surfaces, in which X-ray is used as the irradiation source. The generation process of photoelectron in XPS is shown schematically in Figure 2-5. When an electron is ejected from the K-shell into the vacuum after absorbing the energy of the incident X-ray and becomes a 1s free electron,[89] the kinetic energy of the free electron (KE) is highly dependent of the binding energy of the 1s electron (Equ. 2-2) and thus it provides information about the chemical state of the electron. With higher X-ray energy, electrons from other shells (2s, 2p) can also be ejected and become free electrons. A typical XPS spectrum is illustrated in Figure 2-6.

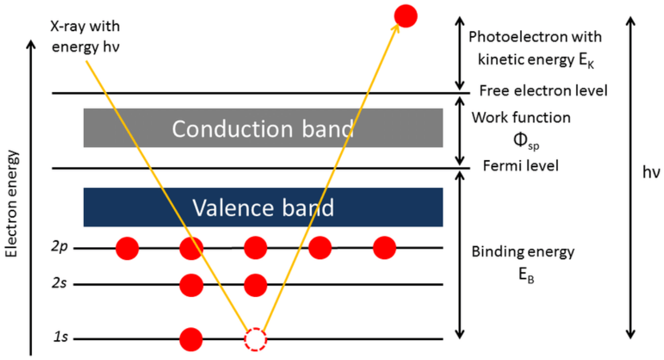

Figure 2-5 Working Principle of XPS[90]

$$KE = hv - (E_B + \varphi) \tag{2-2}$$

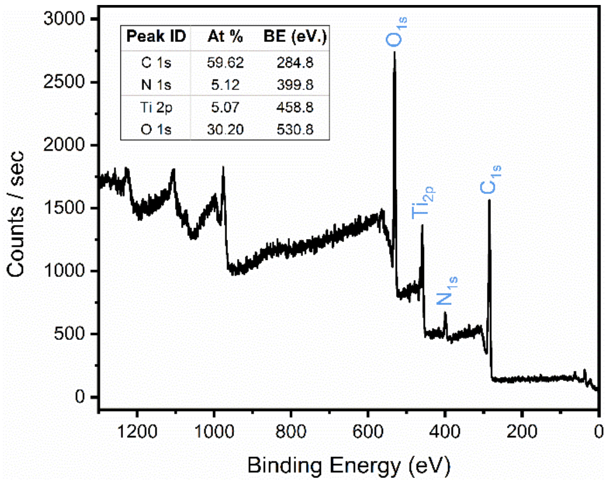

Figure 2-6 XPS spectrum of NH_2-MIL-125-Ti

In this thesis, all measurements were carried out on a custom built SPECS XPS-spectrometer equipped with a monochromatised Al-Kα X-ray source (μFocus 350) and a hemispherical WAL-150 analyzer (acceptance angle: 60°). Pass energies of 100 eV and 30 eV and energy resolutions of 1 eV and 100 meV were used for survey and detail spectra respectively. In case of charge effect, the binding energy calibration was applied by taking the adventitious carbon peak (C-C peak) as a reference signal, at binding energy 284.8 eV.

2.1.2.2 X-ray diffraction (XRD)

XRD is another technique that applies X-ray to detect material and it bases on the diffraction behavior of X-rays to analyze the sample. In 1913, W. Bragg discovered the relationship between the wavelength of incident X-ray beam (λ), the scattering angle (θ) and the interplanar distance (d) (Equ. 2-3), which has become the working principle of this technique.

$$n\lambda = 2dsin\theta \tag{2-3}$$

Figure 2-7 depicts the working process of XRD measurement with a moving detector; the detector detects diffracted X-ray at varying positions. Based on the Bragg's Law, when the values of λ, n, d and θ fulfill the Equ. 2-3, the diffracted X-rays can be detected. The detector outputs the position information as 2θ. As λ of the incident X-ray is fixed, d and θ is thus linked to each other. For a certain crystalline material, the d values of the lattice planes are characteristic, so are the 2θ values. Therefore, XRD measurement reveals the information of the crystal structure and is commonly used for phase identification.

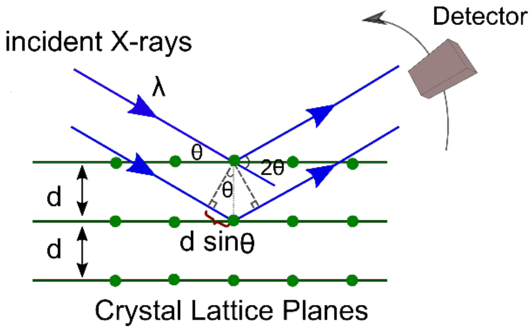

Figure 2-7 Schematic Illustration of XRD Measurement

In addition to phase identification, XRD measurement is capable of defects detection, texture orientation detection and quantitative analysis of phase compositions. Furthermore, crystallite sizes, micro strain, unit cell lattice parameters and Bravais lattice symmetry can also be derived from the measured data.

The average crystallite size d can be determined by the Scherrer equation (Equ. 2-4) for a given phase θ and FWHM (full width at half maximum, *ß*), after correcting the instrumental broadening.

$$d = 0.89\lambda/(ßcos\theta) \tag{2-4}$$

X-ray diffraction (XRD) patterns in this work were collected with PANalytical X'Pert Pro multi-purpose diffractometer (MPD) in XRC, TUWien. The incident X-ray consists of Cu K_α and $K_ß$ radiation (2:1 ratio). The generator voltage and tube current is 45 KV and 40 mA. Solid samples were simply mounted on Si single crystal sample holder.

2.1.2.3 *In-situ XRD*

As implied by its name, is an in-situ technique based on X-ray diffraction, by which the change of sample's crystal structure with temperature can be detected. The in-situ XRD can be conducted under different atmosphere (air, N_2, Ar, He, NH_3, etc.), and the temperature ramping rate can be well controlled. In-situ XRD has been measured with – in XRC, TUWien.

2.1.2.4 *Diffuse Reflectance Ultraviolet-visible Spectroscopy (DR-UV-vis spectroscopy or DRS)*

When an incident beam irradiates onto a matter, the atoms or the molecules can absorb the light. In fact, this light absorption is an energy conversion process, in which the molecules or the electrons of the material take up the energy from the photons and get excited from the ground state. Figure 2-8 illustrates the various transition processes that can be excited by light. Only when the photonic energy matches with the energy gap between the ground states and the excited states, the light can be absorbed. Therefore, the light absorption process is characteristic of the atomic and molecular composition of the material. Thus, the light absorption spectroscopy, which measures the absorption of radiation as a function of wavelength, has been widely used for materials' analysis.

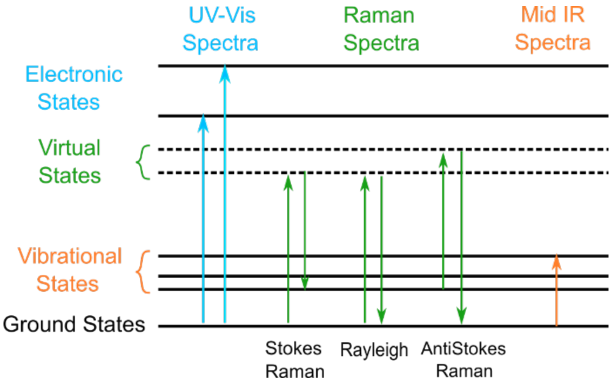

Figure 2-8 Light induced transition process inside the materials

In the ultraviolet-visible (UV-Vis) spectroscopy, as the name implies, the incident light is in the range of 200 nm - 800 nm. UV-Vis probes the electron transition between the ground state and the excited states (Figure 2-8), thus providing information about the electronic structure of materials.

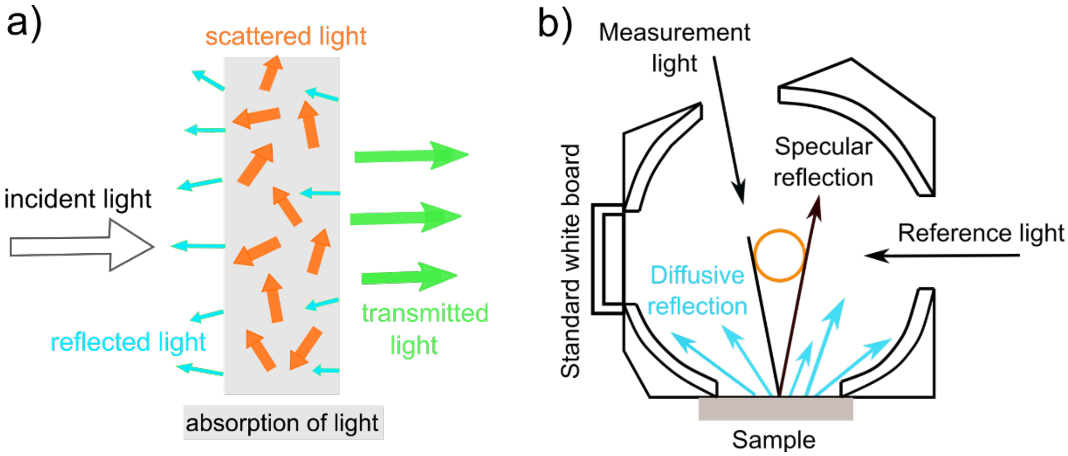

Figure 2-9 a) Light interaction with matter; b) Working principle of DRS-UV-Vis, with integrating sphere collecting the diffusive reflected light.

However, we cannot obtain the absorbance property directly. Regarding the interaction process between light and the irradiated matter (Figure 2-9 (a)), two strategies have been applied to extract the absorption information, transmittance spectroscopy and reflectance spectroscopy. For the solid sample, diffusive reflectance spectra (DRS) has been frequently used, which extracts the absorption information from the diffusive reflected light. The working process for a diffuse reflectance measurement is illustrated in Figure 2-9(b). After measurement, the absorption information can be derived from the measured reflectance data via Equ.2-5.

$$Abs. = \log\frac{1}{R} \qquad or \qquad F(R) = \frac{(1-R)^2}{2R} = \frac{K}{S} \tag{2-5}$$

R is the measured reflectance; Abs. is short for absorbance; F(R) is Kubelka-Munk (K-M) function, K and S are the absorption and scattering coefficient of the sample, respectively. K-M function takes the geometric peculiarities of the inhomogeneous sample into consideration and has been widely employed in the diffusive reflectance spectroscopy.

In addition to the characterization of the absorption property, UV-Vis spectroscopy has been used to acquire the optical band gap of sample based on the Tauc-plot (Equ. 2-6).

$$(hv\alpha)^{1/n} = A(hv - Eg) \tag{2-6}$$

Where h is the Planck's constant, ʋ is the light frequency, α is the absorption coefficient, E_g is the band gap, A is the proportional constant. The value of exponent n depends on the sample transition mode: 1/2 for direct allowed transition; 2 for indirect allowed transition; 3/2 for direct forbidden transition; 3 for indirect forbidden transition.

In this work, Jasco V-670 UV-Vis photo spectrometer has been used to measure diffusive reflectance spectra.

2.1.2.5 Infrared spectroscopy (IR)

As depicted in Figure 2-8, IR is inherently another absorption spectroscopy and it is associated with the transitions between vibrational energy levels. There are different vibration modes in molecules, such as stretching, bending, twisting, etc. To gain a better understanding of the vibration motion in a molecule, we can consider the stretching of a chemical bond as the stretching of a spring in single harmonic motion. Following the Hook's Law, the stretching frequency ʋ of the spring is

$$\upsilon = \frac{\pi}{2}\sqrt{\frac{k}{m}} \tag{2-7}$$

where *k* is the spring constant and *m* is the mass. In the case of the molecular vibration, υ is the vibrational frequency, *k* is related to the strength of the chemical bond and *m* is decided by the mass of two atoms (m_1 and m_2) at the ends of the molecular bond. Therefore, 'reduced mass' *M*, $M=m_1* m_2/(m_1+m_2)$, was introduced. Based on 2-7, the vibrational frequencies of different molecular bonds can be compared. For example, comparing C-C single bond with C=C double bond, *M* is the same and double bond is thought to have roughly two times *k* of single bond. Hence, the stretching frequency of C=C is higher. However, for C-H bond and C-C bond, both are carbon single bonds, *M* is 0.923 and 6 (unit: AMU, atomic mass unit), respectively. Consequently, C-H bond has higher bond stretching frequency. In addition to the vibration modes and the atomic mass, the vibration frequencies depend also on the orientation of the bonds and atoms, bond order and the hydrogen bonding.

It should be noted that only vibrations that produce a change in the dipole moment can be observed as signals on an IR spectrum. The bigger the change in dipole moment is, the higher intensity of the peak in the IR spectrum. In this work, the PerkinElmer Fourier Transform infrared spectrometer (FT-IR) Spectral UATR-TWO with a spectrum Two Universal ATR (Single Reflection Diamond) accessory was used to characterize the molecular structure of solid metal organic framework.

2.1.2.6 Raman

The working principle of Raman spectroscopy has been illustrated in Figure 2-8: Raman is based upon the interaction of light with the chemical bonds, therefore, a vibrational spectroscopic technique. Different from UV-Vis and IR, Raman spectroscopy detects the inelastic scattering of light instead of the absorption of light. Moreover, in IR spectroscopy (also a vibrational spectroscopy), the change in the dipole moment is required for signal detection; whereas in Raman, the change of polarizability generates the signal. Raman can probe the chemical structure, crystal phase, intrinsic stress/strain as well as impurity of the sample and thus is a distinct fingerprint for a particular molecule or material.[91] Moreover, Raman is capable for both qualitative and quantitative analysis purposes.

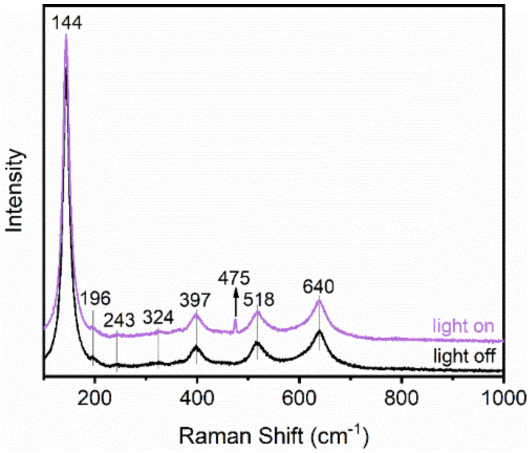

Figure 2-10 Example of Raman Spectra of TiO_2 (anatase phase).

In this work, Raman measurement was conducted with LabRAM HR800 (HORIBA Co.Ltd). Ne:YAG diode was used as 532 nm laser source and the characteristic Raman peak of Si at 520.8 cm^{-1} was used as the calibration peak. Figure 2-10 displays an example of measured Raman spectra. It can be seen that the spectra feature a number of peaks corresponding to certain molecular bond vibrational modes. During measurement, the lab light is suggested to be turned off as indicated in Figure 2-10, TiO_2 has been affected by room light with an additional peak at 475cm^{-1} even with the cover of a black cloth.

2.1.2.7 Photoluminescence Spectroscopy (PL)

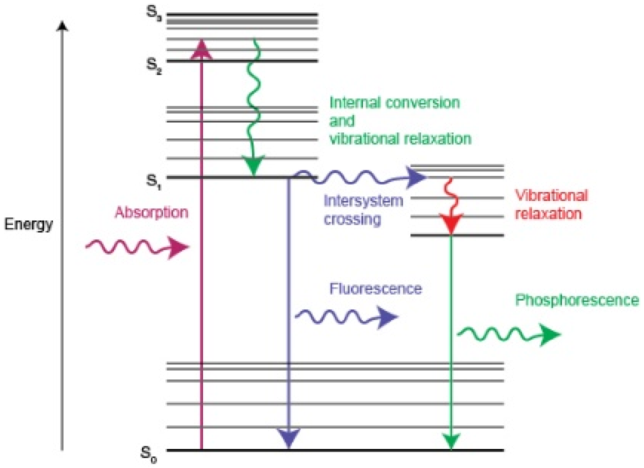

Figure 2-11 Photoluminescence principle as well as Fluorescence

As illustrated in Figure 2-11, a molecule can absorb a photon in the visible region and get excited to higher electronic states (S1, S2, S3..). The electron in a high vibrational level of the excited state first relaxes to the lowest level of the excited state and release the excessive energy non-radiatively. The electron further relaxes from the lowest vibrational level of the excited state to the ground states, which is again accompanied by the release of energy, in the form of either heat or radiation. The radiative transition can occur only when the emission of the donor coincide with the absorption of the acceptor. Moreover, it depends on the intersystem crossing, there are two types of transition radiation, fluorescence and phosphorescence. The PL detects this radiation process and reveals information about the surface structure, material's defect level as well as the interfacial charge transfer. Moreover, time-resolved emission spectrum provides information about carrier relaxation and recombination mechanisms and the lifetime of the excited states can be obtained. Therefore, PL has been widely used in the filed of photocatalysis.

In this work, PL Emission spectra has been measured with Picoquant Fluo Time 300. The spectrometer is equipped with two light source: Xe lamp with wavelength from 250 nm to 800 nm, and laser source with wavelength at 378 nm. The spectrometer is capable for both steady and time-resolved measurement.

2.1.3 Physisorption

The MOF is featured with high surface area and thus the physisorption has been used to analyze its surface area as well as the pore distribution. Compared with the chemisorption, physisorption is based on the non-covalent interaction (e.g. polarization, van der Waals interactions, or field-dipoles) between the probing gas (adsorbate) and the sample (adsorbent).

Physisorption involves the physical adsorption of an inert gas over the entire surface of the sample (including filling pores and cavities), and during this process the amount of adsorbed gas molecules and the adsorptive pressure are measured and illustrated in adsorption isotherms. The converse process of decreasing the amount of adsorbed gas, is called desorption. When the mechanism of mesopore filling varies from mesopore emptying, the discrepancy observed between adsorption and desorption isotherm is called the hysteresis loop.

Adsorption isotherms are displayed in Figure 2-12 with the amount of adsorbate (preferably in mol·g^{-1}) plotted against the equilibrium relative pressure (p/p^0), where p^0 is the saturation pressure of the pure adsorptive at the operating temperature. In 2015, IUPAC updated the classification of physisorption to 6 types.

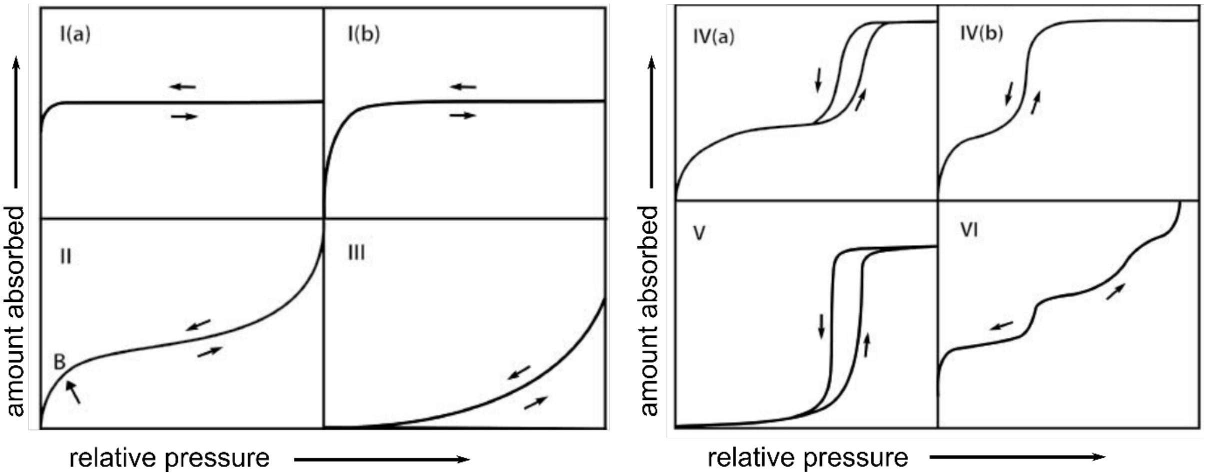

Figure 2-12 Classification of physisorption isotherms[92]

Reversible **Type I** isotherms are typical for microporous materials with relatively small external surfaces (e.g. activated carbon, zeolites). The adsorption is limited by the accessible micropore volume. This type of isotherms are featured with the steep uptake at very low p/p^0, which is due to the enhanced adsorbent-adsorptive interactions in narrow micropores (micropores of molecular dimensions). Type I(a) isotherms are usually given for materials with narrow micropores (width < ~1 nm) while Type I(b) are given by materials with broader pore size distribution (< ~2.5 nm).

Reversible **Type II** isotherms are found with non-porous or macroporous materials. This shape is given by the unrestricted monolayer-multilayer adsorption till high p/p^0. Point B in the isotherm indicates the completion of the monolayer coverage.

Type III isotherms compared with Type II, there is no distinctive point B, which means there is no identifiable monolayer formation during the gas adsorption. This is duo to the relatively weak interactions between adsorbate and adsorbent, and the adsorbed molecules tend to form clusters around the most favorable sites on the surface of a nonporous or a macroporous solid.

Type IV isotherms are characteristic for mesoporous adsorbents (e.g. metal oxides, mesoporous molecular sieves). The low-pressure part resembles that of the Type II isotherm, corresponding to the monolayer-multilayer adsorption on the walls of the mesopores. The subsequent part is the pore condensation, which describes the phenomena of gas condensing in the pore to a liquid-like phase in a pore at a pressure p less than the saturation pressure p^0 of the bulk liquid.[92] Then at high p/p^0, there is a final saturation plateau, of variable length (sometimes reduced to a mere inflexion point). In the case of a Type IV(a) isotherm, hysteresis is observed, which is related to the pore width, the adsorption system and temperature. For example, for N_2 and Ar adsorption in cylindrical pores at 77 K and 87 K, respectively, hysteresis starts to occur for pores wider than ~ 4 nm)

Type V isotherms, in the low p/p^0 range, display a similar shape to that of Type III, due to the relatively weak adsorbent–adsorbate interactions; while in the high p/p^0 range, the shape is attributed to the molecule clustering upon pore filling.

Type VI isotherms are featured with unique stepwise reversible shape, which represents the layer-by-layer adsorption on non-porous surface. A typical example of type VI is the ad/desorption of Ar and Kr at low temperature on graphitized carbon blacks.[92]

The hysteresis loop between the adsorption isotherm and desorption isotherm is generally associated with the capillary condensation. Due to the particular features of the pore structure and the underlying adsorption mechanism, there are different shapes of hysteresis loops (Figure 2-13).

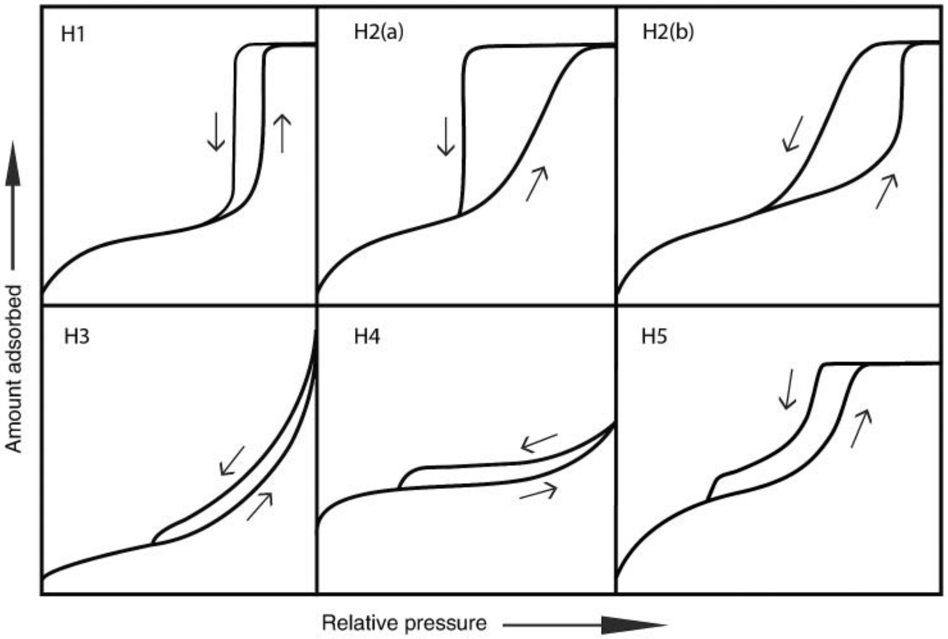

Figure 2-13 Classification of hysteresis loops[92]

Type H1 is characteristic for materials with a narrow range of uniform mesopores, for example, the templated silicas and mesoporous carbons. But H1 has also been found in materials with ink-bottle pores. **Type H2** belongs to more complex pore structure with the unique steep desorption branch, especially in H2(a). Generally, H2 is associated with the pore blocking. The hysteresis loop of H2(a) can be attributed either to the pore-blocking/percolation in a narrow range of pore necks or to the cavitation-induced evaporation (H2(a)), while the pore-blocking, with a larger size distribution of neck widths, contributes to H2(b) loop. The adsorption branch of **Type H3** is similar to the Type II isotherm while its lower limit of the desorption branch is normally located at the cavitation-induced p/p^0. H3 loop is usually given by the non-rigid aggregates of plate-like particles (e.g. certain clays). Aggregated crystals of zeolite, some mesoporous zeolites and micro-mesoporous carbons often have **Type H4** hysteresis loops, and due to the filling of micropores, the uptake at low p/p^0 is more pronounced. T**ype H5** is an unusual loop characteristic for pore structures with open and partially blocked mesopores.

After the acquirement of the isotherms and hysteresis loop, there are several concepts which provide mathematical models in order to extract the required information.

Langmuir theory assumes that only a single layer of gas molecules being adsorbed on the surface of solids. According to the Langmuir equation (Equ. 2-8), the fractional coverage of the surface θ ($0<\theta<1$) is defined by the gas pressure p and the gas constant K_α. The Type I isotherms (Figure 2-12) fits the Langmuir model very well.

$$\theta_1 = \frac{K_\alpha P}{1 + K_\alpha P} \qquad 2\text{-}8$$

However, the physisorption isotherms of Type II to type VI cannot be explained by the Langmuir theory, as they tend to be multilayer adsorption, which fits better with the Brunauer, Emmett and Teller (BET) theory.

The BET model is actually an extension of monolayer molecular adsorption concept to multilayer adsorption, in which it is assumed that the Langmuir theory is applicable to each single layer and there are no more other interactions than the van-der-Waals-force between the single monolayers. The relationship between the total number of molecules adsorbed N with respect to number of surface sites available for adsorption A can be elaborated with Equ. 2-9.

$$\frac{N}{A} = \frac{C * P/P_0}{(1 - P/P_0)(1 + (C - 1) * P/P_0)} \qquad 2\text{-}9$$

where P and P_0 are adsorbate gas pressure at equilibrium and saturation, respectively and C is the BET constant.

The physisorption measurements in this thesis were carried out on a Micromeritics ASAP 2010 and an ASAP 2020 instrument by Micromeritics GmbH (Aachen, Germany). Before measurements, the samples were heated to 150 - 200 °C in vacuum overnight to remove moisture and potential adsorbed gases. The physisorption measurements were carried out at 77 K with nitrogen gas as adsorbate.

It is common to use N_2 adsorption and desorption isotherm to acquire the pore information in MOF field, but there are concerns: the size of pore is often at Angstrom scale, which challenges the reliability of N_2 adsorption and desorption. In addition, the reproducibility of ad/desorption isotherms of MOF is another issue, which needs to be addressed.

2.1.4 Thermogravimetric Analysis (TGA)

TGA detects the weight loss of the sample as a function of elevated temperature. This process can occur in air, in inert gas, or in vacuum. The weight loss can occur due to various reasons, such as the loss of adsorbed species, phase transformation, decomposition of the organic components, etc. Therefore, TGA records the thermal behavior of the sample and consequently provides information about the temperature-dependent chemical and physical transitions. In this thesis, metal organic framework has been the research focus and TGA has been applied to define its thermally stable temperature, as well as the temperature to obtain corresponding metal oxides.

TGA measurements were conducted with TGA 8000 from PerkinElmer. Experimentally, with MOFs, it was found that parameters such as ramp rate, gas supply and initial material amount can affect the weight loss behavior. Moreover, the adsorbed species also influence the comparison between different samples. Therefore, for the TGA measurement of MOF, it is suggested to pre-treat the sample at certain temperature (eg. 150 °C or 200 °C) to get rid of the adsorbed species and to set the same measurement parameters for materials comparison.

2.1.5 Ionic inductively coupled plasma mass spectroscopy (ICP-MS)

ICP-MS is a type of mass spectroscopy which is capable of detecting metal elements and several non-metal elements at an extreme low concentration (10^{15}, ppq). This is achieved by ionizing the target element with inductively coupled plasma and then using a mass spectrometer to separate and quantify those ions.

ICP-MS was conducted with an iCAP 7000 Series (Thermo Fisher Scientific, Braunschweig) with iTEVA Control Center (version 2.4.071) and an iCAP 6000 Series (Thermo Fisher Scientific, Braunschweig) with the Thermo Scientific Qtegra intelligent Scientific Data Solution (ISDS) software in combination with a Cetac ASX520 autosampler. In this work, I measured the Pt loading onto Ti-based MOFs. First, the solid sample was digested in concentrated H_2SO4 at 70 °C overnight. Then the transparent solution was diluted in 1% HNO_3 aqueous solution (common solvent) to the concentration level of ppm. For the stability of titanium during the measurement, 0.1% HF was added. Calibration samples were prepared with the commercial standard solution. In the end, Indium was added to all the samples as internal standard. It is worth pointing out that the sensitivity of ICP-MS is extremely high, therefore, the water used during ICP-MS must be high performance liquid chromatography grade, to avoid impurities. In addition, the digestion of solid sample should aim for atomic/ionic level dispersion of element in the solution, as the cluster of atoms may be taken as another element by the software.

2.2 Characterization of Photocatalytic Hydrogen Evolution from Water

2.2.1 Reactor

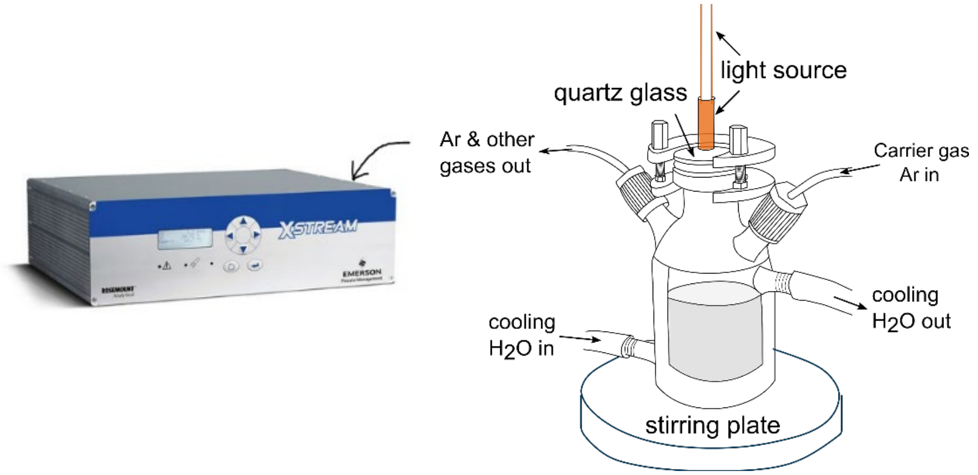

Figure 2-14 Reactor for HER and gas detector – X-stream

The hydrogen evolution reaction (HER) were carried out in a closed custom-made flow reactor (Figure 2-14). The light source was directed via cable and it irradiates from the top of the reactor. The top cap of the reactor was made of quartz. The total volume of the reactor is about 100 mL, usually 40 mL reactant solution was placed inside. During reaction, the suspension was kept under stirring at 250 rpm. There are constant Ar flow controlled by a mass flow controller (Q-flow 140 series, MCC-Instruments) carrying all the gases from the reactor to the gas detector. Before entering the detector, there was a $CaCl_2$ trap to remove the water impurities. The temperature of the reaction system was kept constant with the water cooling system. During HER reaction, the reactor was placed inside a black box to protect the environment from the dangerous light irradiation as well as to avoid the external contributions to the reaction.

2.2.2 Light Source –Hg lamp

Top irradiation was used to excite the catalysis system as shown in Figure 2-14, and the light source was a 200 W Hg lamp (Superlite I 05, Lumatec), which can provide both

UV light (λ= 220 - 400 nm) and visible light (λ= 400 - 700 nm). Figure 2-15 shows the light spectrum of the Hg lamp. Table 2-2 lists the optical output and calculation energy parameters of the lamp, both from optical output results and calculation.

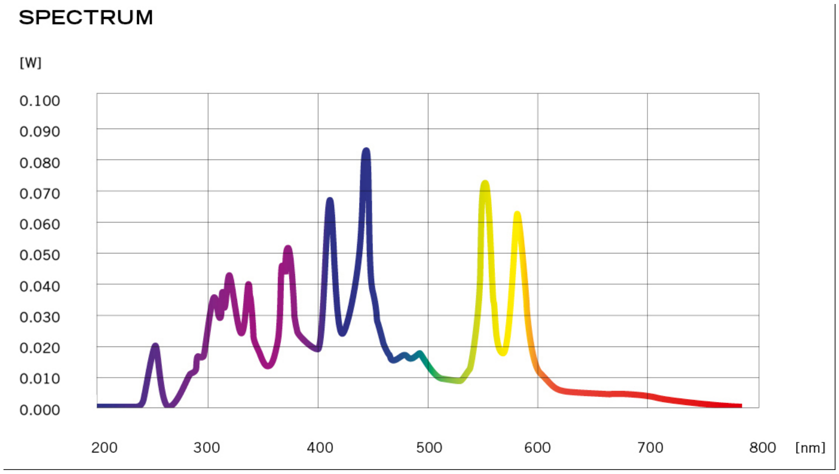

Figure 2-15 Light spectrum of light Source-Hg lamp from Lumatec

Table 2-2 Calculation of number of electrons emitted by the Lumatec Deep UV light source for both UV and white light regimes

Regime	Range	Range/nm	Output power*/nW	Average photon energy/eV	Number of photons/h	Total number of photons/h
UV	UVC	240-280	100	4.75	$4.9*10^{20}$	$2.725*10^{22}$
	UVB	280-320	800	4.1	$4.36*10^{21}$	
	UVA	320-400	130	3.44	$8.5*10^{21}$	
	Blue	400-500	1700	2.74	$1.39*10^{22}$	
White Light	Visible	400-700	4000	2.25	$4.0*10^{22}$	$4.0*10^{22}$

2.2.3 Detection System – Emerson

The gas detector used in this work was X-stream gas analyzer (Emerson Inc.), connecting to the ‘gas outlet’ in Figure 2-14. The remarkable advantage of X-stream is that it realizes a continuous gas analysis and can measure up to four components simultaneously. Different detectors are equipped for different gases. In this work, the amounts of H_2, CO_2 and sometimes, CO in the reactant gases have been monitored: H_2

is detected with the thermal conductivity detector (TCD), CO_2 and CO are detected with the photometric non-dispersive IR gas sensor. The data collected by X-stream is the concentration of target gas in Ar, in ppm, and a further conversion to an absolute value of the hydrogen evolution rate in $\mu molh^{-1}$ is needed.

2.2.4 A typical HER system

hole sacrificial agent

As I focus on the hydrogen generation process, a hole scavenger was used, to consume the holes generated alongside the photogenerated electrons and contribute to a higher photocatalytic efficiency. Methanol (MeOH) has been reported as an efficient hole scavenger for most metal oxide semiconductor, while triethanolamine (TEOA) is used more widely for metal supported NP C_3N_4.[93] In this study, I have selected MeOH as the sacrificial agent.

When used as hole sacrificial agent in an inorganic semiconductor system, it has been reported that the MeOH does not directly react with the holes.[94-96] Prior to the MeOH degradation, the initial step is the reaction between photogenerated holes and H_2O, forming the hydroxyl ($^{\cdot}OH$) and superoxide radical anions ($O_2^{\cdot -}$) as the primary oxidizing species[95-96] (Equ. 4-1 & 2-11).

$$H_2O + h^+ \rightarrow {}^{\cdot}OH + h^+ \qquad \text{2-10}$$

$$CH_3OH + {}^{\cdot}OH \rightarrow {}^{\cdot}CH_2OH + H_2O \qquad \text{2-11}$$

cocatalyst

Typical cocatalysts are nobel metals, which form the Schottky barrier on the interface between them and the catalyst. Therefore, the photoelectrons can easily transfer from catalysts with low work function to cocatalysts with high work function, significantly enhancing the separation and lifetime of photogenerated carriers.[97] Furthermore, the addition of cocatalyst can effectively reduce the overpotential of the oxygen and hydrogen evolution reactions. For example, Y. An and coworkers reported that the oxygen evolution potential shifts from 1.38 to 1.25 V after CoPi deposition, whereas the onset potential for H_2 evolution shift positively from -0.45 V to -0.15 V after Pt loading.[98]

Pt has been the cocatalyst in our HER system via a photo-deposition process, in which H_2PtCl_6 is provided to the catalyst suspension and subject to UV irradiation, get reduced to metallic Pt and deposit onto the catalyst. The amount of added H_2PtCl_6 is determined by the desired wt% of Pt cocatalyst to catalyst.

In my HER protocol, the respective MOF was suspended in an aqueous solution that contained a corresponding amount of H_2PtCl_6 as a precursor, and the subsequent UV illumination reduced the precursor within the first few minutes to yield very small Pt clusters.

Typical HER process

In a typical photocatalytic HER experiment, 10 mg of photocatalyst was first dispersed into 40 mL DI H_2O and HPLC MeOH mixture (1:1 v:v), then subjected to 3 min sonication. After sonication, the reaction mixture was transferred to the reactor described in Figure 2-14 under constant stirring at 300 rpm. The suspension was purged with Ar flow (100 mLmin^{-1}) for 5 min to eliminate the dissolved oxygen. A certain amount of H_2PtCl_6 solution (corresponding to the wt% of Pt:catalyst being 0.5) was then added, after which the reactor was closed and the X-stream was started. The Ar flow was changed to 30 mLmin^{-1} and was held the same for the rest of the reaction. Before light irradiation, the reaction system was kept in darkness for at least 30 min to reach an equilibrium.

– Gas Evolution Activity

The unit of the evolved gas detected by Emerson is ppm; to convert the value into the absolute value of i.e. hydrogen evolution rate in μmol/h, calculation is as follows.

$$activity\left[\frac{mL}{min}\right] = \frac{activity\ [ppm]}{1000000\ [ppm]} * flow\ rate\ (\frac{mL}{min}) \qquad \text{2-12}$$

According to the ideal gas law PV=nRT, the evolution rate can be further written as:

$$activity\left[\frac{\mu mol}{h}\right] = activity\ \left[\frac{mL}{min}\right] * \frac{P\ [Pa]}{T[K]*R\left[\frac{m^3 Pa}{molK}\right]} * \alpha \tag{2-13}$$

Subsequently, the equation can be converted into:

$$activity\left[\frac{\mu mol}{h}\right] = \frac{activity\ [ppm] * flow\ rate(\frac{mL}{min})}{407.5} \tag{2-14}$$

3 Materials Synthesis

3.1 Hydrothermal Synthesis of Ti-based MOF

The reactant precursors were prepared under Ar atmosphere. Experimental details are as follows:

3.1.1 Synthesis of Single-ligand MOF: $MIL_{1-x}(NH_2\text{-}MIL)_x$-125-Ti

1). For MIL-125-Ti, 1 g (6 mmol) of terephthalic acid (H_2BDC) was first dissolved into a mixture of 2 mL HPLC methanol (MeOH) and 18 mL anhydrous dimethylformamide (DMF). Afterwards, 0.568 mL titanium isopropoixde (TTIP) (2 mmol) was added to the solution under stirring. The mixture was then sonicated for 20 min and transferred into an autoclave (volume: 45 mL), reacting at 150 °C for 18 h.

2) For NH_2-MIL-125-Ti, 40 mL of anhydrous DMF and 10 mL of HPLC MeOH were mixed as solvents, then 568.1 mg of 2-amino terephthalic acid (NH_2-BDC) was added to the mixture, stirred at room temperature till the yellow organic linker got fully dissolved. 0.568 mL TTIP was added at the end, followed by stirring for another 3 min. The resultant solution was solvo-thermally reacted in a 100 mL autoclave at 150 °C for 24 h.

3.1.2 Synthesis of Mixed-ligand MOF: $MIL_{1-x}(NH_2\text{-}MIL)_x$-125-Ti

For the mixed-ligand sample $MIL_{1-x}(NH_2\text{-}MIL)_x$-125-Ti, the general procedure and the solvent composition (v/v % MeOH : DMF = 1:9) are the same as the single-ligand MOF; the preparation details regarding the amount of precursors are listed in Table 3-1.

Table 3-1 Preparation Details of the mixed-ligand Ti-MOF as well as the single-ligand MOF

Sample	**$MIL_{1-x}(NH_2\text{-}MIL)_x$-125-Ti**							
x	0	2%	5%	10%	20%	50%	80%	100%
H_2BDC	1 g	1g	1g	1g	398.7 mg	249 mg	99.8 mg	-
NH_2-BDC	-	22.2 mg	57.2 mg	120.8 mg	108.8 mg	271.7 mg	434.7 mg	568.1 mg
TTIP	0.568 mL	0.568 mL	0.568 mL	0.568 mL	0.568 mL	0.568 mL	0.568 mL	0.568 mL
Solvent Volume	20 mL	20 mL	20 mL	20 mL	40 mL	40 mL	40 mL	40 mL
@ 150 °C Time	18 h	18 h	18 h	18 h	24 h	24 h	24 h	24 h
Measured NH_2BDC ratio (x)	0	4%	6.5%	11.5%	18.5%	45.2%	81%	101.2%

Based on the synthesis protocols of MIL-125-Ti and NH_2-MIL-125-Ti, there are two possibilities to prepare mixed-ligand MOFs: adding H_2BC to the NH_2-MIL-125-Ti precursor solution (route 1) or adding ligand NH_2BDC to the MIL-125-Ti precursor solution (route 2). In this work, I started with route 1 and succeeded to obtain samples with x = 20%, x = 50 % and x = 80%. After the photocatalytic characterization, mixed-ligand samples with x < 20% raised our interests. However, based on the route 1, I failed to obtain crystalline materials. Therefore, the procedure was modified according to the route 2, yielding desired crystalline products with x < 20%. Synthetic protocols of $MIL_{1-x}(NH_2\text{-}MIL)_x$-125-Ti for $x < 20\%$ and $x \geq 20$ are presented in Table 3-1 in blue and black, respectively. In short, the major difference between the routes stems from the used organic ligand to Ti-precursor ratio: it is higher for the route 2.

The resultant powders were collected via centrifugation and washed with DMF and MeOH 3 times each. The products were then dried overnight in a vacuum oven at 150 °C. The final dry powders were characterized via XRD, SEM, BET etc. as well as tested with regard to their photocatalytic activity.

3.1.3 Quantitative Analysis of the Actual Fraction of NH_2BDC in $MIL_{1-x}(NH_2\text{-}MIL)_x$-125-Ti

The determination of the actual ratio of NH_2BDC in mixed-ligand MOFs using digestion method modified from the procedure described by Chavan et al[99]. First, the UV-Vis absorption calibration spectra was measured with different concentrations (between 0 and 0.128 mg/mL) of NH_2-BDC ligand in 0.1 M NaOH. Then, 4 mg of MOF powders was dispersed in 3.85 mL 0.1 M NaOH aqueous solution and stirred at room temperature for 1 day. After that, the suspension was left still for another 2 days. Absorbance spectra of the liquid samples were recorded after filtering out the white precipitate (corresponding to titanium hydroxide). The NH_2BDC concentration in the MOF powder could thus be determined by referring to the calibration spectra of the NH_2BDC ligand.

The obtained values for the ratios of NH_2BDC in the mixed-ligand MOFs are listed in Table 3-1.

3.2 TiO_2 derived from Thermal Calcination of MOFs

In this work, TiO_2 derived from MIL-125-Ti will be referred to as TO-x; from NH_2-MIL-125 will be referred to as TO-N-x (x is the calcination temperature). Based on the TGA data (Figure 4-13), to obtain pure TiO_2 based materials, MIL-125-Ti and NH_2-MIL-125-Ti were calcined in muffle oven in air at 550 °C and 600 °C, respectively. The ramp rate and dwell time were chosen the same for both: 5 °C/min and 1 h, respectively. The resultant powders are labeled as TO-550 and TO-N-600. Information about other TiO_x obtained from Ti-based MOF with various calcination parameters is listed in Table 4-9.

3.3 In-situ Investigation of the Thermal Evolution Process of NH_2-MIL-125-Ti

Temperature-programmed in-situ XRD experiments have been conducted in air, either with controllable airflow of 0.5 mL/min, or in open cell. Based on the temperature ramping rate, different measurement programs were carried out.

The slow ramping program is demonstrated in Figure 3-1(a). From 25 °C to 200 °C, the ramp rate is 20 °C/min and the crystal structure of the sample is monitored every 25 °C. The isothermal steps indicate the measuring process; each takes about 45 min. Between 200 °C and 350 °C, the heating rate is 1 °C/min and the measurement interval is every 5 °C. Above 350 °C, the ramp rate is 20 °C/min again.

In a fast ramping program (Figure 3-1(b)), the ramp rate and the measurement temeperature interval are fixed for the entire measurement (from 25°C to 700°C), 20 °C/min and every 25 °C.

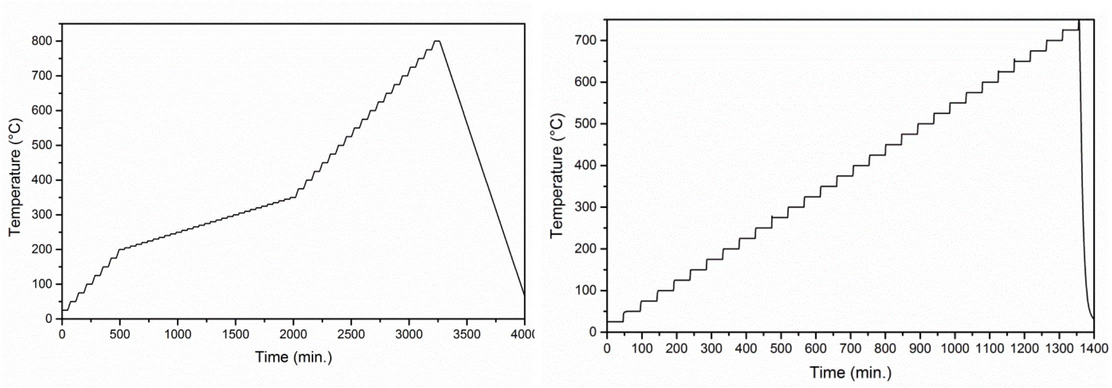

Figure 3-1 In-situ XRD temperature-time program. a) 1 °C/min ramping rate in the range of 200 °C to 350 °C; b). 20 °C/min ramping rate

4 Metal Organic Frameworks for Photocatalytic Application

4.1 Influence of Ligand Tuning on Ti-based MOFs

As stated in Chapter 1.3, one focus of my project is to investigate the impact of ligand tuning on the MOFs' structures and properties based on two common Ti-MOFs: MIL-125-Ti and NH_2-MIL-125-Ti. In addition to the two single-ligand MOFs, a series of mixed-ligand MOFs, $MIL_{1-x}(NH_2\text{-}MIL)_x$-125-Ti (2 % < x < 80 %), have been synthesized.

The preparation of MIL-125-Ti and NH_2-MIL-125-Ti followed the work by Liao et al[100] and Nasalevich *et al.*[26, 101], respectively. The mixed-ligand MOFs, $MIL_{1-x}(NH_2\text{-}MIL)_x$-125-Ti, have been prepared based on the synthesis protocol of single-ligand MOFs, *x* corresponds to the molar percentage of NH_2BDC in the precursor. The actual NH_2BDC ratio in the synthesized MOF has been confirmed using digestion method followed by UV-Vis DRS detection, which does not vary much from the mol % in the precursor. Therefore, in this work, I have referred to the MOF samples with the *x* value in the precursor, for example, $MIL_{0.8}(NH_2\text{-}MIL)_{0.2}$-125-Ti, as the fraction of NH_2BDC in the precursor is 20 %. For experimental details, see Chapter 3.1.

With regard to the mixed-ligand MOFs, however, another question needs to be discussed first regarding the apportionment of different ligands in $MIL_{1-x}(NH_2\text{-}MIL)_x$-125-Ti: whether the ligands are homogeneously distributed within the MOF matrix or form segregated nanodomains. So far, the research about mixed-ligand Ti-MOFs are scarce. Hendon *et al.*[33] have synthesized three aminated MIL-125 analogues, with the molar fraction of NH_2-ligand being 10 %, 50 % and 100 %. However, they focused on the overall narrowing of the band gap and did not pay attention to the distribution of ligand in the structure. Another work is by Chambers and co-workers[102]. They have synthesized $MIL_{1-x}(NH_2\text{-}MIL)_x$-Ti MOFs with x = 20 %, 46 % and 70 %. With TEM-EDX mapping, they stated a homogenous distribution of NH_2-ligand over the framework.

However, the apportionment of the ligands depends on the synthetic procedure;[103] therefore, conclusions by Chambers *et al.* do not necessarily apply to my mixed-ligand system. In the following section, properties of MOF samples as well as the apportionment of NH_2-ligand in the prepared MOF samples will be presented and discussed.

4.1.1 Results and Discussion

4.1.1.1 The Crystalline Structure of both Single- and Mixed-ligand MOFs

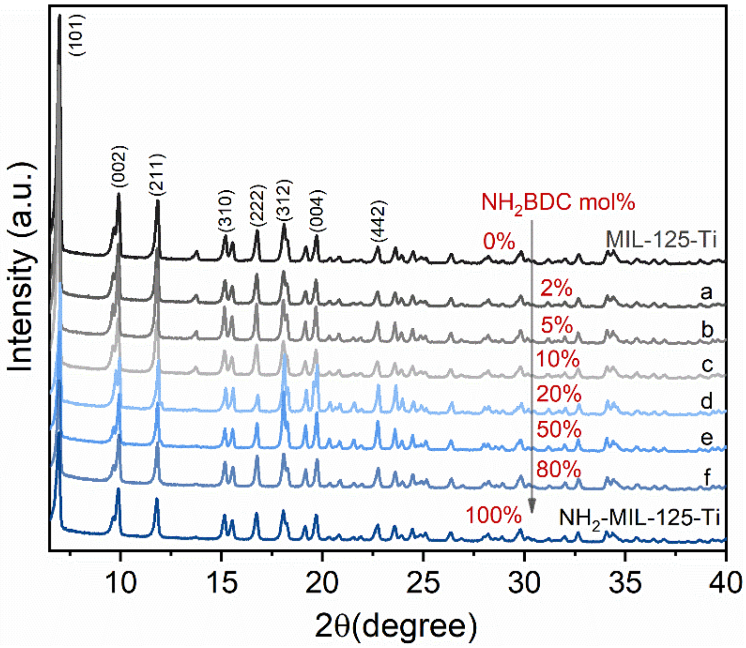

Figure 4-1 XRD patterns of as-prepared MIL-125-125, NH_2-MIL-125-Ti and mixed-ligand MOFs: $MIL_{1-x}(NH_2\text{-}MIL)_x$-125-Ti. 'x' values for plots a, b, c, d, e, f are 2%, 5%, 10%, 20%, 50%, 80%, respectively.

The PXRD results of prepared MOFs are summarized in Figure 4-1, which reveals that all the synthesized MOFs exhibit high crystallinity with sharp distinguishable peaks. Noteworthy, the XRD patterns of the MOFs contain more diffraction peaks than that of typical metal oxides, especially at lower diffraction angels (mainly $2\theta = 6° – 40°$). This can be attributed to the presence of organic ligands, which leads to a larger inter planar distance as well as a higher number of diffraction peaks. The diffraction patterns of MIL-125-Ti and NH_2-MIL-125-Ti resemble each other, due to their identical crystal structure, in accordance with other reports [104,26, 105]. $MIL_{1-x}(NH_2\text{-}MIL)_x$-125-Ti series exhibit similar diffraction pattern as MIL-125-Ti and NH_2-Ti-MOF, suggesting that the ligand mixing does not change the coordination manner between the Ti-oxo cluster and the organic ligand, thus resulting in no noticeable change of the final crystal structure.

Though no drastic change has been observed, there is a non-negligible peak intensity decrease at 2θ = 13.6° (ascribed to facet (202)) with the increase of NH_2-ligand percentage in the material. This peak has not drawn researchers' attention, which may be ascribed to its low intensity though its presence does not show consistency in all the reported XRD patterns of MIL-125-Ti and NH_2-MIL-125-Ti.[79, 105-106] For example, a change of peak intensity has also been presented in the work of Stavroula Kampouri[107] as well as the work of M. W. Anjum[105], however, no attention has been paid to the change.

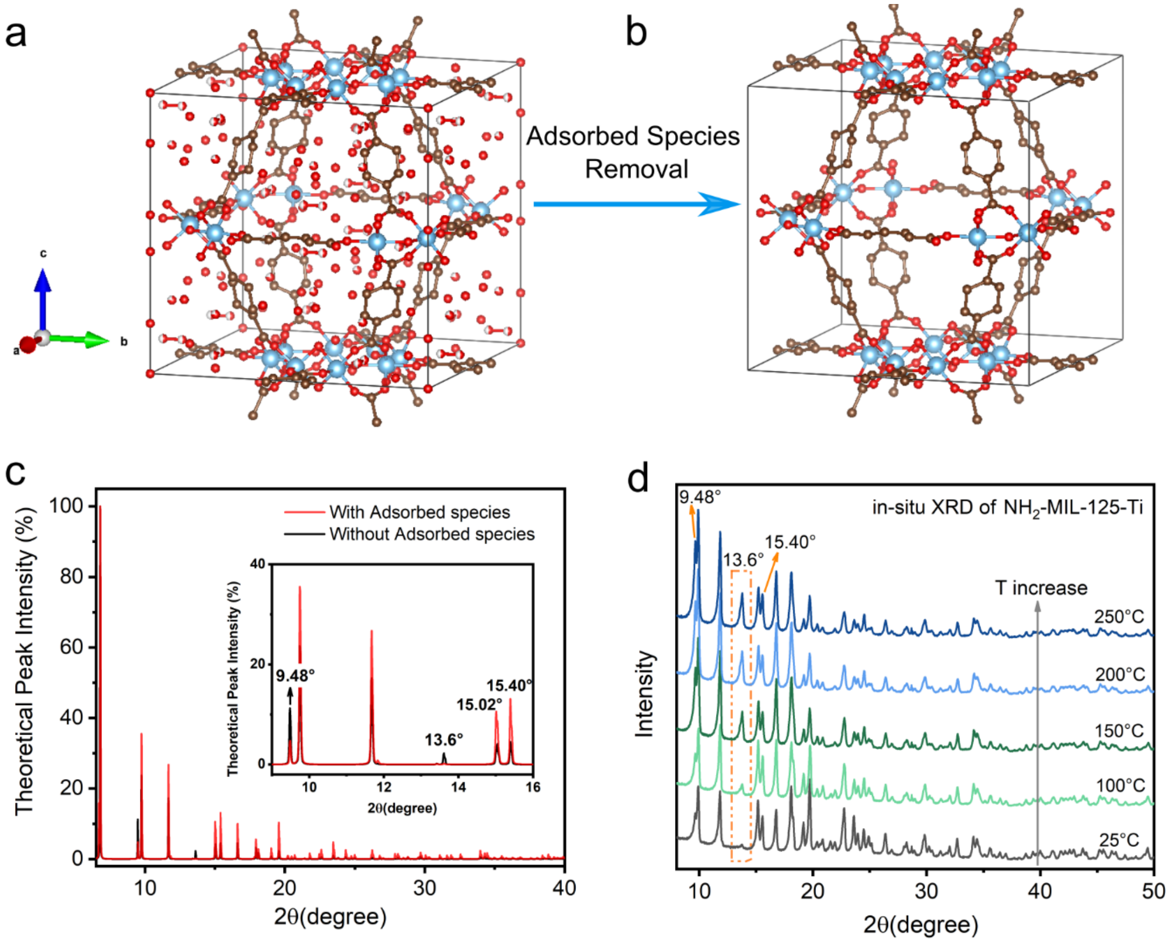

Figure 4-2 a) and b) simulated unit cell of MIL-125-Ti, before and after the removal of the adsorbed species inside the pore, respectively; c) calculated XRD patterns of MIL-125-Ti with and without adsorbed species; d) in-situ XRD patterns of NH_2-MIL-125-Ti from 25 °C to 250 °C.

In order to elucidate the origin of this diffraction peak, I have simulated XRD pattern of the original and modified MOF crystalline lattice using Vesta visualization software.

Figure 4-2(a) and (b) are the schematic illustrations of the unit cell before and after the removal of adsorbed species inside the framework; the resultant diffraction patterns are displayed in Figure 4-2(c). It can be observed that the peak intensities vary with the removal of the adsorbed species, for example, peaks at 2θ = 9.48°, 13.6°, 15.02 and 15.40°. In particular, the intensity of the peak at 2θ = 13.6° is extremely low in the structure with adsorbed species, while in the guest-free MOF, its intensity is 13.7 times higher. Therefore, I attribute the change of the peak intensity observed in mixed-ligand samples (Figure 4-1) to the adsorbed guest species inside the framework. Later, the in-situ XRD investigations (for details, see Chapter 4.4) further confirmed this argumentation. Here, Figure 4-2(d) gives an example based on NH_2-MIL-125 and it can be observed that the peak at 2θ = 13.6° gets intensified at elevated temperature (between 150 °C and 250° C) before thermal decomposition of the MOF takes place. In addition, the intensity variations observed for other peaks, such as 2θ = 9.48° and 15.4°, are also in good agreement with the simulated data, further confirming the impact of the adsorbed species. Another relevant set of data comes from the work of Nasalevich[26]. They have synthesized Co@MOF composite where the Co species reside in the pores of the MOF. Though they did not link the peak intensity of (200) diffraction to the presence of Co inside the pore, the peak in Co@MOF did show an intensity decrease compared to that in pristine MOF, which coincidently supports my conclusion.

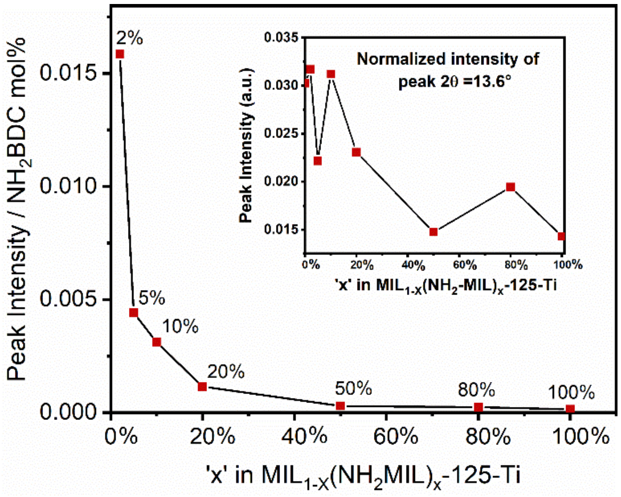

Figure 4-3 The relationship between the peak intensity of (220) and the NH_2BDC concentration in $MIL_{1-x}(NH_2\text{-}MIL)_x$-125-Ti

I have further analyzed the trend of the 13.6° peak intensity against the NH_2BDC concentration (Figure 4-3) to investigate the influence of the ligand on materials' adsorption properties. The peak intensity has been normalized with regard to the most intense diffraction peak at $2\theta = 6.9°$ (corresponding to facet (101)). A general trend can be concluded from the inset of Figure 4-3 that, with the increase of the NH_2BDC concentration, the intensity of peak (202) decreases. Therefore, a higher *x* value in $MIL_{1-x}(NH_2\text{-}MIL)_x$-125-Ti leads to more adsorbed species present inside the pores of as-prepared materials at room temperature (Figure 4-2). This can be ascribed to the presence of the amino-group on the NH_2BDC ligand that enables NH_2BDC to have higher affinity to guest molecules than H_2BDC due to the presence of a strong H-bond donating group. It is noteworthy that the influence of NH_2BDC is more profound at its lower concentration: when $x \leq 20$ %, the increase of the NH_2-ligand percentage in the material is accompanied with a steep decrease of the 13.6° peak intensity and, when $x \geq 50$ %, the peak intensity reaches a stable level. This, however, can be related to the large solvent amount used to prepare sample with $x > 20$ % as described in Chapter 3.1.

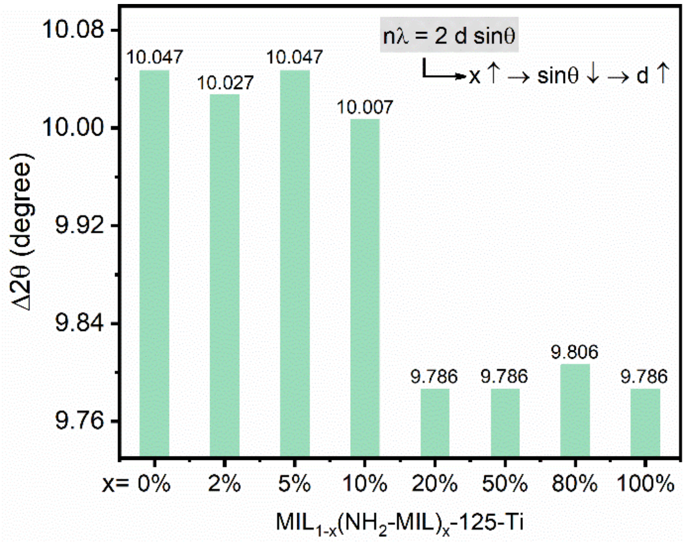

Figure 4-4 Comparison of the position gap between peak (002) and peak (004) in $MIL_{1-x}(NH_2\text{-}MIL)_x$-125-Ti

In addition to peak intensity, slight peak shifts have also been observed owing to the ligand difference. The diffraction peaks centered at around $2\theta = 9.8°$ and 19.7° correspond to facets (002) and (004), respectively, and the difference in the position of these peaks can be directly related to the unit cell constant in '*c*' axis. The difference in peaks in $MIL_{1-x}(NH_2\text{-}MIL)_x$-125-Ti versus NH_2-ligand concentration (*x* value) is summarized in Figure 4-4, calculated from the XRD patterns. On average, the Δ2θ values were about 10.03° and 9.79° for samples with $x < 20$ % and $x > 20$ %, respectively. Therefore, I observe a change of roughly 0.24°. As the XRD measurement step in this work was 0.02°, the observed changes in Δ2θ displayed in Figure 4-4 are significant and cannot be related to an instrumental artefact. According to the Bragg's law (2-3), the smaller Δ2θ indicates a larger lattice spacing. The lattice spacing of facet (001) is further related to the crystal constant '*c*', therefore, the increase in NH_2BDC mol% ($x \geq 20$ %) in the MOF structure induces an increase in the lattice constant 'c', which is in contrary to the reported unit constants (Section 1.3.5), 18.1440 Å for MIL-125-Ti and 18.1380 Å for NH_2-MIL-125.[33] This discrepancy may be caused by the adsorbed species in the framework, which can lead to an expansion of the crystal structure. This supports my aforementioned hypothesis that the higher the NH_2BDC content in the materials, the larger the amount of adsorbed species is, resulting in an increased anisotropic lattice constant.

In summary, XRD patterns verify the crystallinity and the crystal structures of the two single-ligand MOFs as well as the mixed-ligand samples. The crystal structure built with Ti-oxo cluster and dicarboxylic benzoic acid is highly robust, as the change of the functional group from -H to $-NH_2$ in the ligand did not affect the crystal structure. There are no additional peaks belonging to other phases in any of the diffraction patterns, which confirms the purity of the as-prepared materials. Furthermore, the ligand change has a marked impact on both, peak intensity and peak position of some diffractions, which I attribute to adsorbed solvents that enter the pores of the network, attracted by the NH_2-groups, and anisotropically enlarge the crystal lattice in c-direction. To further understand the effect of adsorbed molecules on the diffraction pattern, the assistance of computational simulations will be needed. Lastly, the molar ratio of NH_2BDC at 20 % seems to be a turning point for the impact for the lattice variation, with foreseeable impact on the materials' properties.

4.1.1.2 Morphology Characterization of both Single- and Mixed-ligand MOFs

a) SEM observation of MIL-125-Ti and NH_2-MIL-125-Ti

The morphology and size of the synthesized MOF particles have been characterized with SEM. Figure 4-5 reveals that both single-ligand MOFs are composed of particles with circular plate-like morphology. Their average dimensions are 570 nm * 260 nm and 480 nm * 200 nm for MIL- and NH_2-MIL, respectively. Therefore, MIL-125-Ti has a larger average particle size than NH_2-MIL-125-Ti within shorter solvothermal reaction time (18 h vs. 24 h).

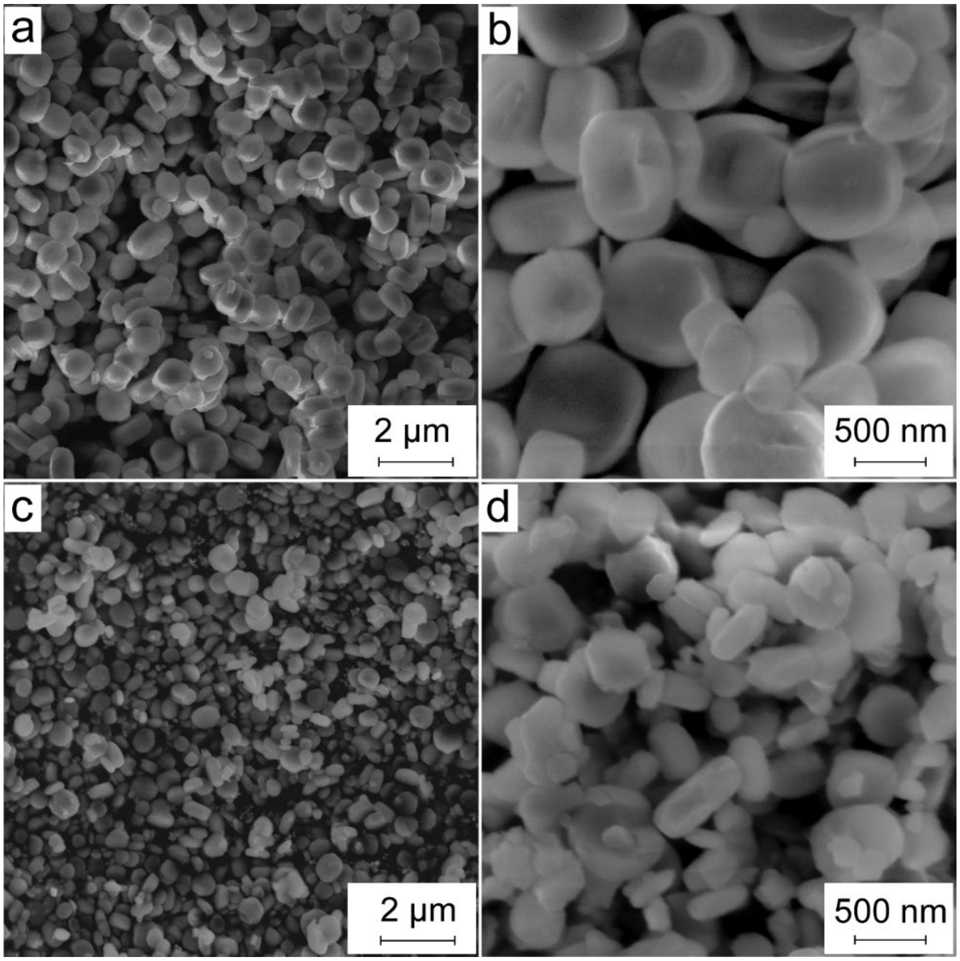

Figure 4-5 SEM images of (a) and (b) MIL-125-Ti; (c) and (d) NH_2-MIL-125-Ti

b) SEM Observation of Mixed-ligand MOFs: $MIL_{1-x}(NH_2\text{-}MIL)_x$-125-Ti

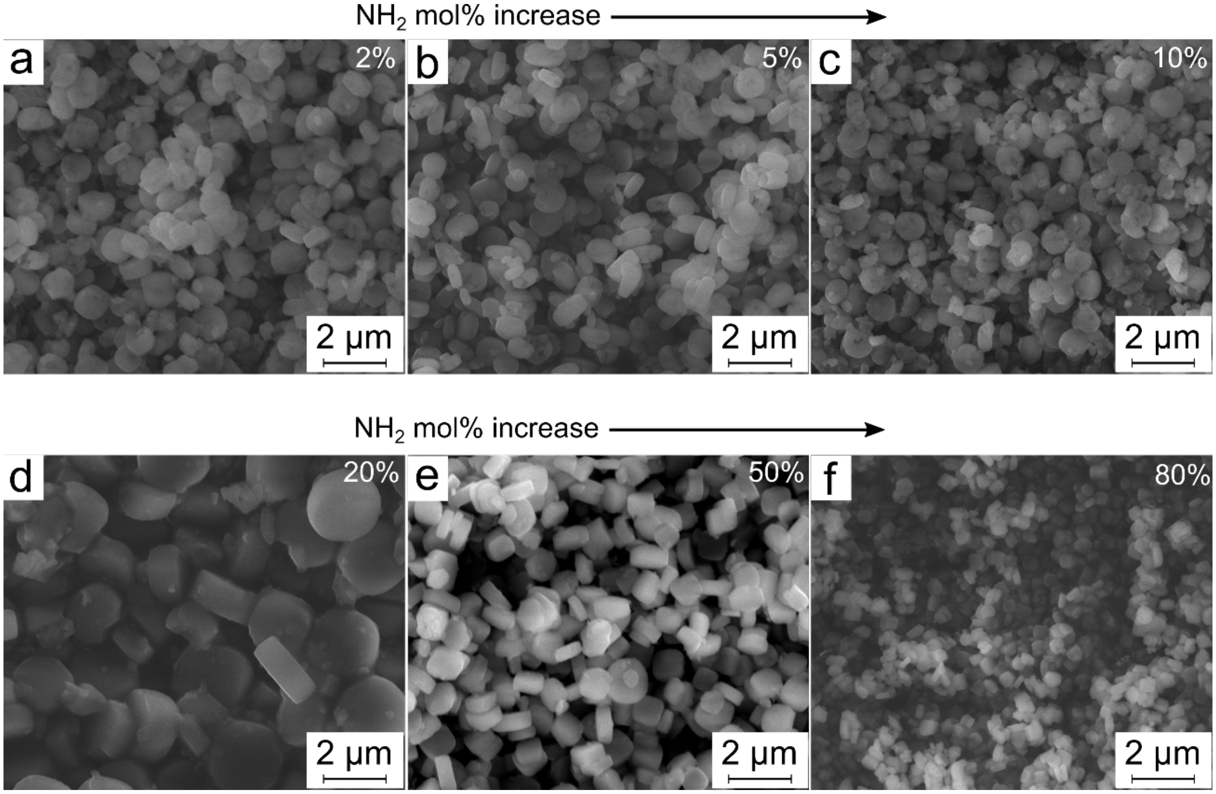

Figure 4-6 SEM images of $MIL_{1-x}(NH_2\text{-}MIL)_x$-125-Ti. 'x' values for a), b), c), d), e), f) are 2 %, 5 %, 10 %, 20 %, 50 %, 80 %, respectively. With increasing NH_2BDC molar fraction, the particles size decreases

The morphology of $MIL_{1-x}(NH_2\text{-}MIL)_x$-125-Ti with x varying from 2 % to 80 % are displayed in Figure 4-6 and it can be seen that all the samples are of similar circulate plate shape. The impact of NH_2BDC ligand on the particle size can be clearly observed: the increase of the NH_2BDC ratio in the precursor leads to a decrease of the particle size, as can be observed from Figure 4-6, when x increases from 2 % to 10 %, and from 20 % to 80 %. Table 4-1and Figure 4-7 summarize the change in the particle size, confirming it to be an isotropic decrease, as both diameter and thickness of the particle decrease following the same trend. The apparent inconsistent trend in particle size for the samples ranging from $MIL_{0.9}(NH_2\text{-}MIL)_{0.1}$-125-Ti to $MIL_{0.8}(NH_2\text{-}MIL)_{0.2}$-125-Ti can be attributed to the different synthesis routes used for the samples $x \leq 10\%$ and $x > 10\%$, respectively (Chapter 0). However, in both sample groups, we observed a clear trend of decreasing particle size with increasing NH_2 content (Figure 4-7).

Table 4-1 Particle Dimensions of $MIL_{1-x}(NH_2MIL)_x$*-125-Ti*

x	Thickness (nm)	Diameter (nm)
2%	441.3	877.4
5%	383.0	801.8
10%	351.7	796.7
20%	725.9	1758.1
50%	382.7	849.0
80%	168.8	361.4

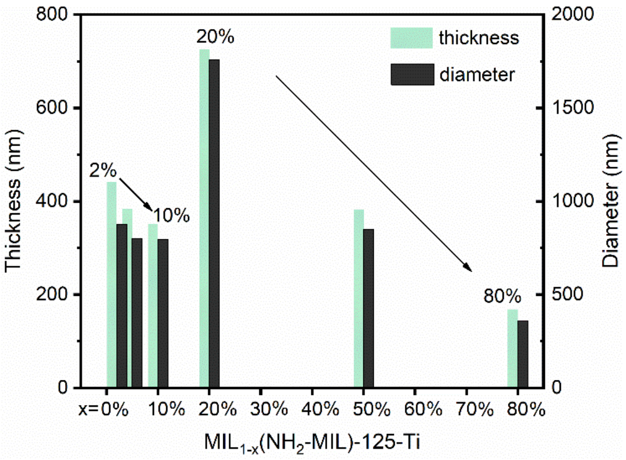

Figure 4-7 Particle Size of $MIL_{1-x}(NH_2\text{-}MIL)_x$*-125-Ti*

Based on the above SEM observation and my experimental efforts, I conclude that the two ligands, H_2BDC and NH_2BDC, affect the MOF crystallization processes, namely nucleation and crystal growth, differently. It seems that formation of crystalline H_2BDC-dominant MOFs requires higher ratio of the ligand to Ti-precursor (Table 3-1, $MIL_{0.8}(NH_2\text{-}MIL)_{0.2}$-125-Ti vs. $MIL_{0.2}(NH_2\text{-}MIL)_{0.8}$-125-Ti) to reach the required saturation and initiate nucleation. As to the crystal growth process, higher H_2BDC percentage results in a larger average particle size with the same solvothermal reaction time (Figure 4-6 (d) vs. (e) vs. (f) and Table 4-1). In contrast, the $–NH_2$ group in the organic ligand is an electron-donating group as well as a Lewis basic site, which can influence the esterification between the carboxylate acids and alcohols. The alcohols are either from reacted Ti-alkoxides or from solvents. Therefore, the NH_2-group can affect both the hydrolysis and the polycondensation process of the Ti precursors. Hence, I suggest that the hydrothermal system with higher H_2BDC percentage is a thermodynamically limited process, while NH_2BDC-dominated system is kinetically limited in its growth.

4.1.1.3 N_2 Physisorption

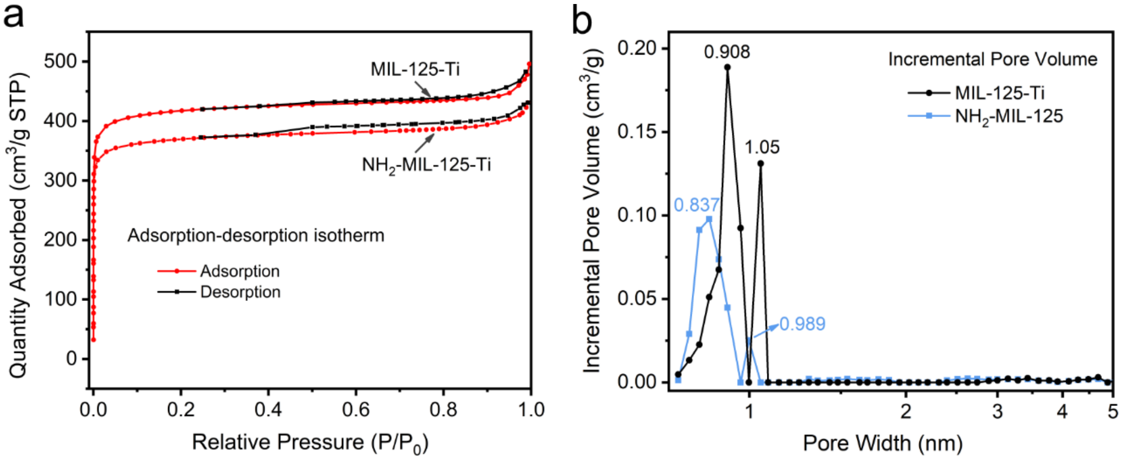

Figure 4-8 BET surface area and pore width distribution of MIL-125-Ti and NH_2-MIL-125-Ti

Table 4-2 Comparison of Physisorption Characteristics of MIL-125-Ti and NH_2-MIL-125-Ti

	BET surface Area	**BET Correlation Coefficient**	**T-plot Micropore Area**	**T-plot Micropore Volume**	**T-plot Correlation Coefficient**
MIL-125-Ti	1412.5 m^2/g	0.9988733	1320.9 m^2/g	0.603 cm^3/g	0.975973
NH_2-MIL-125-Ti	1242.5 m^2/g	0.9988999	1154.9 m^2/g	0.531 cm^3/g	0.974461

N_2 adsorption-desorption isotherms and pore volume distribution curves have been measured with single-ligand MOFs and the results are summarized in Figure 4-8 and Table 4-2. In both cases, the nearly vertically raised isotherms at the low-pressure range (P/P_0 ~0) are indicative of micropores[108]. At higher pressure regime, the isotherms display a typical type-I adsorption, characteristic for microporous materials, indicating a large specific surface area. BET surface areas of MIL and NH_2-MIL are calculated to be 1412 m^2/g and 1242 m^2/g according to the adsorption/desorption isotherm, respectively. Figure 4-8(b) holds the information of the incremental pore volume against pore width, in which the two peaks correlate to the larger micropores of the MOF crystal structures (12.5 Å and 10.7 Å in MIL- and NH_2-MIL, respectively[79-80]). Compared with MIL-125-Ti, the NH_2-MIL-125 has a smaller pore width and a lower micropore portion (Figure 4-8(b)). The t-plot micropore volume of MIL-Ti is higher than that of NH_2-MIL-125-Ti.

The decrease in pore volume as well as the surface area in NH_2-MIL-125-Ti are mainly attributed to the amino group in the organic ligand that stretches itself towards the pore interior[79, 109].

The experimental data on surface area and pore volume are slightly lower than the simulated values for the two MOFs.[47] This is not exceptional, when referring to the rather wide range of values reported in literature so far.[82, 86, 106, 110-111] This may be explained by residual guest species that may remain trapped inside the pores after degassing. The XRD data show the presence of solvents even after heat treatments at 200 °C, i.e. the temperature used to 'degas' the samples for BET analysis. Thus, it is likely that some DMF molecules remained within the micropores, even though degassing temperature is considerably higher than the boiling point of DMF (153 °C), which suggests that the removal of DMF is kinetically restricted by diffusion through the small pores.

Though N_2 ad/desorption results fulfill our expectations regarding surface area and pore dimensions, and N_2 physisorption has become the norm for the analysis of MOFs' porous structure, still, the reliability/applicability of N_2 as the probing gas needs to be addressed. The diameter of N_2 is about 3.7 Å. Considering that the diameter of the pores in the MOF structure is as small as ~4.7 Å, the question arises, whether N_2 is suitable for probing such small pores. Furthermore, the analysis of the data is typically performed following the BET theory, which assumes that all adsorption sites are equal in energy and that no gas interactions are present, both of which cases are not true in MOFs. Therefore, I advise to carry out further investigations using other adsorbates and with the DFT theory to better characterize the samples.

4.1.1.4 UV-Vis Absorption Property

The light response of as-prepared MOFs has been investigated with diffusive reflectance spectroscopy (DRS) and the results are summarized in Figure 4-9 and Figure 4-10. As a reference, the light absorption of the corresponding organic ligands have also been measured.

a) DRS Analysis of Single-ligand MOFs: MIL-125-Ti and NH_2-MIL-125-Ti

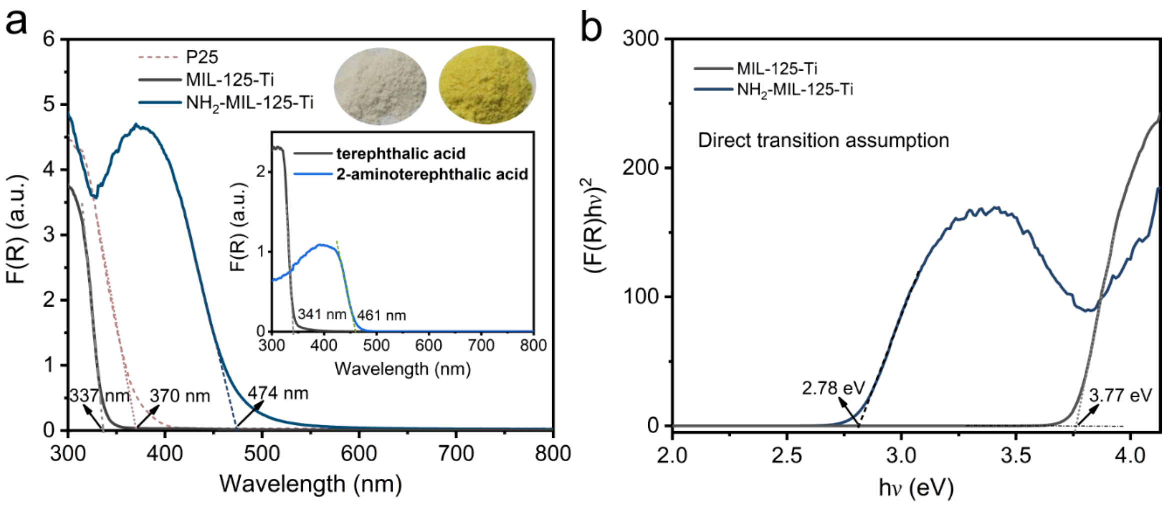

Figure 4-9 (a) Kubelka-Munk function vs. wavelength and (b) Tauc Plot of the as-prepared single-ligand MOFs: MIL-125-Ti in grey, NH_2-MIL-125-Ti in blue. P25 as reference in dotted line. The inset in (a) is the Kubelka-Munk function of the ligands, H_2BDC (grey) and NH_2BDC (blue). The white powder is MIL-125-Ti and the yellow one is the NH_2-MIL-125-Ti.

Figure 4-9(a) compares the Kubelka-Munk function of MIL-125-Ti, NH_2-MIL-125-Ti and their corresponding ligands. Terephthalic acid (H_2BDC) absorbs only in the UV region, with an absorption edge at 341 nm, while the absorption of amino-terephthalic acid (NH_2-BDC) starts from 461 nm. This is because the presence of amino group enables partial delocalization of electrons and introduces a potential n-π* transition, leading to a red-shift.[73] As to the MOFs, MIL-125-Ti starts to absorb from 337 nm while its NH_2-containing counterpart absorbs already below 474 nm, in agreement with their color as well as their band gap structure (Figure 1-15). It has been reported that the light absorption in Ti-based MOFs is realized via a ligand-to-metal charge transfer (LMCT) mechanism, in which the excited electrons transfer from the organic ligands (that constitute HOMO level) to the metal-oxo cluster, namely, $TiO_5(OH)$ clusters (that constitute LUMO levels)[104]. In NH_2-MIL-125-Ti, the absorption peak centered at 380 nm is thus likely attributed to the charge transfer from the $-NH_2$ group to the Ti-oxo cluster. Another absorption edging at around 350 nm is attributable to O to Ti charge transfer (LMCT) in $TiO_5(OH)$ clusters[59], explaining the appearance of the same absorption peak in MIL-125-Ti. As an additional reference, the DRS of P25 TiO_2 has also been measured, revealing the absorption edge at roughly 370 nm.

Figure 4-9(b) displays the Tauc plots of the two single-ligand MOFs, assuming a direct transition (Equation 2-6)[58, 112-113]. The intersects of the tangents with the energy axis mark the optical band gap values of MIL- and NH_2-MIL-125-Ti to be 3.77 eV and 2.78 eV, respectively, in good agreement with the reported data (Table 4-3). It appears that the HOMO of MIL-125-Ti is mainly defined by the π-bonding interactions between the aromatic C atoms in the benzene ring of the BDC linker, with small contributions from the O 2p orbitals[84]. On the other hand, the LUMO is composed of the 3d orbitals of the Ti atoms with almost no contribution from the organic component. Thus, compared with MIL-125-Ti, the HOMO in NH_2-MIL-125-Ti is shifted to higher energies owing to new bands introduced by the electron-donating $–NH_2$ group, which are located above the C 2p orbitals. For the LUMO, as it originates from Ti 3d orbitals, the presence of $–NH_2$ group does not have any strong effect.[33, 104] In conclusion, the narrower band gap in NH_2-MIL-125-Ti is due to the upshift of the HOMO level.

Table 4-3 Band structure of MIL-125-Ti and NH_2-MIL-125-Ti

Material	LUMO (vs. NHE)	HOMO (vs. NHE)	Eg	Comment
MIL-125-Ti	-1.40	2.40	3.80	Theoretical Calculation[98]
	-0.43	3.28	3.71	Exp.[58]
	-0.6	3.2	3.8	Theoretical Calculation[114]
			3.6, 3.67, 3.68	Exp.[33, 113]
			3.77 eV	This work
NH_2-MIL-125-Ti	-0.72	2.02	2.74	Exp.[86]
	-0.6	2.0	2.6	Theoretical Calculation[61, 114]
	-0.74	2.01	2.75	Theo.+Exp.[73]
	-0.40	2.10	2.50	Exp.[115]
			2.65, 2.72, 2.45	Exp.[33, 84, 113]
			2.78 eV	This work

** the value of NHE is taken at 25°C, equals to absolute electrode potential: 4.44 eV.*

Table 4-3 lists the absorption band levels and band gaps of MIL- and NH_2-MIL reported by other researchers, including both experimental and theoretical data. It can be seen that the HOMO of NH_2-MIL-125-Ti compared to that of MIL-125-Ti is about 1 eV less positive, while their LUMO levels are of similar potential, in line with the previous discussion.

The direct transition model has been widely used for the E_g calculation of Ti-MOFs,[33, 82, 109] however, recent studies have reported that the electron transition process in MOFs is more complicated[36]. In addition, the LMCT mechanism makes an indirect transition possible. Therefore, band gaps calculated based on different transition assumptions are listed in Table 4-4.

Table 4-4 Optical band gap based on different transition model assumption

Transition Type	MIL-125-Ti	NH_2-MIL-125-Ti (I)
Direct Allowed (n=1/2)	3.77 eV	2.78 eV
Direct Forbidden (n=3/2)	3.76 eV	2.76 eV
Indirect Allowed (n=2)	3.70 eV	2.62 eV
Indirect Forbidden (n=3)	3.70 eV	2.61 eV

In all the four cases, there are distinct straight tangent lines, which suggest the possibility of the corresponding transition type[116]. It can be seen that the optical E_g of MIL-125-Ti varies less than that of NH_2-MIL-125, while all the values are still in agreement with the reported data (Table 4-3). Therefore, the model for Tauc plot in MOFs requires more attention and further development.

b) DRS Analysis of Mixed-ligand MOFs: $MIL_{1-x}(NH_2\text{-}MIL)_x$-125-Ti

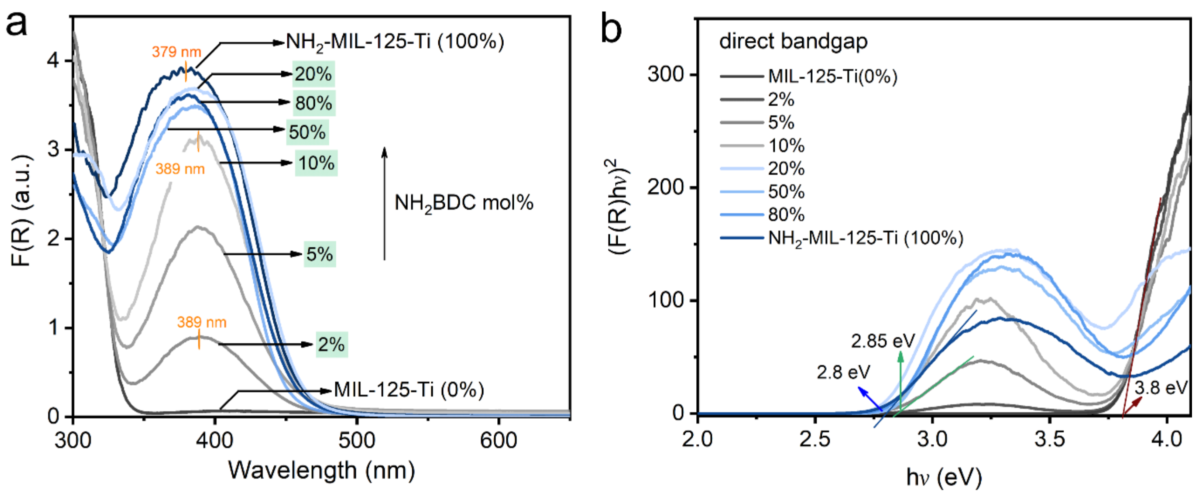

Figure 4-10 a) Kubelka-Munk function and b) Tauc plot of $MIL_{1-x}(NH_2\text{-}MIL)_x$-125-Ti

The light absorption properties of mixed-ligand MOFs, $MIL_{1-x}(NH_2\text{-}MIL)_x$-125-Ti have been characterized via DRS as well and the results are displayed in Figure 4-10. It can be seen in Figure 4-10(a) that the presence of NH_2-ligand in the MOF structure has an instant increase of absorption in the visible light range. The characteristic absorption peak of the n-π* transition introduced by the amino group at around 390 nm can be clearly seen even in $MIL_{0.98}(NH_2\text{-}MIL)_{0.02}$-125-Ti (Figure 4-10(a)) and the absorption intensity of this peak increases consistently with the NH_2-BDC percentage except for the sample of x = 20 %. In addition to this absorption peak at around 380 nm, there is another absorption feature, edging at lower wavelength (~ 340 nm), which is attributed to the absorption within $TiO_5(OH)$ clusters[59] as discussed before. For now, I attribute the inconsistent behavior of x = 20 % sample to the change of synthesis route. As observed from the SEM results, particles of the 20 % sample is almost twice as large in diameter compared to other samples, which may induce different reflection/scattering behavior.

The Tauc plots based on direct transition model (Figure 4-10(b)) have been used to calculate the band gaps of the mixed-ligand samples. The band gaps decrease dramatically upon the presence of NH_2-ligand as expected. The E_g of $MIL_{1-x}(NH_2\text{-}MIL)_x$-125-Ti is close to that of NH_2-MIL-125-Ti, around 2.8 eV (vs. MIL-125-Ti, 3.8 eV), in accordance with the work of C. H. Hendon *et al.*[33]. Again according to the onset at higher energy, samples can be divided into two groups, $x \leq 10\%$ and $x \geq 20\%$. As discussed before, the optical band gap of MOF derived from DRS is debatable, especially for the sample with x = 2 % and 5 %. Thus, clarification requires in-depth characterization of E_g as well as the positions of HOMO and LUMO of MOFs using other techniques, such as ultraviolet photoelectron spectroscopy (UPS) and impedance spectroscopy/Mott-Schottky measurements.

In summary, the UV-Vis absorption confirms that the ligand modification had a marked effect on light absorption and thus the electronic structure (e.g. band gap).

First, the amino groups induce an absorption band in the visible range, which increase in intensity with increasing NH_2 content. Furthermore, the samples with $x \geq 20\,\%$ demonstrate the same light absorption properties as single-ligand NH_2-MIL-125-Ti, as can be concluded from the change of both the center of amino chromophore dominated absorption peak (from 389 nm to 379 nm) and the Ti-oxo cluster dominated absorption edge (Figure 4-10).

Thus, the question remains as to why the absorption behaviors are different with *x* below and above 20 %. I have two assumptions here. One possibility (a) is that when x < 20 %, the NH_2- ligand failed to coordinate with the metal cluster during the synthesis, ending up as adsorbed species inside the framework. However, when x > 20 %, likely driven by the higher concentration, NH_2BDC started to coordinate forming to main MOF framework.

Another possibility (b) is that, even if in the case of x < 20 % samples, the NH_2-ligand was successfully incorporated in the main MOF framework forming coordination bonds with the metal cluster, the small fraction of the NH_2-ligand (there are 12 positions for ligand per unit cell) was not able to dominate the electron properties of the entire framework. If that is the case, the ligand became more influential only in samples with higher NH_2BDC content ($x \geq 20$ %), and consequently rendered the mixed-ligand MOF with similar absorption properties as those of the NH_2-MIL-125.

Both scenarios are possible; however, the scenario (a) would imply that the MOF network should contain uncoordinated NH_2BDC ligand after the synthesis. To confirm or discard this possibility, IR of the as-prepared MOFs has been performed.

4.1.1.5 Infrared Spectroscopy (IR)

a) IR Analysis of Single-ligand MOFs: MIL-125-Ti and NH_2-MIL-125

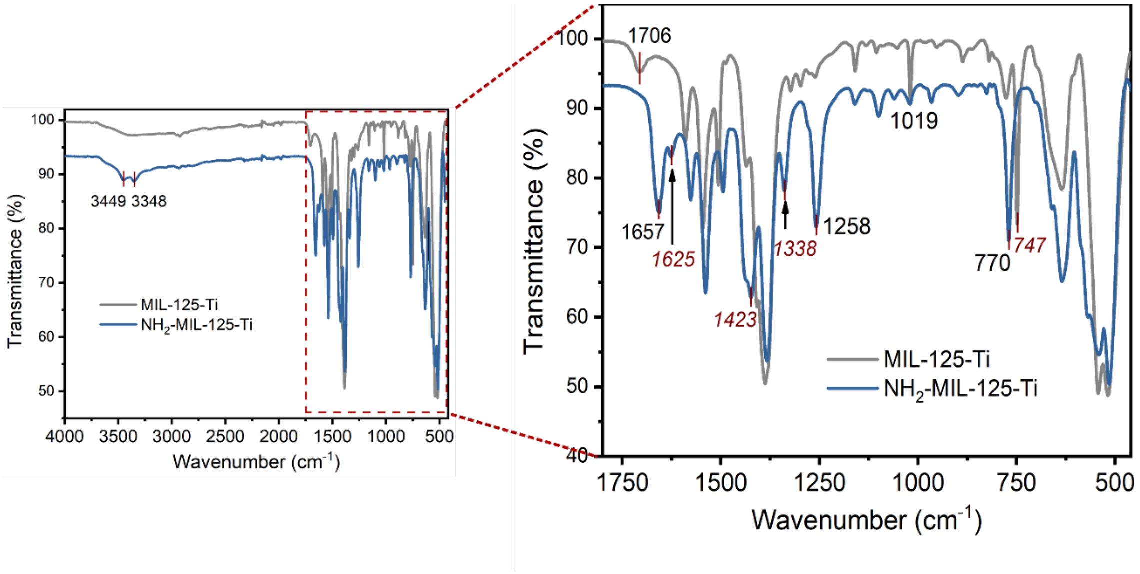

Figure 4-11 IR spectra of MIL-125-Ti and NH_2-MIL-125-Ti

Figure 4-11 displays the IR spectra of NH_2-MIL-125-Ti and MIL-125-Ti. First, the two additional bands at 3449 cm^{-1} and 3348 cm^{-1} in NH_2-MIL-125, correspond to the symmetric and asymmetric vibrational bands of $–NH_2$ groups[101, 111], confirming that the amine groups are indeed present in the structure and are free of binding partners. The broad band at around 3430 cm^{-1} for both samples can be attributed to solvent molecules trapped within the pores; for example, the stretching vibrations of the O–H groups of the adsorbed water emerge in this wavelength range. A magnified spectral range below 2000 cm^{-1} is relevant to further compare these two MOFs. There are common features in these two spectra: the characteristic peaks at 400-700 cm^{-1} can be assigned to the stretching vibrations of O-Ti-O[111,117]; vibrational bands in the region of 1400–1700 cm^{-1} are typical for the carboxylic acid-coordinated MOF structure. To be more specific, two absorption bands at around 1590 and 1500 cm^{-1} are due to the asymmetric stretching vibrations, whereas bands at about 1430 and 1380 cm^{-1} can be assigned to symmetric stretching vibrations of O-C-O in the framework. Compared with the free carboxylic acid, in which the carbonyl stretch ($\upsilon_{C=O}$) and C-OH vibrations ($\upsilon_{C\text{-}OH}$) locate at around 1690 cm^{-1} and 1280 cm^{-1}, respectively[118-119], in MOFs, the $\upsilon_{C=O}$ shifts to lower energy while the $\upsilon_{C\text{-}OH}$ shifts to higher energy due to the coordination with the metal-oxo cluster, forming O-C-O bonding. The band at 1258 cm^{-1} belongs to the C–H symmetric stretching vibrations of the benzene ring[111,120]. The asymmetric stretching mode of O-C-O located at ~1590 cm^{-1} is characteristic of the coordination between the metal cluster and organic ligand. A frequency shift has been observed between these two MOFs, 1579 cm^{-1} in NH_2-MIL-125-Ti compared with 1595 cm^{-1} in MIL-125-Ti. This red shift is caused by the $–NH_2$ group in the NH_2BDC – its electron donating property leads to a resonance effect[121] and consequently lowers the frequency of the O-C-O signal. For both MOF samples, I have not detected any of the characteristic peaks of free-carboxylic acid. Given the high sensitivity of IR spectroscopy, this result preclude the existence of unreacted ligands residing in the framework, thus disregarding our scenario (a).

Despite the common features, the presence of $–NH_2$ group brings new peaks in the IR spectrum of the NH_2-containing-MIL. For example, the new peak at 1335 cm^{-1} is the characteristic absorption of C-N stretching vibration between the carbon atom connected with the benzene ring and the nitrogen atom in the amino group[122]. Another new peak at

1625 cm^{-1} is attributed to the N-H bending vibration[111]. Furthermore, the change in intensity of certain absorption bands has been observed. The peaks at around 1258 and 770 cm^{-1} (which can be attributed to the C–H in-plane and out-of-plane bending vibrations[123]) show an increase of intensity in NH_2-MIL-125-Ti. On the other hand, bands at 1020 and 747 cm^{-1} can be assigned to the vibrations of benzene rings: their relative intensity decreased in NH_2-MIL-125-Ti. In addition, the band at 1658 cm^{-1} can be attributed to the carbonyl group in DMF[85], indicating a higher amount of residual solvent (presumably in the MOF pores), correlating well to the previous XRD observation.

b) IR Analysis of Mixed-ligand MOFs: MIL$_{1-x}$(NH_2-MIL)$_x$-125-Ti

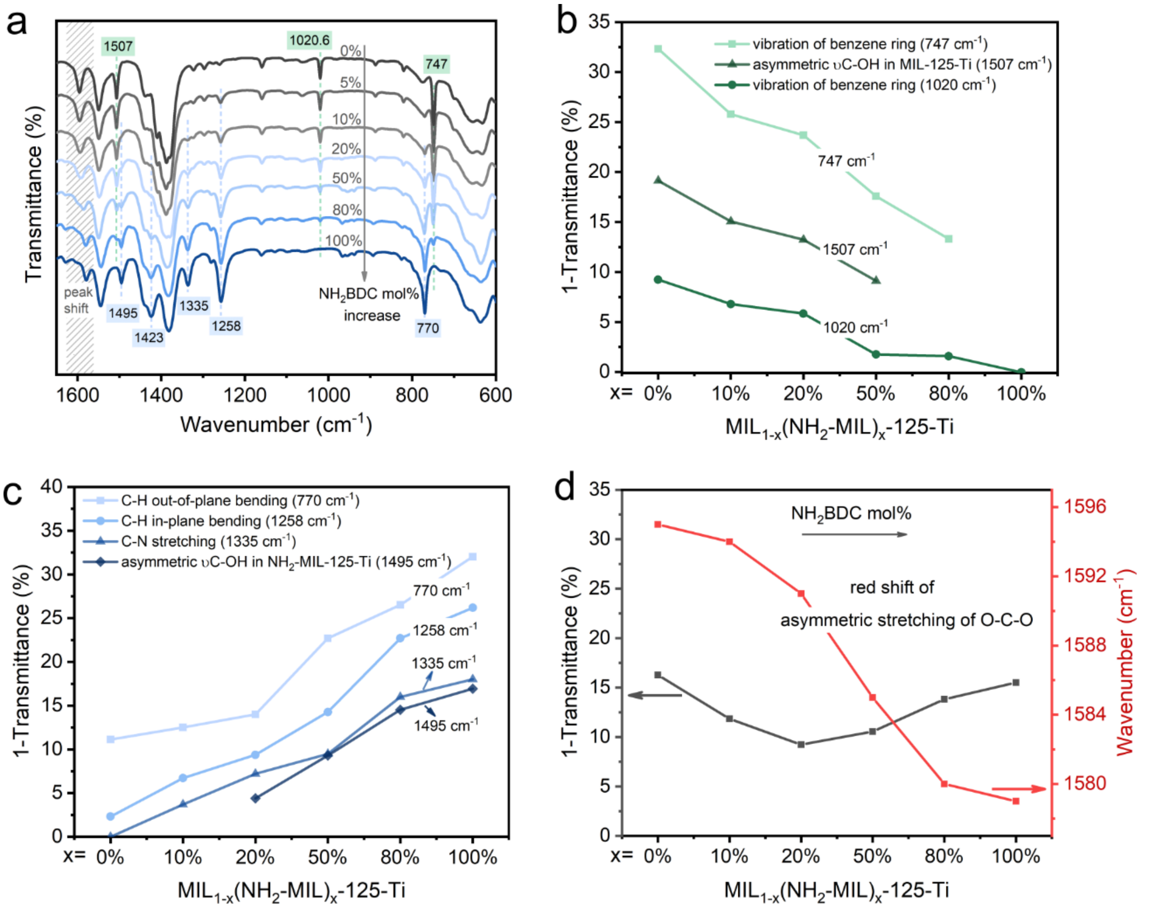

Figure 4-12 IR spectra of mixed-ligand MIL$_{1-x}$(NH_2-MIL)$_x$-125-Ti. (a) Enlarged spectra focused on the characteristic peaks representing the influence of ligand; peaks with green shades are dominant in MIL-125-Ti and peaks with blue shades are dominant in NH_2-MIL-125-Ti. (b) & (c) The change of peak intensities with respect to the x values: (b) peaks preferred in MIL-125-Ti; (c) peaks preferred in NH_2-MIL-125-Ti. (d) The position and intensity of asymmetric stretching of O-C-O with respect to NH_2BDC percentage.

Figure 4-12(a) shows that all the samples exhibit similar IR spectra: neither new peaks, nor characteristic absorption of carboxylic acid (1280 cm^{-1}) are present in the mixed-ligand samples, confirming the phase purity and the absence of free (uncoordinated) organic ligand. All samples have been investigated with respect to intensity and position of the most characteristic peaks. Figure 4-12(b) and Figure 4-12(c) plot the intensity change of peaks representative for MIL-125-Ti and NH_2-MIL-125-Ti, respectively. It can be concluded that with the increase of x, the intensity of peaks dominating in MIL-125-Ti decreases gradually and is accompanied by a continuous intensity increase of those peaks that dominate NH_2-MIL-125-Ti spectrum, such as the stretching of C-N vibration. This change can be attributed to the fact that the peak intensity between different samples is related to the amount of corresponding component in the material, and thus varies with the value x.

In addition to peak intensity change, peak shifts have been observed between $MIL_{1-x}(NH_2\text{-}MIL)_x$-125-Ti samples with different x as indicated with patterned area in Figure 4-12(a). Detailed analysis of this peak position charge is summarized in Figure 4-12(d). This peak at around 1590 cm^{-1} – ascribed to the asymmetric stretching of O-C-O – and its red shift between MIL-125-Ti and NH_2-MIL-125-Ti has been discussed before and is attributed to the resonance effect induced by the $–NH_2$ group. My data further demonstrates that this peak shows a continuous shift with the increasing NH_2BDC amount in the structure, which indicates a continuous change of the coordination strength in the framework. It has been discussed by Fend and Zhou[103], that in MOFs composed of two linkers, the non-dominant linker can disperse in the matrix of the dominant linker either in random/ordered form with no domain structure or by forming domains. Based on the observed continuous peak shift, I assume that in mixed-ligand $MIL_{1-x}(NH_2\text{-}MIL)_x$-125-Ti, different ligands are random distribution among the framework rather than forming domains; as in domains, there are supposed to exhibit two peaks with competing intensity.

In summary, IR spectroscopy is sensitive to analyze the mixed-ligand MOFs and provides valuable information enabling to confirm the phase purity as well as to characterize the molecular structure. Furthermore, IR spectra indicate that the MIL_{1-}

$_x$(NH_2-MIL)$_x$-125-Ti samples do not contain free uncoordinated ligand molecules, thus discrediting the first assumption proposed from DRS data. Based on the peak shift, the apportionment of the ligands has hitherto been supposed to be a homogeneous distribution over the framework, however, other characterization, such as solid-state NMR, is required to further confirm this.

4.1.1.6 Thermalgravimetric Analysis (TGA)

The thermal stability of the MOFs has been investigated by TGA. Being composed of organic ligands, MOFs undergo an oxidative degradation process when calcined at elevated temperatures (usually above 300 °C), leading to the 'break-down' of MOF structure.

a) TGA of Single-ligand MOFs: MIL-125-Ti and NH_2-MIL-125-Ti

Figure 4-13 displays the TGA results of MIL-125-Ti and NH_2-MIL-125-Ti as well as the ligands, H_2BDC and NH_2BDC. Figure 4-13(a) compares the TGA curves of MIL-125-Ti and NH_2-MIL-125-Ti. Based on the thermal derivatives of the weight loss with respect to the temperature, both curves can be divided into four weight loss stages.

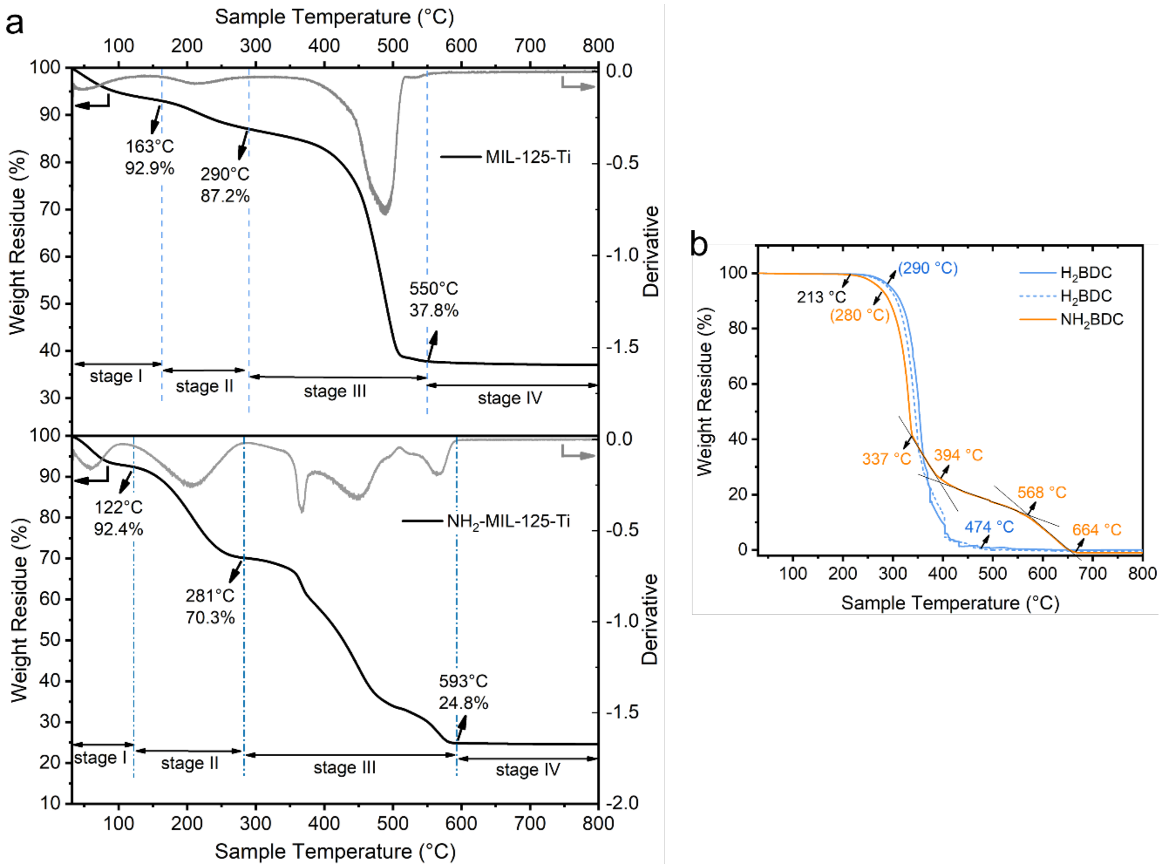

Figure 4-13 TGA results of a) MIL-125-Ti and NH$_2$-MIL-125-Ti; b) H$_2$BDC and NH$_2$BDC: two H$_2$BDC results are from two measurements to illustrate the reproducibility of the fluctuation of the data. All TGA measurements were conducted with the same parameter, 5 °C/min ramp rate, 20 mL/min air flow.

Stage Ⅰ in Figure 4-13(a) occurs at lower temperature and can be ascribed to the release of the adsorbed guest molecules, such as water and solvent molecules. It needs to be noted here that the surface-adsorbed water molecules evaporate below 100 °C; however, when water molecules get adsorbed inside the pores of MOFs, they interact more strongly with the matrix and a much higher temperature is required for H_2O to escape, which can be as high as 190 °C depending on the strength of the interaction.[103] Thus, the entire weight loss (~ 10 %) until 160 °C can be attributed to the evaporation of water. The slow weight loss during the Stage Ⅱ can be caused by the removal of chemisorbed solvent molecules and unreacted organic chemicals trapped within the MOF pores.[124]

The Stage Ⅲ, starting at around 290 °C for MIL-125-Ti and at 280 °C for NH$_2$-MIL-125, is due to the degradation of the framework, which correlates to the decomposition of H$_2$BDC and NH$_2$-BDC linkers, respectively, starting with a decarboxylation process.[102, [105, 125] Figure 4-13(b) provides the TGA data of the organic ligands and both ligands are stable till 213 °C; due to the fluctuation of weight residue at high temperature (above 350 °C), the derivative of weight loss is not shown in the graphs. But the difference between the thermal degradation process of the two ligands can still be clearly seen. Compared with H_2BDC, NH_2BDC displays step-wise weight loss occurring in several stages, as indicated with temperature marks: 337 °C, 394 °C and 568 °C. The processes occurring at the different stages are yet unknown, however, this complex kinetics coincides well with the behavior observed in NH_2-MIL-125-Ti during the Stage Ⅲ. The resemblance of the thermal behaviours between the MOFs and their corresponding organic ligands confirms that the decarboxylation process takes place before the ligand decomposition. The strong weight loss is then attributed to the loss of the organic ligands. It is known that the structural reorganization of $Ti_8O_8(OH)_4$ units and the corresponding formation of 3D Ti-O-Ti networks happens simultaneously with the ligand removal during this stage.[124] Therefore, the residue in the Stage Ⅳ is TiO_2, which co-exist in both anatase and rutile phase depending on the temperature (phase transformation of anatase to rutile happens at around 600 °C[126]). The phases of oxide materials at different stages have been further confirmed with in-situ XRD investigation (Chapter 4.4).

According to the chemical formula of MIL-125-Ti ($Ti_8O_8(OH)_4(C_6H_4C_2O_4)_6$) and NH_2-MIL-125-Ti ($Ti_8O_8(OH)_4(C_6H_3C_2O_4NH_2)_6$), when the product of MOF calcination is TiO_2, the maximal theoretical mass loss for these two MOFs should account for 59.1 % and 61.3 %, respectively. However, the weight loss between RT and 700 °C derived from our TGA data amounts to 62.9 % and 75.2 %, respectively. These values are higher than the theoretically calculated, which can be caused by the presence of the adsorbed species inside the MOFs. Instead, the weight loss of the single Stage Ⅲ (56.7 % for MIL- and 64.7 % for NH_2-MIL-) matches better with the calculated weight loss, which in turn confirms that the decomposition of organic component including carbon oxidation indeed takes place in this temperature window.

The influence of the amino group on the thermal stability can be elucidated from Figure 4-13(a): 1) compared with MIL-125-Ti, NH_2-MIL-125-Ti adsorbs more guest molecules (larger weight loss below 280 °C); 2) though the decarboxylation process happens at lower temperature (280 °C vs 290 °C), NH_2-MIL-125-Ti requires higher temperature to complete the organic removal process (593 °C vs 550 °C).

b) TGA of Mixed-ligand MOFs: $MIL_{1-x}(NH_2\text{-}MIL)_x$-125-Ti

To further prove the influence of NH_2-containing ligand, TGA curves of mixed-ligand samples have been measured (Figure 4-14). To minimize the adsorption capacity difference between samples, I applied a new measurement protocol with an additional isothermal treatment in the TGA chamber during the heating ramp. According to Figure 4-13(a), main framework of both MIL-125-Ti and NH_2-MIL-125-Ti are stable till 281 °C. Therefore, the temperature of the isothermal treatment was set to 200 °C and the subsequent ramping started automatically when the software detected a weight change of less than 0.01 %/min. In Figure 4-14, the stable sample weight at 200 °C is set as the starting value (100 %). It also needs to be noted that the ramp rate was set to 10 °C/min, different from the previous measurement, which was 5 °C/min.

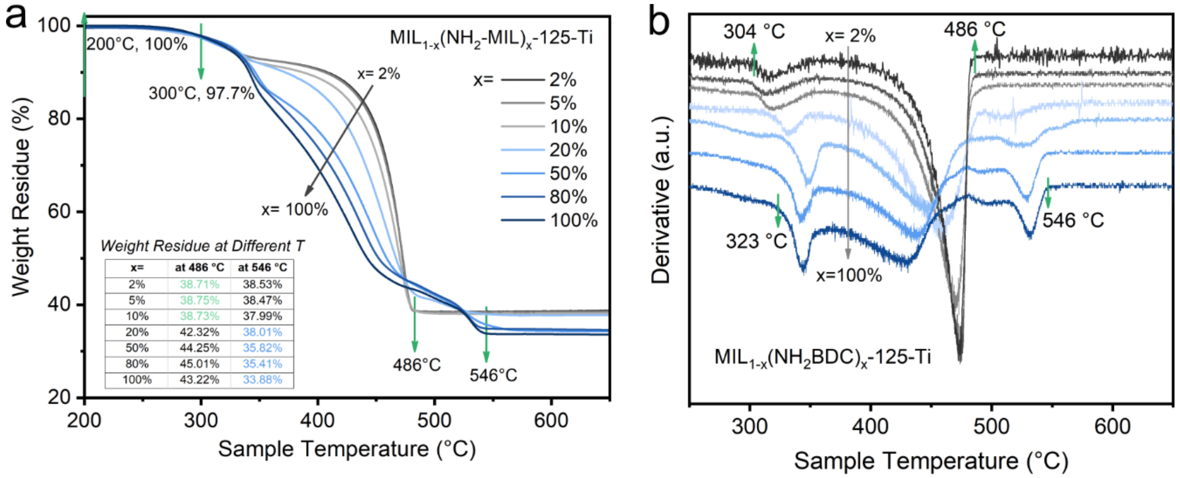

Weight Residue at Different T

x=	at 486 °C	at 546 °C
2%	38.71%	38.53%
5%	38.75%	38.47%
10%	38.73%	37.99%
20%	42.32%	38.01%
50%	44.25%	35.82%
80%	45.01%	35.41%
100%	43.22%	33.88%

Figure 4-14 a). TGA of $MIL_{1-x}(NH_2\text{-}MIL)_x$-125-Ti; b) Derivatives of weight loss against temperature of $MIL_{1-x}(NH_2\text{-}MIL)_x$-125-Ti.

Figure 4-14(a) shows the weight residue vs. temperature and Figure 4-14(b) shows the first derivative of the weight residue with respect to the temperature, from which the initiation temperature of different process can be derived. It is noteworthy that the initiation temperature of the decomposition process (Stage III) increases with the increasing NH_2BDC proportion. With the value of x varying from 2 % to 100 %, the initiation temperature rises from 304 °C to 323 °C. As to the completion of the thermal decomposition of $MIL_{1-x}(NH_2\text{-}MIL)_x$-125-Ti, samples with a higher x value requires a higher temperature, in line with the previous observation from Figure 4-13. However, due to the higher ramp rate (10 °C/min vs. 5 °C/min), a lower temperature is observed for the completion of ligand removal and TiO_2 crystallization in both MIL- and NH_2-MIL dominant samples, compared with that of lower ramp rate, 486 °C vs. 550 °C and 546 °C vs. 593 °C. The impact of ramp rate on the MOFs' thermal evolution process has been investigated in more detail in Chapter 4.4 with various in-situ techniques. The overall weight loss of the powders increases with the NH_2BDC percentage in the MOFs, in agreement with the theoretical calculation. However, the weight loss for all the samples are larger than that suggested by theoretical calculations, which further strengthens my doubt regarding physisorption measurement that 200 °C may not be enough to get rid of the chemisorbed species.

The derivative curves of weight loss against temperature of $MIL_{1-x}(NH_2\text{-}MIL)_x$-125-Ti (Figure 4-14) can be classified into two groups. One group is samples with $x < 20$ %, with 2 peaks observed in the derivative curve, similar to that of the MIL-125-Ti (Figure 4-13). Second group is samples with $x \geq 20$ %, with at least 3 peaks in the derivative curve, similar to that of the NH_2-MIL-125-Ti MOF. The data again indicates that the property of the series of these mixed-ligand MOFs changes at $x = 20$ %, as has been observed with DRS. Could this be caused by a higher amount of adsorbed species inside the framework when $x > 20$ %? Have the gaseous products of the calcination process varied with different *x*? Due to equipment accessibility, I did not investigate this issue in detail, though it would be interesting to conduct in-situ IR or thermogravimetric analysis/mass spectrometry (TGA-MS) to learn about the process.

4.1.1.7 Photocatalytic Hydrogen Evolution Activity

As discussed in the introduction of this chapter, ligand tuning has the potential to optimize the light absorption properties of MOFs. NH_2-MIL-125-Ti, in contrast to MIL-125-Ti, has been widely used as photocatalysts due to its visible light absorption property. However, the impact of ligand tuning on the materials' electronic and catalytic properties has been rarely investigated. Thus, the synthesized $MIL_{1-x}(NH_2\text{-}MIL)_x$-125-Ti samples offer a great chance for the exploration of ligand influence. To my knowledge, only the group of Draznieks[102] has briefly investigated the photocatalytic activity of MIL-and NH_2-MIL mixed Ti-MOFs, but only for x ≥ 20 % and only for the oxidation of benzyl alcohol. In this work, the catalytic properties of $MIL_{1-x}(NH_2\text{-}MIL)_x$-125-Ti, with a broader range of *x*, were investigated towards photocatalytic hydrogen generation from water.

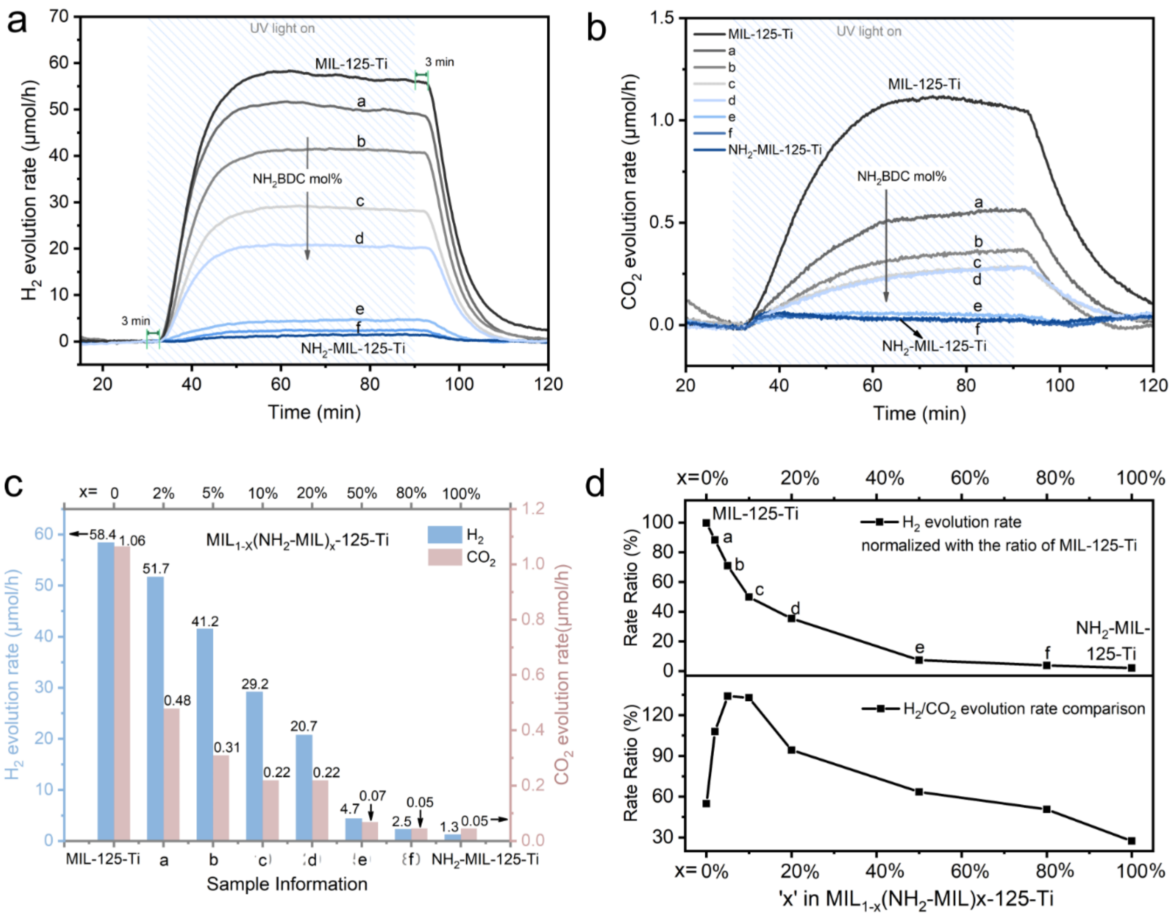

Figure 4-15 Photocatalytic results for $MIL_{1-x}(NH_2\text{-}MIL)_x$-125-Ti, x=0, 2 %, 5 %, 10 %, 20 %, 50 % and 100 % (10 mg MOF powders; 20 mL H_2O + 20 mL MeOH; Pt:MOF wt% = 0.5; light irradiation wavelength range: 280 nm – 400 nm; patterned area indicates illumination time.) Transient changes in a) H_2 evolution rate & b) CO_2 evolution rate upon 1 h irradiation; c) H_2 and CO_2 evolution rates reached after 30 min of irradiation; d) normalized H_2 evolution rate and H_2/CO_2 rate ratio with respect to the NH_2BDC content in MOF.

The photocatalytic experiments have been conducted using our unique continuous-flow set-up described in Chapter 0. As the band gap of MIL-125-Ti is 3.8 eV, UV irradiation was applied to enable activation, for which I used a Hg-lamp (Chapter 2.2, the output spectrum of the light source is displayed in Figure 2-15). All experimental parameters were set identical for all MOF samples.

Figure 4-15(a) shows the time course of the photocatalytic H_2 evolution rates of $MIL_{1-x}(NH_2\text{-}MIL)_x$-125-Ti. Owing to the unique H_2 detection system, continuous H_2 generation behavior under illumination can be recorded. The signal of produced H_2 starts to be detected 3 min after the light is switched on, due to the gas diffusion from the reactor to the detector. No O_2 has been detected in present setup; therefore, the process is referred to as hydrogen evolution reaction (HER), rather than water splitting. Both single-ligand MOFs and mixed-ligand MOFs are active for hydrogen evolution. However, the HER rate decreases with increasing of NH_2BDC concentration in the structure, with a maximum rate of 58.4 μmol/h (5840 $\mu molh^{-1}g^{-1}$) observed in MIL-125-Ti that gradually decreases to 1.5 μmol/h (150 $\mu molh^{-1}g^{-1}$) in NH_2-MIL-125-Ti.

Carbon dioxide is one of the possible oxidation products of the hole sacrificial agent, MeOH,[95, 127-128] and can thus be considered as an additional indicator of the photocatalytic activity (refer to Section 0). Figure 4-15(b) shows that the CO_2 generation rates of $MIL_{1-x}(NH_2\text{-}MIL)_x$-125-Ti declined with increasing NH_2BDC mol %, in accordance with the trend of hydrogen generation rates. Figure 4-15(d) provides a qualitative analysis of the impact of ligand choice and concentration. First, the H_2 evolution rate did not decrease linearly with increasing NH_2 content; instead, it shows a steep drop when $x \leq 10$ %, then from $x = 20$ %, the decrease starts to slow down.

Another interesting observation is that the ratio of evolution rates for H_2 versus CO_2 changed non-linearly with the ligand content, showing a maximum at values between $x = 5$ % and 10 %. A recurring question in the community is whether the hydrogen formed in photocatalytic hydrogen generation systems containing MeOH stems solely from the alcohol, i.e. via the steam reforming process of the MeOH.[94-96] This has been observed in the work of D. Bahnemann,[94] in which the amount of evolved H_2/CO_2 was around 3:1. In this work, the amount of evolved H_2 is far more than 3 times higher than that of evolved CO_2: in fact, the mole ratio of H_2 to CO_2 is in the range of 26 to 132. Therefore, either a large part of MeOH was oxidized into other products rather than CO_2, e.g. HCOOH, or there is hydrogen generated from water. Future studies with isotope labelling (e.g. D_2O) shall uncover the extent to which the water is involved, while in-situ IR-ATR will help unravelling the reaction mechanism.

Based on Figure 4-15, the observations can be summarized as follows: 1) both H_2 and CO_2 generation are hindered by the presence of NH_2BDC in the material; 2) the trends of gas evolution against NH_2BDC concentration in the case of H_2 and CO_2 show strong differences.

In $MIL_{1-x}(NH_2\text{-}MIL)_x$-125-Ti, I assume there are different secondary-building units (SBUs) distinguished by the dominant ligand, i.e. BDC-SBU and NH_2BDC-SBU, as a function of x. The H_2 evolution rates of pure MIL-125-Ti and NH_2-MIL-125-Ti (Figure 4-15) suggest that the BDC-SBU is more active than the NH_2BDC-SBU. The reason for the inferior activity of NH_2BDC-SBU is yet unclear, which may be caused by an intense charge recombination, thus, less electrons have been transferred to Ti-cluster to conduct the reduction reaction; this will be addressed in detail in the next Chapter.

The deterioration of H_2 generation rate with the increase of the NH_2BDC percentage in $MIL_{1-x}(NH_2\text{-}MIL)_x$-125-Ti can be attributed to the decrease of the relative amount of the active BDC-based SBU. However, if that would be the only mechanism of activity decrease, one would expect a linear correlation of photocatalytic activity with the NH_2BDC percentage – which is not the case. The data suggest that the presence of NH_2BDC-SBUs not only reduces the amount of active species in the system, but also has a synergistic effect further affecting the activity of BDC-SBUs.

How comes this negative impact of NH_2BDC-SBU to BDC-SBU?

One possibility to explain this trend is related with the presence of adsorbed guest species inside the micropores, which can block the diffusion of reactants into the framework, as well as hinder the exposure of the reactive sites in MOF. According to the XRD observation (Figure 4-3), the adsorption behavior of guest species demonstrates a quasi-exponential increase when the low amount of NH_2BDC linker is present in the mixed-ligand MOF. This trend coincides well with the decline of the H_2 evolution rate seen in Figure 4-15(d).

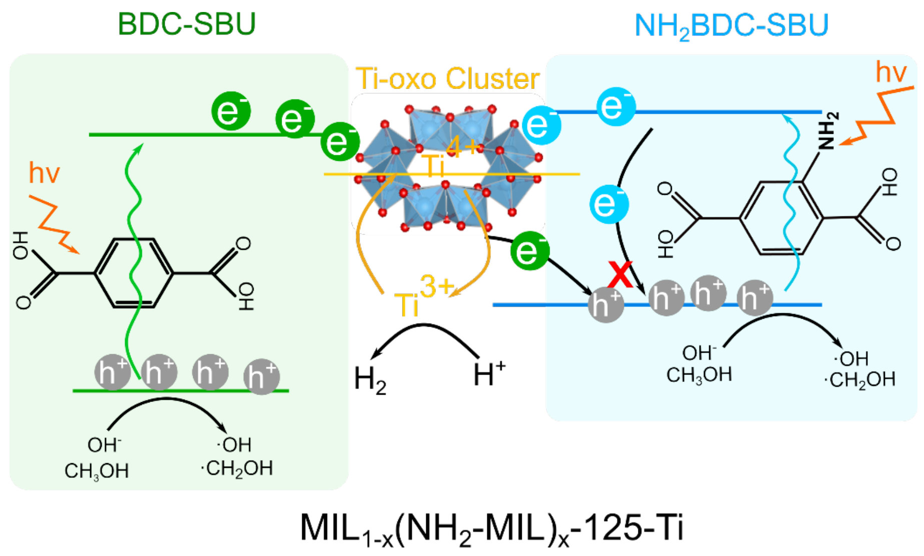

Figure 4-16 Illustration of possible charge transfer in mixed-ligand $MIL_{1-x}(NH_2\text{-}MIL)_x$*-125-Ti with relative energy levels of different components. The horizontal lines in green represent the LUMO and HOMO levels in* H_2BDC*; the horizontal lines in blue are the HOMO and LUMO levels in* NH_2BDC*; the yellow line on the Ti-oxo cluster mainly consists of the d orbitals of the* Ti^{4+}*. Cocatalyst is not included, as the state of Pt in the HER system is yet unknown.*

Another possibility to explain this synergistic effect is illustrated in Figure 4-16. I propose that in mixed-ligand $MIL_{1-x}(NH_2\text{-}MIL)_x$-125-Ti, the lower HOMO level of NH_2BDC-SBU can become the charge recombination center for the electrons originally excited in the BDC site. This model is based on the previously discussed mechanism of electron photo-generation and transfer that occurs via LMCT mechanism in both single-ligand MOFs.[70, 104, 129] According to LMCT, the organic linker first gets excited and then transfers the photoexcited electrons to the metal-oxo cluster, as discussed earlier in Section 1.3.4.2. The LMCT process with BDC-SBU and NH_2BDC-SBU are illustrated in Figure 4-16 (blue and green areas). After the charge transfer, the Ti^{4+} in the metal-oxo cluster is reduced to Ti^{3+}; while subsequent H^+ reduction (H_2 evolution) on the Ti^{3+} species and MeOH oxidation by the holes residing on the organic linkers regenerate the system. However, in the case of the mixed-ligand MOF, where both organic linkers co-exist and are likely connected to the same Ti-oxo custers, the process of charge transfer and recombination pathways are likely to be affected as illustrated by the Figure 4-16. The electrons generated by BDC-SBU are transferred to the Ti-cluster with the LMCT mechanism; however, they can undergo another transfer to the HOMO level of the NH_2BDC-SBU due to the position of the energy levels and thermalize there. This would explain that the presence of NH_2BDC-SBU in the material deteriorates the activity in the observed non-linear way, contributing to a strong H_2 generation drop upon NH_2BDC incorporation.

As to the case of CO_2 evolution (Figure 4-15), the appearance of NH_2BDC in the MOF structure leads to an instant drop in its generation, which may be due to a superior adsorption property of the NH_2-group that tends to trap the produced CO_2 inside the framework. Another possibility can be that the mechanism for MeOH oxidation follows a different pathway in NH_2BDC-containing MOFs. This may involve the formation of formaldehyde, methyl formate and other intermediates instead of CO_2. The issue needs to be investigated in the future with a dedicated detection system (e.g. GC) and simultaneous analysis of both gas and liquid phases of the reaction.

In the next chapter, a detailed investigation based on MIL-125-Ti and NH_2-MIL-125-Ti will be made to elaborate the reason for the strong differences in their photocatalytic performance.

4.1.2 Conclusion

In this chapter, a series of $MIL_{1-x}(NH_2\text{-}MIL)_x$-125-Ti (x = 0 %, 2 %, 5 %, 10 %, 20 %, 50 %, 100 %) has been synthesized; various characterizations including XRD, SEM, DRS, IR, TGA and photocatalytic hydrogen evolution experiments have been conducted to reveal the materials' structure and properties, in order to elaborate the influence of ligand. The key points are summarized as follows:

1) The synthesis of $MIL_{1-x}(NH_2\text{-}MIL)_x$-125-Ti is dependent on the value of x. When x > 20 %, route 1 worked better, with H_2BDC being added to NH_2-MIL-125-Ti precursor solution; while for samples with x < 20 %, synthesis succeeded with NH_2BDC being added to MIL-125-Ti precursor.

2) The crystallinity of $MIL_{1-x}(NH_2\text{-}MIL)_x$-125-Ti remained unchanged with different NH_2BDC content in the structure as confirmed by XRD, while the primary particle size varied with the ligand composition.

3) The NH_2-ligand present in the structure facilitates adsorption of guest species inside the microspores of the resulting MOF, as confirmed by XRD and TGA observation.

This can be ascribed to the formation of stronger hydrogen bonds induced by the $–NH_2$ group. The presence of adsorbed species inside the network induce a lattice constant change, as indicated by XRD patterns. Impact of the adsorbed species on the structural and functional properties of the MOFs – such as the pore size and volume as well as the photocatalytic performance – has also been discussed, but needs further confirmation.

4) The IR studies revealed the influence of ligand composition on the molecular structure, with both peak intensity and peak position displaying a consistent trend with respect to ligand concentration. As to the apportionment of different ligands in the structure, for now, I deduct that instead of forming domains, the minor ligand tends to distribute randomly over the framework.

5) The light absorption properties are improved with the NH_2BDC in the structure, even at low NH_2 contents such as x = 2 % (as indicated by the apparent shift into the visible light range). The intensity of the absorption peak introduced by the NH_2-ligand (centered at around 380 nm) increases consistently with the concentration of NH_2BDC in the material.

6) With the present HER setup, under UV light, MIL-125-Ti is the most efficient catalyst for hydrogen evolution among all $MIL_{1-x}(NH_2\text{-}MIL)_x$-125-Ti samples. Though the mixing of NH_2-ligand improves light absorption, it seems to be detrimental to the materials' photocatalytic activity: a decrease of H_2 generation rate has been observed with the increase of NH_2BDC ratio in the material. I further proposed two assumptions to explain the disproportionate decrease of H_2 evolution rate with the increase of x, related to the presence of adsorbed species and related to the charge recombination between SBUs. Moreover, based on the change of H_2/CO_2 evolution rate ratio with respect to ligand composition, a different MeOH oxidation process can be expected for different SBUs. These assumptions, however, necessitate further in-depth investigations.

4.2 Investigation of the photocatalytic behavior of single-ligand MIL-125-Ti and NH$_2$-MIL-125-Ti

Last section has witnessed differences in photocatalytic performance of various MIL$_{1-x}$(NH$_2$-MIL)$_x$-125-Ti MOFs towards HER, which has been ascribed to the ligand difference. Especially, MIL-125-Ti greatly outperformed NH$_2$-MIL-125-Ti in HER activity – contrary to what one would expect based on the light absorption properties of the two compounds, where NH$_2$-based MOF shows an extended absorption profile (Figure 4-9). Therefore, this section aims to figure out the reason for this observation by examining material's stability, choice of hole sacrificial agent, cocatalyst loading amount and possible charge recombination processes.

Table 4-5 Literature references on the photocatalytic performance of Ti-based MOFs

Ti-based MOF	Cocatalyst	Light source	Solvent & hole sacrificial agent	H_2 evolution rate	References
NH$_2$-MIL-125-Ti	Co(TPA)Cl$_2$ encapsulated into the cage of NH$_2$-MIL-125-Ti	Visible light (385 nm cut-off filter)	82% CH_3CN, 16% TEOA, 2% H_2O	49.3 μmolh^{-1}g^{-1}	ref[73]
NH$_2$-MIL-125-Ti	ZnIn$_2$S$_4$@NH$_2$-MIL-125(Ti) nanocomposites	A 300 W Xenon lamp with cut-off filter (420 nm)	aqueous solution containing 0.25 M $Na_2SO_3$and 0.35 M Na_2S as sacrificial reagents	2204.2 μmolh^{-1}g^{-1}	ref[86]
NH$_2$-MIL-125-Ti	Ni@NH$_2$-MIL-125(Ti)	A 100 W ultraviolet lamp	acetonitrile (17 mL), triethylamine (4 mL) and water (400 μL) mixture	1180 μmolh^{-1}g^{-1}	ref[70]
NH$_2$-MIL-125-Ti	NiP$_2$/ NH$_2$-MIL-125-Ti	300 W Xe lamp, Visible, λ>420 nm	79:19:5 v/v/v% acetonitrile/triethylamine/water	1230 μmolh^{-1}g^{-1}	ref[107]
NH$_2$-MIL-125-Ti	Ni$_{15.8}$P$_{2.1}$/ NH$_2$-MIL-125-Ti/0.75g-C$_3$N$_4$	300 W Xe lamp, Visible light	1 v/v% TEOA aqueous solution, Eosin Y as the photosensitizer	8700 μmolh^{-1}g^{-1}	ref[130]
MIL-125-Ti	MIL-125-Ti/CoPi-Pt	300 W Xe lamp, UV-Vis	24 mL water, 6 mL CH_3OH. Overall water splitting	401.5 μmol h^{-1}g^{-1} in H_2 evolution, 63 μmol h^{-1}g^{-1} in overall evolution	ref[98]
MIL-125-Ti	MIL-125-Ti/Pt	300 W Xe lamp (320-780 nm)	10 v/v% TEOA aqueous solution	154.72 μmolh^{-1}g^{-1}	ref[97]
MIL-125-Ti	**MIL-125-Ti/Pt**	**300 W Hg lamp** **(300-400 nm)**	**20 mL water, 20 mL CH_3OH**	**5800 μmolh^{-1}g^{-1}**	**This work**
NH$_2$-MIL-125-Ti	**NH$_2$-MIL-125-Ti/Pt**			**150 μmolh^{-1}g^{-1}**	**This work**

* Unit for the hydrogen evolution rate: $\mu mol \cdot h^{-1} \cdot g_{catalyst}$

Table 4-5 lists the photocatalytic performances of MIL- and NH_2-MIL-125-Ti for hydrogen evolution based on literature data. First, it can be seen that no direct comparison of the photocatalytic performance between these two MOFs has been reported so far, as most research focused solely on the visible light performance of NH_2-MIL-125-Ti. Second, under UV irradiation, the HER rate of MIL-125-Ti obtained in this work surpasses all of the reports (Table 4-5). The HER is more than 30 times higher than the work by Wu et al[97], which used a similar light source as well Pt as cocatalyst, but a different sacrificial agent (TEOA). This suggests that MeOH, used in this work, is a superior sacrificial agent for MIL-125-Ti, which is a surprising result. As to the NH_2-MIL-125, the hydrogen evolution rate of NH_2-MIL in this work is not among the best. However, considering the cocatalyst and solvent used in Table 4-5, it is nevertheless hard to obtain a solid comparison. Therefore, in this thesis, I have focused on the comparison of the photocatalytic performances between MIL-125-Ti and NH_2-MIL-125-Ti under the same conditions.

4.2.1 Influence of Hole Sacrificial Agent

It has been reported that the photocatalytic performance of photocatalysts is highly dependent on the sacrificial agent[86]; therefore, to exclude the possibility that the difference of the photocatalytic performance between the two MOFs is merely contributed by the choice of hole sacrificial agent, I have experimented with different hole sacrificial agents before exploring contributions related to the materials property. Triethanolamine (TEOA) is a commonly used hole sacrificial agent for NH_2-MIL-125-Ti under visible light irradiation (Table 4-5), the HER activities of MIL- and NH_2-MIL thus have also been measured with TEOA. The comparison of MOFs' photocatalytic performance with TEOA and MeOH are summarized in Figure 4-17 and Table 4-6, in which the H_2 and CO_2 generation rates have been recorded.

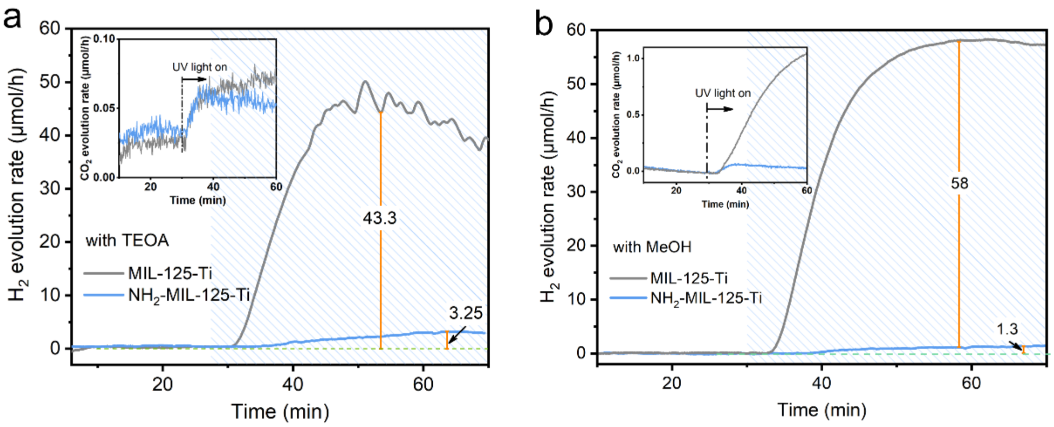

Figure 4-17 H_2 and CO_2 evolution rate of MIL-125-Ti and NH_2-MIL-125-Ti in different hole sacrificial agents: a) in 0.005M TEOA aqueous solution and b) in 50 % v/v MeOH aqueous solution.

Table 4-6 H_2 and CO_2 evolution rate of MIL-125-Ti and NH_2-MIL-125-Ti in different hole sacrificial agents

	H_2 Evolution Rate (μmol/h)		**CO_2 Evolution Rate (μmol/h)**	
Sample	with MeOH	with TEOA	with MeOH	with TEOA
MIL-125-Ti	58	43.3	1.06	0.05
NH_2-MIL-125-Ti	1.3	3.25	0.05	0.03

The H_2 evolution rate for MIL-125-Ti fluctuates with time, whereas it is rather stable for NH_2-MIL-125-Ti. Later MIL-125-Ti was measured in 0.01 M TEOA aqueous solution, with no fluctuation and similar H_2 evolution rate. Therefore, the H_2 evolution rate here can still be valid for comparison. The average H_2 generation rates for MIL-125-Ti and NH_2-MIL-125-Ti are 43.3 μmol/h and 3.25 μmol/h, respectively. For the CO_2 evolution, both MOFs exhibit almost no CO_2 formation in TEOA solution, different from the HER system with MeOH where the CO_2 has been clearly detected, suggesting that complete mineralization of TEOA is not a dominant process.

1. H_2 evolution rate of NH_2- MIL: 3.25 μmolh^{-1} with TEOA vs. 1.3 μmolh^{-1} with MeOH

   The main differences between TEOA and MeOH lie in their oxidation potential, polarity and molecular sizes, which may influence the HER activity of the two MOFs. Kampouri et al have used cyclic voltammetry (CV) to determine their redox behaviors in a non-aqueous solution[107]. They found oxidation peaks at 0.797 V and 0.963 V and current densities of 2 mAcm^{-2} and 1.61 mAcm^{-2} for TEOA and MeOH, respectively. Therefore, it is kinetically and thermodynamically easier to oxidize TEOA than MeOH, which may make TEOA, a more efficient hole scavenger. Therefore, NH_2-MIL in TEOA has an increased H_2 evolution rate compared to that in MeOH.

2. H_2 evolution rate of MIL: 43.3 $\mu molh^{-1}$ with TEOA vs. 58 $\mu molh^{-1}$ with MeOH:

> The explanation of the observed reduced activity of MIL-125-Ti in TEOA compared to MeOH is more complex. It appears that the differences in hole scavenging capability is negligible and thus doesn't play a decisive role in MIL-125-Ti, in contrast to the NH_2-sample. Another explanation addresses the higher polarity and bigger molecular size of TEOA as compared to MeOH, which possibly hinders the diffusion of TEOA into the pores of MOF, leading to decrease in the H_2 evolution rate.

Another difference brought by TEOA is the evolution behaviour of CO_2 (see inset in Figure 4-17). Different from the case of MeOH, the most common oxidation products of TEOA are various organic species such as aminyl radical, iminium species rather than CO_2[131], therefore, CO_2 does not follow a similar evolution trend as H_2 evolution. The observed rise of CO_2 in the system under light irradiation corresponds to a background signal that may originate from the minor amounts of CO_2 previously dissolved in the solvent.

In conclusion, the choice of hole sacrificial agent does affect the photocatalytic performance, however, it is not convincing enough to be the dominant reason for the large efficiency difference between MIL- and NH_2-MIL-, as with TEOA, MIL-MOF still greatly outperforms NH_2-MIL with 13 times higher H_2 evolution rate. Therefore, the reasons for the superior performance of MIL-125-Ti to NH_2-MIL-125-Ti demand further investigation.

In the following section, the properties of these two MOFs are compared in the HER system with MeOH as hole sacrificial agent, if not stated otherwise.

4.2.2 Material's Stability during photocatalytic process

First, I investigated the stability/degradation of both catalysts with respect to the applied photocatalytic conditions as a possible reason for the different photocatalytic performance. It is well-known that MOFs, being organic-inorganic hybrid materials, can suffer from instability towards various solvents.[132-134] This may apply to the current scenario, where the solvent changed when transferred from the synthesis solution (i.e. DMF/MeOH) to the photocatalytic reaction solution (i.e. H_2O/MeOH). In addition, the degradation of the framework can also be triggered by UV irradiation or by hydrogen evolution upon the photocatalytic process itself. Therefore, after HER experiment, the suspensions were filtered, and the collected powders were dried for XRD, SEM and TEM measurements to reveal the state of the material.

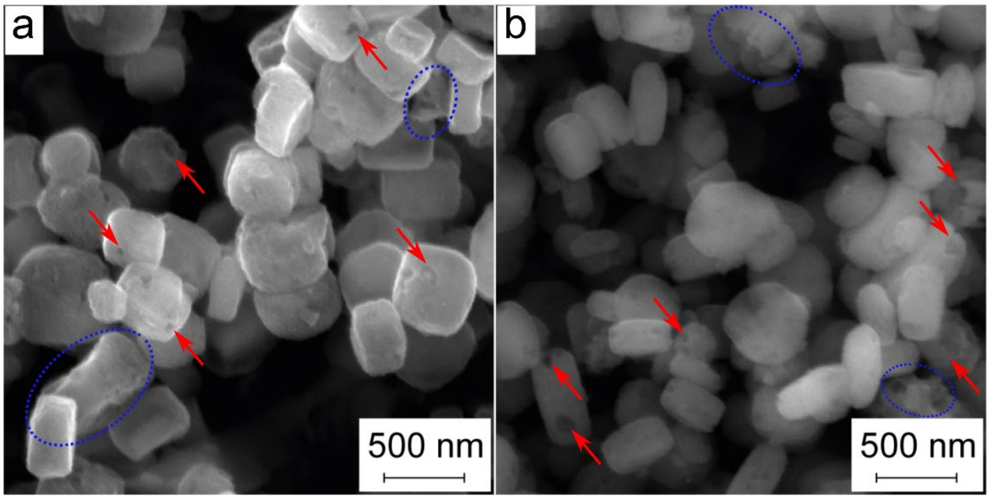

Figure 4-18 SEM images of a) MIL-125-Ti and b) NH_2-MIL-125-Ti after HER

Figure 4-18 shows SEM images of the two MOFs after water splitting and reveals that the surface of both MOFs become coarsened after the photocatalytic reaction as compared to original SEM in Figure 4-5, while the shape of circulate plates were generally retained. There are shallow holes or voids visible on the surface, as indicated by the red arrows in Figure 4-18. Moreover, some of the particles seem 'corroded', as documented by the loss in the plate-shape morphology (blue-dotted circles). In addition to surface morphology, the particle size also changed, especially for the MIL-125-Ti. The average diameter of the circular plates decreases from around 570 nm to 500 nm, indicating a moderate shrinkage or ablation of crystal layers. In NH_2-MIL-125-Ti, the average diameter of the circular plates decreases from 480 nm to 420 nm. The appearance of such surface 'imperfection' along with size shrinkage indicate a possible damage or degradation of the overall materials' crystal structure.

It has been reported that the photo-deposition process of H_2PtCl_6 in MeOH aqueous solution typically results in the formation of uniform platinum nanoparticles with average sizes of 2-6 nm[135-138]. Unfortunately, SEM cannot provide sufficient information on the size and distribution of the photo-deposited platinum cocatalyst due to the resolution limitation. TEM offers the required resolution, but is also of limited use, as it does not allow to investigate Pt species that reside within the micropores.

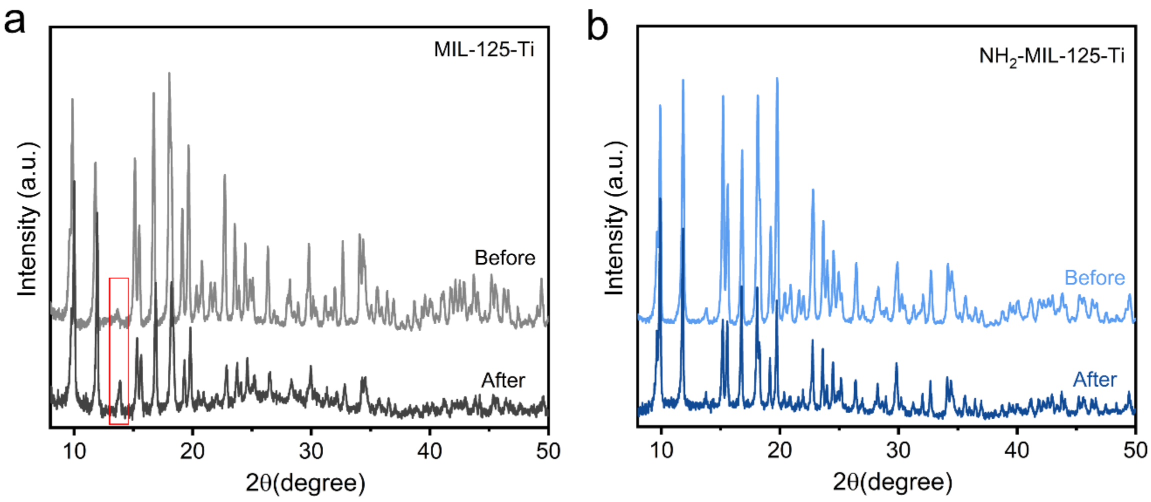

Figure 4-19 Comparisons of XRD patterns before and after HER: a) MIL-125-Ti and b) NH_2-MIL-125-Ti

Figure 4-19 compares XRD patterns before and after hydrogen evolution reaction. The two Ti-MOFs preserve their original crystal structure after the photocatalytic reaction and no additional peaks are visible suggesting that no new phase appeared. The main difference observed between the XRD patterns of the two MOFs after reaction compared with the original MOF patterns is a minor change of relative peak intensities. Specifically, for both used MOFs, the diffraction peaks at $2\theta > 14°$ are weakened compared with the two peaks located at $2\theta = 9.8°$ and 11.8°, representing (002) and (211) reflections, respectively, which can be related to the partial particle corrosion observed with SEM. In addition to this trend observed for both MIL- and NH_2-MIL, there is an incongruous rise of peak intensity at $2\theta = 13.8°$ noticeable only in MIL-125-Ti (Figure

4-19(a), red box). This peak has already been discussed before in Chapter 4.1.1.1 and is related to the adsorbed species inside the framework. Therefore, a higher amount of adsorbed species is expected to reside inside the framework of MIL-125-Ti after HER, which implies higher accessibility of the pores in the structure. This increased accessibility can lead to facilitated reactant diffusion to and from the active sites inside the microporous structure thus potentially contributing to different HER rates in the MIL-MOF. Yet, judging from the strong difference in HER performance, this contribution is likely not the decisive factor.

XRD patterns do not provide any hint attributable to Pt (Figure 4-19), whether before or after photocatalytic reaction. It is likely that either the low loading amount of Pt in my HER system (0.5 wt % of Pt to MOF) or the size of Pt species limit XRD analysis. Moreover, Lee et al[137] has only observed the characteristic peak of Pt (111) ($2\theta = 39.8°$) in her 1 wt % Pt loaded TiO_2 as a small broad hump in the XRD pattern. Therefore, the presence of multiple peaks of the MOFs in the same region (~ 39.8°, see Figure 4-19) renders it challenging to unambiguously identify the presence of Pt.

Based on SEM observations, it appears that the breakdown of MOF particles (particles inside blue circle, Figure 4-18) occurs anisotropically, with preference to certain crystal facets. Yet, the following questions remain unanswered: a) How does the structure disintegrate (e.g. proportional or disproportionate loss of ligands and oxo-clusters)? b) Does the loss of crystallinity originate from UV irradiation, the presence of solvents, an interaction with Pt catalysts, or a combination of these effects? No systematic study on MOFs' stability has been reported in literature.

For whatever the reasons, this structural breakdown is likely to have a considerable effect on the photocatalytic performance. Indeed, it can be seen from Figure 4-15 that at the end of 1 h light irradiation, the hydrogen generation activity of MIL-125-Ti declined. This slight decrease of photocatalytic activity may be ascribed to the change of crystal structure during water splitting process. Therefore, from both fundamental and application point of view, a more detailed investigation of the mechanism of structural change under photocatalytic conditions as well as the optimization of the photocatalytic stability are required to fully harness the MOFs' potential as photocatalyst.

Based on the above discussions, the stability difference – although it contributes to the observed HER profiles – can also be excluded as the dominant factor that defines different photocatalytic activity of these two MOFs.

4.2.3 Investigation of Cocatalyst: loading amount, distribution, role

As described in Chapter 0, the loading with Pt cocatalyst proceeds via in-situ photodeposition. In short, the respective MOF powder is suspended in an aqueous solution that contains a corresponding amount of H_2PtCl_6 as a precursor and subsequently illuminated with UV light, which reduces the precursor within the first few minutes to yield very small Pt nanoparticles[136-138]. Pt further acts as a cocatalyst to facilitate the HER reaction. Another contribution to the different HER performance of the two MOFs could stem from a difference in dispersion/location of photo-deposited Pt, which may also change during the photocatalytic reaction.

HRTEM investigation reveals the morphology and distribution of the cocatalyst in MOF. Figure 4-20 and Figure 4-21 are HRTEM observations of MIL-125-Ti and NH_2-MIL with cocatalysts after photocatalytic experiment, respectively, in comparison with pristine MOFs observed before HER.

Both pristine MOFs (Figure 4-20 and Figure 4-21: (d) & (e)) exhibit smooth surface morphology. In contrast, the particles collected after HER experiment consist of particulates, demonstrating a rough surface, which is also in accordance with the SEM observation. In addition, dark spots distributed homogeneously over the MOF particles can be observed in both cases (Figure 4-20(c) and Figure 4-21(c), red arrows). With higher magnification, clear lattice fringes can be observed (Figure 4-20 and Figure 4-21(b)), corresponding to the (111) of metallic Pt (0.226 nm)[97], confirming that the dark spots are the expected Pt nanoparticles. With an average size of 3 nm, metallic Pt particles share an intimate interface with the MOF substrate.

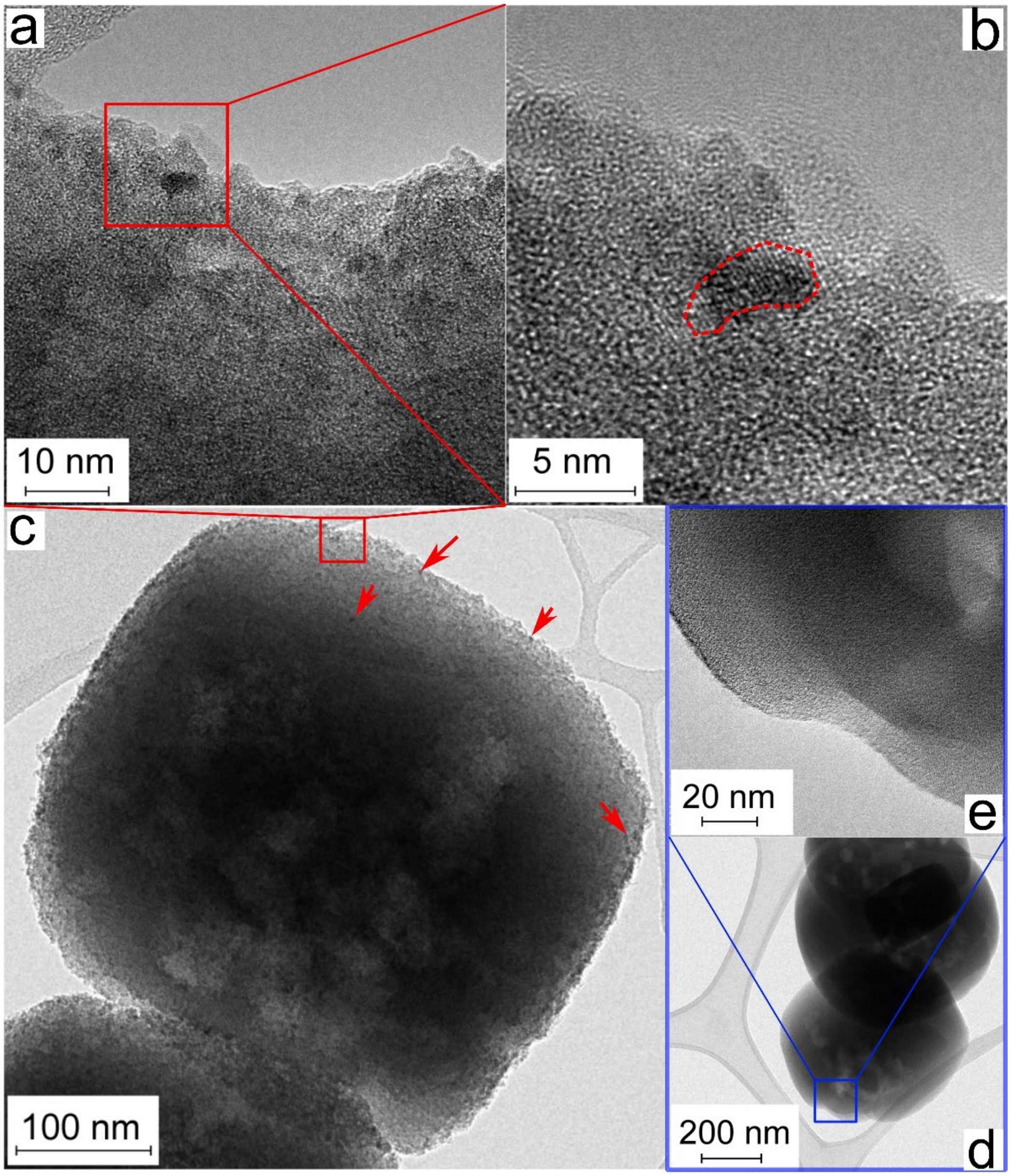

Figure 4-20 (a)-(c) TEM images of MIL-125-Ti after HER experiment; (e) & (d) TEM images of pristine MIL-125-Ti

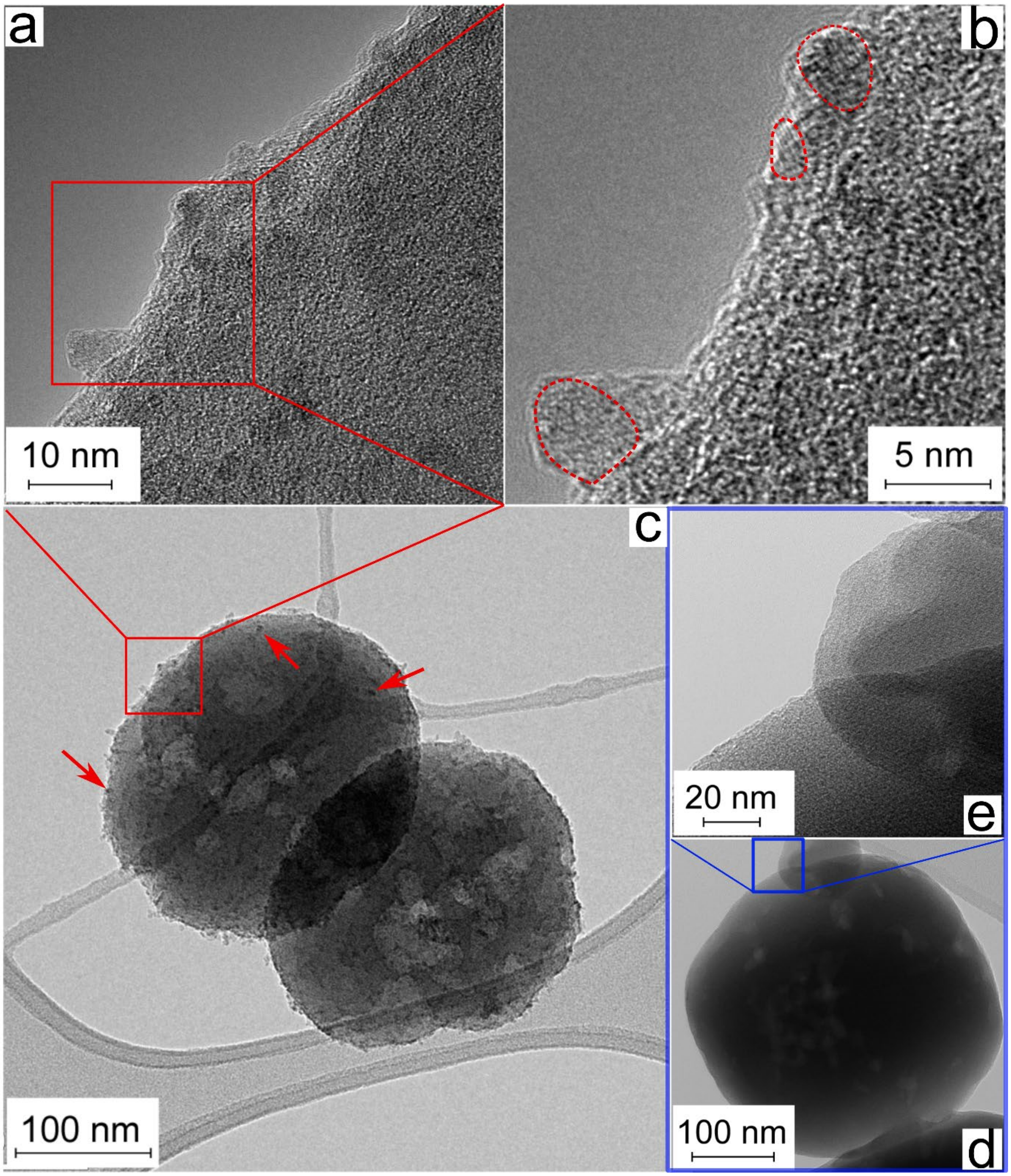

Figure 4-21 (a)-(c) TEM images of NH_2-MIL-125-Ti after HER experiment; (e) & (d) TEM images of pristine NH_2-MIL-125-Ti

Considering that the maximum pore width of both MOFs is less than 1.5 nm, these observed Pt nanoparticles are assumed to be located only on the surface of the MOF particles; however, the possibility, that some of the $PtCl_6^{2-}$ ions from the Pt precursor diffused into the pores of MOF and consequently formed Pt species inside the pores, cannot be excluded. Analytical TEM techniques, like depth profile EDX may be able to testify the existence of Pt inside MOFs, which will be especially interesting to elaborate more on the affinity of the Pt precursor species to the different ligands.

The amount of Pt loaded onto MOF particles was determined by ICP-MS for samples after photocatalytic reaction.

Table 4-7 Measured and calculated Pt/Ti at % values after HER with different photocatalysts

Photocatalyst	ICP-MS results	Theoretical Calculation	Measured/Calculated
MIL-125-Ti	0.0041	0.0051	80.4%
NH_2-MIL-125-Ti	0.0052	0.0053	98.1%

Table 4-7 lists the measured Pt/Ti at % obtained from ICP-MS data and the calculated values based on the amount of Pt precursor added into the HER suspension. The Pt/Ti at % in the case of MIL-125-Ti and NH_2-MIL-125-Ti are 0.0041 and 0.0052, respectively (compared to expected 0.0051 and 0.0053). The latter small mismatch can be attributed to the standard deviation (STD) of the ICP-MS measurement, associated with the small detection volume of just 62.6 µL.

However, the discrepancy between the measured data and the calculated data for MIL-Ti is around 20 % and requires further explanation. I see three possibilities:

1) The measured Pt content is lower than the theoretical value due to miscalculation and addition of insufficient amounts of Pt precursor. However, the reproducibility of the ICP-MS results renders this possibility rather unlikely.

2) The deposited Pt nanoparticles detach from the MOF matrix during the photocatalytic experiment. Considering that the Pt content is about 20 % lower than the theoretical value (ratio ~ 80 %), a decrease in activity upon leaching during the reaction of the same extent is expected. However, Figure 4-15 shows a minor decrease of HER performance that does not agree with this scenario.

3) The third scenario is based on the instability of MOF, as suggested by the aforementioned partial degradation/ablation of the MOF particles observed by SEM (Figure 4-18) and XRD (Figure 4-19). In this scenario, small chunks of MOF, along with

surface-attached Pt, detach from the MOF matrix (rather than individual Pt particles described in scenario 2). After HER, the detached MOF pieces are presumably too small to be collected by filtration, thus leading to a loss of both Ti and Pt. Now, I propose two possibilities: a) if Pt was well dispersed throughout the MOF, such as, e.g. in NH_2-MIL-125-Ti, the detachment would result in a proportionate loss of Pt and Ti during HER. I would observe no changes in HER upon reaction and also no difference in Pt content upon ICP-MS analysis. b) If Pt was deposited mostly on the external surface, however, the detached pieces would contain a larger portion of Pt. This would not affect the H_2 evolution rate during the reaction either, but it would lead to a disproportionate loss of Ti and Pt and thus lower Pt:Ti ratio in ICP-MS than calculated. This would be the case for MIL-125-Ti.

This scenario has a considerable consequence to the photocatalytic activities of MOFs, as it postulates that Pt deposition (i.e. dispersion, size etc) is different in the two MOFs and greatly relies on the chemistry of the organic ligand.

It certainly warrants more detailed experiments and characterizations, such as using ex-situ deposition of Pt nanoparticles, changing the particle loading and size, as well as altering the porosity of the MOFs.

In general, the combined ICP-MS and TEM results indicate that the Pt has been successfully loaded in both Ti-MOFs, in the form of metallic nanoparticles. The amount of Pt in the system after HER was higher in NH_2-MIL-125-Ti than in MIL-125-Ti, which is supposed to benefit the photocatalytic activity of the system. Based on ICP-MS studies, I further suggest that the deposition of Pt happens differently in NH_2-MIL-125-Ti and MIL-125-Ti MOFs, namely, Pt precursor resides inside the micropores of the former sample to more extent. Another important criteria of Pt loading would be the interface between the Pt and the MOF (e.g. with the Ti-oxo cluster or the linker) – but this is out of scope of this thesis.

4.2.4 Liquid-Phase Photoluminescence Investigation of MIL- and NH_2-MIL-125-Ti

Photoluminescence spectroscopy (PL), has been widely used to probe the recombination of photogenerated electrons and holes as well as the charge separation properties of photocatalysts.[62, 115, 139-142] For example, Fu et al[115] synthesized Cobalt-doped NH_2-MIL-125-Ti and observed a decreased PL emission intensity compared to the pristine NH_2-MIL-125-Ti. As the emission spectra originates from the radiative recombination of photogenerated charge carriers[84], the introduction of Cobalt prohibited charge recombination and improved the photogenerated charge separation efficiency. Consequently, an increased photocatalytic efficiency towards CO_2 reduction has been achieved with the Cobalt-doped NH_2-MIL-125-Ti.

In this work, I utilized PL emission spectra to compare the charge recombination behavior of MIL-125-Ti and NH_2-MIL-125-Ti. To mimic the environment of HER, I measured PL in liquid phase, while the mechanistic role of the sacrificial agent and cocatalyst have also been probed. Samples for PL measurements were prepared by dispersing MOF powders into H_2O (denoted as H) as well as MeOH aqueous solution (50 % v/v, denoted as M). For the samples with cocatalyst, Pt was added via the photo-deposition process in same way as during the HER process. Both the sample preparation and the measurement parameters were set the same for a solid comparison between MIL-125-Ti and NH_2-MIL-125-Ti.

Figure 4-22 displays the emission spectra recorded at 280 nm excitation. MIL-125-Ti (Figure 4-22(a)) shows a very weak (or no) emission peak in the detection range of 350 - 530 nm, while its NH_2-counerpart displays a broad emission peak centered at 441 nm. Moreover, the intensity of the emission peak detected for NH_2-MIL-125-Ti (Figure 4-22(b)) is dependent on the solvent as well as on the addition of Pt.

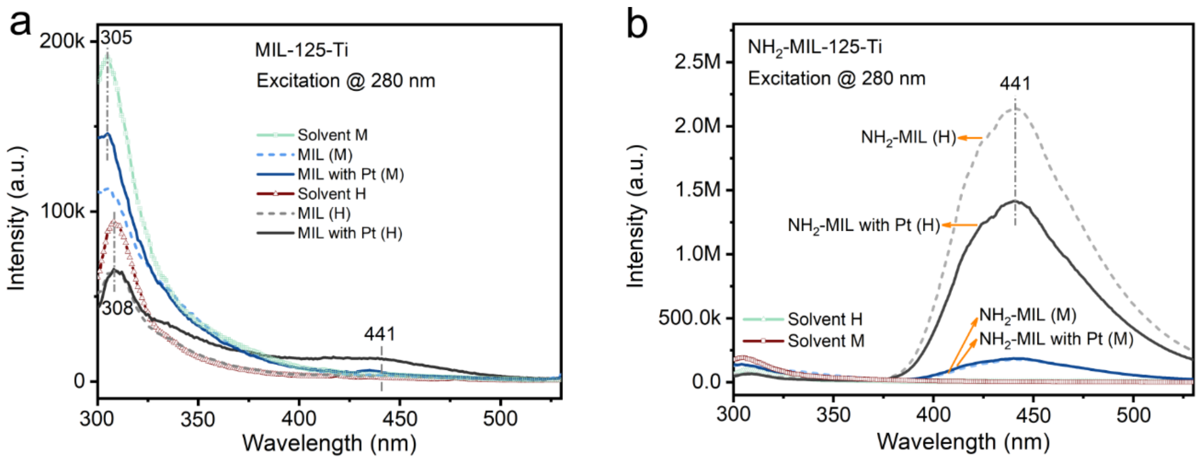

Figure 4-22 PL emission spectra of (a) MIL-125-Ti and (b) NH$_2$-MIL-125-Ti in different solvents under excitation wavelength of 280 nm. Solvent M: mixture of MeOH+H$_2$O (50 % v/v); Solvent H: distilled H$_2$O. MOFs powders were dispersed in different solvents assisted with sonication (1 mg/50 mL); thus obtained spectra are shown in dashed lines. The spectra displayed in solid lines are from the MOF suspensions after Pt photo-deposition.

Little work has been devoted to study the luminescent properties of MIL-125-Ti. To my knowledge, only Yuan et al. have reported that the emission peak of MIL-125-Ti occurs at around 531 nm when excited at 265 nm[140] and An et al have excited MIL-125-Ti at 300 nm ascribing the maximum emission peak at 468 nm to the π→π* transition of the benzene ring[98]. However, both reports did not specify whether the spectra have been measured in solid or liquid phase. No strong emission peak has been observed as shown in Figure 4-22(a), suggesting a negligible radiative recombination process in MIL-125-Ti under the present measurement conditions.

In the case of NH$_2$-MIL-125-Ti, it has been consistently shown that the radiative charge recombination takes place on the ligand and results in emission at 435 nm.[26, 62, 115, 139, 142] Therefore, the main peak in Figure 4-22(b), centered at 441 nm, can be ascribed to the charge recombination in the organic ligand, NH$_2$-BDC.

4.2.4.1 Impact of Sacrificial Agent

MeOH is used as hole sacrificial agent (electron donor) for HER experiments in this work and the role of MeOH is clearly indicated in Figure 4-22(b). NH$_2$-MIL-125-Ti has three orders of magnitude lower emission intensity in MeOH+H$_2$O (spectra with (M), in blue) than in H$_2$O (spectra with (H), in grey), which suggests a strongly reduced recombination process with the presence of MeOH. Considering the stronger electron donating property of MeOH (compared to H$_2$O), it can be assumed that MeOH effectively consumes the photogenerated holes, and thus reduces the recombination process in NH_2-MIL-125-Ti, fulfilling the task of hole sacrificial agent. However, the impact of MeOH can hardly be concluded with MIL-125-Ti, due to the ambiguous emission peak.

4.2.4.2 Impact of Cocatalyst

The addition of Pt into the MIL-125-Ti samples did not show any pronounced influence on the emission spectra. The observed hump at 441 nm, that appeared in MIL- sample in H_2O after Pt photodeposition (Figure 4-22(a), solid black line), cannot be attributed to the characteristic emission of MIL-125-Ti and, based on its intensity, is likely related to the Raman scattering of water[143].

In contrast, the effect of cocatalyst is more pronounced in the NH_2-MIL-125 (H) sample (Figure 4-22(b), solid line and dashed line in grey) where the addition of Pt quenched 35 % of the characteristic emission peak. The decrease in intensity can as well be ascribed to the capability of Pt to withdraw the photo-excited electrons and thus to prevent the radiative electron-hole recombination. However, for NH_2-MIL-125 (M), the addition of Pt shows no such quenching effect (Figure 4-22(b), solid line and dashed line in blue), in contrast to what one would expect.

To explain this, it is important to note another related observation from Figure 4-22 that the use of MeOH as a solvent results in lower PL emission recorded for the NH_2-MIL sample compared to that in H_2O. This can be related to the stronger hole accepting property of MeOH and is another factor to be considered when comparing the NH_2-MIL-125 (M) and (H) samples. I suggest that due to the low loading amount of Pt, the reduced amount of electrons did not contribute to prevent recombination in the sample NH_2-MIL (M), thus the emission intensity showed no decrease. This hypothesis needs further investigation, by tuning the addition amount of Pt in NH_2-MIL-125 (M).

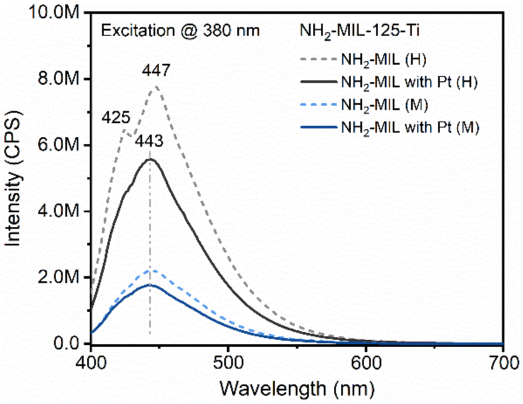

Figure 4-23 PL emission spectrum of NH$_2$-MIL-125-Ti samples excited at 380 nm. The materials preparation as well as the data instructions can refer to Figure 4-26.

To further elaborate on the origin of the emission peak at 441 nm in NH$_2$-MIL-125-Ti, PL emission spectra have been recorded after excitation at 380 nm (Figure 4-23). According to the light absorption properties of NH$_2$-MIL, the amino-functional group in the ligand is responsible for the visible light response of this MOF and the wavelength of 380 nm should be sufficient to excite the electron transition within the ligand. Indeed, the resulting PL spectra contain a strong emission peak centred at 443 nm, same as for excitation spectrum recorded at 280 nm (Figure 4-22).

Though the intensities of all the emission peaks excited at 380 nm are much higher than when excited at 280 nm, due to different intensity of the excitation pulse, it is impossible to assign this difference to any of the material’s properties. However, by comparing relative changes between spectra in Figure 4-23 and in Figure 4-22, one can see smaller peak differences observed between NH$_2$-MIL-125-Ti (H) and NH$_2$-MIL-125-Ti with Pt (H) as well as between NH$_2$-MIL-125-Ti (H) and NH$_2$-MIL-125-Ti (M). Based on this, it can be concluded that the quenching effects of Pt and MeOH are less significant when excited at 380 nm.

Why would different excitation wavelength make a difference? It seems that at 380 nm, the excitation occurs in the ligand, then electrons go to the metal cluster and then into Pt, while at 280 nm, the excitation could as well happen in the metal cluster, followed by a direct electron transfer to Pt (Section 1.3.4.2, ***D**ual **E**xcitation **P**athway*). Therefore, the excitation and transfer at 280 nm is more efficient than that at 380 nm, with a possible implication to the photocatalytic activity/quantum efficiency. However, for the moment, wavelength-selective HER experiments are beyond the scope of this project, but will be interesting for further studies.

In summary, the above PL spectra provide a preliminary study on the ligand influence, the role of hole sacrificial agent as well as the role of cocatalyst. First, the emission intensity in NH_2-MIL-125-Ti is undeniably higher than that in MIL-125-Ti, which indicates a higher radiative recombination in NH_2-MIL-125-Ti than that in MIL-125-Ti. Therefore, though the presence of $-NH_2$ in the organic ligand of NH_2-MIL-125-Ti extends the light absorption range into the visible spectrum compared to the MIL-125-Ti counterpart, the newly created excited states are prone to strong recombination. Referring back to the photocatalytic activity of the two MOFs towards HER, the inferior hydrogen revolution rate in NH_2-MIL-MOF can be now attributed to this recombination. In addition, both the hole sacrificial agent and the cocatalyst have demonstrated their capability of facilitating charge transfer and reducing charge recombination with NH_2-MIL-125-Ti.

4.2.5 Hydrogen Evolution in Darkness

To further elaborate the role of cocatalyst in our HER system, photocatalytic experiments without Pt have been conducted. The entire experimental flow along with the hydrogen and CO_2 generation are shown in Figure 4-24.

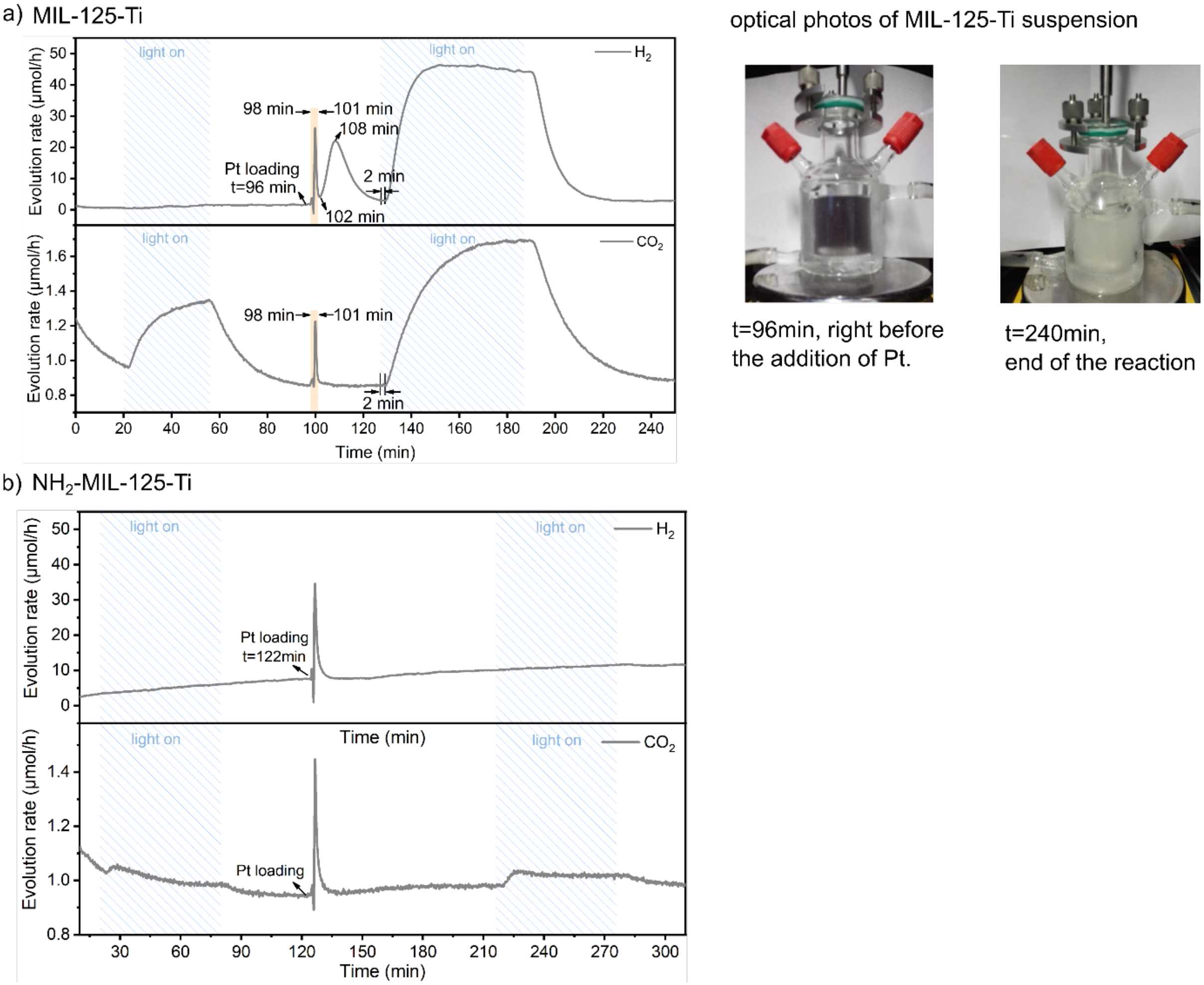

Figure 4-24 Role of Pt cocatalyst for hydrogen evolution reaction: HER experiments were conducted with both MIL- and NH_2-MIL-125-Ti; the suspension was irradiated for 2 times, first without the addition of Pt, then with the addition of Pt.

Taking MIL-125-Ti as an example, the reaction suspension was first subjected to UV irradiation, starting at t = 20 min until t = 56 min, without the addition of the cocatalyst solution, as shown in Figure 4-22(a). After UV irradiation, the suspension was kept in darkness for about 40 min and then the Pt precursor (H_2PtCl_6 aqueous solution) was added at t = 96 min. Immediately before addition of the precursor, sharp peaks appeared at around t = 98 min in both H_2 and CO_2 profiles. These were caused by the opening of the reactor, which was necessary to inject the solution. After the addition of Pt precursor and closing the reactor, the system needed about 3 - 4 min to recover back to the original baseline profile.

The reactor was kept in the dark for another 30 min to ensure a stable baseline. However, something completely unexpected happened; a strong HER peak appeared, while the

CO_2 was at its baseline level. After the HER rate dropped again, the MIL-125-Ti system was subjected to a second UV irradiation between t = 127 min and t = 187 min (Figure 4-22(a)), upon which both, H_2 and CO_2 increased as expected. It is important to note that this 'unusual' H_2 revolution peak in the dark (Figure 4-25, t = 102 - 127 min) has been reproduced in several experiments.

For comparison, the NH_2-MIL-125-Ti was tested in a similar experimental setup: first irradiated without Pt precursor and then the Pt precursor was present in the solution additionally as shown in Figure 4-27(b). The sample performed in a way expected for the NH_2-MIL as can be seen from the H_2 and CO_2 evolution profiles. However, no HER peak in the dark was observed.

First, it is clear from Figure 4-24 that the presence of Pt is indispensable for the H_2 production, since no H_2 has been detected during the first UV irradiation period, while the HER was strong in the second UV period after the addition of Pt, reaching rates as high as 45 μmol/h. Second, it also clear that the H_2 and CO_2 evolution rates were considerably weaker in the case of NH_2-MIL-125-Ti (Figure 4-24(b)).

The 'unusual' H_2 evolution in the dark upon addition of Pt, which has only been seen in the MIL-125-Ti samples, is truly unique and I could not find anything similar to that in the literature for any photocatalyst reported. Since this peak is not accompanied by a CO_2 evolution, there is one important question: Where does the H_2 come from, especially since no photons have been provided to trigger a photocatalytic process?

To understand this phenomenon, let us look at Figure 4-24(a), which presents the digital photographs of the reaction cell at different crucial time points. The MIL-125-Ti suspension had a dark purple color after the first UV irradiation and before the addition of Pt precursor. After the second cycle of UV irradiation, the photocatalyst turned white. It has been reported that, when alcohols (such as MeOH) are adsorbed inside the MOF pores under inert atmosphere, UV irradiation can initiate a photochromic effect in MIL-125-Ti.[80] This photochromic behavior is related to the presence of intervalence electron transfer bands introduced by the optically induced hopping of electrons from Ti^{3+} to Ti^{4+} sites in the titanium-oxo clusters of MIL-125-Ti.[80] Therefore, I ascribe the dark color of the reaction solution to the presence of Ti^{3+}. Hereby, I propose that Ti^{3+} species are generated during the first light irradiation period; however, without Pt cocatalyst, the Ti^{3+} (which hold the reactive electrons) cannot be effectively utilized for the reduction of water and remain reduced. Our experiments revealed that these Ti^{3+} color centers can be preserved in the MOF matrix for at least 40 min. Such unusually long lifetimes have not been reported before at all. This explains the dark color of the suspension before the H_2PtCl_6 addition. After the precursor injection, the photogenerated electrons - stored in Ti^{3+} - transfer to $[PtCl_6]^{2-}$ and reduce Pt^{4+} to Pt^0, completing the conventional photo-deposition process without additional light supply. Consequently, with the assistance of newly cleated Pt cocatalyst sites, electrons from Ti^{3+} can further reduce H^+ into H_2, contributing to the H_2 generation event under darkness in Figure 4-24(a), from t=102 min to t =127 min.

In contrast, in the case of NH_2-MIL-125-Ti, there is no immediate hydrogen generation after the addition of Pt, which, based on our previous assumption, can now be ascribed to the absence of long-lived Ti^{3+} active species. To verify the above assumption I have also taken digital photographs of the NH_2-MIL suspension after the first light illumination cycle. In fact, there was no color change observed for this MOF suspension.

Based on above discussion, our data shows that the Ti^{3+} species in MIL-125-Ti have much longer lifetime than those in NH_2-MIL-125-Ti and this key difference between the two material is expected to contribute to the prominent difference in their photocatalytic HER activity .

In order to further confirm my assumption about hydrogen generation process in darkness with the presence of Ti^{3+} and Pt, and to exclude the influence of the H^+ and Cl^+ present in the H_2PtCl_6 precursor, a set of experiments was conducted where the same amount of H^+ was provided via the addition of HCl.

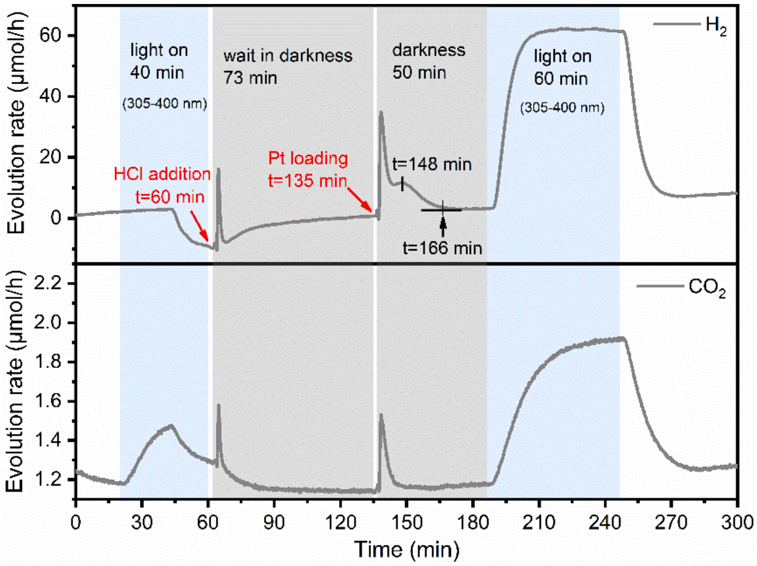

Figure 4-25 The comparison of the addition of HCl and H_2PtCl_6 after light irradiation. When irradiation started, no cocatalyst was added. When t = 60 min, the reactor was opened and HCl was added; when t = 135 min, the reactor was opened again and H_2ClPt_6 was added.

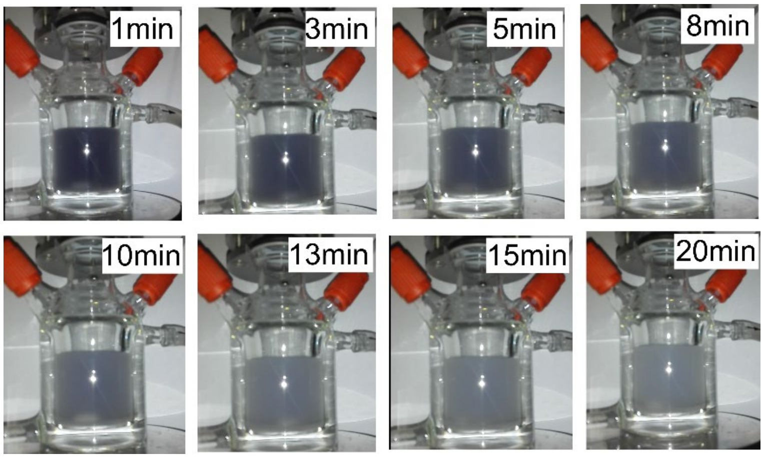

Figure 4-26 The color change of the suspension after Pt addition, roughly from t = 137 min in Figure 4-26.

The plot in Figure 4-25 demonstrates how the addition of HCl and subsequent addition of H_2PtCl_6 affects H_2 and CO_2 generation rates. After HCl addition, no H_2 evolution was detected; while later, after the addition of Pt precursor, the H_2 peak appeared, which was in accordance with my assumption. Therefore, the presence of Pt is indispensable for the H_2 evolution in present HER system, under both 'dark' and 'irradiation' conditions. Figure 4-26 shows the change of the suspension color after the addition of Pt precursor. As previously discussed, the dark purple color indicates the presence of Ti^{3+}. Therefore, the fading of the suspension after the addition of Pt manifests the 'quenching effect' of Pt on Ti^{3+}. The fading process lasted for more than 20 min, corresponding to the H_2 generation in Figure 4-25 around t = 148 min.

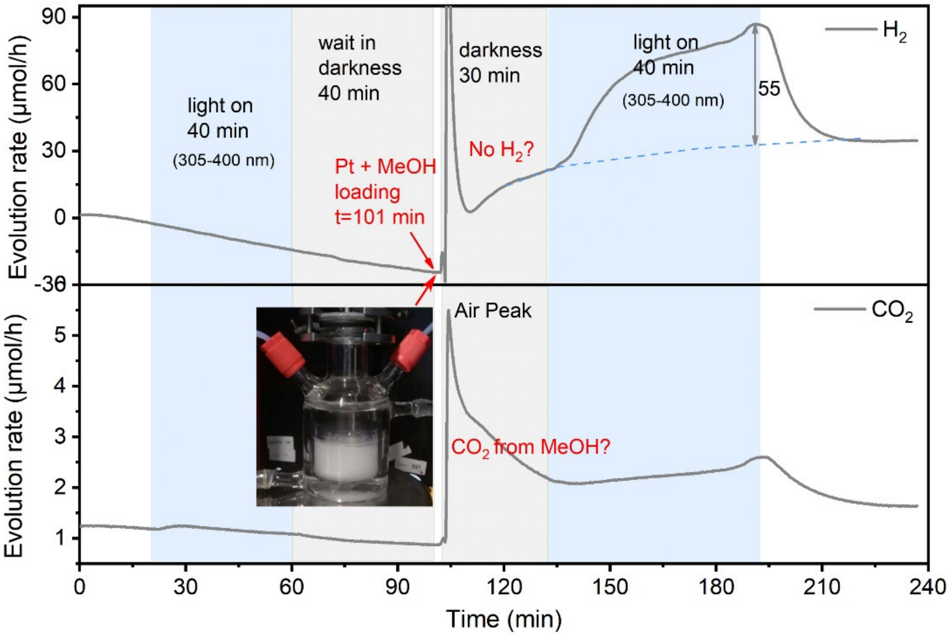

Figure 4-27 Investigation on the role of MeOH in HER: The HER system of MIL-125-Ti was irradiated twice, first without MeOH, then with MeOH.

To elucidate the role of MeOH in the generation of stable Ti^{3+} species, another experiment has been conducted. The suspension with MIL-125-Ti in pure DI water was first irradiated, then Pt precursor together with MeOH was added at t = 101 nm (Figure 4-27). After 30 min in darkness, the final suspension as subjected to the second UV irradiation cycle. No apparent H_2 generation was observed after the H_2PtCl_6-MeOH addition, which was complemented by the observation that the colour of the suspension after the first irradiation period remained white, unlike previously observed dark purple colour. No stable long-lived Ti^{3+} species existed at this stage, corresponding to no H_2 generation, which corroborates that Ti^{3+} is indeed responsible for the H_2 evolution. In addition, the data confirms that the presence of an alcohol (MeOH in our case) is necessary to obtain the stable Ti^{3+} species, which is in agreement with the observation by Dan-Hardi et al[80] who suggested that the photoassisted reduction of Ti^{4+} into Ti^{3+} is coupled with the oxidation of the alcohols.

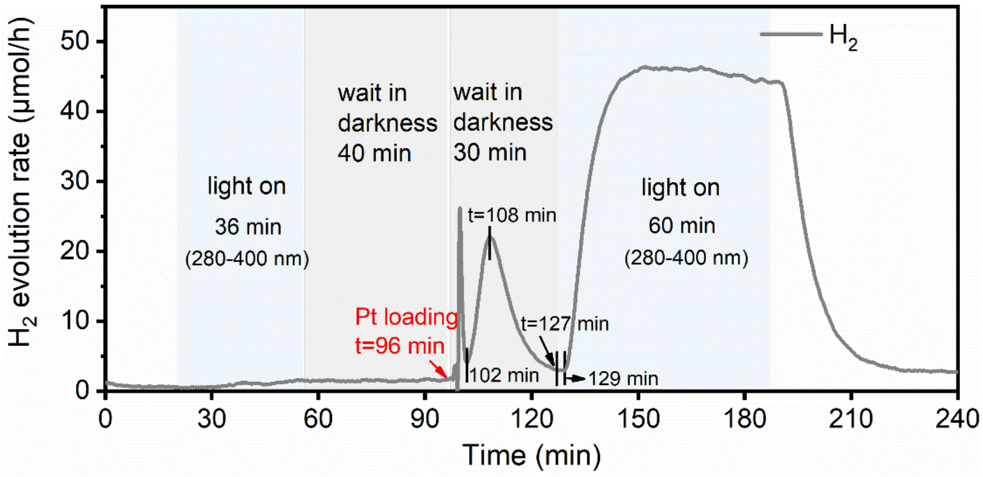

Figure 4-28 Calculation of Hydrogen Evolution Volume

Although a possible formation of Ti^{3+} states in Ti-based MOF has been reported, this storage of photo-excited electrons is a truly novel finding. Moreover, the utilization of the photogenerated electrons stored in such way may have potential practical applications. In fact, I have for the first time successfully accumulated the energy of light photons, stored it in the form of partially reduced Ti states for indefinite time and, importantly, released this potential energy on demand in darkness, thus fueling a photocatalytic system for hydrogen evolution. This process can be described with the following scheme: photon → Ti^{3+} → Pt^{4+} (P^{o}) → H^{+} (H_2)

Next, I would like to estimate the Ti^{3+} percentage in MIL-125-Ti from the evolved H_2, which can further clarify whether or not the H_2 evolution stems solely from the Pt precursor.

The volume of H_2 generated in darkness after the addition of Pt can be obtained by calculating the area under the H_2 profile (Figure 4-28, between t = 102 min to t = 127 min) which amounts to 4.26 μmol of H_2. Based on the structural formula of MIL-125-Ti $Ti_8O_8(OH)_4$-$(BDC)_6$ (1587.56 g/mol) and the mass of MOF used in the HER system - 10 mg - the amount of titanium centres can be calculated to 50.4 μmol of Ti^{4+}. To take the electrons consumed by the deposition of Pt^{4+} into account, the addition of 0.256 μmol H_2PtCl_6 requires 1.024 μmol of electrons. In total, to generate 4.26 μmol H_2, the system will consume 9.544 μmol of electrons. Given that all the electrons are provided by the Ti^{3+}, there are at least 9.544/50.4 = 18.93 % of the Ti centres in the Ti-oxo clusters present as Ti^{3+} before the addition of Pt precursor takes place.

Considering the loss of Ti^{3+} during the opening of the reactor (partial reoxidation due to O_2 diffusion from air) and the possible decay during the waiting time in darkness, the Ti^{3+} proportion is likely higher than 18.93 %.

The situation was entirely different in the case of NH_2-MIL-125-Ti. The experiments did not show this H_2 evolution in the dark, which can have several reasons. First, the photogenerated holes in these two MOFs are of different state. The HOMO level of MIL-125-Ti is more positive than that of NH_2-MIL-125, which is preferable for the holes transfer MeOH and will consequently lower the probability of charge recombination.

Second, as indicated by the PL data, the recombination probability in NH_2-MIL-125-Ti is higher, suggesting less efficient charge utilization.

The third possible reason is also related to the photogenerated holes. Walsh et al[129] used DFT simulations to predict that, in addition to being transferred to a sacrificial agent, the photogenerated holes in MIL-125-Ti can also facilitate the oxidation of the Ti-oxo species, leading to the formation of an oxygen vacancy in the cluster and stabilizing the Ti^{3+}. For NH_2-MIL-125-Ti, such predictions have not been reported. Therefore, it appears that the MIL-125-Ti has more possibilities to consume holes, which lowers the charge recombination probability and preserves the photo-reduced Ti^{3+}.

4.2.6 Working Mechanism of MIL- and NH_2-MIL for photocatalytic hydrogen evolution

The ligand-metal charge transfer (LMCT) mechanism has been proposed to describe the working principles of Ti-MOFs as photocatalysts,[26, 69, 129] as detailed in Chapter 1.3.4.2. ESR studies have further revealed the presence of Ti^{3+} under light irradiation in both MIL-125-Ti and NH_2-MIL-125-Ti.[26, 59, 79, 110] These works confirmed the formation of Ti^{3+} in MIL-125-Ti under photocatalytic conditions as well as UV irradiation and uncovered a surprising stability in aqueous solutions.

A possible working principle of MIL-125-Ti is illustrated in Figure 4-29, based on previous observations and discussions. According to the LMCT mechanism, photoexcited electrons transfer from the ligand to the Ti-oxo clusters and reduce Ti^{4+} to Ti^{3+}. The potential of Ti^{3+} is more negative than the water reduction level,[62] therefore, the photogenerated Ti^{3+} further reduces H^+ to H_2 with the help of a cocatalyst (Pt). At the same time, the Ti^{3+} gets regenerated back to Ti^{4+}, while the holes - left in the organic linker - get consumed by the sacrificial agent, which is MeOH in this case. One oxidation product of MeOH, CO_2, has been clearly detected, however, for now, the existence of CH_2O, $HCOCH_3$ etc cannot be excluded.

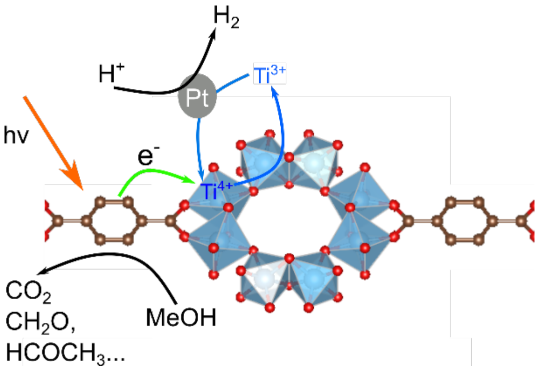

Figure 4-29 HER process of MIL-125-Ti in MeOH aqueous solution with Pt as cocatalyst

Compared with MIL-125-Ti, the working mechanism of NH_2-MIL-125-Ti is less clear. With regard to the oxidation process of MeOH: while the quenching effect of MeOH over the emission spectra of NH_2-MIL-125-Ti demonstrated the charge transfer between MeOH and MOF, the behavior of CO_2 generation observed during HER (Chapter 4.1.1.7) indicated that the MeOH oxidation with NH_2-MIL-125-Ti happens in a different way from that with MIL-125-Ti. Besides, the role of Pt is still ambiguous. As observed from the PL emission spectra in Figure 4-23, the addition of Pt did not significantly diminish the emission upon charge recombination in NH_2-MOF. Although this may be attributed to the low amount of Pt, it still raises doubts about the role of Pt in the NH_2-MIL system, which needs to be addressed to further improve the photocatalytic efficiency of NH_2-MIL-125-Ti.

4.2.7 Conclusion and outlook

a) Conclusion

NH_2-MIL-125-Ti, an aminated analogue of MIL-125-Ti, is a successful example of improving MOFs' light absorption property via ligand tuning. Consequently, research on the photocatalytic activity of Ti-based MOFs has concentrated predominantly on NH_2-MIL-125-Ti as a visible-light active photocatalyst. Therefore, there has been very few direct comparisons of the photocatalytic activity between MIL-125-Ti and NH_2-MIL-125-Ti.

Based on the obtained data, especially the PL emission spectra and the HER experiment where active Ti^{3+} species have been stabilized, I can ascribe the inferior photocatalytic efficiency of NH_2-MIL-125-Ti mainly to its intense charge recombination.

In summary, the ligand tuning in MOF can bring more effects in addition to light absorption modification, which needs to be carefully addressed. Other strategies to improve the light absorption, such as the incorporation of organic dyes, etc. can therefore be considered as an alternative. Moreover, I think, efforts should be devoted more to the improvement of the photocatalytic efficiency under solar simulated spectrum, rather than the sole visible spectrum or UV spectrum.

Lastly, it is remarkable that the excited state (Ti^{3+}) in MIL-125-Ti can be preserved after light irradiation for at least 45 min. This offers a new type of a photocatalyst material with the potential to initiate a desired reaction in the dark at a desired time. More experiments are required to fully exploit this phenomenon.

b) Outlook

Due to the time constrains and the equipment accessibility, the following issues have not been addressed in this thesis, but require further investigation in the future:

1) In-situ FTIR-ATR and EPR experiments shall unravel details regarding the photocatalytic reaction mechanism, charge transfer pathways as well as the formation and stability of the Ti^{3+} species.
2) HRTEM-EDX mapping, STEM and possibly tomography shall reveal size variations and distributions of Pt within the micropores of MOFs.

3) Long-term experiments shall uncover the stability of the MOFs for HER performance.
4) The incorporation of MIL-125-Ti with dye-based sensitizers shall be explored as another potential method to improve its photocatalytic activity under visible light irradiation.
5) Further variation of process parameters, such as sacrificial agent, co-catalyst, light source etc., shall shed more light on the novel ‘switch-on’ hydrogen evolution process, to improve its performance and to find alternatives to trigger the H_2 generation.

4.3 Metal oxides derived from Ti-based MOFs

When MOFs are subjected to high temperature treatment in ambient atmosphere, the organic ligand undergoes a thermal decomposition and when given proper temperature and time, metal oxides can be obtained; for example, TiO_2 can be derived from Ti-based MOFs. Metal oxides derived via calcination of MOFs may feature a considerably large surface area, pore volume, and comparatively ordered porous structure – 'hierarchical' pores that can be partially preserved from parent MOFs – have attracted attention of researchers for various applications, e.g., as anode material in Li-ion battery,[144-146] as compactors[147-149] and as catalysts[147, 150-153].

The following section focuses on the metal oxides derived from Ti-based MOF and their applications in photocatalytic hydrogen evolution (HER). Moreover, last section has witnessed the impact of ligands on MOFs' photocatalytic activity; whether different functional group in the organic ligand can further influence the properties of obtained metal oxides is still an open question. Therefore, titania materials derived from both MIL-125-Ti and NH_2-MIL-125-Ti have been investigated in this section.

4.3.1 Results and Discussion

4.3.1.1 SEM

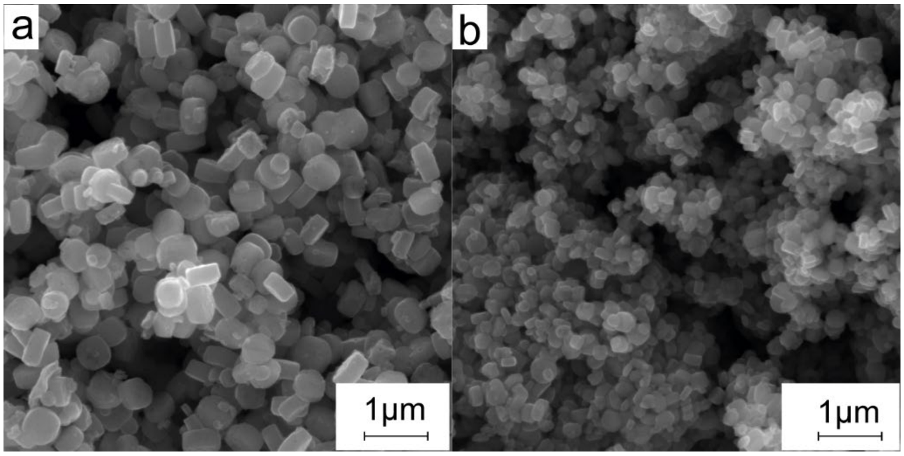

*Figure 4-30 SEM images of a) TO-550, calcined from MIL-125-Ti at 550 °C; cake-like plates, c.a. 443 nm*235 nm; b) TO-N-600, calcined from NH_2-MIL-125-Ti at 600 °C; cake-like plates, c.a. 231 nm*120 nm.*

As described in Chapter 3.2, TO-x and TO-N-x are oxides obtained from MIL-125-Ti and NH_2-MIL-125-Ti, respectively; *x* indicates the calcination temperature.

SEM images of TO-550 and TO-N-600 are displayed in Figure 4-30. The primary particles of both powders are of similar morphology, both cake-like plates, inherited from the parent MOFs. No obvious particle collapse has been observed upon calcination, as both samples are composed of intact particles with clean and smooth surfaces. The average size of TO-550, around 443 nm * 235 nm, is bigger than that of TO-N-600, 231 nm * 120 nm. Compare with the pristine MOF sizes (Figure 4-5), both oxides suffer a volume shrinkage (ca. 50 % and 85 %, respectively), which can be ascribed to the loss of organic matter during calcination as well as the pore collapse. In fact, if Ti-oxo clusters in the parent MOFs transform into a densely packed TiO_2 crystal structure, based on the unit-cell volume of MIL-125-Ti and anatase, the volume shrinkage of both parent MOFs can be as high as 95 %. Therefore, the volume shrinkage observed in TO-550 and TO-N-600 is less than expected for complete collapse, hence the resulting materials still contain some porosity inherited from their parent MOFs. The reason for the higher volume loss of NH_2-MIL-125-Ti during calcination is not yet clear.

4.3.1.2 XRD

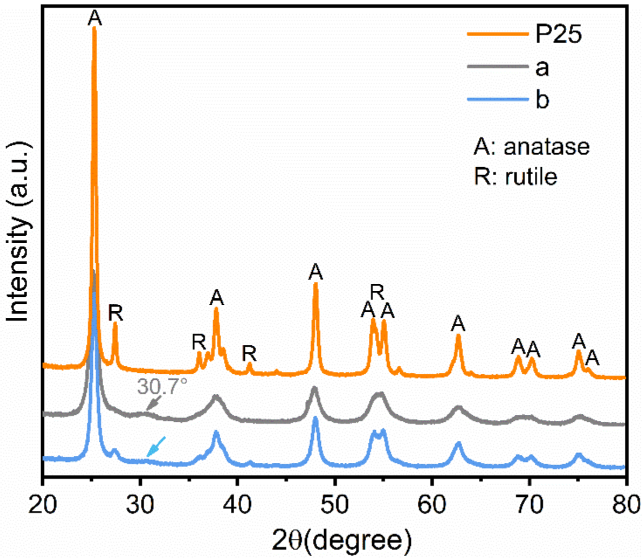

Figure 4-31 XRD patterns of P25, and TO-550 (a) calcined from MIL-125-Ti at 550 °C and TO-N-600 (b) calcined from NH_2-MIL-125-Ti at 600 °C. Commercial P25 is composed of anatase and rutile; TO-550 is composed of anatase and brookite; TO-N-600 is composed of anatase, rutile and brookite.

XRD patterns in Figure 4-31 reveal the crystal phase of the calcined samples. P25 as a benchmark for TiO_2 has also been measured and provided as a reference. For both calcined samples, diffraction peaks assigned to anatase can be clearly detected. In TO-N-600, the diffraction peaks at $2\theta = 27.4°$ and $2\theta = 41.3°$ confirm the existence of rutile, but no obvious rutile peaks present in TO-550, which can be ascribed to the fact that higher temperature is required for anatase to rutile transformation (ART). Compared with P25, there is a minor hump at $2\theta = 30.7°$ in the diffraction patterns of both calcined samples, but especially in TO-550. This hump can be assigned to another TiO_2 phase, (211) of brookite (JCPDS 65-2448)[154]. So far, there is no report about the presence of brookite in the calcination products derived from Ti-based MOFs, as brookite itself is a metastable TiO_2 phase, referring to the preparation conditions of brookite from amorphous TiO_2 or sol-gel route. The sizes of crystallites were calculated according to the Scherrer equation (Equ. 2-4), with the information of peak (101) ($2\theta = 25.3°$) for anatase. The crystallite size of anatase in TO-550 and TO-N-600 are 9.5 nm and 13 nm, respectively.

XRD patterns have confirmed the phase composition of the calcined products; however, whether the calcination process is enough to remove/oxidize all the organic components, or there are trace impurities remaining from organic ligand, is hard to tell from XRD. In fact, Wu et al has filed a patent about the preparation of N-doped TiO_2 via the calcination treatment of NH_2-MIL-125-Ti.[155] Therefore, EDX and Raman spectroscopy were applied to identify residual nitrogen and carbon in the calcined products.

4.3.1.3 EDX

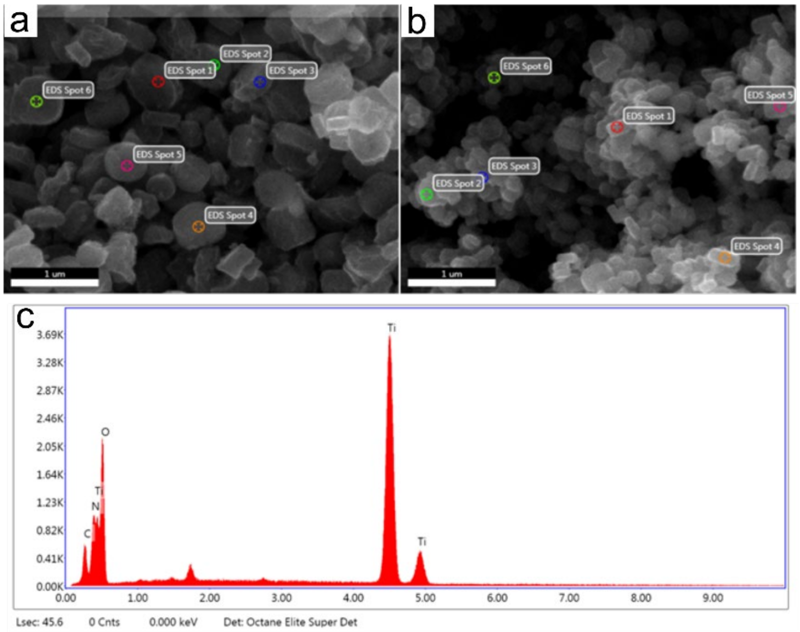

Figure 4-32 SEM-EDX point analysis of a) TO-550; b) TO-N-600; c) EDX spectra of TO-N-600.

SEM-EDX has been used to characterize the elemental composition, as shown in Figure 4-32 by means of point analysis. TO-550 has been measured as a reference giving the mean average N/Ti at % ratio of 0.061 %, while EDX of the TO-N-600 powder showed a higher ratio of 0.105 %. The presence of N in TO-550 is most likely an analysis artifact of the software, caused by the peak overlap between $N_{K\alpha}$ (0.40 V) and $Ti_{L\alpha}$ (0.45 V), as illustrated in Figure 4-32. In case that the nitrogen of the $-NH_2$ group is fully preserved in the calcination product, the N/Ti at % ratio in TO-N-600 would be expected to amount to 0.75 %. Therefore, the measured N content in TO-N-600 is much less than one would expect in this case, which can be attributed to several reasons: a) not all the nitrogen remains in the sample during calcination; b) the intrinsic low sensitivity of the EDX for light elements does not provide accurate values. For more reliable and accurate determination of carbon and nitrogen concentration in the samples, combustion-gas chromatography is recommended for further characterization. Nevertheless, by comparing the N/Ti at % ratios in these two samples, I can still suggest that the TO-N-600 derived from NH_2-containing MOF has a significant nitrogen residue in the resulting TiO_2.

4.3.1.4 Raman

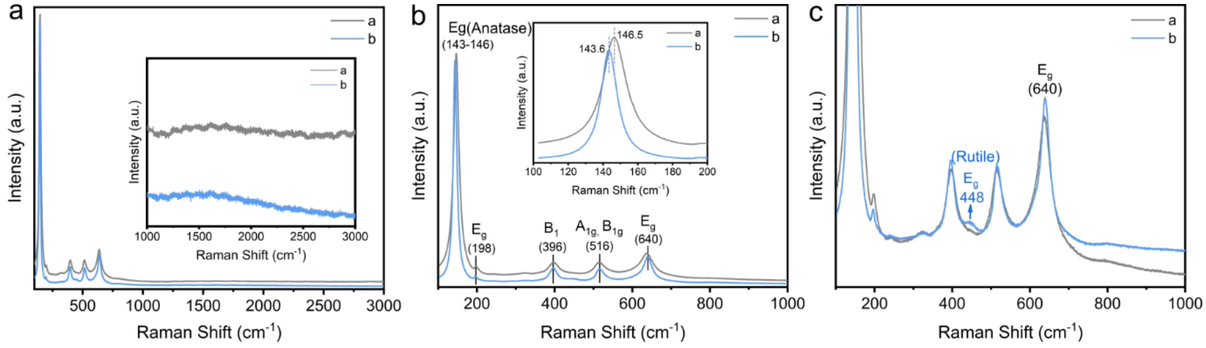

Figure 4-33 Raman Spectra of TO-550 (plot a) and TO-N-600 (plot b). a), b) and c) are the same spectra with different Raman shift range. Wavelength of laser: 532 nm; laser powder: 5 mW.

Raman measurements have been conducted to verify the existence of residual carbon (Figure 4-33).

Raman shifts of both samples have been recorded in the range of 100 - 3000 cm^{-1} (Figure 4-33(a)). No first order characteristic carbon bands (D and G bands), located at 1347 and 1586 cm^{-1},[156] respectively, have been detected for any of the calcined samples, also no second order bands, which suggests that TO-550 and TO-N-600 are free of carbon species. However, it needs to be noted that this observation does not exclude the possibility of carbon existing as dopant in the TiO_2 matrix, for which we have to take a closer look at the peaks.

Figure 4-33(b) is a magnified spectrum of TO-550 and TO-N-600 showing the range of 100 - 1000 cm^{-1}. The two samples exhibit similar Raman characteristics, with peaks present at around 145, 198, 396, 516 and 640 cm^{-1} assigned to the E_g, E_g, B_1, A_{1g}+B_{1g} and E_g modes of anatase phase, respectively.[157] The inset further compares the main characteristic peak of anatase and a noticeable peak shift can be observed between TO-550 and TO-N-600, 146.5 cm^{-1} vs. 143.6 cm^{-1}. In addition to the peak shift, the FWHMs are also different, 16.14 cm^{-1} for TO-550 compared to 11.33 cm^{-1} for TO-N-600. Since the absolute E_g peak positions reported for anatase are not highly consistent (from 144 to 147 cm^{-1})[157-160], in this work the observed peak shifts, i.e. 146.5 cm^{-1} vs. 143.6 cm^{-1}, will be focused. It is known that the peak shift in Raman can be caused by different reasons, including the crystallite size,[161] crystal strain,[158] non-stoichiometry/doping,[162] surface adsorbed species,[161] etc.. The crystallite size of TO-N-600 is bigger than that of TO-550 according to the XRD data, which is supposed to induce a red shift[163,164-165], therefore, the crystallite size difference can be ruled out from the contributions to the observed blue shift. Moreover, due to the low percentage of rutile phase in TO-N-600, the interference from the B_{1g} mode (144 cm^{-1}) of rutile in the peak shift can also be excluded. Another difference between the two oxides, which can induce the shift, is nitrogen doping in TO-N-600. Cheng *et al.*[162] have observed a 5 cm^{-1} red shift in their 3 mol % N-doped TiO_2 compared with the un-doped sample.[162] Similar Raman red-shift has also been reported by Yang and co-workers though they attributed the shift to the crystallite size only.[166] In fact, Raman shift has only been observed with substitutionally N-doped TiO_2; whereas with interstitial doping, peak broadening instead of peak shift has been observed.[167-168,169] Thus, considering the above discussion and based on the EDX elemental analysis, it may be suggested that the anatase E_g peak shift recorded between the samples corresponds to the substitutional doping of nitrogen in TO-N-600.

In addition to the peak shift, it is well established that the FWHM of the anatase E_g mode (~ 146 cm^{-1}) reflects the stoichiometric ratio of O/Ti.[157, 159] In the oxidation annealing experiment of TiO_{2-x} performed by Parker and Siegel,[159] the authors have discovered that the FWHM above 13 cm^{-1} indicates that the oxide is oxygen deficient ($x > 0$); and the higher the FWHM value is, the higher does the oxygen deficiency (x) get. The FWHM of our two samples are, 16.14 cm^{-1} for TO-550 and 11.33 cm^{-1} for TO-N-600, suggesting an oxygen deficiency for TO-550. Moreover, as confirmed by XRD, TO-550 contains brookite, which is more likely to have defects, specifically V_o, among the three TiO_2 phases,[170] further strengthening the argumentation that TO-550 contains oxygen defects. For TO-N-600, the stoichiometry ratio of O/Ti is approximately 2, indicating much less oxygen deficiency; one possibility can be that the substitutional nitrogen sits on the oxygen vacancies coincidently, thus ‘healing’ the oxygen defects.

Figure 4-33(c) provides another magnified view on the spectra, now focusing on the E_g mode of rutile phase: the peak at 448 cm^{-1} indeed confirms the presence of rutile in TO-N-600. However, Raman peaks of brookite, such as 153 cm^{-1} and 247 cm^{-1}, cannot be distinctly detected, which can be ascribed to the low percentage of brookite, the peak overlap between brookite (153 cm^{-1}) and anatase (144 cm^{-1}), or the lack of brookite presence on the surface.

In summary, Raman spectra confirms a) the absence of carbon species in the calcined samples; b) the main TiO_2 crystal phases observed in XRD. Importantly, c) the peak shifts and peak broadening suggest the presence of defects: oxygen deficiency in TO-550 and substitutional N-doping in TO-N-600.

4.3.1.5 UV-Vis spectroscopy

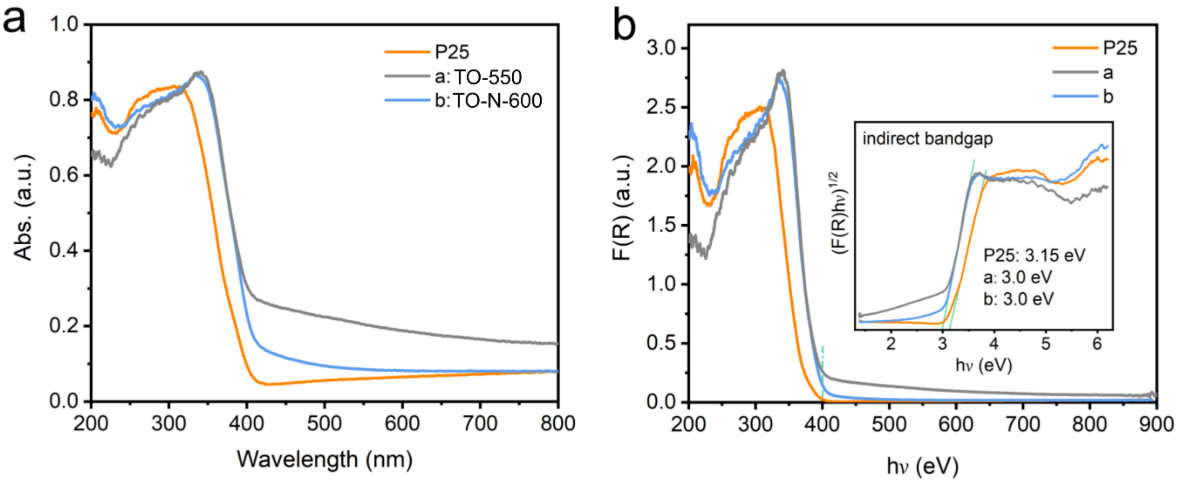

Figure 4-34 UV-Vis DRS of P25, TO-550 (plot a) and TO-N-600 (plot b): a) Absorbance; b) Kubelka-Munk function and Tauc plot

UV-Vis light absorption of the two calcined samples including P25 have been measured with DRS (Figure 4-34). Judging from the strong differences in the visible range, the light absorption ability is descending in the sequence TO-550 > TO-N-600 > P25. Compared with P25, the absorption onsets of TO-550 and TO-N-600 show a red shift, especially distinguishable for TO-550 that has an absorption tail extending into NIR region. As the particles of both TO-550 and TO-N-600 are comparable in size to the wavelength of the light, a contribution by light scattering cannot be excluded.[171] Therefore, to restrain the influence of particle size difference between TO-550 and TO-N-600 on the absorbance spectra, the acquired diffusive reflectance has been converted to Kubelka-Munk function in Figure 4-34(b). Consistent with Figure 4-34(a), the calcination products demonstrate increased light absorption property compared to P25. However, the TO-550 absorbed almost in the whole visible range, while TO-N-600 did not, indicating a different absorption-enhancement mechanism in these two samples, in accordance with the Raman observation about different defect types. The optical band gap is calculated with the indirect-allowed transition model (Equ. 2-6) (Figure 4-34(b)), as the main crystal phase for all the three oxides, anatase, is indirect-allowed band transition material[172-173]. MOF derived oxides have a narrower band gap of 3.0 eV than the 3.15 eV of P25.

Based on Raman observation, TO-550 is oxygen deficient. Zhou *et al.*[174] have prepared oxygen defective TiO_2 via one-step molten salt method and obtained a largely identical light absorbance spectra to what was obtained in Figure 4-34. TO-N-600, based on the previous conclusion drawn from EDX and Raman observation, is a substitutionally N-doped TiO_2. It is agreed that the substitutional nitrogen shifts the VB of TiO_2 upward while the interstitial nitrogen introduces new electronic states inside the forbidden band.[175-177, 178-179] In Figure 4-34, the band gap narrowing of TO-N-600 compared with P25 is only as much as 0.1 eV and there is no profound absorbance shoulder in the absorbance, the measured DRS data thus features a substitutionally N-doped TiO_2[180-182].

In summary, due to defects, TO-550 and TO-N-600 show enhanced light absorption with narrower band gaps compared to standard anatase TiO_2 (3.0 eV vs 3.2 eV). Notably, the defect type is different for the two: oxygen vacancies for TO-550 and substitutional N-doping for TO-N-600.

4.3.1.6 Photocatalytic Hydrogen Evolution Activity

As has been clarified in the introduction of this section, we are interested in the photocatalytic performance of TiO_2 derived from Ti-based MOFs. Above characterizations have revealed the materials' nature and even confirmed the presence of defects. How do the defects affect the photocatalytic performance? Do they act as charge recombination or light absorption centers? HER has been conducted to investigate this issue as well as to illustrate the potential of MOF-derived oxides for photocatalytic application.

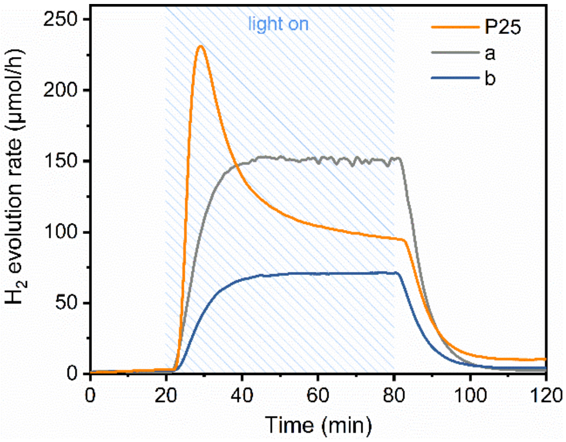

Figure 4-35 Hydrogen evolution rate of P25 (plot in orange), TO-550 (plot a, in grey) and TO-N-600 (plot b, in blue).

The photocatalytic activities were tested under UV irradiation (Figure 4-35) as the samples are not effectively visible-light active. P25 behaves differently from TO-550 and TO-N-600 featuring a drastic deactivation: the H_2 evolution rate first rises to 230 μmolh^{-1} after about 7 min irradiation, then suddenly drops to ~ 170 μmolh^{-1} within 10 min, followed by a slower decrease. The H_2 evolution rate of P25 is 95.5 μmolh^{-1} after 1 h irradiation, which may not be a stable level yet. In contrast to P25, TO-550 and TO-N-600 exhibit no deactivation within 1 h irradiation reaching hydrogen evolution rates of 151.9 and 70.7 μmolh^{-1}, respectively. The sudden drop of P25 HER rate (catalyst deactivation) has also been observed by other researchers. With the same HER setup, Haselmann and Eder have investigated the deactivation and attributed the deactivation to the ratio of cocatalyst (i.e. Pt) to oxygen vacancies as well as the encapsulation of the Pt by the TiO_2 matrix.[138]

To elucidate the different photocatalytic behaviors of these three oxides, Table 4-8 compares the possible contributing factors including crystal phase composition, crystallite size, the defects type, etc..

Table 4-8 Comparisons between P25 and TiO_2 derived from MIL and NH_2-MIL-125

Sample Information	H_2 evolution rate (μmol·h^{-1})	Crystal Phase	Crystallites size of anatase (nm)	DRS	Defects
P25	95.50	A+ R	20	Eg=3.15 eV	V_o
TO-550	151.9	A+ B	9.5	Eg=3.00 eV	V_o
TO-N-600	70.70	A+ R	17	Eg=3.00 eV	N_s

* Hydrogen evolution rate was collected after 60 min irradiation.

* Crystal Phase: A is short for anatase; R is short for rutile and B is short for brookite.

* Crystallite size were calculated with Scherrer Equation, with the peak (101) of anatase at 2θ=25.3°

The HER rate of TO-550 doubles that of TO-N-600 and Table 4-8 shows that the samples differ in phase composition, crystallite size as well as the defect type. It is hard to identify the main factors attributing to the different photocatalytic activities. Taking P25 into comparison, P25 and TO-550 exhibit oxygen vacancies (V_o),[138, 183] maybe the defects are not comparable; yet, both of them demonstrate a higher HER rate than the TO-N-600, which contains N as dopants. Therefore, it can be speculated that the defect type is likely to account for the different HER rates between TO-550 and TO-N-600.

Researchers have revealed that the surface V_o can help water adsorption and dissociation on the surface of defective TiO_2.[184-185,186,187-188] When water dissociates at the V_o site, it can form either surface-terminated –OH groups, O-bridging groups or •OH radicals.[189] Hydroxyl groups can create a hydrophilic surface, which is beneficial for the adsorption of reactant species onto the catalyst. The formation of radicals can act in a different way: Guzman *et al.*[95] performed D_2O studies and proposed that during HER process, the MeOH reacts with •OH rather than directly with photo-excited holes h^+. Therefore, an increased concentration of •OH radicals, possibly induced by the V_o, can facilitate the MeOH oxidation process, contributing to the H_2 evolution efficiency of TO-550. In contrast to oxygen vacancy, nitrogen defects are rather known as recombination centers[177]. Therefore, despite of the increased light absorption, the photocatalytic activity of TO-N-600 decreased.

So far, I have discussed about the characterization related to oxygen defects, as well as the possible contribution of oxygen defects to the photocatalytic activity. In all scenarios, the defect concentration plays an integral role. There is not much known about oxygen defects in MOFs-derived oxides. Likely, they are formed upon oxidation of the rather high percentage of organic components in MOFs. Due to restricted access to oxygen from the atmosphere, the organic component consumes additional O from the neighboring Ti-oxo clusters, resulting in an O_2 deficient environment for the crystallization of titania.

To verify the hypothesis as well as to gain control over the V_o, MOFs calcined with different parameters have been investigated. Moreover, the obtained samples possibly could have different crystal phase composition, which will help to clarify the influence of crystal phase on the photocatalytic performance that has not been discussed here.

4.3.1.7 Primary Attempts to Control V_o Concentration via Calcination

Table 4-9 lists the information of metal oxides derived from MIL-125-Ti and NH_2-MIL-125-Ti with different calcination parameters. The TO-550(a) and TO-N-600(b) are listed as reference; calcination temperature, calcination rate as well as the amount of MOF powders used for one batch calcination have varied in comparison to them.

Table 4-9 Sample Information of Metal Oxides derived from Ti-MOFs

MOF	Metal Oxides	Calcination T	Ramp rate	Comments	label in graph
MIL-125-Ti	TO-550	550 °C	5 °C/min	as 'reference'	a
	TO-550'	550 °C	5 °C/min	higher mass	a1
	TO-550''	550 °C	1 °C/min	lower ramp rate	a3
	TO-600	600 °C	5 °C/min	higher cal. T	a2
NH_2-MIL-125-Ti	TO-N-550	550 °C	5 °C/min	lower cal. T	b1
	TO-N-600	**600 °C**	**5 °C/min**	**as 'reference'**	**b**
	TO-N-600'	600 °C	5 °C/min	higher mass	b2

Since the muffle oven provides kind of semi-sealed environment, I studied the impact of amount of starting material as well as of the calcination ramp rate on the oxygen supply during calcination. Furthermore, the influence of calcination temperature on phase composition and crystallite size was investigated.

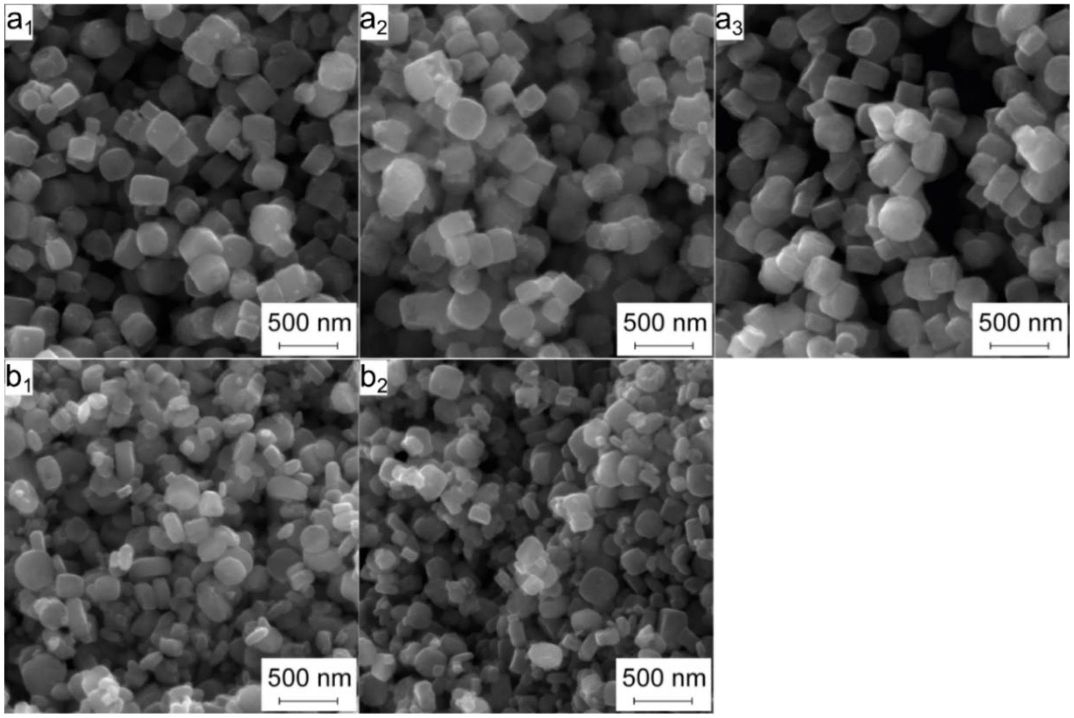

Figure 4-36 SEM characterizations of titania derived from MOFs: a_1) TO-550'; a_2) TO-600; a_3) TO-550''; b_1) TO-N-550; b_2) TO-N-600'.

The morphologies of the newly obtained titania have been characterized in Figure 4-36. The following conclusions can be drawn from the SEM images: 1) a lower calcination temperature (550 °C) resulted in a smoother surface, while a higher calcination temperature (600 °C) led to small particle 'cracks' or 'voids' (compare a_1 vs. a_2, b_1 vs. b_2); 2) the influence of calcination ramp rate on morphology is not very obvious as both samples have the same circulate shape and similar surface smoothness (compare a_1 vs. a_3).

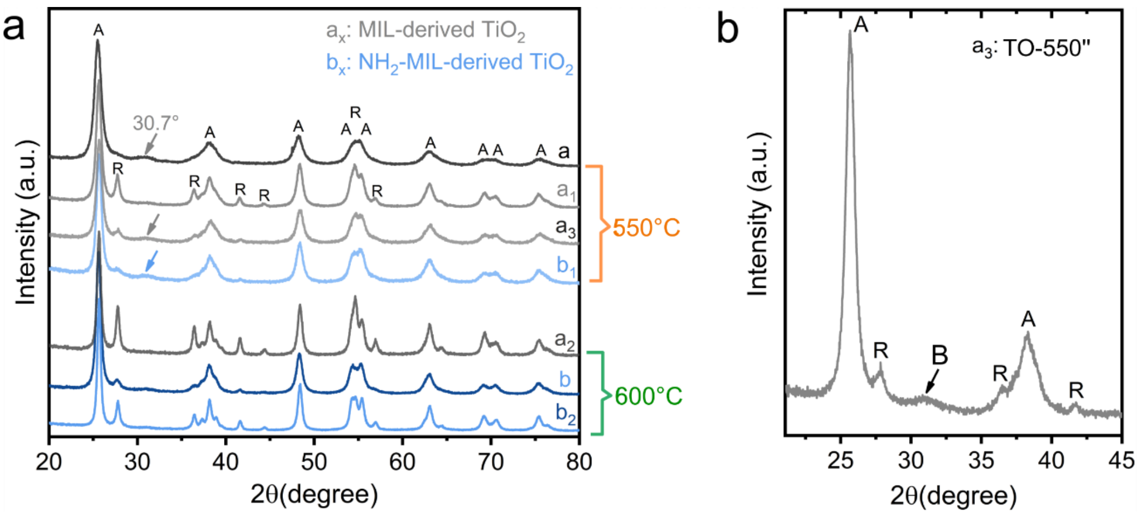

Figure 4-37 a) XRD patterns of titania derived from MOFs: a_1) TO-550'; a_2) TO-600; a_3) TO-550''; b_1) TO-N-550; b_2) TO-N-600'. b) Enlarged XRD pattern of sample a_3.

Figure 4-37 shows the XRD patterns of the obtained titania and Table 4-10 summarizes the phase composition as well as crystallite size derived from XRD patterns. The average size of the crystallites was calculated according to the Scherrer equation (2-4), using the peaks at 2θ=25.3° and 2θ=27.3° for anatase and rutile phase, respectively. The weight ratio of rutile were calculated according to Spurr & Meyers equation (Equ.4-1)[190].

$$Rutile\ \% = \frac{1}{1 + 0.79 * \frac{I_A}{I_R}} \qquad \text{4-1}$$

** I_A is peak intensity of anatase (101); I_R is the peak intensity of rutile (110).*

Table 4-10 Crystal Phase Analysis of Different TiO_2

MOF	Metal Oxides	Calcination T	Comments	Crystal Phase	R/A ratio	Crystallite Sizes (nm)	label in graph
MIL-125-Ti	**TO-550**	**550 °C**	as 'reference'	**A+B**	-	9.5	a
	TO-550'	550 °C	higher mass	**A+R**	25.8%	13 /63	a_1
	TO-550''	550 °C	lower ramp rate	A+R+B	18.6%	12 /42	a_3
	TO-600	600 °C	higher cal. T	A+R	34.7%	19 /83	a_2
NH_2-MIL-125-Ti	TO-N-550	550 °C	lower cal. T	A+R+B	17.3%	13 /25	b_1
	TO-N-600	**600 °C**	**as 'reference'**	**A+R**	13.7%	17 /38	**b**
	TO-N-600'	600 °C	higher mass	A+R	23.7%	21 /84	b_2

Based on the information in Figure 4-37 and Table 4-10, we can conclude:

1) Anatase is the main crystal phase for all of the samples, if the calcination temperature is not higher than 550 °C. Comparing the rutile ratios in TO-550 (34.7 %) with TO-N-600 (13.7 %), the TO-x tends to experience anatase to rutile transformation earlier than TO-N-x, which can be ascribed to the fact that the transformation of MIL into metal oxides is completed at lower temperatures than NH_2-MIL, demonstrated by TGA (Figure 4-13).

2) The starting mass of MOFs has a marked influence. It needs to be noted that the crucible used to hold MOFs powders is of fixed size, therefore, a higher mass means a thicker powder layer. On the one hand, a thick layer may restrict the diffusion and acquisition of oxygen for the bottom powders, leading to an oxygen insufficiency; on the other hand, a thicker layer is prone to an inhomogeneous temperature distribution over the samples, which means partial over/under-heating. It has been reported that oxygen defects favor the phase transformation of rutile,[185-186] therefore, comparing a vs. a_1 and b vs. b_2, the higher rutile percentage induced by higher initial MOF masses (a_1 and b_1) can be ascribed to the limited oxygen supply as well as the over-heating. This phase composition change induced by initial powder mass can lead to the reproducibility problem; a thin layer is thus suggested for the MOF calcination.

3) A slower ramp rate did influence not only the oxygen supply, but also a longer heating process. Compared with TO-550(a), TO-550''(a_3) has rutile phase (Figure 4-37(b)).

4) The presence of brookite phase is related to the calcination temperature. Brookite has been observed in sample obtained at 550 °C rather than samples obtained at 600 °C. Moreover, comparing a, a_1 and a_3, a higher rutile ratio is accompanied by the disappearance of brookite. The transformation between brookite and rutile has been reported, which can occur either via an indirect route, brookite → anatase → rutile, or via a direct route, brookite → rutile. Both routes have been reported in the crystallization of amorphous TiO_2, in wet-chemical synthesis.[191] However, the appearance of brookite in the calcination of Ti-based MOF has not yet been revealed, neither the transformation process. An in-depth investigation into the calcination process of MIL-125-Ti and NH_2-MIL-125-Ti based on a series of in-situ techniques is presented in Chapter 4.4.

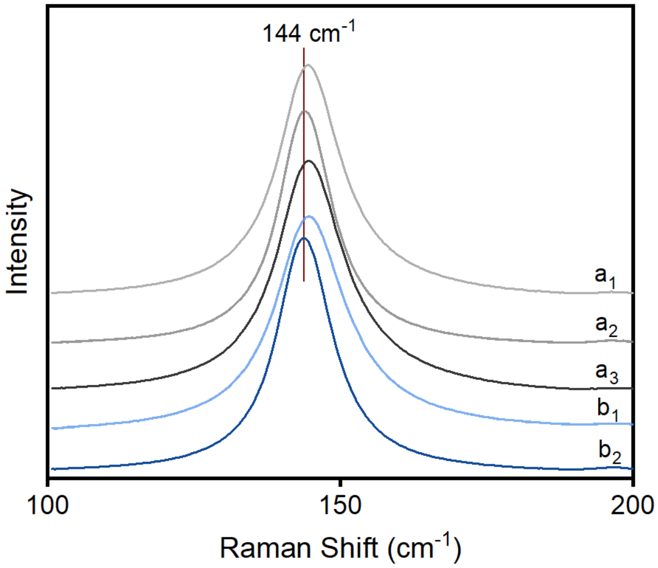

Figure 4-38 Raman observation of metal oxides with focus on the E_g mode of anatase

Table 4-11 Raman Analysis of TiO_2

Sample	Position	FWHM
a	146.5	16.14
a_1	144.96	13.35
a_2	144.27	11.14
a_3	145.11	14.44
b	143.6	11.33
b_1	144.83	14.53
b_2	144.11	11.11

Figure 4-38 and Table 4-11 provide detailed information about the characteristic Raman peak of anatase.

The wavenumber of the Raman peak is $b < b_2 < a_2 < b_1 < a_1 < a_3 < a$. Based on our previous argumentation, this can be concluded as 1) the peak for NH_2-MIL-125-Ti derived 'b-series' is at a smaller wavenumber, which is attributed to the substitutional N; 2) the peak in TiO_x (b, b_2 and a_2) obtained at high calcination temperature shifts to smaller wavenumbers due to higher crystal strain.

The FWHM values follow $b_2 < a_2 < b < a_1 < a_3 < b_1 < a$; as has been discussed before, this can be related to the stoichiometric ratio of O/Ti, while the higher FWHMs indicate a larger oxygen deficiency. Referring to the calcination parameters, a general trend can be concluded that the lower calcination temperature and the higher mass of raw materials favors oxygen deficiency in the oxides. Moreover, take the XRD patterns (Figure 4-37) into account, it can be seen that the FWHM sequence is highly related with the percentage of rutile and brookite in the material: the less rutile and the more brookite, the larger the value of FWHM. This can be explained by 1) brookite is likely to have a higher density of V_o than other TiO_2 phases; 2) the Raman shift of the E_g mode in brookite (153 cm^{-1}) can overlap with the E_g mode in anatase (144 cm^{-1}), thus broadening the observed peak at around 144 cm^{-1} and increasing the FWHM value.

In summary, Raman studies revealed that the calcination parameters strongly affected both the crystal strain and the defect concentration in the calcined oxides. One consequence is that the calcination parameters directly influence the stoichiometric ratio of O/Ti in the materials. The other impact is that the calcination parameters influence the phase composition of the oxides, for example, favoring the formation of defect-rich phase – brookite, which can also result in a high oxygen defects concentration in the materials.

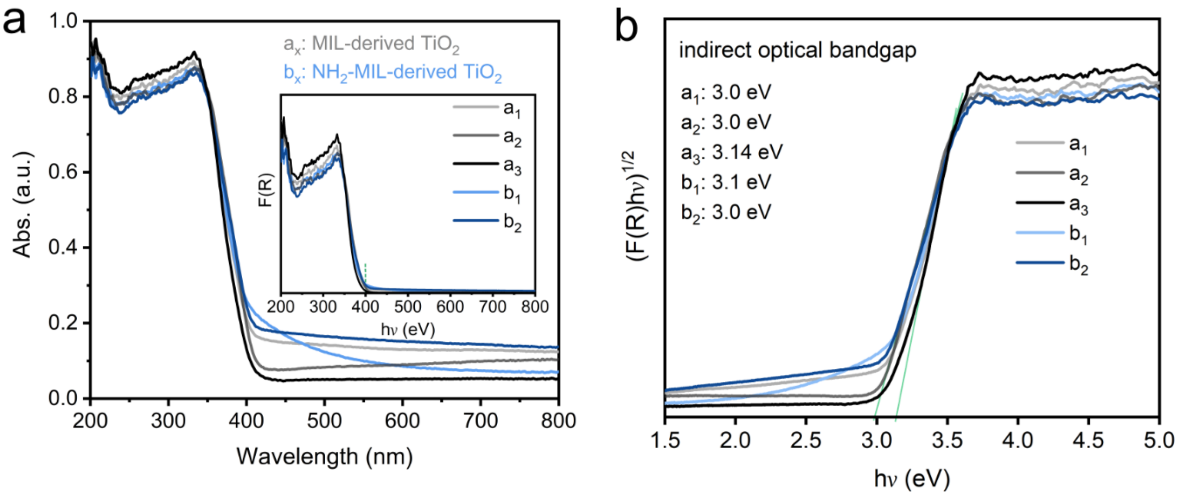

Figure 4-39 Absorbance and optical band gap of TO-x and TO-N-x: a_1) TO-550', a_2) TO-600, a_3) TO-550'', b_1) TO-N-550, b_2) TO-N-600'

Figure 4-39 displays the DRS absorbance spectra as well as the optical band gaps of the obtained metal oxides. The absorption edge for all the oxides are similar, starting at around 400 nm. The Tauc plots in Figure 4-39(b) were calculated with the indirect-allowed transition model. It can be seen that the tangents of the main slope of the plots intersect with the x-axis in the range of 3.0 eV and 3.14 eV, which are smaller than the E_g of anatase (3.2 eV), suggesting the existence of defects. Notably, TO-N-550 (b_1) display a shoulder, typical for the N-doped TiO_2, suggesting a higher nitrogen doping concentration when calcined at lower temperature. A detailed discussion about the influence of defects on the light absorption property can refer to Chapter 4.3.1.5.

Photocatalytic Studies:

HER experiments were conducted with all the oxides under same conditions to investigate the influence of calcination-process-induced materials' differences, including phase composition, crystallites size, light absorbance, as well as defects type and concentration, on their photocatalytic activity. H_2 and CO_2 evolution rates are plotted in Figure 4-40.

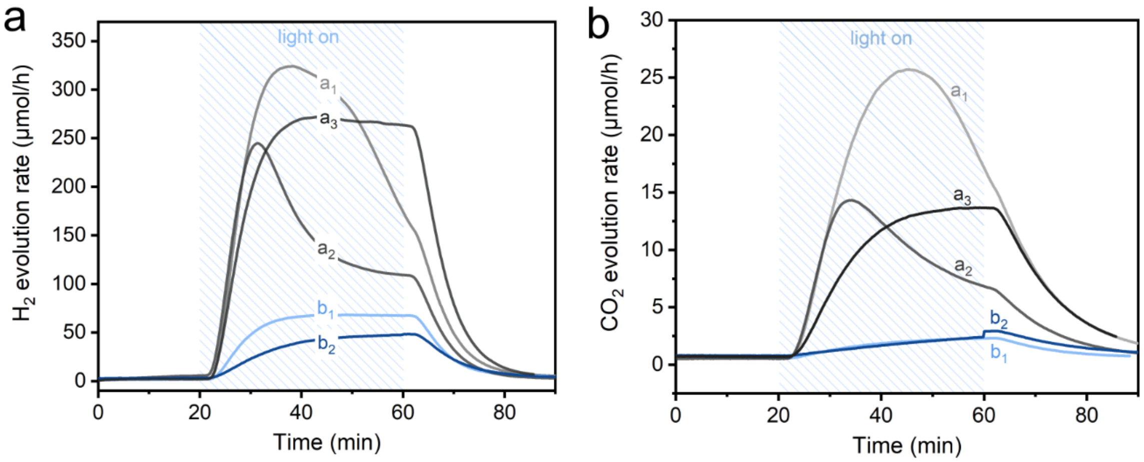

Figure 4-40 HER performances of TiO_2 obtained from MIL-125-Ti and NH_2-MIL-125-Ti. HER parameters were: 10 mg TiO_x powders; 20 mL H_2O + 20 mL MeOH; Pt:TiO_x wt% = 0.5; light source: Lumateic, Hg lamp; irradiation time: 40 min.

The HER rates of two MIL-125-Ti derived oxides, TO-550'(a_1) and TO-600(a_2), deteriorate with increasing reaction time, albeit with different trends. The HER rate of a_2 starts with a drastic drop, identical to the deactivation behavior of P25, as observed in Figure 4-35, while the HER rate of a_1 suffers a gradual drop during the whole irradiation time. The other oxides, TO-500'(a_3), TO-N-550(b_1) and TO-N-600'(b_2) demonstrate no deactivation behavior within 1 h irradiation, instead, the H_2 evolution rate of b_2 seems to increase over time. The parent MOF makes a difference in the photocatalytic performance of the oxides, as NH_2-MOF derived TiO_x are less efficient than MIL-MOF derived TiO_x, confirmed by the performance of b, b_1 and b_2. As to the calcination temperature, higher calcination temperature is not favorable for hydrogen evolution reaction, observation from both TO-x and TO-N-x. Regarding the mass used for calcination, it affects the materials' activity as well, but the influence is different for TO-x and TO-N-x. Specifically, TO-550' (higher mass) has a higher H_2 generation rate than that of TO-550 (lower mass), however, with a deactivation; while TO-N-600’ (higher mass), it demonstrates a lower photocatalytic efficiency than TO-N-600 (lower mass).

Table 4-12 Summarization of TiO_2 obtained from Ti-based MOFs under different calcination parameters

MOF	**Metal oxides**	**Comments**	**Crystal phase**	**R/A ratio**	**Crystallite sizes of anatase**	**Surface area**	**H_2 evolution rate**	**Defects**	**label**
MIL-125-Ti	**TO-550**	**as 'reference'**	**A+B**	**-**	**9.5**		**151**	Vo	**a**
	TO-550'	higher mass	**A+R**	25.8%	13	45.5	168/325	Vo	a_1
	TO-550"	lower ramp rate	A+R+B	18.6%	12	92.0	264	Vo	a_3
	TO-600	higher cal. T	A+R	34.7%	19		109/243	Vo	a_2
NH_2-MIL-125-Ti	TO-N-550	lower cal. T	A+R+B	17.3%	13		67.4	Ns	b_1
	TO-N-600	**as 'reference'**	**A+R**	**13.7%**	**17; 38**		**70.7**	**Ns**	**b**
	TO-N-600'	higher mass	A+R	23.7%	21	22.0	48.4	Ns	b_2
P25	P25		A+R	17.3%	20	54	105/230	Vo	

* H_2 evolution rate is the value obtained after 40 min irradiation; for the samples with deactivation behaviour, another value is their highest H_2 evolution rate.

To clarify the reasons for the different photocatalytic activities, as well as to demonstrate the influence of calcination parameters, Table 4-12 summarizes the various properties of different oxides.

It can be concluded that the surface area seems to contribute greatly to the photocatalytic performance, as TO-550’’ with 92 m^2/g shows the highest H_2 evolution rate, 264 μmol/h. Meanwhile, the surface area is closely related to the calcination ramp rate, as with higher ramp rate, the surface area of obtained TO-550’ decreases to 45.5 m^2/g.

Despite their similar surface areas, the photocatalytic performance of TO-550, TO-550’ and P25 differs greatly from each other, indicating that other factors such as phase composition and oxygen defects in the materials are contributing to the photocatalytic activity. The measured FWHM of Raman peak for P25 is only 9.9 cm^{-1}, while that for TO-x is above 11 cm^{-1}. Therefore, I attribute the superior photocatalytic performance of MOF-derived oxides, TO-x, to their higher defect level, as well as to the smaller crystallite sizes.

Another observation concluded from Table 4-12 is related to the deactivation. All the three samples (marked in red in Table 4-12), which demonstrate a decreasing H_2 generation rate, are composed of anatase and rutile, while the other two oxides derived from MIL-125-Ti containing brookite phase do not show a deactivation. Why are the deactivation behaviors of TO-550' and TO-600 different? Does the brookite phase prohibit the deactivation? These questions cannot be answered in this thesis and needs further investigation.

4.3.2 Conclusion and Outlook

In this chapter, I calcined MIL-125-Ti and NH_2-MIL-125-Ti into TiO_x and investigated their photocatalytic activity. The present results demonstrate that MOF-derived metal oxides hold great potential for photocatalytic hydrogen generation. The highest H_2 evolution rate 26400 μmolh^{-1}g^{-1} has been obtained by the oxide (TO-550'') calcined from MIL-125-Ti at 550 °C, with 1 °C/min ramp rate and 1 h dwell time, while the H_2 evolution rate of P25, the benchmark material for TiO_2, is 10500 μmolh^{-1}g^{-1} under the same conditions.

Another key information of this chapter is that the parameters of MOF calcination process are of vital importance to the properties of obtained oxides. The parameters, including the calcination temperature, the calcination ramp rate, as well as the mass of starting MOF powders, strongly influence the surface area, phase composition, crystallite sizes and defects of the obtained oxides. Consequently, the resultant hydrogen evolution rates vary considerably between 10900 and 32500 μmolh^{-1}g^{-1}.

Though the microporous structure of the MOFs collapses during the calcination process, with careful control of the calcination process, such as a lower ramp rate, the obtained oxides can still be highly porous and obtain a surface area close to 100 m^2/g. In general, for a higher photocatalytic efficiency as well as for a better reproducibility, a low ramp rate and small amount of raw materials are suggested for the calcination.

Compared with TiO_2 obtained via other preparation methodology, the calcined products have shown the appearance of brookite, especially the co-existence of anatase, rutile and brookite. No deactivation in the oxides with brookite was observed, however, a conclusive explanation of the role of brookite needs further investigation.

Moreover, I have investigated the defects introduced to the metal oxides during the calcination process. The functional group in the organic ligand of MOF enables elemental doping of the calcined products. In this work, the amino group in NH_2-MIL-125-Ti has

successfully introduced N dopants to the oxides. However, as the oxides derived from NH_2-MIL-125 have always performed worse than those derived from MIL-125-Ti, it can be concluded that the N-dopants are detrimental to hydrogen evolution with the current HER system. In addition to the nitrogen defects, the results suggest the presence of oxygen defects in the MOF-derived oxides. Due to the high content of organic component in MOFs, their calcination and conversion into TiO_2 occur under an oxygen deficient environment, thus it is likely that the resulting material is a substoichiometric TiO_{2-x}. This has been supported by Raman characterization, however, further characterizations, for example, the determination of the Ti^{3+} in the oxides with EPR, remain to be done to elucidate this issue.

4.4 Investigation of the Thermal Decomposition Process of NH_2-MIL-125-Ti into TiO_x

As an organic-inorganic hybrid framework, the stability of MOFs has raised concern, especially the thermal stability. The presence of organic linker limits the thermal stability of most MOFs to below 300 °C, as at higher temperature, the crystal structure experiences irreversible changes.

The low thermal stability of MOFs on one hand limits its application to low temperature; on the other hand, this instability has enabled MOFs to become a new type of template for porous materials. The last chapter has witnessed the potential of MOFs derived metal oxides; moreover, it has demonstrated that the calcination process is of vital importance to the properties of the obtained materials, such as the calcination temperature, ramp rate, as well as the oxygen supply. To obtain oxides with desired phase, size and morphology, the transformation process from MOFs to metal oxides thus needs a better understanding and control. However, the phase transformation during this calcination process is yet unclear.

In-situ techniques have been widely used to characterize the crystallization and phase transformation process; however, in-situ investigations on the thermal decomposition process of MOFs is rare. In-situ variable-temperature XRD was employed to study phase transition of one Co-based MOF, but only in the temperature range of 100-300 K[192]. For the broader temperature range investigation, Zhang *et al.*[193] has investigated the thermal decomposition of Zn-based MOF with in-situ DRIFTS IR.

In this work, with the assistance of in-situ XRD and in-situ Raman spectroscopy, the thermal decomposition process of MOFs has been revealed and the impact of different calcination parameters has been elucidated.

4.4.1 Results and Discussions

4.4.1.1 In-situ XRD with different ramp rate with controlled air flow

NH_2-MIL-125-Ti has been selected as the candidate for in-situ investigation and its TGA data can be seen in Figure 4-41. Based on the TGA discussions in Section 4.1.1.6, the stage III corresponds to the decomposition of MOF and the crystallization of TiO_2, the objective stage of my investigation.

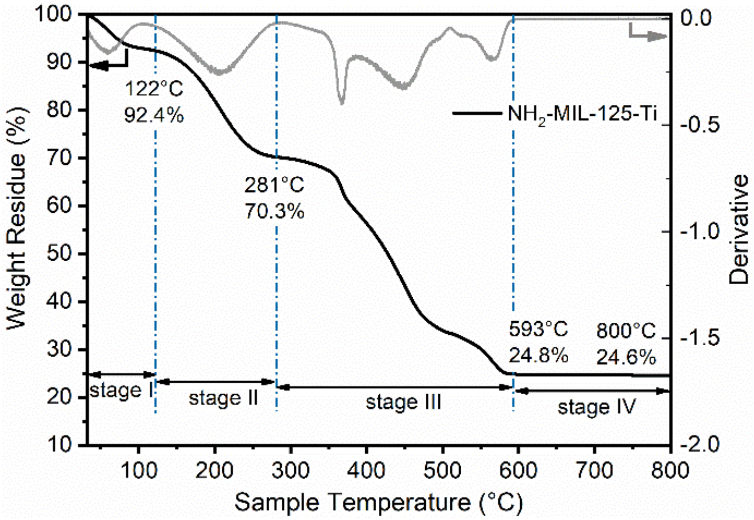

Figure 4-41 TGA results of NH_2-MIL-125-Ti, airflow: 20 mL/min, ramp rate: 5 °C/min.

For the in-situ XRD measurements, the powders were placed in a semi-sealed chamber, with a fixed air flow passing through it. Concluded from Chapter 4.3, the calcination ramp rate influences the properties of the obtained metal oxides, such as the surface area and defects concentration. However, whether the ramp rate affects the intermediate products as well as the transformation process, is yet unknown. Therefore, in this work, in-situ XRD with different ramp rates, 1 °C/min, 10 °C/min and 20 °C/min were employed to investigate the impact of the ramp rate on the thermal evolution process of NH_2-MIL-125-Ti under controlled air flow. The detailed measurement programs are already described in Chapter 3.3.

Figure 4-42 summarizes the results and the overall decomposition process have been divided into 3 stages, below 250 °C, 250 °C to 500 °C and above 500 °C, as indicated by ‘x_1’‘x_2’‘x_3’, for all the ramp rates.

Within the first temperature region (Figure 4-42: a_1, b_1 & c_1), the main crystalline structure of MOF was intact with the increasing temperature, regardless of the ramp rate. Minor changes in the diffraction patterns were detected; for example, the intensity of the peak at 2θ = 13.8° increased with the temperature. This change is ascribed to the removal of adsorbed guest species in the framework, which has been discussed before in Chapter 4.1, with Figure 4-2. The in-situ XRD results agree with the TGA observation, that during stage I and stage II, the weight loss is attributed to the loss of adsorbed species.

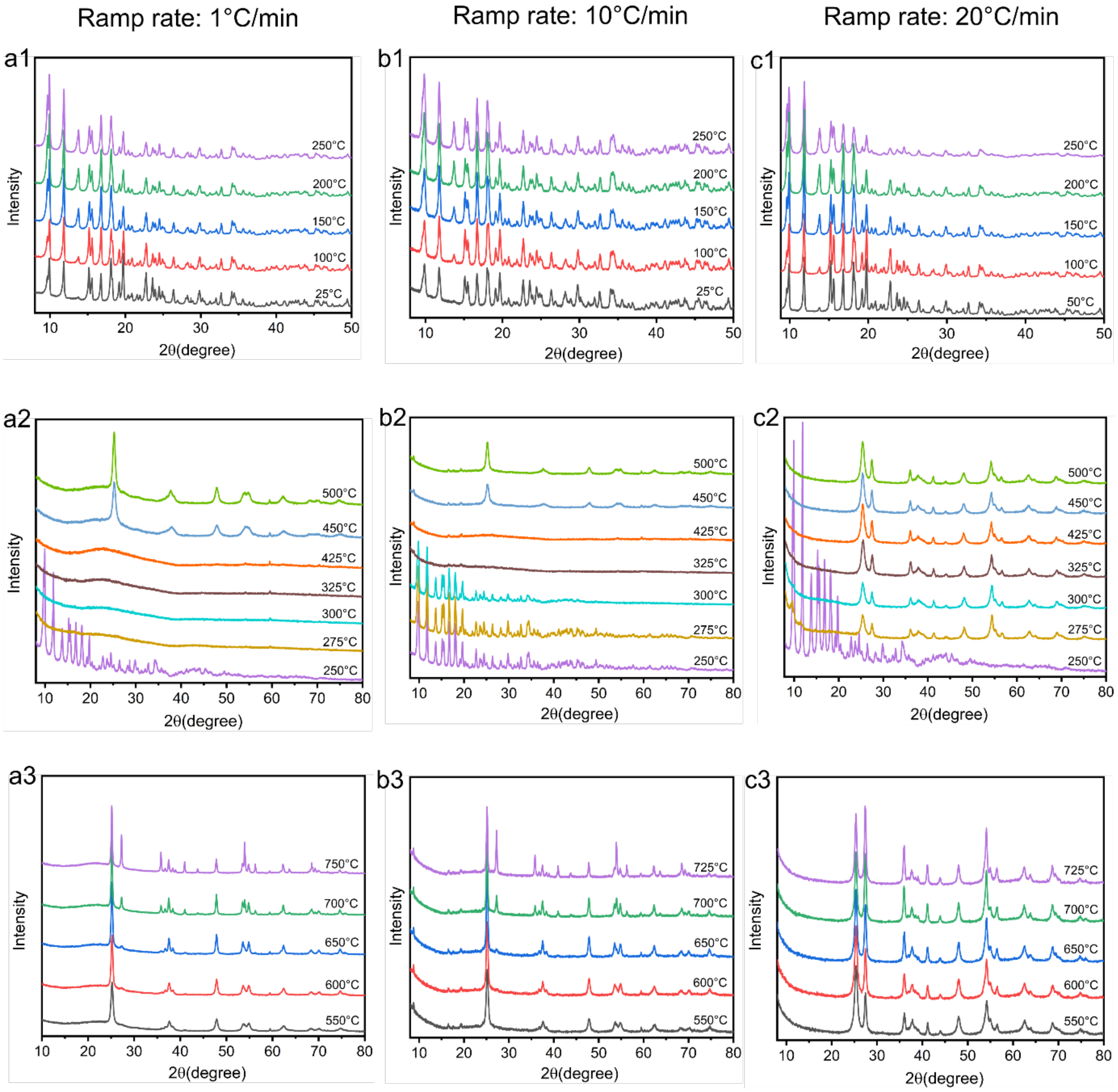

Figure 4-42 In-situ XRD patterns of NH_2-MIL-125-Ti from room temperature to 750 °C with different ramp rates under fixed airflow, 0.5 mL/min. a_x), b_x) and c_x) refer to ramp rates of 1 °C/min, 10 °C/min and 20 °C/min, respectively.

MOFs decomposition and TiO_2 crystallization occur within the intermediate temperature region (Figure 4-42: a_2, b_2 & c_2). It can be seen that the structure of NH_2-MIL-125-Ti was preserved until 250 °C, then with different ramp rates, different thermal evolution processes occurred:

1) When the ramp rate was 1 °C/min, with elevated temperature, NH_2-MIL-125-Ti was first decomposed into an amorphous state and this state lasted until 425 °C. At 425 °C, the broadening of an amorphous hump at 22.5° can be clearly seen. A distinguishable peak of crystalline anatase ($2\theta = 25.4°$) showed up at 450 °C and the peak intensity increased with the increasing temperature, indicating the enhancement of crystallinity.

Recent research has broadened the field of MOF with increasing focus on amorphous MOFs (a-MOFs)[194]. It has been reported that the a-MOFs retain the basic building blocks and connectivity of their crystalline counterparts, though they lack any long-range periodic order. A periodic arrangement of atoms result in their X-ray diffraction patterns being dominated by broad ‘humps’. As to the amorphous state observed in this work, whether it is amorphous MOF or amorphous TiO_2, needs further confirmation. But due to the center of the hump is close to that of anatase (101) peak, it is likely to be amorphous TiO_2.

2) When the ramp rate was set to 10 °C/min, the MOF structure was preserved to a higher temperature, until 300 °C. Then the material also experienced an amorphous stage, which was shorter compared to that in the case of 1 °C/min ramping; however, the emergence temperature of anatase phase in these two measurements were roughly the same, at 450 °C.

3) With 20 °C/min ramp rate (Figure 4-42(c_2)), the thermal transformation behavior of MOF differed greatly from that with a lower ramp rate. At 250 °C, the diffraction pattern corresponding to the MOF structure was recorded to be the same structure as in the other measurement cases. Then the diffraction pattern of the MOF powder changed dramatically and only two mall peaks at $2\theta = 9.6°$ and 11.6° remained from the original MOF structure at 275 °C, while the characteristic peaks of anatase and rutile appeared simultaneously. From 300 °C onwards, no MOF peaks were presented anymore.

During the last temperature region investigated by in-situ XRD (Figure 4-42: a_3, b_3 & c_3), in addition to crystal growth, the main process happening was the anatase to rutile transformation. For the measurements operated with 1 °C/min and 10 °C/min ramp rates, rutile appeared at 650°C. For the 20 °C/min ramping process, anatase and rutile appeared together at 275 °C; during this stage, the ART was demonstrated by the decrease of the anatase intensity accompanied by the increase of the rutile intensity.

The summarization of the thermal decomposition processes of NH_2-MIL-125-Ti with different ramp rates is as follows:

– **1°C/min ramping**: MOF (250 °C) → amorphous (275 °C - 425 °C) → anatase (450 °C - 600 °C) → anatase + rutile (650 °C -);

– **10°C/min ramping**: MOF(300 °C) → amorphous (325 °C - 425 °C) → anatase (450 °C - 600 °C) → anatase+rutile (650 °C -);

– **20°C/min ramping**: MOF (250 °C) → anatase + rutile (275 °C -).

A dependence of the decomposition process on the ramp rate can be firmly concluded. With 20 °C/min heating rate, there is no 'amorphous stage' after the damage of MOF crystal structure, instead, an instant crystallization into rutile and anatase has been observed.

Comparing the measurement program with low and high ramp rates, the points below may contribute to explain the different transformation processes:

1) A slower ramping means a longer heating time, and thus the sample receives more thermal energy input. According to Figure 4-42, it seems that a higher energy input favors the amorphization process of MOFs.

2) Whether the sample can reach an equilibrium at a certain temperature when the X-ray started to scan, especially in the case of fast ramping. In the case of a 20 °C/min heating rate, the ramp time required from 250 °C to 275 °C is only 1.25 min, which was immediately followed by the XRD scan. Can the sample reach the temperature equilibrium within 1.25 min?

3) The 25 °C temperature gap vs. 20 °C/min ramp rate makes the 'over-heating' of the heating component possible. However, the temperature log recorded by the thermocouple which was attached to the sample stage showed that the temperature deviation was about 2-4 °C.

Therefore, I speculate the different decomposition process is mainly ascribed to the first two considerations.

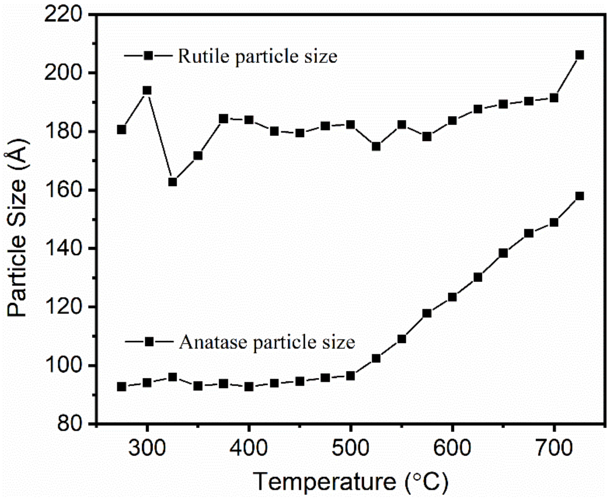

Figure 4-43 Crystallite size analysis of anatase and rutile phase during in-situ XRD measurement. Calculated with data in Figure 4-42 'Cx' series, 20 °C/min ramp rate,

To investigate the state of the anatase and rutile evolved with 20 °C/min, the Scherrer equation (Equ. 2-4) with the FWHM of the anatase (101) peak and rutile (110) peak (from Figure 4-42) was calculated to estimate the mean crystallite size of obtained anatase and rutile and the results are displayed in Figure 4-43. It can be seen that below 500 °C, there is no obvious size change for both phases. The average size of anatase crystallites is 9 – 10 nm, smaller than that of rutile, which is around 18 nm. Above 500 °C, the crystallites of anatase start to grow bigger, while the rutile crystallites show a slight increase above 600 °C, and then above 700 °C they start to grow dramatically.

Referring to Figure 4-42, the trends of the crystallite size, for both phases, coincide with the XRD results of lower ramp rate measurements. The crystallite size of rutile started to increase above 600 °C, in accordance with the emergence temperature of rutile in the XRD patterns observed with 1 °C/min and 10 °C/min, which can be ascribed to the anatase to rutile transformation. These results imply that though the rutile phase crystallized at 275 °C, it might have been a metastable phase, therefore, no rutile crystal growth was observed below 600 °C. As to the constant crystallite size of anatase below 500 °C, I speculate that this is due to the residue of organic ligand in the material. One possibility is that the TiO_2 crystallites were isolated from each other by the organic species, i.e. the organic species wrapped the TiO_2 crystallite. Therefore, it is at around 500 °C when most of the organic component were oxidized, that anatase had the chance to grow. To certain extent, the TGA data supports this assumption, as the temperature for the complete removal of organic ligand is as high as 593 °C (Figure 4-41).

Moreover, the appearance of rutile at 275 °C can also be associated with the organic ligands. It has been reported by Ocaña[195] that depending on the amount, organic impurities can be responsible for the nucleation of rutile.

Therefore, the preliminary conclusion for the moment is that the higher ramp rate induces a metastable state of the sample, contributing to a higher amount of organic residue in the material, and further leading to a different thermal decomposition process.

4.4.1.2 Isotherm TGA

To demonstrate the time required to complete the corresponding process at certain temperature, I have monitored the weight loss at two transition temperatures with the iso-therm TGA program. Specifically, NH_2-MIL-125-Ti was heated up from room temperature to 400 °C with ramp rate of 20 °C/min and dwelled at 400 °C for 2 h, 4 h and 6 h, respectively. Then the sample was cooled down to room temperature. The weight loss of the whole process was recorded and the results are displayed in Figure 4-44, labelled as ‘xx (dwell time) at 400 °C’. Another series of measurements have been conducted with another dwelling temperature, 275 °C. The dwell time varied from 2 h to 26 h, as can be seen in Figure 4-44(c) and (d).

Based on TGA, at 400 °C, the weight loss can be attributed to the decomposition of organic ligand. The iso-TGA results in Figure 4-44(a) & (b) reveal that 2 h is required for the completion of weight loss at 400 °C. The weight residue at the end of the measurement is 30.15 %, less than the theoretical TiO_2 residue percentage (38.7 %), slightly higher than the data obtained with a conventional TGA, which is 24.8 % at

600 °C (Figure 4-41). However, due to the adsorbed guest species inside the framework, it is hard to conclude at the end of 400 °C dwelling, whether there is organic residue in the sample or not. For the measurements conducted at 275 °C, the weight of the sample kept decreasing even after 26 h (Figure 4-44), suffering a weight loss of 51.4 %. Due to the high percentage value, it is likely in addition to the adsorbed guest species, the organic ligand of the framework contributed to the weight loss as well. Therefore, at 275 °C, with enough time, the organic ligand in NH_2-MIL-125-Ti can experience a decomposition. However, in both the conventional TGA and in-situ XRD, the dwell time is not long enough to complete the decomposition process. Whether the duration of weight loss is dependent on the ramp rate, needs further investigation. Also, this needs to be noted that different from the in-situ XRD measurement, the air flow for TGA is 20 mL/min.

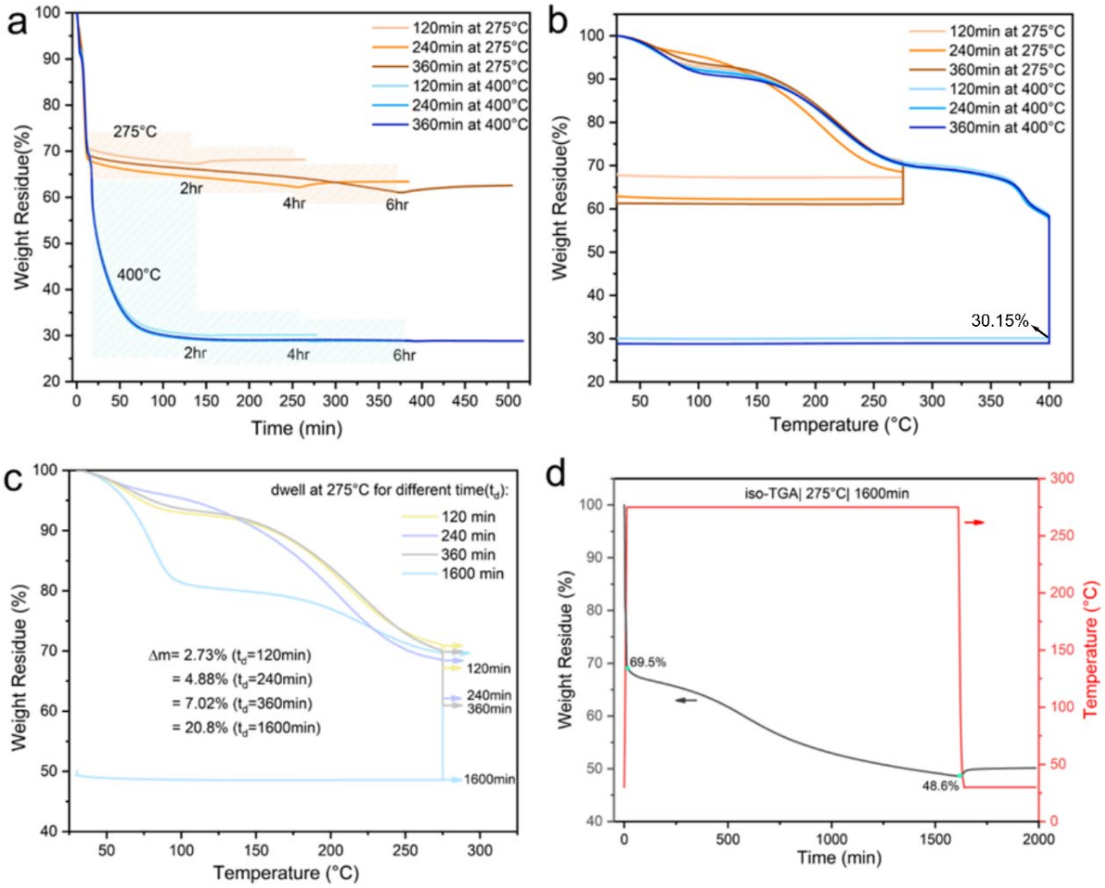

Figure 4-44 Isotherm TGA at 275°C and 400°C with 20 °C/min ramp rate

4.4.1.3 Raman Measurement

a) Temperature - Programmed Raman Experiment

Temperature-programmed in-situ Raman spectroscopy has been performed to investigate the thermal evolution process of organic species in the sample. NH_2-MIL-125-Ti was first heated from room temperature to 450 °C with the ramp rate 20 °C/min, and then the powder was dwelled at 450 °C for about 80 min. The sample holder was connected to open air. The results are summarized in Figure 4-45.

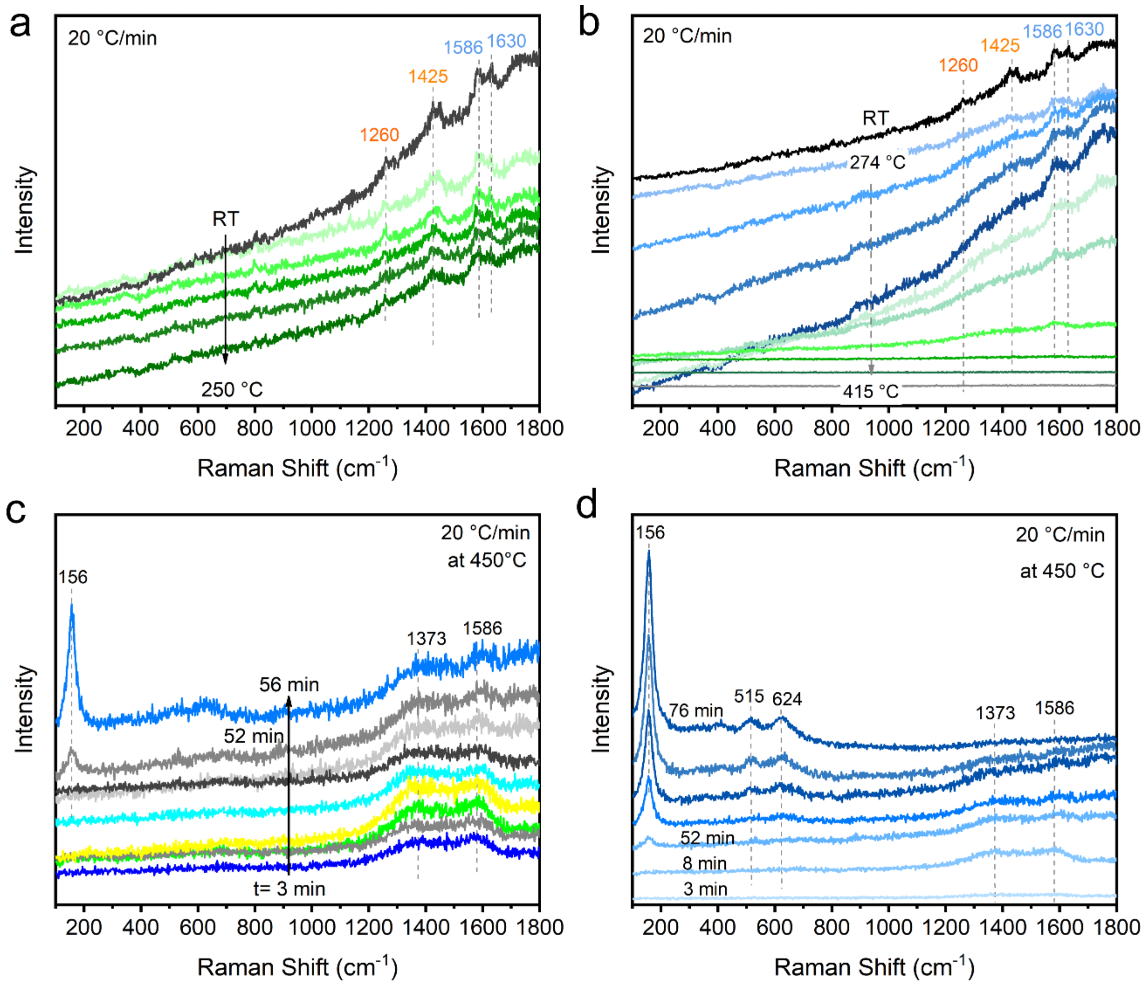

Figure 4-45 Raman spectra of temperature-programmed Raman measurements: (a) spectra recorded from room temperature to 250 °C; (b) spectra recorded from 274 °C to 415 °C; (c) spectra recorded at 450 °C, dwell time varies from 3 min to 56 min; (d) spectra recorded at 450 °C, dwell time varies from 3 min to 76 min

Figure 4-45(a) records the change of Raman spectra from room temperature untill 250 °C. There are mainly four shifts observed in NH_2-MIL-125-Ti. The peaks at 1260 cm^{-1} and 1425 cm^{-1} are related to the bending and symmetric stretching of the framework Ti-O-Ti-O octamic ring species.[82, 196] The peaks at 1586 cm^{-1} and 1630 cm^{-1} corresponds to the C-C and N-H bond bending vibrations of the organic linker.[82, 196] The presence of these peaks are indicative of the –COOH group from the organic ligand being connected to the Ti-oxo cluster. It can be seen that the characteristic Raman peaks of NH_2-MIL-125-Ti were preserved till 250 °C, in good agreement with the in-situ XRD results. Then with temperature further increasing, the MOF structure was damaged as the Raman peaks, 1260 cm^{-1} and 1425 cm^{-1}, which represents the coordination between the Ti-oxo cluster and the organic ligand started to diminish from 275 °C. On the other hand, the characteristic peaks of the organic ligands (1596 cm^{-1} and 1630 cm^{-1}) were still distinguishable till 310 °C. Therefore, it can be assumed that that the decomposition of MOF structure started with the 'break-down' of the coordination bond between the metal cluster and the organic ligands. When the temperature reached 415 °C (Figure 4-45), the characteristic peaks of NH_2-MIL could be barely seen, implying an amorphous state of sample.

Two peaks at 1373 cm^{-1} and 1586 cm^{-1} (Figure 4-45(c)) were observed at 450 °C, which can be ascribed to the D band and G band of graphitic carbon[197], suggesting the evolution of organic ligand into carbon species. In general, the Raman spectrum of graphite exhibits a 'G band' at 1580 cm^{-1} and a 'D band' at 1350 cm^{-1}.[198] Therefore, compared with the standard band position, both D and G observed in Figure 4-45 demonstrated a blue shift as well as peak broadening, which can be attributed to the oxidation of graphite, investigated in the work of Nanda *et al.*[198]. With the increasing of dwell time at 450 °C, the intensities of the D and G bands decreased, as illustrated in Figure 4-45(c), which can be explained by the oxidation of the carbon species. The characteristic peak of anatase at 154 cm^{-1} appeared after 52 min dwelling at 450 °C. Further prolonging the dwell time (Figure 4-45(d)), the intensity of anatase peak got intensified as the other anatase bands at 403 cm^{-1}, 511 cm^{-1} and 626 cm^{-1} can also be distinguished; while the peaks representative for graphitic carbon disappeared (t = 76 min).

Based on the Raman spectra, the thermal decomposition of NH_2-MIL-125-Ti can be summarized as MOF → amorphous state → anatase; meanwhile the organic species experienced graphitization and oxidation. The time required to obtain organic component-free TiO_2 is ≥ 76 min, which fits the results of isotherm-TGA. Though, with a 20 °C/min ramp rate, the MOF decomposition process exhibited in Raman resembles to that observed in in-situ XRD with lower ramp rate (1°C/min or 10 °C/min). For now, I attribute this difference to the different air supply.

Moreover, the Raman results confirmed the presence of carbon species, which supports the previous assumption that the TiO_2 crystallites are likely to be surrounded by the organic residue during the decomposition process.

b) Raman Laser – induced Thermal Decomposition of MOFs

In fact, NH_2-MIL-125-Ti is vulnerable to laser beam during Raman measurement, as can be seen in Figure 4-46(a).

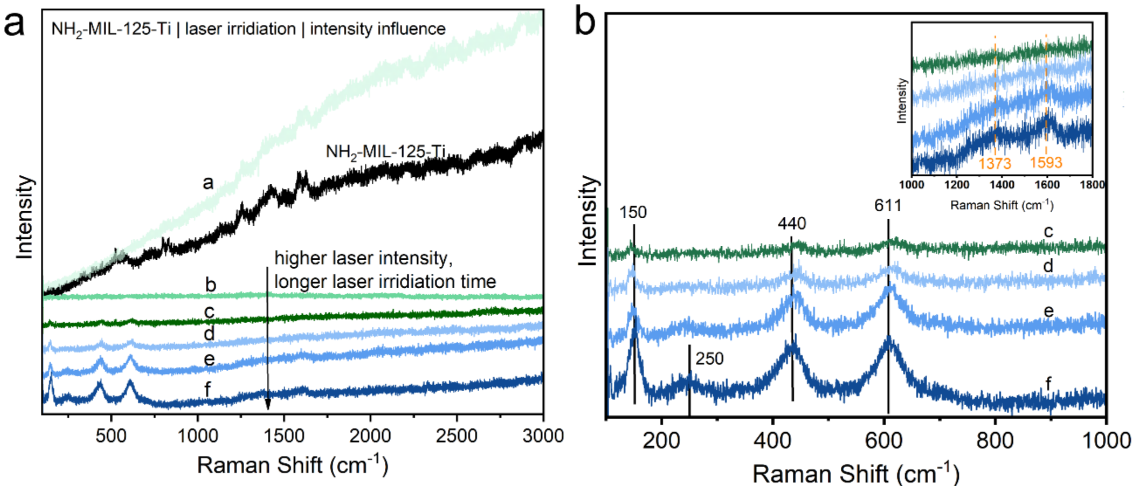

Figure 4-46 a) A summary and b) Enlarged view of the spectra obtained from the same spot of the sample under laser irradiation. Spectra a - b: laser power was fixed, 0.5 mW, the irradiation time was 10 min and 30 min, respectively. Spectra c - f: laser power was increased: spectrum c was collected after b, with laser power of 5 mW; spectra d, e, f were collected in sequence, with laser power being 12.5 mW, 25 mW and 50 mW, respectively. Plot in black, the original spectra of NH_2-MIL-125-Ti;

The MOF spectra (Figure 4-46(a), black) were measured with 0.5 mW green laser (532 nm), correlating to 1 % power output of the laser source. The characteristic peaks of NH_2-MIL-125-Ti were observed, confirming the MOF structure. The laser was irradiated onto the same spot of the MOF sample, and with increasing time (Figure 4-46, plot a → c), MOF became amorphous, with no bands being detected. Plot 'c' is the Raman spectra collected after 30 min of laser irradiation. This MOF → amorphous state transformation is nothing special, as it has been observed both with in-situ XRD and temperature-programmed Raman, which can be ascribed to the energy provided by the incident laser beam to the MOF powders, namely, simulating a thermal treatment/calcination process[79].

However, when the laser intensity was increased (plot c→f), the phase transformation demonstrated different features from the typical calcination process.

First, the phase of the obtained TiO_2 varied from the obtained anatase in Figure 4-45(b). The Raman shifts at 150, 250, 440, and 611 cm^{-1} can be ascribed to the rutile phase[199], while with temperature-programmed Raman, anatase was obtained.

Second, the inset in Figure 4-45(b) showed that the D and G bands did not appear when rutile crystallized (Figure 4-45(b), plot c), instead, it showed up with the increasing laser as well as the increasing crystallinity of rutile (Figure 4-45(b), plot f). Therefore, in this case, the crystallization of rutile occurred before the graphitization of organic species, which is in contrary to the previous conclusion with Figure 4-45(c).

However, with these two sets Raman spectra, the consistency between Raman results and the in-situ XRD results has been obtained.

4.4.2 Conclusion and Outlook

a) Conclusion

With various in-situ techniques, I have investigated the thermal decomposition of NH_2-MIL-125-Ti. Albeit the different equipment conditions, the thermal decomposition starts with the 'break-down' of the coordination bond between the metal cluster and the organic ligand.

The metal cluster then crystallized to metal oxide, while the decomposition of organic ligand is accompanied by the graphitization. These two processes are influenced by various parameters, such as ramp rate and the oxygen supply.

It can be further proposed that with high power input to the thermal decomposition system (such as high ramp rate, high laser intensity), the Ti-oxo cluster tends to crystallize into rutile, and the graphitization of organic ligand is likely to lag behind this process. Therefore, within certain time/temperature regime, the TiO_2 crystallites are surrounded by carbon species, which hinder the crystal growth process.

On the other hand, with steady/low power input, the graphitization of organic species will be initiated earlier, then accompanied by the crystallization of Ti-oxo cluster to the anatase, as in the case of low ramp rate in-situ XRD and temperature-programmed Raman.

Another factor that may influence the thermal decomposition process is the oxygen supply. For the moment, I speculate that it is related to the discretion of 'uneven' energy input, which needs further confirmation.

b) Outlook

First, the hypothesis that titanium crystallites under certain conditions are surrounded by carbon species needs to be confirmed, which can be realized by TEM-EDX, assisted with materials etching.

A fixed air supply for the convenience of comparison between different in-situ technique is recommended.

5 Perovskite Solar Cells

5.1 Theoretical Background of Perovskite Solar Cells (PSCs)

Just a few years ago, in 2009,[200] saw the introduction of a new generation of photovoltaic devices, perovskite solar cells (PSCs),[201] which are based on hybrid organic-inorganic perovskites; later referred to as perovskite. Recently, the certified power conversion efficiency (PCE) has reached 22.1 % in 0.028 cm^2 single PSC and the conversion efficiency of 1 cm^2 perovskite-silicon tandem solar cell has reached 27.3 %, which made it a world record in June 2018[202] and demonstrates great potential for commercialization. Perovskites are the main component of this new type of photovoltaics (PV), wherein they work as both, light absorber and charge generator.

Perovskites refer to a class of materials that resemble the crystal structure of calcium titanate, with a general formula of ABX_3 (with A = Ca, B = Ti, X = O). The first HOIP has been reported in 1978 by Weber.[203] However, it was untill 1991 that HOIP was introduced to the photovoltaic field by Miyasaka.[200] The crystal structure of HOIP is illustrated in Figure 5-1. For the inorganic-organic perovskite used in PSCs, the 'A' sites are occupied by organic cations, such as methylammonium ions (MA^+) or formamidinium ions (FA^+), while the 'B' sites are usually divalent cations, such as Pb^{2+}, Sn^{2+}, and Bi^{2+}. 'X' sites can be different halogenides, e.g. Cl^-, Br^- or I^-.

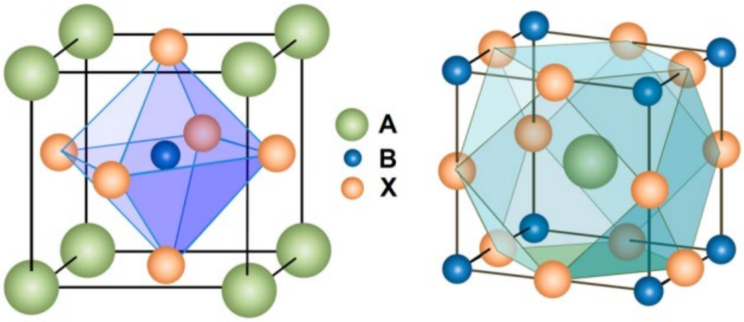

Figure 5-1 ABX_3 perovskite structure showing (left) BX_6 octahedral and (right) AX_{12} cuboctahedral geometry. In organic-inorganic hybrid perovskite, alkali atoms occupying the A sites, Pb atoms occupying the B sites, and halogen atoms occupying the X sites.[204]

The structure and properties of HOIP bare certain tunability, realized by the choice of different ions for the lattice sites. For instance, the electronic band gap, as well as the light absorption property, can be easily tuned by the size of the ionic radius. $MAPbI_3$ has a smaller band gap than $MAPbBr_3$ (1.55 eV vs 2.3 eV)[205] due to a change in the volume of the crystal unit as well as the electronegativity. This tunability in composition and structure is favorable for the materials design. Recently, a variety of new HOIP has been developed, with bi- or tri-cations, such as $FAMAPbI_3$, CsFAMAPbIBr.[201]

Figure 5-2 illustrates the band structure of a typical PSC composed of electrodes, an electron transporting layer (ETL), perovskite layer and hole transporting layer (HTL). The band gap of perovskites used in PSC is usually in the range of 1.5 eV- 2.5 eV. Under light irradiation, the electrons in the valence band absorb light with a photonic energy higher than the E_g and form excitons. The binding energy of excitons is very low, around 0.03 eV[192, 206], which means that the excitons can dissociate into free carriers at room temperature. Therefore, the photogenerated electrons jump into the conduction band of perovskite, leaving a hole behind. The separated electrons and holes then transfer to the ETL and HTL, respectively, due to the band alignment.

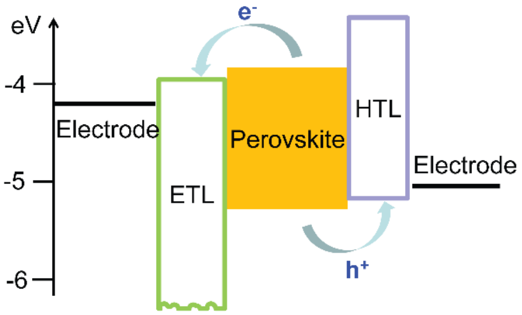

Figure 5-2 Schematic Illustration of PSCs

As an ambipolar material, the perovskite can transport both electrons and holes, thus it can serve not only as a light absorbing layer but also an electron and hole transporting layer. Therefore, the ETL and HTL are optional in the solar cell configuration.

5.2 Handbook for the Fabrication of PSCs

As PSC constituted an entirely new research field, both for me and for our research group, I first started my PSC project with the basic solar cell fabrication. I have fabricated PSCs from the very beginning, with the preparation of substrates, till the doctor-balding of the counter electrode, and have varied a range of parameters to identify the best PSC under current lab conditions. In this section, I will present only the optimized procedure for cell fabrication under current lab conditions.

5.2.1 Typical Perovskite Solar Cell Configurations

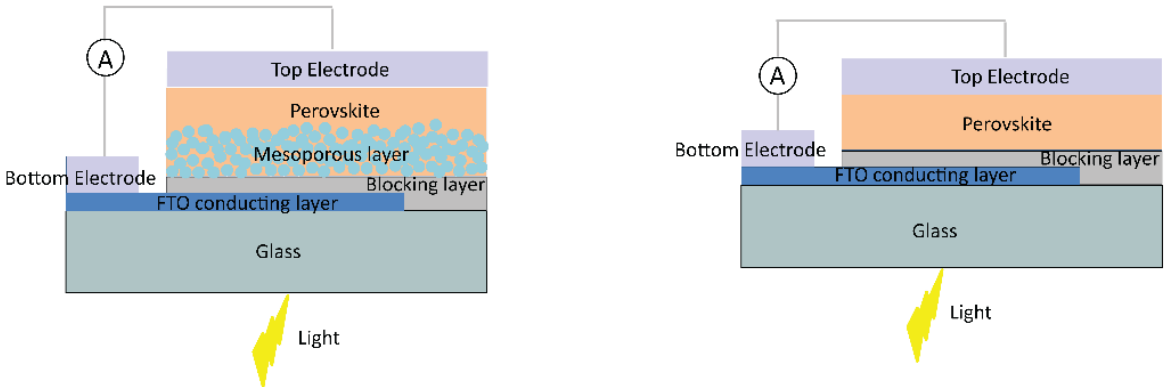

Figure 5-3 Two Typical Configuration of PSCs (left) mesoscopic perovskite solar cell; (right) planar-type perovskite solar cell).

A working PSC can be generally classified into two categories, mesoscopic type[207-208] and planar type[209-210] as illustrated in Figure 5-3. Both PSCs are built on the transparent fluorine-doped tin oxide (FTO) glass with a hole blocking layer (bl-layer), usually TiO_2. In the mesoscopic type, a mesoscopic layer (meso-layer) consisting of a metal oxide is deposited on-top of the hole-blocking layer and acts as a scaffold for the subsequent perovskite deposition. Ideally, the perovskite penetrates the meso-layer and additionally forms an overlayer, as illustrated in Figure 5-3(a). In most cases, the metal oxide of the mesoscopic layer acts also as the electron transporting material (ETM) and contributes to the electron extraction and transportation process in the PSCs. In contrast, in the planar type, the perovskite layer is deposited onto the hole-blocking layer directly. Thus, compared with the planar type, the mesoscopic type has a smaller hysteresis in cells' photovoltaic performances[206, 211]. However, there are also drawbacks of the mesoscopic type PSCs. For example, the currently most popular ETM, TiO_2, has a rather low conductivity and electron mobility, which is unfavorable for electron transportation and limits the pursuit of higher power conversion efficiency[212].

As perovskites can transport both electron and holes, and the carrier mobility for the hole is much higher than that for the electron, 12.5 ~ 66 $cm^2V^{-1}s^{-1}$ vs. 7.5 $cm^2V^{-1}s^{-1}$,[213] the hole transporting layer (HTL) in PSCs is not really required anymore. Moreover, the deposition of most HTL materials (such as spiro-OMeTAD) needs to be conducted within N_2 glovebox, therefore, most PSCs have been fabricated without HTL in this thesis. Finally, a top electrode (either Ag or Conductive carbon) is deposited to complete the working circuit.

5.2.2 Substrate Preparation

In this work, all PSCs have been prepared on FTO glass sheets (15 mm * 20 mm), which act as a transparent substrate and electron collector. The washing procedure of FTO is crucial, as impurities can undermine the subsequent deposition process, as well as the electron collection process. Hence, I developed a washing procedure that starts with brushing the glass sheet with a washing reagent. After rinsing with water, the glass sheets were subjected to sonication in a mixture of ethanol (EtOH), acetone and distilled water (v:v:v=1:1:1) for 30 min. After that, the glass sheets were sonicated for another 30 min in isopropanol (IPA). In the end, they were rinsed with fresh IPA and purged with compressed air/N_2.

5.2.2.1 Blocking layer Preparation

With a suitable band structure and electron mobility, TiO_2 has been widely used as both bl-layer (blocking layer) and mp-layer (mesoporous layer) in PSC. I have also utilized TiO_2 as bl and mp material in my PSCs. Titanium alkoxides were used as metal precursor and first spin-coated onto FTO sheets and then crystallized into TiO_2 through hydrolysis and subsequent calcination. The precursor solution was prepared as below:

Solution *A* was prepared by adding 254 μL Titanium diisopropoxide bis(acetylacetonate) (75 wt % in isopropanol) (Sigma Aldrich, CAS:17927-72-9) into 1690 μL absolute EtOH and stirred for 2 min. Solution *B* was prepared by mixing 34 μL 2M HCl with another 1690 μL absolute EtOH and stirred also for 2 min.

After both solutions were ready, solution *B* was added dropwise to solution *A* under stirring. The mixture was stirred for another 5 to 10 min, then occasionally formed large agglomerates were separated by filtration, using a 0.45 μm PTFE filter, resulting in a transparent solution that is used as the precursor. To further avoid precipitates, solution A can be placed in an ice bath. When not in use, the stock solution should be kept in the fridge.

The spin-coating process determines the thickness of bl-layer. In the optimal spin-coating procedure that I have defined, 35 μL precursor was used for one FTO piece, and the bl-layer was deposited via a dynamic dispense, in which the FTO first started spinning and reached 2000 rpm, then the bl-precursor was dispensed into the center of the substrates. The FTO rotated at 2000 rpm for 40 s. After the deposition, the film was annealed in muffle oven. To obtain a homogeneous thin layer, a multi-step heating program was utilized (Figure 5-4). After 500 °C calcination, a device with ~ 50 nm TiO_2 (anatase) bl-layer was obtained.

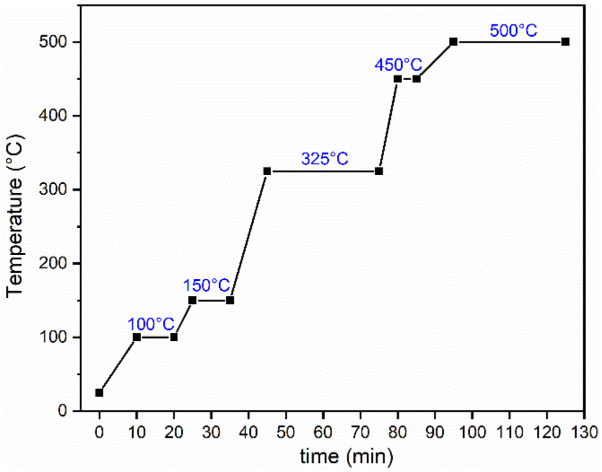

Figure 5-4 Temperature Program for the calcination of blocing layer

After calcination, the FTO piece with ~ 50 nm TiO_2 (anatase) bl-layer was obtained.

5.2.2.2 Mesoporous layer Preparation

The next step was the deposition of the mesoporous layer, which was prepared by spin-coating a nanoparticular metal oxide paste onto the bl-substrate prepared in Section

5.2.2.1. The typical material for meso-layer is also TiO_2, and the TiO_2 paste can be either purchased or home-made according to the procedure reported elsewhere[214].

In short, an ethyl cellulose (EC) powder was dissolved in EtOH to yield a 10 wt% solution. Then 20 g of this solution were added to a round-bottomed flask containing a mixture of 4 g TiO_2 and 16.2 g α-terpineol. The resulting suspension was diluted with ethanol to a total volume of 70 mL. The mixture was then sonicated with a sonication horn for 3 times each 3 min. Most of ethanol was later removed by rotary-evaporator to yield a paste that is composed of 18 wt % TiO_2, 9 wt % EC and 73 wt % α-terpineol. The paste was then diluted with EtOH (v:v = 1:5) and stirred overnight to achieve a homogeneous and stable dispersion.

A static dispense was applied for the meso-layer spin-coating, in which the paste was first spread over the bl substrate. After spin-coating, the substrates were calcined in muffle oven to remove EC and α-terpineol, as well to form the network of TiO_2 nanoparticles. The calcination program is illustrated in Figure 5-5; it is a step-by-step heating program, which aims to hinder the formation of cracks in the film.

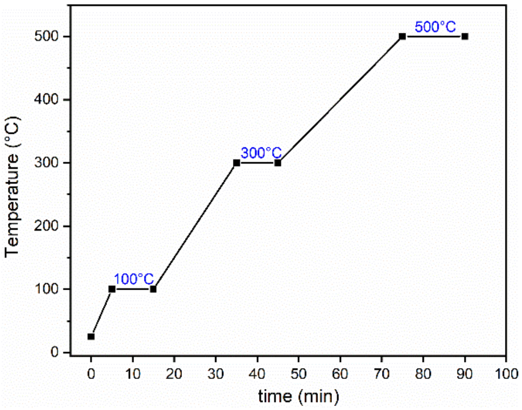

Figure 5-5 Temperature Program for the calcination of Mesoporous layer

In this work, I tested three precursors as a starting material for the TiO_2 paste, i.e. pure anatase and rutile nanoparticles as well as the commercial mixture P25. Anatase and rutile were both less efficient than P25, hence I focused on P25 in the following experiments.

Figure 5-6 demonstrates the porous morphology of the prepared mesoporous layers. The thickness of the film can be tuned with different spin-coating parameters. For example, the film in Figure 5-6(a) was spin-coated at 2000 rpm and had a thickness of 1.2 µm, while Figure 5-6(b) was the spin-coated at 5000 rpm, which reduced the thickness by 75% down to 0.3 µm.

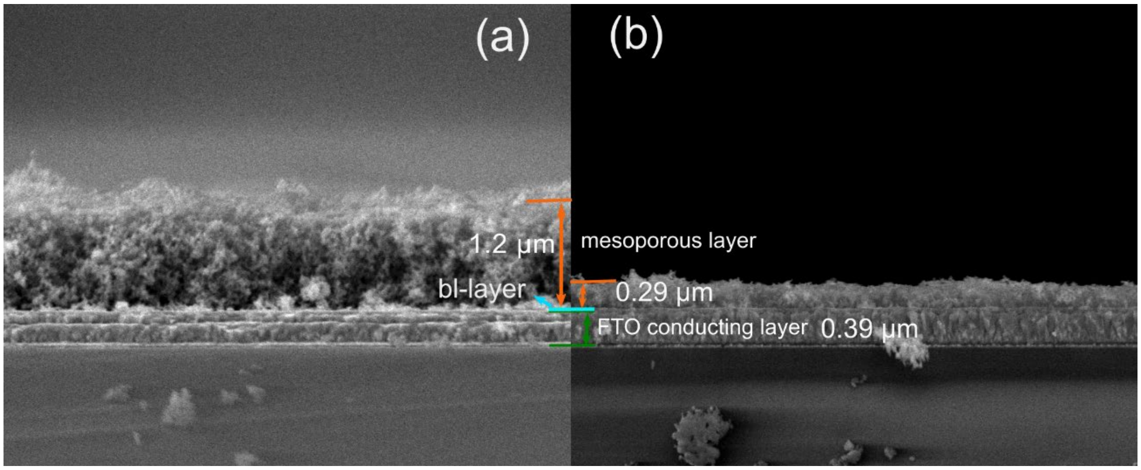

Figure 5-6 SEM observation of mesoporous layer spin-coated on FTO

5.2.3 PVK Liquid-phase preparation: Spin-coating

After substrates preparation, the next step is PVK layer deposition. If the substrates are not freshly prepared, a pre-treatment at 150 °C for 10-15 min before PVK preparation is recommended to remove the moisture.

There are different strategies for PVK preparation, including vapor, liquid, and vapor-liquid combined route. I have opted for liquid-phase preparation in this work and compared two general PVK deposition routes: one-step spin coating and two-step spin coating.

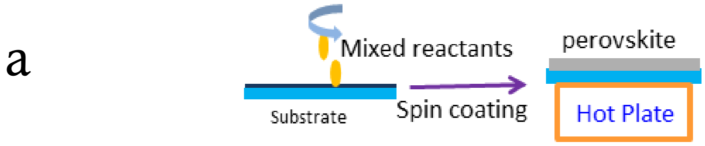

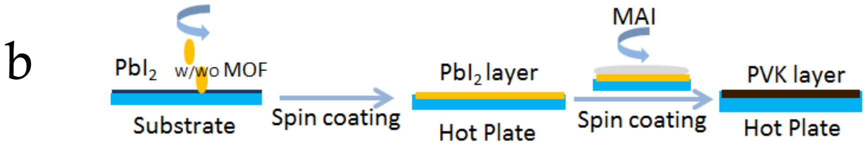

Figure 5-7 PVK spin-coating procedure

As has been mentioned before, the organic-inorganic perovskite used for PSCs can be tuned through the organic cations (e.g. MA, FA, or their mixtures), the metal cations (e.g. Pb^{2+}, $Sn^{2+,}$ and Bi^{2+}), and the halide ions (e.g. I^-, Br^-, Cl^-). In this work I focused on methylammonium lead iodide, $MAPbI_3$.

a) One-step PVK spin coating

To prepare $MAPbI_3$ film with one-step spin coating, the precursor was first prepared in DMF. Methylammonium iodide (MAI) and PbI_2 with stoichiometric ratio were dissolved into DMF, reaching a final concentration of 40 wt%. Then the precursor was spin-coated onto the substrates. The optimal spinning coating parameter is: for each FTO sheet (1.0 cm * 1.5 cm), 38 μL PVK precursor was used for spin coating. A dynamic dispense process was applied, the spinning speed was 2000 rpm, for 40 s. After deposition, the film was first dried at 40 °C for 10 min, then at 100 °C for another 5 min.

b) Two-step PVK spin coating

For the two-step PVK spin coating, PbI_2 and MAI solution were prepared separately. As can be seen in the illustration, PbI_2 layer was first spin-coated onto the substrates, and then the organic part was 'provided' by spin-coating or immersion. With an annealing process, the solvent evaporated away and black perovskite crystallized.

The PV tests showed that the best spin coating procedure with the highest PCE output was: 1.0 M PbI_2 in DMF solution was first prepared, then for 1.0 cm * 1.5 cm FTO sheet, 38 μL PbI_2 was spin-coated with a dynamic dispense at 7000 rpm. The rotating time was 20 s. After spin coating, DMF was evaporated by heating the FTO sheets at 100 °C hot plate for 5 min. After drying, yellow PbI_2 was obtained. The PbI_2 film was cooled down to room temperature and then subjected to the 2nd step spin coating. 300 μL MAI in IPA solution (8 $mg \cdot mL^{-1}$) was spin-coated onto each PbI_2 layer. Note that I waited for 40s before adding the MAI solution onto the PbI_2 layer upon starting the rotation process at

2000 rpm for 45 s. After that, FTO sheets were again heat-treated at 100 °C, for another 5 min. During the heat treatment process, the color of the film from red-brown turned into black PVK film.

5.2.4 PSC fabrication

Table 5-1 Perovskite Solar Cells based on Different Preparation Procedure

	bl- substrate	bl + meso- substrate
One-step PVK spin-coating	B1	M1
Two-step PVK spin-coating	B2	M2

Based on the combination of different substrates and PVK spin-coating procedure, four PSC configurations have been prepared in this work and summarized in Table 5-1. For instance, PSC type - ‘B1' means the PVK layer is spin-coated with the one-step procedure on blocking layer substrate, while in ‘M2' type, PVK layer is prepared with two-step spin-coating and the substrate is ‘M’ type.

In the end, the counter electrode of carbon (JELCON CH-8 carbon ink, sheet resistance 10 $\Omega \cdot cm^{-1}$, JUJO Printing Supplies & Technology (Pinghu) Co., Ltd., China) was fabricated by a blade-coating method on top of the PVK film. Then the carbon electrode was dried in a vacuum oven at 45 °C for 3 h. After that, the HTL-free PSC was obtained.

5.3 Incorporation of NH_2-MIL-125-Ti into PSC as Electron Transporting Material

In previous section, the difference between the PSC configurations, planar type and mesoscopic type have been discussed. One problem about the mesoscopic type PSC is the choice of the material. For instance, the widely used TiO_2, there are many defects such as oxygen vacancies and metal interstitials at the surface and grain boundaries of TiO_2, which can act as charge traps and hinder the cell's performance[215-216]. Various work has been done with electron transporting material (ETM) to obtain high-efficiency perovskite solar cells, such as incorporating graphene with TiO_2[217], using [6,6]-phenyl-C_{61}-butyric acid methyl ester to passivate the TiO_2 surface[218] and using SnO_2 to substitute TiO_2[219]. Another big issue about typical mesoscopic type PSCs is the high calcination temperature (around 500 °C) needed to prepare the mesoscopic layer, which not only hinders the processibility of the devices but also limits the application of organic electrodes in PSCs. Therefore, searching for new ETM with lower fabrication temperature has always been a hot topic.

The working mechanism of ETM in a PSC is based on the match of the conduction bands between perovskite and ETM. Based on Figure 5-2, to ensure the photo-generated electrons transportation from perovskite to ETM, the conduction band of perovskite must be higher than ETM. However, the larger band difference between the two will lead to the decrease of the cells' open circuit voltage (V_{oc}). Thus to obtain a higher V_{oc}, the conduction band of ETM should lie right below that of perovskite. As discussed in Chapter 1.3, the conduction band of NH_2-MIL-125-Ti lies around 4.0 eV, which matches the conduction band of most photovoltaic perovskites,[220-221] thus makes it a theoretically applicable ETM in PSC. In addition, the microporous structure of MOF particles may favour the diffusion of the PVK into the particle, resulting a decreased charge diffusion pathway. Therefore, I applied NH_2-MIL-125-Ti as a new ETM for PSC.

To solve the issue of the high fabrication temperature for typical mesoscopic electron transporting layer, in this work, I introduced a new strategy to incorporate the NH_2-MIL-125-Ti into the perovskite layer. With this new strategy, I have prepared the ETM layer with less than 150 °C, which could be further extended to other organic flexible substrates and multi-junction devices.

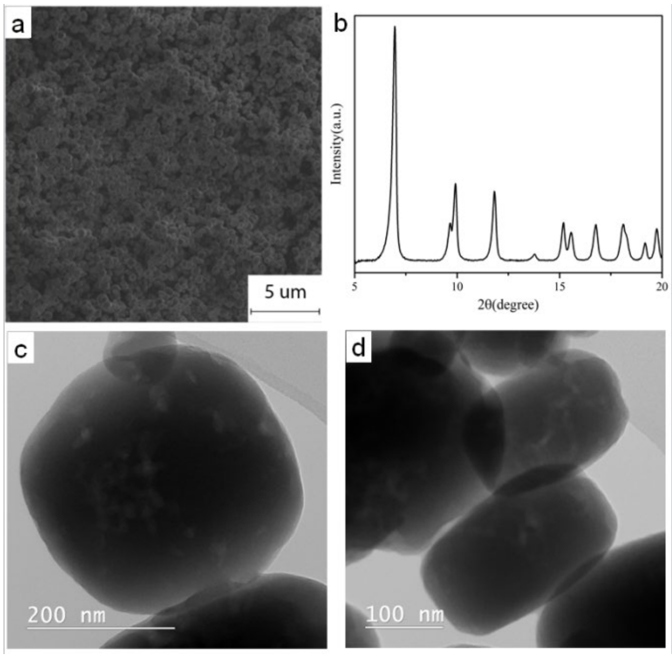

Figure 5-8 SEM, XRD and TEM results of NH_2-MIL-125-Ti

Figure 5-8 shows the morphology and crystallinity of the NH_2-MIL-125-Ti used as ETM in this work; the preparation details and more characterizations can refer to Chapter 4.1.1.

Methylamine lead iodide ($MAPbI_3$) was prepared via a two-step spin-coating. Lead iodide (PbI_2) was first spin-coated onto the substrates, and then the methylamine iodide (MAI) was spin-coated above the PbI_2 layer. After evaporation of the solvent, $MAPbI_3$ perovskite (PVK) film was obtained.

To prepare Ti-MOF PVK film, Ti-MOF powders were mixed with PbI_2 solution in the first spin-coating step. Instead of the typical mesoporous layer preparation which requires high temperature calcination (450 – 500 °C), Ti-MOF was incorporated into perovskite film with a simple mixing process. To demonstrate the effect of the Ti-MOF on the photovoltaic performance of the perovskite solar cell, different concentrations of MOF powders have been investigated. The mass ratio of Ti-MOF to perovskite was varied from 0 wt% to 10 wt%. The corresponding films were named as 10% MOF PVK, for instance.

Figure 5-9 FTO sheets after spin coating of different layers. a) Substrate: FTO+ bl-layer; b) After PbI_2 deposition; c) After spin coating of MAI, black PVK layer forms.

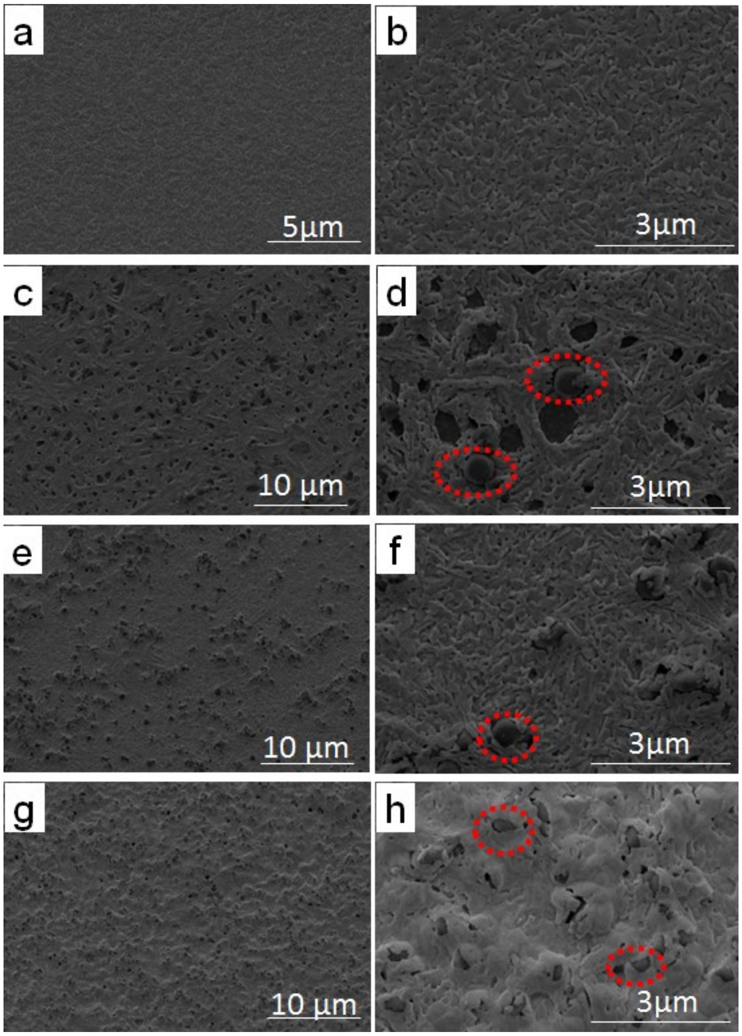

Figure 5-10 SEM images of PbI_2 layers with a) and b) 0% MOF addition; c) and d) 2% MOF addition; e) and f) 5% MOF addition; g) and h) 10% MOF addition at various magnifications.

The morphology of the prepared PbI_2 and PVK films are summarized in Figure 5-10 and Figure 5-11.

Pristine PbI_2 layer is composed of layered particles and covers the substrate uniformly. The incorporation of MOF powders can be clearly detected in SEM (Figure 5-10, inside the red circle). At lower incorporation concentration, 2 % and 5 %, it seems that the PbI_2 layer is not influenced by the guest species – MOF powders, as the morphology of the film resembles that of 0% MOF PbI_2, composing of layered-like particles. However, with 10 % MOF incorporation, the impact of MOF on the crystallization of PbI_2 is not negligible anymore, as the PbI_2 film has a more integrated morphology rather than distinctive layered-like particles.

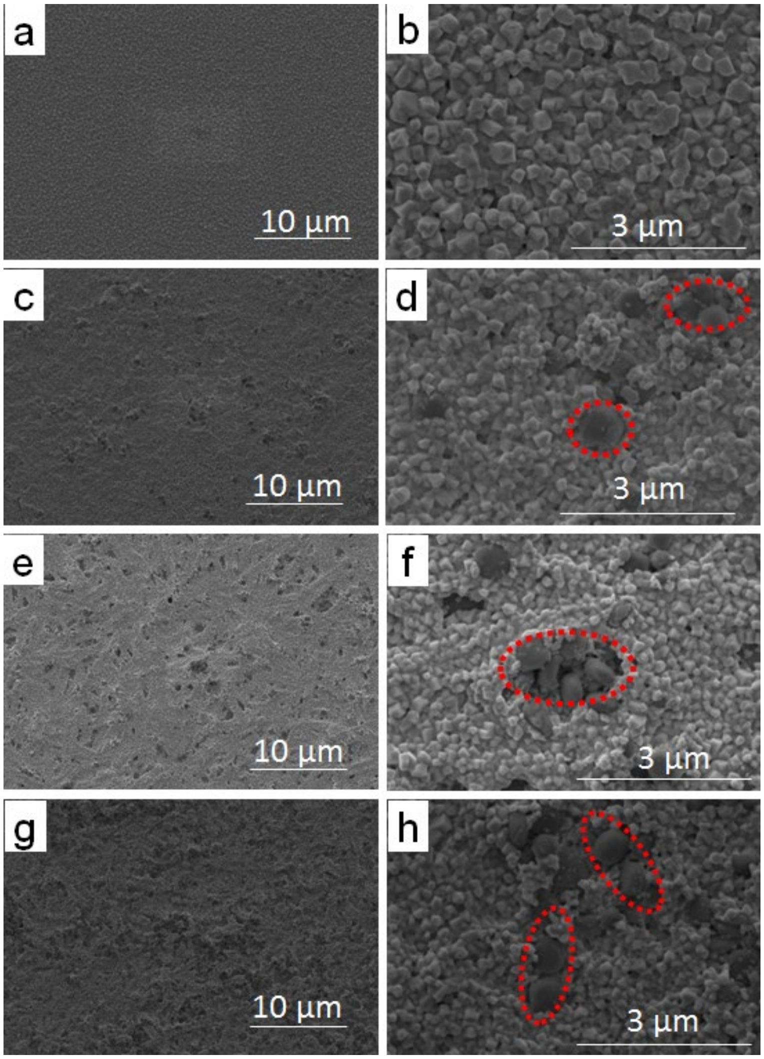

Figure 5-11 SEM images of PVK layers with a) and b) 0% MOF addition; c) and d) 2% MOF addition; e) and f) 5% MOF addition; g) and h) 10% MOF addition at various magnifications.

Figure 5-11 displays the morphology of the PVK film, after the 2nd time spin-coating. It can be seen that the pristine 0 % MOF film is composed of cubic perovskite particles in the range of 200 – 300 nm. For 2 %, 5 % and 10 % MOF PVK films (Figure 5-11, (c) - (h)), with the increase of MOF addition concentration, the perovskite particles size decreases slightly. The Ti-MOF particles can still be observed in the top view, surrounded by perovskite particles (Figure 5-16, red circle).

To elaborate the influence of the MOF powders on the perovskite film, DRS and XRD measurements of the films have been conducted. Figure 5-12(a) and (b) display the light absorption properties of the FTO substrate, the PbI_2 layer and the PVK layer. Compared the absorption properties of 0 % MOF PVK, the addition of MOF shifts the absorption edge to a longer wavelength and increase the absorbance as well, which is expected to contribute to a more efficient charge generation process.

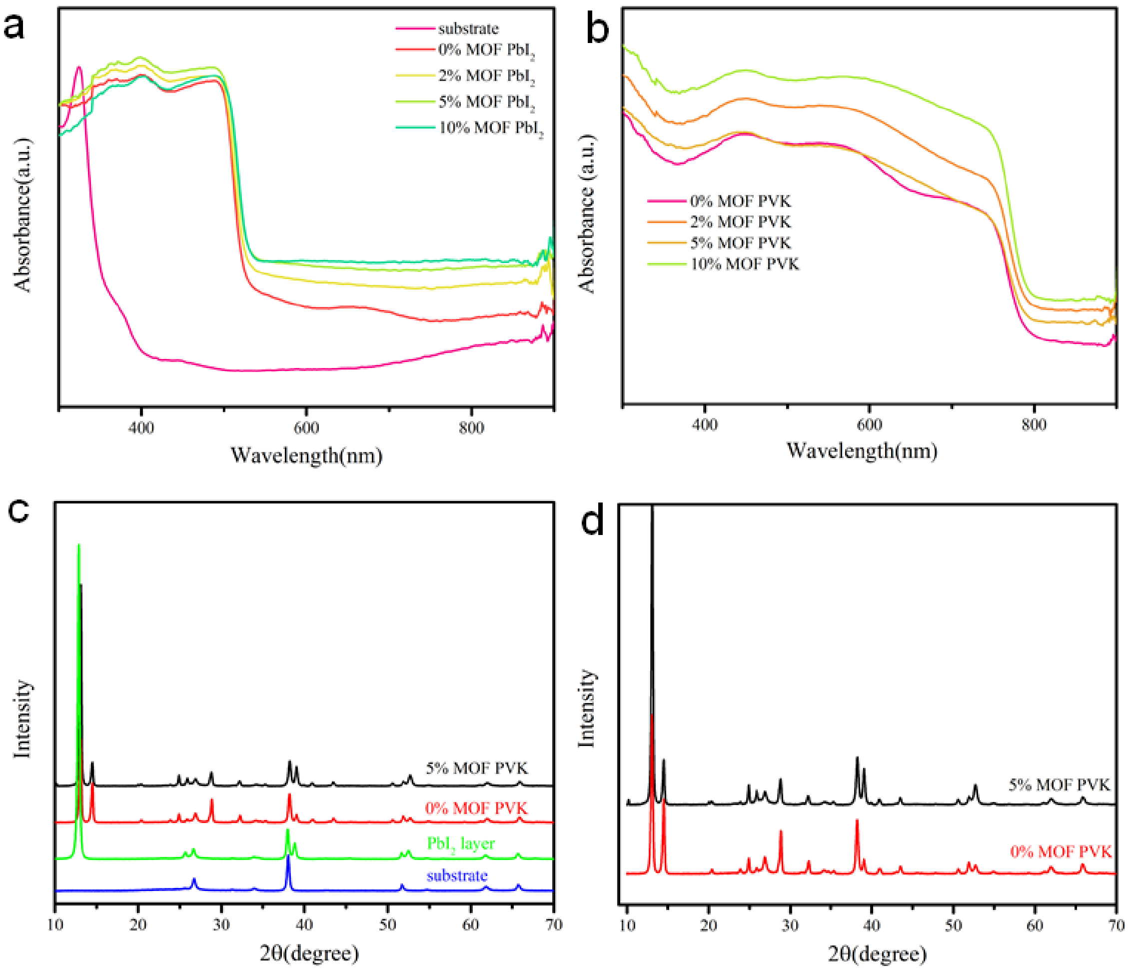

Figure 5-12 a) and b) UV-Vis absorbance; c) and d) XRD patterns of of PbI_2 and PVK films with different Ti-MOF incorporation

Figure 5-12(c) confirms the existence of perovskite in both 0 % MOF PVK and 5% MOF PVK. Moreover, the XRD patterns indicate that PbI_2 did not converted into PVK completely, as the diffraction peaks corresponding to PbI_2 can be clearly seen in both

PVK films. Figure 5-12(d) further compares the XRD patterns to trace the incorporated MOF powders. However, there is no additional peaks appeared in sample 5 % MOF PVK which can be attributed to NH_2-MIL-125-Ti (Figure 5-8(b)). As the MOF powders have been clearly detected with SEM, the absence of MOF in XRD can be attributed to the low incorporation of MOF powders in the film, as well as to the MOF character that the diffraction peak intensities are pretty low at $2\theta > 10°$.

After the formation of the perovskite film, carbon paste was used as the counter electrode. The photovoltaic performance of the fabricated solar cells was measured under 100 mW/cm^2 simulated solar light with working area of 0.01 cm^2. The short circuit density (J_{sc}) and open circuit voltage (V_{oc}) of prepared PSCs are summarized in Figure 5-13.

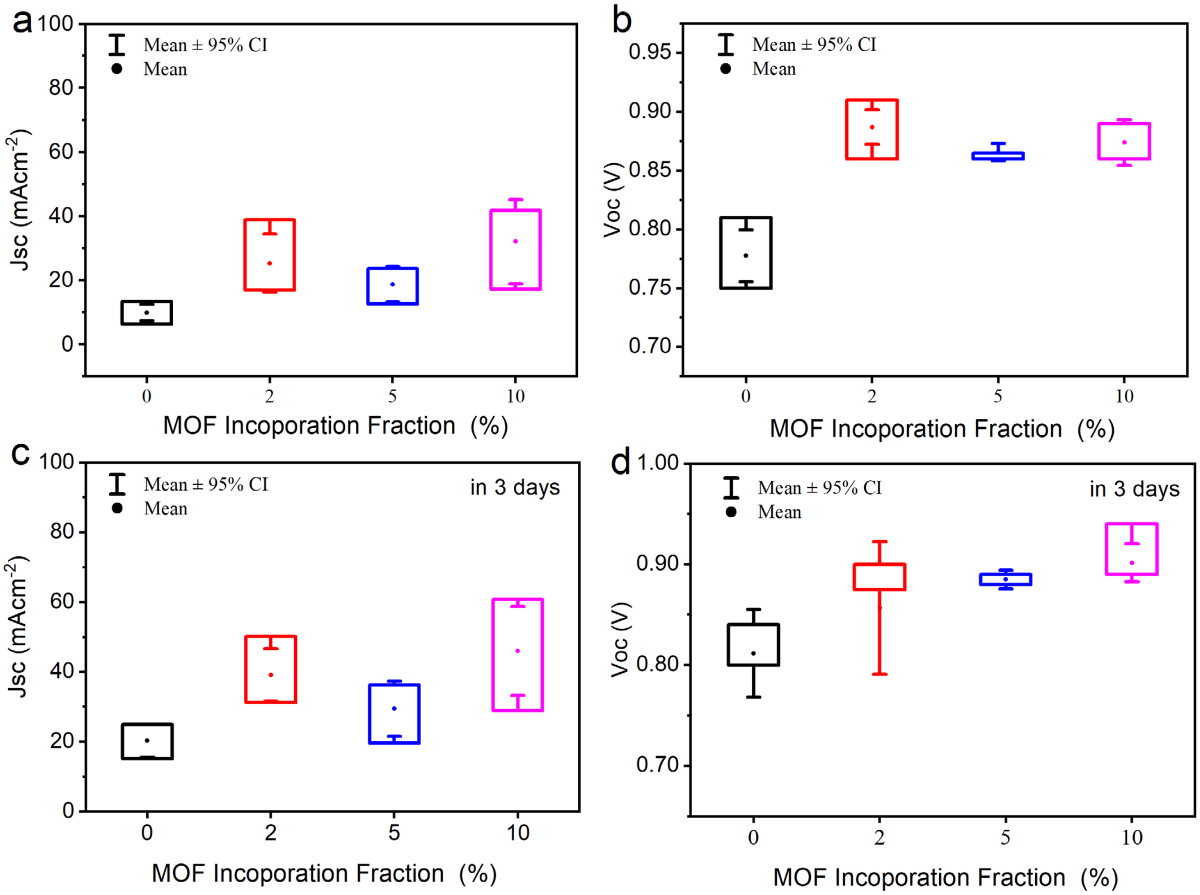

Figure 5-13 a) Short circuit density and b) open circuit voltage of prepared PSCs, with respect to different MOF incorporation fraction, measured right after fabrication; c) short circuit density and d) open circuit voltage of MOF incorporated PSCs, after 3 days in air.

It can be concluded from Figure 5-13 that after the incorporation of Ti-MOF into perovskite layer, the V_{oc} of MOF-PVK cells increased slightly, with 5 % MOF film having the highest V_{oc}. However, the J_{sc} changed more dramatically. The J_{sc} values of different films are 5 % MOF PVK>10 % MOF PVK >2 % MOF PVK >0 % MOF PVK, which is in agreement with the power conversion efficiency (PCE) output. All the MOF-incorporated samples show better performance than reference perovskite film

As to the higher V_{oc} of the Ti-MOF solar cells, this can be explained with the closer bandgap position between the $MAPbI_3$ and Ti-MOF. The working flow inside a perovskite solar cell highly depends on the alignment of band structure between different opponents. Thus, compared with 0 % MOF sample, in 2 % MOF, 5 % MOF and 10 % MOF addition samples, the existence of Ti-MOF modified the interface between the perovskite and the substrate. V_{oc} in the perovskite solar cell is related with the band difference between different opponents. Thus the better band match between the conduction band of perovskite and the conduction band of Ti-MOF decreased the V_{oc} loss and output a higher Voc. Moreover, with the bandgap matching, the photo-generated charge carriers in perovskite, here means electrons can easily jumps to the conduction band of Ti-MOF, which favours the electron abstraction and transportation process, preventing the charge recombination.

Moreover, the stability of the perovskite solar cells with the incorporation of MOFs was investigated (Figure 5-13).

In summary, with the simple mixing strategy, Ti-MOF (NH_2-MIL-125-Ti) was for the first time incorporated into PSCs with less than 100 °C. Current-Voltage measurements show that the incorporation of NH_2-MIL-125-Ti into the perovskite solar cell leads to an improved photovoltaic performance, with a 15% increase in short circuit current and a 10% increase in open circuit voltage. This can be attributed to the conduction band match between perovskite and NH_2-MIL-125-Ti. While the conduction band of NH_2-MIL-125-Ti is lower than that of perovskite, NH_2-MIL-125-Ti acts as the electron transporting material and facilitates the electron transportation process compared with no incorporation cells, which can be confirmed by the EIS results. On the other hand, the conduction band gap between the two is smaller than in the case of typical electron transportation material TiO_2, therefore, the output voltage of a solar cell with NH_2-MIL-125-Ti is higher than conventional mesoscopic TiO_2 PSCs. In addition to the photovoltaic improvements, the highest fabrication temperature for NH2-MIL-125-Ti incorporated PSC was only 100 °C, which compared with typical mesoscopic PSCs provides more possibility for different electrode substrates. Therefore, our work successfully incorporated NH_2-MIL-125-Ti into a PSC as a new electron transporting material with a feasible, low temperature process. NH_2-MIL-125-Ti with organic substrates PSCs is under investigation.

5.4 Work with collaborator

Lead-based perovskites are toxic and suffer from an instability that leads to degradation over time upon illumination in air. In contrast, organic-inorganic bismuth perovskite have drawn considerable inter ests due to their non-toxicity and high air stability. However, the power conversion efficiency (PCE) of MBI-based PSC is pretty low due to various factors, including the rough film surface, inherent mismatch large band gap, and poor charge transport.[222]

In this work, I have also investigated the non-toxic perovskite, $(CH_3NH_3)_3Bi_2I_9$ (MBI), in collaboration with researchers from Hubei University, China. To improve the PCE of Bi-based PSCs, we have conducted two projects with different strategies:

1) *Nontoxic $(CH_3NH_3)_3Bi_2I_9$ perovskite solar cells free of hole conductors with an alternative architectural design and a solution-processable approach*[223] (DOI: 10.1039/C7RA04924B)

The focus of this project was to prepare high-quality, homogeneous, and compact MBI thin for photovoltaic purposes. The typical MBI preparation is a one-step liquid phase spin coating process (1-S), which typically results in loosely packed 2-D MBI plates. In this project, we developed a new two-step process based on a soaking-assisted sequential drop-cast method (2-S) that I adopted from my aforementioned studies with $MAPbI_3$. The morphology of the films prepared with different methods is summarized in Figure 5-14. It can be seen that the MBI films prepared with the 2-S route are composed of considerably smaller MBI plates than the 1-S route, and the plates are closely stacked. In contrast, the larger 2-D MBI plates in the 1-S route contained large unfilled voids have. The MBI films have been prepared both on the bl-substrate and the meso-substrate, the trends in particle size and packing are the same with both substrates.

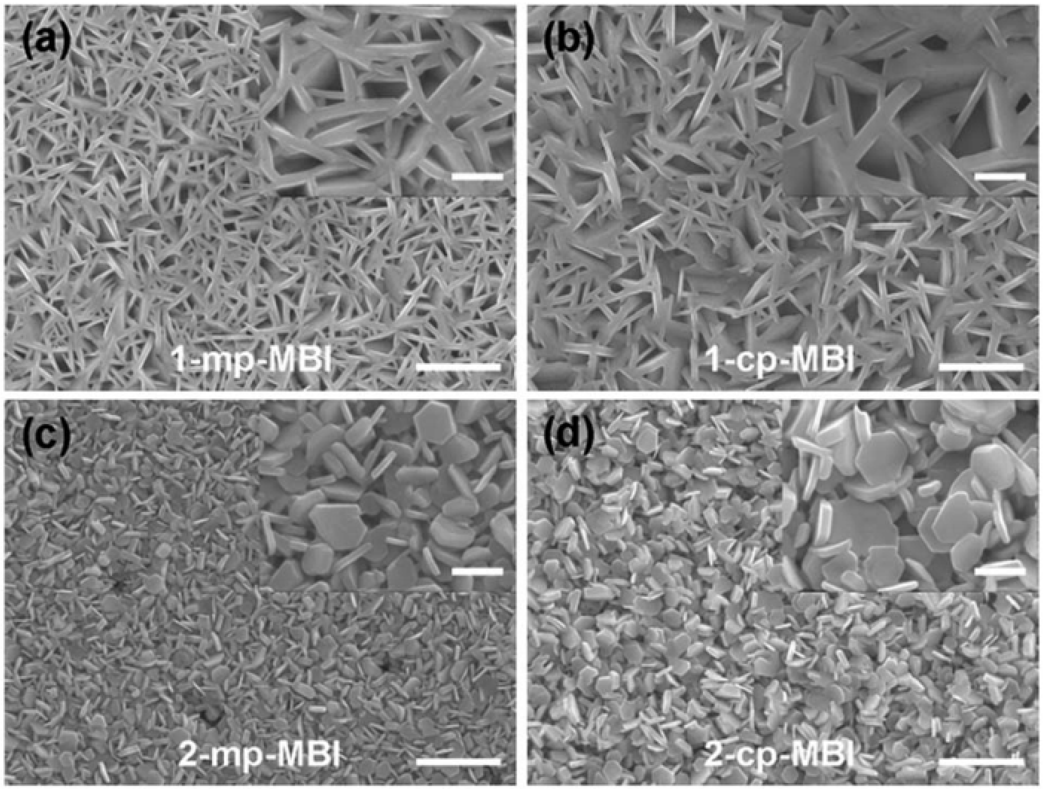

Figure 5-14 Top-view FE-SEM images of the MBI perovskite layer: (a) 1-mpMBI, (b) 1-cp-MBI, (c) 2-mp-MBI and (d) 2-cp-MBI. The insets are the the high resolution images, and the scale bars on the images and the insets are 2 mm and 500 nm, respectively.

Subsequent characterizations including AFM, DRS, EIS, and J-V curve have been performed to reveal the influence of morphologies of MBI films on the devices' performance. Generally, the mesoporous structured devices possess higher PCE than the planar structured devices. However, surprisingly, despite the better contact between the nanoplates, the 2-S prepared MBI films did not demonstrate superior performance over 1-S prepared MBI films, as can be seen from the IV performance of the film in Figure 5-15. This suggests that either the limiting process is the size rather than the particle packing, or there are hitherto unnoticed differences in the crystal structure or defect concentration that need to be further investigated. However, all devices demonstrated excellent thermal and long-term stabilities, even after storage in ambient air for 32 days, which confirms the potential of Bi-based perovskite for air-stable PSCs.

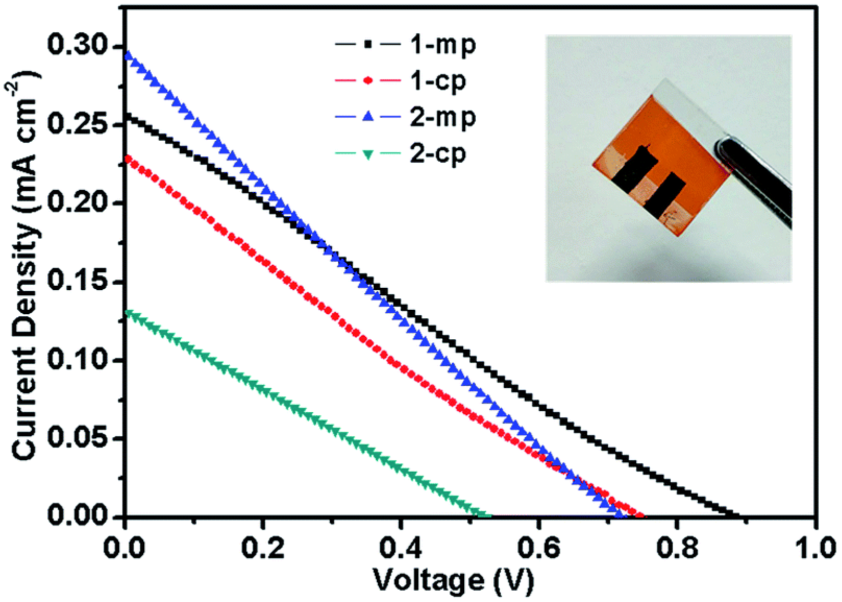

Figure 5-15 The IV performances of obtained Bi-based cells

2) Influence of Rutile-TiO_2 nanorod arrays on Pb-free $(CH_3NH_3)_3Bi_2I_9$-based hybrid perovskite solar cells fabricated through two-step sequential solution process[224] (10.1016/j.jallcom.2017.12.188)

The second strategy for improving the PCE of Bi-based PSC was to facilitate the charge collection as well as the charge transfer property via the optimization of the electron-transporting layer.

Herein, we used Rutile-TiO_2 nanorod arrays (r-TNRA) as our ETL candidates. Due to improved transfer channels introduced by the one-dimensional nanostructure, we expect a higher electron mobility of rutile compared to the other TiO_2 materials, as well as a higher conduction band potential. R-TNRA were successfully deposited onto FTO via direct frequency reactive magnetron sputtering. $MABiI_3$ was subsequently deposited onto the r-TNRA. The configuration and working principle of thus obtained PSC can be seen in Figure 5-16(a) and (b). All the devices were fabricated in ambient air.

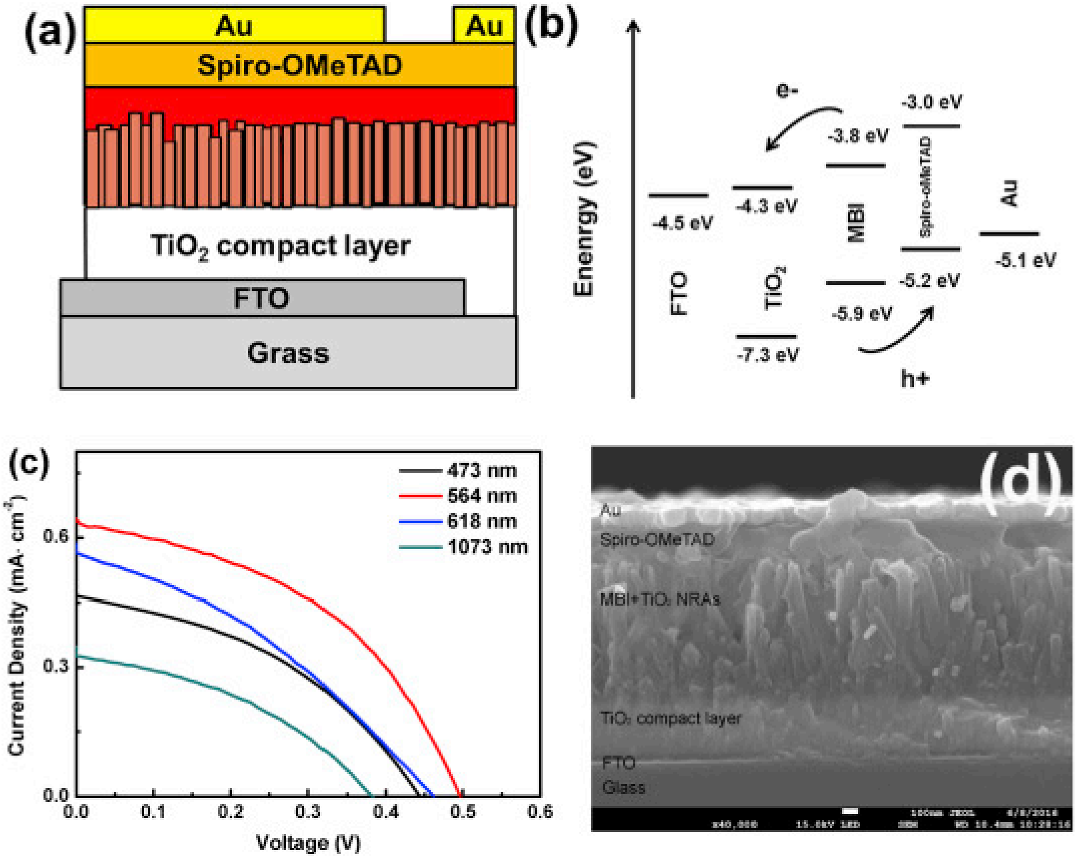

Figure 5-16 a) Schematic illustration of the device structure; b) Energy level diagram of the MBI PSCs; c) J-V curves of MBI PSCs based on different thickness of rutile TiO_2 NRA films; d) SEM cross-sectional structure of the MBI PSCs based 564 nm- TiO_2 NRA, scale bar, 100 nm

The impact of rutile-TiO_2 ETL thicknesses (473 nm-1073 nm) on the photogenerated carrier behavior and the photovoltaic performance of the fabricated solar cells have been investigated with time-resolved photoluminescence decay and J-V measurement. The highest PCE is obtained with a thickness at 564 nm (Figure 5-16). Further, SEM characterization shows that the $MABiI_3$ penetrated into the rutile array and formed a close contact with the electron transporting layer which is beneficial for the charge separation and transportation.

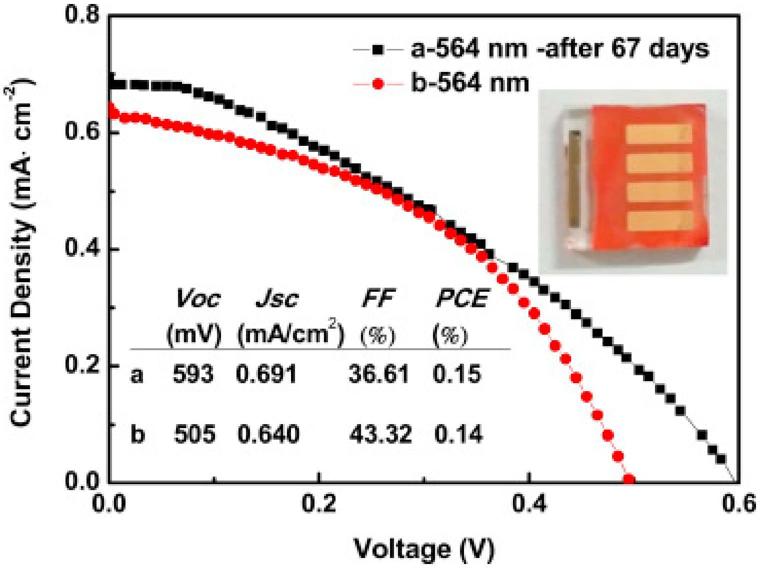

Figure 5-17 J-V curves of MBI PSC based on 564 nm-TiO_2 NRA films under simulated AM 1.5G (100 mW cm^{-2} irradiance), which measured immediately and exposed to humid dark environment without any sealing (> 50 % relative humidity) for 67 days, the inset shows an digital image of MBI PSCs after 67 days.

The most appealing characteristic of r-TNRA prepared PSCs is their ultra-high stability. Figure 5-17 compares the J-V curve of freshly prepared PSC and the PSC exposed to the humid dark environment without any sealing (> 50 % relative humidity) for 67 days, and it can be observed that the PCE of the cell in the humid environment has increased by approximately 7 %. This remarkable stability enables MBI-based PSC great advantage over the typical Pb-based PSCs. Moreover, this is attributed by the r-TNRA, as the photovoltaic analysis of MBI PSCs prepared on the anatase TiO_2-particle mesoporous layer decreases approximately 25 % for 10 weeks in ambient condition. However, the highest efficiency achieved with r-TNRA is only 0.15 %; to fulfill the potential of Bi-based PSC, the photovoltaic efficiency needs to be improved.

Bbibliography

1. *Coordination Chemistry Research Progress*. Nova Science Pub Inc: 2008; p 73.

2. Wu, H. W.; Emadi, A.; de Graaf, G.; Leijtens, J.; Wolffenbuttel, R. F., Design and Fabrication of an Albedo Insensitive Analog Sun Sensor. *Procedia Engineering* **2011,** *25*, 527-530.

3. Yoshikawa, K.; Kawasaki, H.; Yoshida, W.; Irie, T.; Konishi, K.; Nakano, K.; Uto, T.; Adachi, D.; Kanematsu, M.; Uzu, H.; Yamamoto, K., Silicon heterojunction solar cell with interdigitated back contacts for a photoconversion efficiency over 26%. *Nature Energy* **2017,** *2*, 17032.

4. Crabtree, G. W.; Lewis, N. S., Solar energy conversion. *Physics Today* **2007,** *60* (3), 37-42.

5. Berzelius, J. J., Årsberättelsen om framsteg i fysik och kemi. *Royal Swedish Academy of Sciences* **1838**.

6. Lindström, B.; Pettersson, L., *A Brief History of Catalysis*. 2003; Vol. 7, p 130-138.

7. Fujishima, A.; Honda, K., Electrochemical Photolysis of Water at a Semiconductor Electrode. *Nature* **1972,** *238* (5358), 37-38.

8. Park, J. H.; Kim, S.; Bard, A. J., Novel Carbon-Doped TiO2 Nanotube Arrays with High Aspect Ratios for Efficient Solar Water Splitting. *Nano Letters* **2006,** *6* (1), 24-28.

9. Ni, M.; Leung, M. K. H.; Leung, D. Y. C.; Sumathy, K., A review and recent developments in photocatalytic water-splitting using TiO2 for hydrogen production. *Renewable and Sustainable Energy Reviews* **2007,** *11* (3), 401-425.

10. Sun, J.; Qiao, L.; Sun, S.; Wang, G., Photocatalytic degradation of Orange G on nitrogen-doped TiO2 catalysts under visible light and sunlight irradiation. *Journal of Hazardous Materials* **2008,** *155* (1), 312-319.

11. Qian, W.; Greaney, P. A.; Fowler, S.; Chiu, S.-K.; Goforth, A. M.; Jiao, J., Low-Temperature Nitrogen Doping in Ammonia Solution for Production of N-Doped TiO2-Hybridized Graphene as a Highly Efficient Photocatalyst for Water Treatment. *ACS Sustainable Chemistry & Engineering* **2014,** *2* (7), 1802-1810.

12. Mishra, M.; Chun, D.-M., α-Fe2O3 as a photocatalytic material: A review. *Applied Catalysis A: General* **2015,** *498*, 126-141.

13. Jang, J. S.; Yoon, K. Y.; Xiao, X.; Fan, F.-R. F.; Bard, A. J., Development of a Potential Fe2O3-Based Photocatalyst Thin Film for Water Oxidation by Scanning Electrochemical Microscopy: Effects of Ag−Fe2O3 Nanocomposite and Sn Doping. *Chemistry of Materials* **2009,** *21* (20), 4803-4810.

14. Skrzypkiewicz, M.; Lubarska-Radziejewska, I.; Jewulski, J., The effect of Fe2O3 catalyst on direct carbon fuel cell performance. *International Journal of Hydrogen Energy* **2015,** *40* (38), 13090-13098.

15. Zeghbroeck, B. J. V., Carrier generation and recombination. **1996**.

16. Lindsay Leveen, S. P. I., The Five Myths of the Hydrogen Fueled Vehicle. **2003**.

17. Center, H. E., THE BENEFITS OF HYDROGEN WILL HELP MOVE US TO A SUSTAINABLE ENERGY ECONOMY.

18. Maeda, K.; Domen, K., New Non-Oxide Photocatalysts Designed for Overall Water Splitting under Visible Light. *The Journal of Physical Chemistry C* **2007,** *111* (22), 7851-7861.

19. Pai, M. R.; Banerjee, A. M.; Tripathi, A. K.; Bharadwaj, S. R., 14 - Fundamentals and Applications of the Photocatalytic Water Splitting Reaction. In *Functional Materials*, Banerjee, S.; Tyagi, A. K., Eds. Elsevier: London, 2012; pp 579-606.

20. Kudo, A.; Miseki, Y., Heterogeneous photocatalyst materials for water splitting. *Chemical Society Reviews* **2009,** *38* (1), 253-278.

21. Takeshi, M.; Ryoji, A.; Takeshi, O.; Koyu, A.; Yasunori, T., Band-Gap Narrowing of Titanium Dioxide by Nitrogen Doping. *Japanese Journal of Applied Physics* **2001,** *40* (6A), L561.

22. Braun, A.; Akurati, K. K.; Fortunato, G.; Reifler, F. A.; Ritter, A.; Harvey, A. S.; Vital, A.; Graule, T., Nitrogen Doping of TiO2 Photocatalyst Forms a Second eg State in the Oxygen 1s NEXAFS Pre-edge. *The Journal of Physical Chemistry C* **2010,** *114* (1), 516-519.

23. Pelaez, M.; Nolan, N. T.; Pillai, S. C.; Seery, M. K.; Falaras, P.; Kontos, A. G.; Dunlop, P. S. M.; Hamilton, J. W. J.; Byrne, J. A.; O'Shea, K.; Entezari, M. H.; Dionysiou, D. D., A review on the visible light active titanium dioxide photocatalysts for environmental applications. *Applied Catalysis B: Environmental* **2012,** *125*, 331-349.

24. Aschauer, U.; Selloni, A., *Hydrogen interaction with the anatase TiO2(101) surface*. 2012; Vol. 14.

25. Cherevan, A.; Robbins, S.; Dieterle, D.; Gebhardt, P.; Wiesner, U.; Eder, D., *Ordered Gyroidal Tantalum Oxide Photocatalysts: Eliminating Diffusion Limitations and Tuning Surface Barriers*. 2016; Vol. 8.

26. Nasalevich, M. A.; Becker, R.; Ramos-Fernandez, E. V.; Castellanos, S.; Veber, S. L.; Fedin, M. V.; Kapteijn, F.; Reek, J. N. H.; van der Vlugt, J. I.; Gascon, J., Co@NH2-MIL-125(Ti): cobaloxime-derived metal–organic framework-based composite for light-driven H2 production. *Energy & Environmental Science* **2015,** *8* (1), 364-375.

27. Yaghi, O. M.; Li, G.; Li, H., Selective binding and removal of guests in a microporous metal–organic framework. *Nature* **1995,** *378*, 703.

28. MacGillivray, L. R.; Groeneman, R. H.; Atwood, J. L., Design and Self-Assembly of Cavity-Containing Rectangular Grids. *Journal of the American Chemical Society* **1998,** *120* (11), 2676-2677.

29. Li, H.; Eddaoudi, M.; O'Keeffe, M.; Yaghi, O. M., Design and synthesis of an exceptionally stable and highly porous metal-organic framework. *Nature* **1999,** *402*, 276.

30. Yang, G.-Y.; Sevov, S. C., Zinc Phosphate with Gigantic Pores of 24 Tetrahedra. *Journal of the American Chemical Society* **1999,** *121* (36), 8389-8390.

31. Seo, J. S.; Whang, D.; Lee, H.; Jun, S. I.; Oh, J.; Jeon, Y. J.; Kim, K., A homochiral metal–organic porous material for enantioselective separation and catalysis. *Nature* **2000,** *404*, 982.

32. Yaghi, O. M.; Li, H., Hydrothermal Synthesis of a Metal-Organic Framework Containing Large Rectangular Channels. *Journal of the American Chemical Society* **1995,** *117* (41), 10401-10402.

33. Hendon, C. H.; Tiana, D.; Fontecave, M.; Sanchez, C.; D'arras, L.; Sassoye, C.; Rozes, L.; Mellot-Draznieks, C.; Walsh, A., Engineering the Optical Response of the Titanium-MIL-125 Metal–Organic Framework through Ligand Functionalization. *Journal of the American Chemical Society* **2013,** *135* (30), 10942-10945.

34. Pan, L.; Woodlock, E. B.; Wang, X.; Zheng, C., A New Porous Three-Dimensional Lanthanide Coordination Polymer. *Inorganic Chemistry* **2000,** *39* (18), 4174-4178.

35. Spanopoulos, I.; Xydias, P.; Malliakas, C. D.; Trikalitis, P. N., *Inorg. Chem.* **2013,** *52*, 855.

36. Nasalevich, M. A.; Goesten, M. G.; Savenije, T. J.; Kapteijn, F.; Gascon, J., Enhancing optical absorption of metal–organic frameworks for improved visible light photocatalysis. *Chemical Communications* **2013,** *49* (90), 10575-10577.

37. Chen, B.; Eddaoudi, M.; Hyde, S. T.; O'Keeffe, M.; Yaghi, O. M., Interwoven Metal-Organic Framework on a Periodic Minimal Surface with Extra-Large Pores. *Science* **2001,** *291* (5506), 1021-1023.

38. Yang, Q.; Liu, D.; Zhong, C.; Li, J. R., *Chem. Rev.* **2013,** *113*, 8261.

39. Yu, D.; Ghosh, P.; Snurr, R. Q., *Dalton Trans.* **2012,** *41*, 3962.

40. Kim, K. C.; Yu, D.; Snurr, R. Q., *Langmuir* **2013,** *29*, 1446.

41. Farha, O. K.; Eryazici, I.; Jeong, N. C.; Hauser, B. G.; Wilmer, C. E.; Sarjeant, A. A.; Snurr, R. Q.; Nguyen, S. T.; Yazaydın, A. Ö.; Hupp, J. T., Metal–Organic Framework Materials with Ultrahigh Surface Areas: Is the Sky the Limit? *Journal of the American Chemical Society* **2012,** *134* (36), 15016-15021.

42. Rojo-Gama, D.; Etemadi, S.; Kirby, E.; Lillerud, K. P.; Beato, P.; Svelle, S.; Olsbye, U., Time- and space-resolved study of the methanol to hydrocarbons (MTH) reaction – influence of zeolite topology on axial deactivation patterns. *Faraday Discussions* **2017,** *197* (0), 421-446.

43. Peralta, D.; Chaplais, G.; Simon-Masseron, A.; Barthelet, K.; Chizallet, C.; Quoineaud, A. A.; Pirngruber, G. D., *J. Am. Chem. Soc.* **2012,** *134*, 8115.

44. Wu, H.; Gong, Q.; Olson, D. H.; Li, J., *Chem. Rev.* **2012,** *112*, 836.

45. Li, J.-R.; Kuppler, R. J.; Zhou, H.-C., Selective gas adsorption and separation in metal-organic frameworks. *Chemical Society Reviews* **2009,** *38* (5), 1477-1504.

46. Zhaoxu, W.; Xin, L.; Baishu, Z.; Lu, H.; Cheng, H.; Yinchun, J.; Xiyang, C.; Wenjiang, Z.; Ruirui, Y., Highly Selective Carbon Dioxide Capture and Cooperative Catalysis of a Water ‐ Stable Acylamide ‐ Functionalized Metal ‐ Organic Framework. *European Journal of Inorganic Chemistry* **2018,** *2018* (11), 1309-1314.

47. Vaesen, S.; Guillerm, V.; Yang, Q.; Wiersum, A. D.; Marszalek, B.; Gil, B.; Vimont, A.; Daturi, M.; Devic, T.; Llewellyn, P. L.; Serre, C.; Maurin, G.; De Weireld, G., A robust amino-functionalized titanium(iv) based MOF for improved separation of acid gases. *Chemical Communications* **2013,** *49* (86), 10082-10084.

48. Oveisi, M.; Alinia-Asli, M.; Mahmoodi, N. M., *MIL-Ti metal-organic frameworks (MOFs) nanomaterials as superior adsorbents: Synthesis and ultrasound-aided dye adsorption from multicomponent wastewater systems*. 2018; Vol. 347, p 123–140.

49. Molavi, H.; Hakimian, A.; Shojaei, A.; Raeiszadeh, M., Selective dye adsorption by highly water stable metal-organic framework: Long term stability analysis in aqueous media. *Applied Surface Science* **2018,** *445*, 424-436.

50. Moreira, M. A.; Santos, J. C.; Ferreira, A. F. P.; Loureiro, J. M.; Ragon, F.; Horcajada, P.; Shim, K. E.; Hwang, Y. K.; Lee, U. H.; Chang, J. S.; Serre, C.; Rodrigues, A. E., *Langmuir* **2012,** *28*, 5715.

51. DeCoste, J. B.; Peterson, G. W., Metal–Organic Frameworks for Air Purification of Toxic Chemicals. *Chemical Reviews* **2014,** *114* (11), 5695-5727.

52. Zhang, L.; Wang, L. L.; Gong, L. L.; Feng, X. F.; Luo, M. B.; Luo, F., Coumarin-modified microporous-mesoporous Zn-MOF-74 showing ultra-high uptake capacity and photo-switched storage/release of UVI ions. *Journal of Hazardous Materials* **2016,** *311*, 30-36.

53. Pi, Y.; Li, X.; Xia, Q.; Wu, J.; Li, Y.; Xiao, J.; Li, Z., Adsorptive and photocatalytic removal of Persistent Organic Pollutants (POPs) in water by metal-organic frameworks (MOFs). *Chemical Engineering Journal* **2018,** *337*, 351-371.

54. Lin, S.; Liu, X.; Tan, L.; Cui, Z.; Yang, X.; Yeung, K. W. K.; Pan, H.; Wu, S., Porous Iron-Carboxylate Metal–Organic Framework: A Novel Bioplatform with Sustained Antibacterial Efficacy and Nontoxicity. *ACS Applied Materials & Interfaces* **2017,** *9* (22), 19248-19257.

55. Rubin, H. N.; Neufeld, B. H.; Reynolds, M. M., Surface-Anchored Metal–Organic Framework–Cotton Material for Tunable Antibacterial Copper Delivery. *ACS Applied Materials & Interfaces* **2018,** *10* (17), 15189-15199.

56. Roy, A.; Srivastava, A. K.; Singh, B.; Shah, D.; Mahato, T. H.; Srivastava, A., Kinetics of degradation of sulfur mustard and sarin simulants on HKUST-1 metal organic framework. *Dalton Transactions* **2012,** *41* (40), 12346-12348.

57. Roy, A.; Srivastava, A. K.; Singh, B.; Shah, D.; Mahato, T. H.; Srivastava, A., *Dalton Trans.* **2012,** *41*, 12346.

58. Zhang, R.; Li, G.; Zhang, Y., Photochemical synthesis of CdS-MIL-125(Ti) with enhanced visible light photocatalytic performance for the selective oxidation of benzyl alcohol to benzaldehyde. *Photochemical & Photobiological Sciences* **2017,** *16* (6), 996-1002.

59. Sun, D.; Ye, L.; Li, Z., Visible-light-assisted aerobic photocatalytic oxidation of amines to imines over NH2-MIL-125(Ti). *Applied Catalysis B: Environmental* **2015,** *164*, 428-432.

60. Kawakami, T.; Takamizawa, S.; Kitagawa, Y.; Maruta, T.; Mori, W.; Yamaguchi, K., Theoretical studies of spin arrangement of adsorbed organic radicals in metal-organic nanoporous cavity. *Polyhedron* **2001,** *20* (11), 1197-1206.

61. Li, Z.; Xiao, J.-D.; Jiang, H.-L., Encapsulating a Co(II) Molecular Photocatalyst in Metal–Organic Framework for Visible-Light-Driven H2 Production: Boosting Catalytic Efficiency via Spatial Charge Separation. *ACS Catalysis* **2016,** *6* (8), 5359-5365.

62. Karthik, P.; Balaraman, E.; Neppolian, B., Efficient solar light-driven H2 production: post-synthetic encapsulation of a Cu2O co-catalyst in a metal–organic framework (MOF) for boosting the effective charge carrier separation. *Catalysis Science & Technology* **2018,** *8* (13), 3286-3294.

63. Lavine, M. S., A Marriage of POM and MOF. *Science* **2011,** *334* (6056), 569-569.

64. Kong, X.-J.; Lin, Z.; Zhang, Z.-M.; Zhang, T.; Lin, W., Hierarchical Integration of Photosensitizing Metal–Organic Frameworks and Nickel-Containing Polyoxometalates for Efficient Visible-Light-Driven Hydrogen Evolution. *Angewandte Chemie International Edition* **2016,** *55* (22), 6411-6416.

65. Qu, L.-L.; Wang, J.; Xu, T.-Y.; Chen, Q.-Y.; Chen, J.-H.; Shi, C.-J., Iron(iii)-based metal–organic frameworks as oxygen-evolving photocatalysts for water oxidation. *Sustainable Energy & Fuels* **2018,** *2* (9), 2109-2114.

66. Zhou, T.; Zhang, G.; Zhang, H.; Yang, H.; Ma, P.; Li, X.; Qiu, X.; Liu, G., Highly efficient visible-light-driven photocatalytic degradation of rhodamine B by a novel Z-scheme Ag3PO4/MIL-101/NiFe2O4 composite. *Catalysis Science & Technology* **2018,** *8* (9), 2402-2416.

67. Abazari, R.; Mahjoub, A. R., Amine-Functionalized Al-MOF#@yxSm2O3–ZnO: A Visible Light-Driven Nanocomposite with Excellent Photocatalytic Activity for the Photo-Degradation of Amoxicillin. *Inorganic Chemistry* **2018,** *57* (5), 2529-2545.

68. Sun, D.; Fu, Y.; Liu, W.; Ye, L.; Wang, D.; Yang, L.; Fu, X.; Li, Z., Studies on Photocatalytic CO2 Reduction over NH2-Uio-66(Zr) and Its Derivatives: Towards a Better Understanding of Photocatalysis on Metal–Organic Frameworks. *Chemistry – A European Journal* **2013,** *19* (42), 14279-14285.

69. Santaclara, J. G.; Kapteijn, F.; Gascon, J.; van der Veen, M. A., Understanding metal–organic frameworks for photocatalytic solar fuel production. *CrystEngComm* **2017,** *19* (29), 4118-4125.

70. Meyer, K.; Bashir, S.; Llorca, J.; Idriss, H.; Ranocchiari, M.; van Bokhoven, J. A., Photocatalyzed Hydrogen Evolution from Water by a Composite Catalyst of NH2-MIL-125(Ti) and Surface Nickel(II) Species. *Chemistry – A European Journal* **2016,** *22* (39), 13894-13899.

71. Wang, D.; Wang, M.; Li, Z., Fe-Based Metal–Organic Frameworks for Highly Selective Photocatalytic Benzene Hydroxylation to Phenol. *ACS Catalysis* **2015,** *5* (11), 6852-6857.

72. De Vos, A.; Hendrickx, K.; Van Der Voort, P.; Van Speybroeck, V.; Lejaeghere, K., Missing Linkers: An Alternative Pathway to UiO-66 Electronic Structure Engineering. *Chemistry of Materials* **2017,** *29* (7), 3006-3019.

73. Nasalevich, M. A.; Hendon, C. H.; Santaclara, J. G.; Svane, K.; van der Linden, B.; Veber, S. L.; Fedin, M. V.; Houtepen, A. J.; van der Veen, M. A.; Kapteijn, F.; Walsh, A.; Gascon, J., Electronic origins of photocatalytic activity in d0 metal organic frameworks. *Scientific Reports* **2016,** *6*, 23676.

74. Shi, L.; Wang, T.; Zhang, H.; Chang, K.; Meng, X.; Liu, H.; Ye, J., An Amine-Functionalized Iron(III) Metal–Organic Framework as Efficient Visible-Light Photocatalyst for Cr(VI) Reduction. *Advanced Science* **2015,** *2* (3), 1500006.

75. Wang, D.; Huang, R.; Liu, W.; Sun, D.; Li, Z., Fe-Based MOFs for Photocatalytic CO2 Reduction: Role of Coordination Unsaturated Sites and Dual Excitation Pathways. *ACS Catalysis* **2014,** *4* (12), 4254-4260.

76. Zhou, T.; Du, Y.; Borgna, A.; Hong, J.; Wang, Y.; Han, J.; Zhang, W.; Xu, R., Post-synthesis modification of a metal–organic framework to construct a bifunctional photocatalyst for hydrogen production. *Energy & Environmental Science* **2013,** *6* (11), 3229-3234.

77. Nasalevich, M. A.; van der Veen, M.; Kapteijn, F.; Gascon, J., Metal–organic frameworks as heterogeneous photocatalysts: advantages and challenges. *CrystEngComm* **2014,** *16* (23), 4919-4926.

78. Li, M.; Wang, J.; Zheng, Y.; Zheng, Z.; Li, C.; Li, Z., Anchoring NaYF4:Yb,Tm upconversion nanocrystals on concave MIL-53(Fe) octahedra for NIR-light enhanced photocatalysis. *Inorganic Chemistry Frontiers* **2017,** *4* (10), 1757-1764.

79. Fu, Y.; Sun, D.; Chen, Y.; Huang, R.; Ding, Z.; Fu, X.; Li, Z., An Amine-Functionalized Titanium Metal–Organic Framework Photocatalyst with Visible-Light-Induced Activity for CO2 Reduction. *Angewandte Chemie International Edition* **2012,** *51* (14), 3364-3367.

80. Dan-Hardi, M.; Serre, C.; Frot, T.; Rozes, L.; Maurin, G.; Sanchez, C.; Férey, G., A New Photoactive Crystalline Highly Porous Titanium(IV) Dicarboxylate. *Journal of the American Chemical Society* **2009,** *131* (31), 10857-10859.

81. Zlotea, C.; Phanon, D.; Mazaj, M.; Heurtaux, D.; Guillerm, V.; Serre, C.; Horcajada, P.; Devic, T.; Magnier, E.; Cuevas, F.; Férey, G.; Llewellyn, P. L.; Latroche, M., Effect of NH2 and CF3 functionalization on the hydrogen sorption properties of MOFs. *Dalton Transactions* **2011,** *40* (18), 4879-4881.

82. Hu, S.; Liu, M.; Li, K.; Zuo, Y.; Zhang, A.; Song, C.; Zhang, G.; Guo, X., Solvothermal synthesis of NH2-MIL-125(Ti) from circular plate to octahedron. *CrystEngComm* **2014,** *16* (41), 9645-9650.

83. Qiu, J.; Zhang, X.; Feng, Y.; Zhang, X.; Wang, H.; Yao, J., Modified metal-organic frameworks as photocatalysts. *Applied Catalysis B: Environmental* **2018,** *231*, 317-342.

84. An, Y.; Xu, B.; Liu, Y.; Wang, Z.; Wang, P.; Dai, Y.; Qin, X.; Zhang, X.; Huang, B., Photocatalytic Overall Water Splitting over MIL‐125(Ti) upon CoPi and Pt Co‐catalyst Deposition. *ChemistryOpen* **2017,** *6* (6), 701-705.

85. Abdelhameed, R. M.; Simões, M. M. Q.; Silva, A. M. S.; Rocha, J., Enhanced Photocatalytic Activity of MIL-125 by Post-Synthetic Modification with CrIII and Ag Nanoparticles. *Chemistry – A European Journal* **2015,** *21* (31), 11072-11081.

86. Liu, H.; Zhang, J.; Ao, D., Construction of heterostructured ZnIn2S4@NH2-MIL-125(Ti) nanocomposites for visible-light-driven H2 production. *Applied Catalysis B: Environmental* **2018,** *221*, 433-442.

87. Electron Interaction with Matter from Wikimedia Commons. https://commons.wikimedia.org/wiki/File:Electron_Interaction_with_Matter.svg#file.

88. TEM and ED principle.

89. Embong, Z., *XPS, AES and laser raman spectroscopy: A fingerprint for a materials surface characterisation*. 2011; Vol. 23, p 26-45.

90. Vandenbroucke, A., *Abatement of volatile organic compounds by combined use of non-thermal plasma and heterogeneous catalysis*. 2015.

91. HORIBA, What is Raman Spectroscopy?

92. Thommes, M.; Kaneko, K.; Neimark Alexander, V.; Olivier James, P.; Rodriguez-Reinoso, F.; Rouquerol, J.; Sing Kenneth, S. W., Physisorption of gases, with special reference to the evaluation of surface area and pore size distribution (IUPAC Technical Report). In *Pure and Applied Chemistry*, 2015; Vol. 87, p 1051.

93. Jones, W.; Martin, D. J.; Caravaca, A.; Beale, A. M.; Bowker, M.; Maschmeyer, T.; Hartley, G.; Masters, A., A comparison of photocatalytic reforming reactions of methanol and triethanolamine with Pd supported on titania and graphitic carbon nitride. *Applied Catalysis B: Environmental* **2017**.

94. Kandiel, T. A.; Ivanova, I.; Bahnemann, D. W., Long-term investigation of the photocatalytic hydrogen production on platinized TiO2: an isotopic study. *Energy & Environmental Science* **2014,** *7* (4), 1420-1425.

95. Guzman, F.; Chuang, S. S. C.; Yang, C., Role of Methanol Sacrificing Reagent in the Photocatalytic Evolution of Hydrogen. *Industrial & Engineering Chemistry Research* **2013,** *52* (1), 61-65.

96. Lin, W.-C.; Yang, W.-D.; Huang, I. L.; Wu, T.-S.; Chung, Z.-J., Hydrogen Production from Methanol/Water Photocatalytic Decomposition Using Pt/TiO2−xNx Catalyst. *Energy & Fuels* **2009,** *23* (4), 2192-2196.

97. Shen, L.; Luo, M.; Huang, L.; Feng, P.; Wu, L., A Clean and General Strategy To Decorate a Titanium Metal–Organic Framework with Noble-Metal Nanoparticles for Versatile Photocatalytic Applications. *Inorganic Chemistry* **2015,** *54* (4), 1191-1193.

98. An, Y.; Xu, B.; Liu, Y.; Wang, Z.; Wang, P.; Dai, Y.; Qin, X.; Zhang, X.; Huang, B., Photocatalytic Overall Water Splitting over MIL-125(Ti) upon CoPi and Pt Co-catalyst Deposition. *ChemistryOpen* **2017,** *6* (6), 701-705.

99. Chavan, S. M.; Shearer, G. C.; Svelle, S.; Olsbye, U.; Bonino, F.; Ethiraj, J.; Lillerud, K. P.; Bordiga, S., Synthesis and Characterization of Amine-Functionalized Mixed-Ligand Metal–Organic Frameworks of UiO-66 Topology. *Inorganic Chemistry* **2014,** *53* (18), 9509-9515.

100. Liao, Y.-T.; Huang, Y.-Y.; Chen, H. M.; Komaguchi, K.; Hou, C.-H.; Henzie, J.; Yamauchi, Y.; Ide, Y.; Wu, K. C. W., Mesoporous TiO2 Embedded with a Uniform Distribution of CuO Exhibit Enhanced Charge Separation and Photocatalytic Efficiency. *ACS Applied Materials & Interfaces* **2017,** *9* (49), 42425-42429.

101. hu, S.; Liu, M.; Li, K.; Zuo, Y.; Zhang, A.; Song, C.; Zhang, G.; Guo, X., *Solvothermal synthesis of NH2-MIL-125(Ti) from circular plate to octahedron*. 2014; Vol. 16.

102. Chambers, M. B.; Wang, X.; Ellezam, L.; Ersen, O.; Fontecave, M.; Sanchez, C.; Rozes, L.; Mellot-Draznieks, C., Maximizing the Photocatalytic Activity of Metal–Organic Frameworks with Aminated-Functionalized Linkers: Substoichiometric Effects in MIL-125-NH2. *Journal of the American Chemical Society* **2017,** *139* (24), 8222-8228.

103. Feng, L.; Yuan, S.; Zhang, L.-L.; Tan, K.; Li, J.-L.; Kirchon, A.; Liu, L.-M.; Zhang, P.; Han, Y.; Chabal, Y. J.; Zhou, H.-C., Creating Hierarchical Pores by Controlled Linker Thermolysis in Multivariate Metal–Organic Frameworks. *Journal of the American Chemical Society* **2018,** *140* (6), 2363-2372.

104. Horiuchi, Y.; Toyao, T.; Saito, M.; Mochizuki, K.; Iwata, M.; Higashimura, H.; Anpo, M.; Matsuoka, M., Visible-Light-Promoted Photocatalytic Hydrogen Production by Using an Amino-Functionalized Ti(IV) Metal–Organic Framework. *The Journal of Physical Chemistry C* **2012,** *116* (39), 20848-20853.

105. Waqas Anjum, M.; Bueken, B.; De Vos, D.; Vankelecom, I. F. J., MIL-125(Ti) based mixed matrix membranes for CO2 separation from CH4 and N2. *Journal of Membrane Science* **2016,** *502*, 21-28.

106. Kim, S.-N.; Kim, J.; Kim, H.-Y.; Cho, H.-Y.; Ahn, W.-S., Adsorption/catalytic properties of MIL-125 and NH2-MIL-125. *Catalysis Today* **2013,** *204*, 85-93.

107. Kampouri, S.; Nguyen, T. N.; Spodaryk, M.; Palgrave, R. G.; Züttel, A.; Smit, B.; Stylianou, K. C., Concurrent Photocatalytic Hydrogen Generation and Dye Degradation Using MIL-125-NH2 under Visible Light Irradiation. *Advanced Functional Materials* **2018,** *28* (52), 1806368.

108. Tang, R.; Xie, Z.; Zhou, S.; Zhang, Y.; Yuan, Z.; Zhang, L.; Yin, L., Cu2ZnSnS4 Nanoparticle Sensitized Metal–Organic Framework Derived Mesoporous TiO2 as Photoanodes for High-Performance Dye-Sensitized Solar Cells. *ACS Applied Materials & Interfaces* **2016,** *8* (34), 22201-22212.

109. Wang, H.; Yuan, X.; Wu, Y.; Zeng, G.; Dong, H.; Chen, X.; Leng, L.; Wu, Z.; Peng, L., In situ synthesis of In2S3@MIL-125(Ti) core–shell microparticle for the removal of tetracycline from wastewater by integrated adsorption and visible-light-driven photocatalysis. *Applied Catalysis B: Environmental* **2016,** *186*, 19-29.

110. Li, X.; Pi, Y.; Hou, Q.; Yu, H.; Li, Z.; Li, Y.; Xiao, J., Amorphous TiO2@NH2-MIL-125(Ti) homologous MOF-encapsulated heterostructures with enhanced photocatalytic activity. *Chemical Communications* **2018,** *54* (15), 1917-1920.

111. Oveisi, M.; Asli, M. A.; Mahmoodi, N. M., MIL-Ti metal-organic frameworks (MOFs) nanomaterials as superior adsorbents: Synthesis and ultrasound-aided dye adsorption from multicomponent wastewater systems. *Journal of Hazardous Materials* **2018,** *347*, 123-140.

112. Nasalevich, M. A.; Goesten, M. G.; Savenije, T. J.; Kapteijn, F.; Gascon, J., Correction: Enhancing optical absorption of metal–organic frameworks for improved visible light photocatalysis. *Chemical Communications* **2015,** *51* (5), 961-962.

113. Wang, H.; Yuan, X.; Wu, Y.; Zeng, G.; Chen, X.; Leng, L.; Wu, Z.; Jiang, L.; Li, H., Facile synthesis of amino-functionalized titanium metal-organic frameworks and their superior visible-light photocatalytic activity for Cr(VI) reduction. *Journal of Hazardous Materials* **2015,** *286*, 187-194.

114. Butler, K. T.; Hendon, C. H.; Walsh, A., Electronic Chemical Potentials of Porous Metal–Organic Frameworks. *Journal of the American Chemical Society* **2014,** *136* (7), 2703-2706.

115. Fu, Y.; Yang, H.; Du, R.; Tu, G.; Xu, C.; Zhang, F.; Fan, M.; Zhu, W., Enhanced photocatalytic CO2 reduction over Co-doped NH2-MIL-125(Ti) under visible light. *RSC Advances* **2017,** *7* (68), 42819-42825.

116. Patil, P. S.; Kadam, L. D.; Lokhande, C. D., Preparation and characterization of spray pyrolysed cobalt oxide thin films. *Thin Solid Films* **1996,** *272* (1), 29-32.

117. Guo, H.; Lin, F.; Chen, J.; Li, F.; Weng, W., Metal–organic framework MIL-125(Ti) for efficient adsorptive removal of Rhodamine B from aqueous solution. *Applied Organometallic Chemistry* **2015,** *29* (1), 12-19.

118. Cabaniss, S. E.; Leenheer, J. A.; McVey, I. F., Aqueous infrared carboxylate absorbances: aliphatic di-acids. *Spectrochimica Acta Part A: Molecular and Biomolecular Spectroscopy* **1998,** *54* (3), 449-458.

119. Cabaniss, S. E.; McVey, I. F., Aqueous infrared carboxylate absorbances: aliphatic monocarboxylates. *Spectrochimica Acta Part A: Molecular and Biomolecular Spectroscopy* **1995,** *51* (13), 2385-2395.

120. Zhou, G.; Wu, M.-F.; Xing, Q.-J.; Li, F.; Liu, H.; Luo, X.-B.; Zou, J.-P.; Luo, J.-M.; Zhang, A.-Q., Synthesis and characterizations of metal-free Semiconductor/MOFs with good stability and high photocatalytic activity for H2 evolution: A novel Z-Scheme heterostructured photocatalyst formed by covalent bonds. *Applied Catalysis B: Environmental* **2018,** *220*, 607-614.

121. Flakus, H. T., Effect of the resonance of molecular vibrations on the ir spectra of hydrogen bonds. *Journal of Molecular Structure* **1981,** *72*, 107-117.

122. Wu, Z.; Huang, X.; Zheng, H.; Wang, P.; Hai, G.; Dong, W.; Wang, G., Aromatic heterocycle-grafted NH2-MIL-125(Ti) via conjugated linker with enhanced photocatalytic activity for selective oxidation of alcohols under visible light. *Applied Catalysis B: Environmental* **2018,** *224*, 479-487.

123. Wang, M.; Yang, L.; Yuan, J.; He, L.; Song, Y.; Zhang, H.; Zhang, Z.; Fang, S., Heterostructured Bi2S3@NH2-MIL-125(Ti) nanocomposite as a bifunctional photocatalyst for Cr(vi) reduction and rhodamine B degradation under visible light. *RSC Advances* **2018,** *8* (22), 12459-12470.

124. Chi, W. S.; Roh, D. K.; Lee, C. S.; Kim, J. H., A shape- and morphology-controlled metal organic framework template for high-efficiency solid-state dye-sensitized solar cells. *Journal of Materials Chemistry A* **2015,** *3* (43), 21599-21608.

125. Liu, Z.; Wu, Y.; Chen, J.; Li, Y.; Zhao, J.; Gao, K.; Na, P., Effective elimination of As(iii) via simultaneous photocatalytic oxidation and adsorption by a bifunctional cake-like TiO2 derived from MIL-125(Ti). *Catalysis Science & Technology* **2018,** *8* (7), 1936-1944.

126. Hanaor, D. A. H.; Sorrell, C. C., Review of the anatase to rutile phase transformation. *Journal of Materials Science* **2011,** *46* (4), 855-874.

127. Zhang, J.; Nosaka, Y., Photocatalytic oxidation mechanism of methanol and the other reactants in irradiated TiO2 aqueous suspension investigated by OH radical detection. *Applied Catalysis B: Environmental* **2015,** *166-167*, 32-36.

128. Anderson, A. B.; Asiri, H. A., Reversible potentials for steps in methanol and formic acid oxidation to CO2; adsorption energies of intermediates on the ideal electrocatalyst for methanol oxidation and CO2 reduction. *Physical Chemistry Chemical Physics* **2014,** *16* (22), 10587-10599.

129. Walsh, A.; Catlow, C. R. A., Photostimulated Reduction Processes in a Titania Hybrid Metal–Organic Framework. *ChemPhysChem* **2010,** *11* (11), 2341-2344.

130. Xu, J.; Gao, J.; Wang, C.; Yang, Y.; Wang, L., NH2-MIL-125(Ti)/graphitic carbon nitride heterostructure decorated with NiPd co-catalysts for efficient photocatalytic hydrogen production. *Applied Catalysis B: Environmental* **2017,** *219*, 101-108.

131. Pellegrin, Y.; Odobel, F., Sacrificial electron donor reagents for solar fuel production. *Comptes Rendus Chimie* **2017,** *20* (3), 283-295.

132. Zhao, P.; Lampronti, G. I.; Lloyd, G. O.; Wharmby, M. T.; Facq, S.; Cheetham, A. K.; Redfern, S. A. T., Phase Transitions in Zeolitic Imidazolate Framework 7: The Importance of Framework Flexibility and Guest-Induced Instability. *Chemistry of Materials* **2014,** *26* (5), 1767-1769.

133. DeCoste, J. B.; Peterson, G. W.; Jasuja, H.; Glover, T. G.; Huang, Y.-g.; Walton, K. S., Stability and degradation mechanisms of metal–organic frameworks containing the Zr6O4(OH)4 secondary building unit. *Journal of Materials Chemistry A* **2013,** *1* (18), 5642-5650.

134. Deria, P.; Chung, Y. G.; Snurr, R. Q.; Hupp, J. T.; Farha, O. K., Water stabilization of Zr6-based metal–organic frameworks via solvent-assisted ligand incorporation. *Chemical Science* **2015,** *6* (9), 5172-5176.

135. Luo, M.; Yao, W.; Huang, C.; Wu, Q.; Xu, Q., Shape effects of Pt nanoparticles on hydrogen production via Pt/CdS photocatalysts under visible light. *Journal of Materials Chemistry A* **2015,** *3* (26), 13884-13891.

136. Wenderich, K.; Mul, G., Methods, Mechanism, and Applications of Photodeposition in Photocatalysis: A Review. *Chemical Reviews* **2016,** *116* (23), 14587-14619.

137. Jiang, Z.; Zhang, Z.; Shangguan, W.; Isaacs, M. A.; Durndell, L. J.; Parlett, C. M. A.; Lee, A. F., Photodeposition as a facile route to tunable Pt photocatalysts for hydrogen production: on the role of methanol. *Catalysis Science & Technology* **2016,** *6* (1), 81-88.

138. Haselmann, G. M.; Eder, D., Early-Stage Deactivation of Platinum-Loaded TiO2 Using In Situ Photodeposition during Photocatalytic Hydrogen Evolution. *ACS Catalysis* **2017,** *7* (7), 4668-4675.

139. Xu, X.-Y.; Yan, B., An efficient and sensitive fluorescent pH sensor based on amino functional metal–organic frameworks in aqueous environment. *Dalton Transactions* **2016,** *45* (16), 7078-7084.

140. Yuan, X.; Wang, H.; Wu, Y.; Zeng, G.; Chen, X.; Leng, L.; Wu, Z.; Li, H., One-pot self-assembly and photoreduction synthesis of silver nanoparticle-decorated reduced graphene oxide/MIL-125(Ti) photocatalyst with improved visible light photocatalytic activity. *Applied Organometallic Chemistry* **2016,** *30* (5), 289-296.

141. Yan, B.; Zhang, L.; Tang, Z.; Al-Mamun, M.; Zhao, H.; Su, X., Palladium-decorated hierarchical titania constructed from the metal-organic frameworks NH2-MIL-125(Ti) as a robust photocatalyst for hydrogen evolution. *Applied Catalysis B: Environmental* **2017,** *218*, 743-750.

142. Guo, W.; Lv, H.; Chen, Z.; Sullivan, K. P.; Lauinger, S. M.; Chi, Y.; Sumliner, J. M.; Lian, T.; Hill, C. L., Self-assembly of polyoxometalates, Pt nanoparticles and metal–organic frameworks into a hybrid material for synergistic hydrogen evolution. *Journal of Materials Chemistry A* **2016,** *4* (16), 5952-5957.

143. Kalita, A.; Deka, K.; Kalita, M. P. C., On the influence of Raman scattering of water in the photoluminescence measurement of water dispersed ZnO nanocrystals. *Methods and Applications in Fluorescence* **2017,** *5* (2), 027001.

144. Xiu, Z.; Alfaruqi, M. H.; Gim, J.; Song, J.; Kim, S.; Duong, P. T.; Baboo, J. P.; Mathew, V.; Kim, J., MOF-derived mesoporous anatase TiO2 as anode material for lithium–ion batteries with high rate capability and long cycle stability. *Journal of Alloys and Compounds* **2016,** *674*, 174-178.

145. Zhang, H.; Wang, Y.; Zhao, W.; Zou, M.; Chen, Y.; Yang, L.; Xu, L.; Wu, H.; Cao, A., MOF-Derived ZnO Nanoparticles Covered by N-Doped Carbon Layers and Hybridized on Carbon Nanotubes for Lithium-Ion Battery Anodes. *ACS Applied Materials & Interfaces* **2017,** *9* (43), 37813-37822.

146. Ma, Y.; He, J.; Kou, Z.; Elshahawy, A. M.; Hu, Y.; Guan, C.; Li, X.; Wang, J., MOF-Derived Vertically Aligned Mesoporous Co3O4 Nanowires for Ultrahigh Capacity Lithium-Ion Batteries Anodes. *Advanced Materials Interfaces* **2018,** *5* (14), 1800222.

147. Salunkhe, R. R.; Kaneti, Y. V.; Yamauchi, Y., Metal–Organic Framework-Derived Nanoporous Metal Oxides toward Supercapacitor Applications: Progress and Prospects. *ACS Nano* **2017,** *11* (6), 5293-5308.

148. Linnemann, J.; Taudien, L.; Klose, M.; Giebeler, L., Electrodeposited films to MOF-derived electrochemical energy storage electrodes: a concept of simplified additive-free electrode processing for self-standing, ready-to-use materials. *Journal of Materials Chemistry A* **2017,** *5* (35), 18420-18428.

149. Wang, Y. C.; Li, W. B.; Zhao, L.; Xu, B. Q., MOF-derived binary mixed metal/metal oxide @carbon nanoporous materials and their novel supercapacitive performances. *Physical Chemistry Chemical Physics* **2016,** *18* (27), 17941-17948.

150. Liao, Y.-T.; Matsagar, B. M.; Wu, K. C. W., Metal–Organic Framework (MOF)-Derived Effective Solid Catalysts for Valorization of Lignocellulosic Biomass. *ACS Sustainable Chemistry & Engineering* **2018,** *6* (11), 13628-13643.

151. Ma, B.; Guan, P.-Y.; Li, Q.-Y.; Zhang, M.; Zang, S.-Q., MOF-Derived Flower-like MoS2@TiO2 Nanohybrids with Enhanced Activity for Hydrogen Evolution. *ACS Applied Materials & Interfaces* **2016,** *8* (40), 26794-26800.

152. Santos, V. P.; Wezendonk, T. A.; Jaén, J. J. D.; Dugulan, A. I.; Nasalevich, M. A.; Islam, H.-U.; Chojecki, A.; Sartipi, S.; Sun, X.; Hakeem, A. A.; Koeken, A. C. J.; Ruitenbeek, M.; Davidian, T.; Meima, G. R.; Sankar, G.; Kapteijn, F.; Makkee, M.; Gascon, J., Metal organic framework-mediated synthesis of highly active and stable Fischer-Tropsch catalysts. *Nature Communications* **2015,** *6*, 6451.

153. Mondal, I.; Pal, U., Synthesis of MOF templated Cu/CuO@TiO2 nanocomposites for synergistic hydrogen production. *Physical Chemistry Chemical Physics* **2016,** *18* (6), 4780-4788.

154. Xu, J.; Li, K.; Wu, S.; Shi, W.; Peng, T., Preparation of brookite titania quasi nanocubes and their application in dye-sensitized solar cells. *Journal of Materials Chemistry A* **2015,** *3* (14), 7453-7462.

155. Wu, L. H., Linjuan; Shen, Lijuan; Qin, Na; Xiong, Jinhua, Nitrogen-doped TiO2 catalyst with large specific surface area and visible light response and its preparation method. **2015**.

156. Cabo-Fernandez, L.; Mueller, F.; Passerini, S.; Hardwick, L. J., In situ Raman spectroscopy of carbon-coated ZnFe2O4 anode material in Li-ion batteries – investigation of SEI growth. *Chemical Communications* **2016,** *52* (20), 3970-3973.

157. Kernazhitsky, L.; Shymanovska, V.; Gavrilko, T.; Naumov, V.; Fedorenko, L.; Kshnyakin, V.; Baran, J., *Laser-excited excitonic luminescence of nanocrystalline TiO2 powder*. 2014; Vol. 59, p 246-253.

158. Liu, G.; Sun, C.; Yang, H. G.; Smith, S. C.; Wang, L.; Lu, G. Q.; Cheng, H.-M., Nanosized anatase TiO2 single crystals for enhanced photocatalytic activity. *Chemical Communications* **2010,** *46* (5), 755-757.

159. Parker, J. C.; Siegel, R. W.; P., A. R.; S., A. R.; L., B. W.; E., B. L.; A., G. W.; A., K.; G., L. S.; M., M.; S., P. P.; J., R. S.; W., S. R.; F., S.; Y., W., Calibration of the Raman spectrum to the oxygen stoichiometry of nanophase TiO2. *Applied Physics Letters* **1990,** *57* (9), 943-945.

160. Verma, R.; Gangwar, J.; Srivastava, A. K., Multiphase TiO2 nanostructures: a review of efficient synthesis, growth mechanism, probing capabilities, and applications in bio-safety and health. *RSC Advances* **2017,** *7* (70), 44199-44224.

161. Xu, C. Y.; Zhang, P. X.; Yan, L., Blue shift of Raman peak from coated TiO2 nanoparticles. *Journal of Raman Spectroscopy* **2001,** *32* (10), 862-865.

162. Cheng, X.; Yu, X.; Xing, Z.; Yang, L., Synthesis and characterization of N-doped TiO2 and its enhanced visible-light photocatalytic activity. *Arabian Journal of Chemistry* **2016,** *9*, S1706-S1711.

163. Lottici, P. P., Bersani, D., Braghini, M. et al., Raman scattering characterization of gel-derived titania glass. *Journal of Materials Science* **1993,** *28* (1), 177-183.

164. Chandramohan, P.; Srinivasan, M. P.; Velmurugan, S.; Narasimhan, S. V., Cation distribution and particle size effect on Raman spectrum of CoFe2O4. *Journal of Solid State Chemistry* **2011,** *184* (1), 89-96.

165. Yassin, O. A.; Alamri, S. N.; Joraid, A. A., Effect of particle size and laser power on the Raman spectra of CuAlO2 delafossite nanoparticles. *Journal of Physics D: Applied Physics* **2013,** *46* (23), 235301.

166. Yang, G.; Jiang, Z.; Shi, H.; Xiao, T.; Yan, Z., Preparation of highly visible-light active N-doped TiO2 photocatalyst. *Journal of Materials Chemistry* **2010,** *20* (25), 5301-5309.

167. Surmacki, J.; Wroński, P.; Szadkowska-Nicze, M.; Abramczyk, H., Raman spectroscopy of visible-light photocatalyst – Nitrogen-doped titanium dioxide generated by irradiation with electron beam. *Chemical Physics Letters* **2013,** *566*, 54-59.

168. Raut, N. C.; Mathews, T.; Panda, K.; Sundaravel, B.; Dash, S.; Tyagi, A. K., Enhancement of electron field emission properties of TiO2−x nanoplatelets by N-doping. *RSC Advances* **2012,** *2* (3), 812-815.

169. Di Valentin, C.; Pacchioni, G.; Selloni, A., Origin of the different photoactivity of N-doped anatase and rutile ${\mathrm{TiO}}_{2}$. *Physical Review B* **2004,** *70* (8), 085116.

170. Zhao, H.; Pan, F.; Li, Y., A review on the effects of TiO2 surface point defects on CO2 photoreduction with H2O. *Journal of Materiomics* **2017,** *3* (1), 17-32.

171. HARRICK, http://mmrc.caltech.edu/FTIR/Literature/Diff%20Refectance/Kubelka-Munk.pdf. *Solutions in Optical Spectroscopy*.

172. Zhang, J.; Zhou, P.; Liu, J.; Yu, J., New understanding of the difference of photocatalytic activity among anatase, rutile and brookite TiO2. *Physical Chemistry Chemical Physics* **2014,** *16* (38), 20382-20386.

173. Madhusudan Reddy, K.; Manorama, S. V.; Ramachandra Reddy, A., Bandgap studies on anatase titanium dioxide nanoparticles. *Materials Chemistry and Physics* **2003,** *78* (1), 239-245.

174. Zou, Y.; Yang, K.; Chen, Q.; Wang, H.; Meng, X., Molten salt construction of stable oxygen vacancies on TiO2 for enhancement of visible light photocatalytic activity. *RSC Advances* **2018,** *8* (64), 36819-36825.

175. Yalçın, Y.; Kılıç, M.; Cinar, Z., *The Role of Non-Metal Doping in TiO2 Photocatalysis*. 2010; Vol. 13, p 281-296.

176. Cong, Y.; Zhang, J.; Chen, F.; Anpo, M.; He, D., Preparation, Photocatalytic Activity, and Mechanism of Nano-TiO2 Co-Doped with Nitrogen and Iron (III). *The Journal of Physical Chemistry C* **2007,** *111* (28), 10618-10623.

177. Wang, J.; Tafen, D. N.; Lewis, J. P.; Hong, Z.; Manivannan, A.; Zhi, M.; Li, M.; Wu, N., Origin of Photocatalytic Activity of Nitrogen-Doped TiO2 Nanobelts. *Journal of the American Chemical Society* **2009,** *131* (34), 12290-12297.

178. Zeng, L.; Song, W.; Li, M.; Jie, X.; Zeng, D.; Xie, C., Comparative study on the visible light driven photocatalytic activity between substitutional nitrogen doped and interstitial nitrogen doped TiO2. *Applied Catalysis A: General* **2014,** *488*, 239-247.

179. Mrowetz, M.; Balcerski, W.; Colussi, A. J.; Hoffmann, M. R., Oxidative Power of Nitrogen-Doped TiO2 Photocatalysts under Visible Illumination. *The Journal of Physical Chemistry B* **2004,** *108* (45), 17269-17273.

180. Yang, X.; Cao, C.; Erickson, L.; Hohn, K.; Maghirang, R.; Klabunde, K., Synthesis of visible-light-active TiO2-based photocatalysts by carbon and nitrogen doping. *Journal of Catalysis* **2008,** *260* (1), 128-133.

181. Liu, G.; Zhao, Y.; Sun, C.; Li, F.; Lu, G. Q.; Cheng, H.-M., Synergistic Effects of B/N Doping on the Visible-Light Photocatalytic Activity of Mesoporous TiO2. *Angewandte Chemie International Edition* **2008,** *47* (24), 4516-4520.

182. Dawson, M.; Soares, G. B.; Ribeiro, C., Influence of calcination parameters on the synthesis of N-doped TiO2 by the polymeric precursors method. *Journal of Solid State Chemistry* **2014,** *215*, 211-218.

183. Ma, S.; Reish, M. E.; Zhang, Z.; Harrison, I.; Yates, J. T., Anatase-Selective Photoluminescence Spectroscopy of P25 TiO2 Nanoparticles: Different Effects of Oxygen Adsorption on the Band Bending of Anatase. *The Journal of Physical Chemistry C* **2017,** *121* (2), 1263-1271.

184. Zhang, H.; Cai, J.; Wang, Y.; Wu, M.; Meng, M.; Tian, Y.; Li, X.; Zhang, J.; Zheng, L.; Jiang, Z.; Gong, J., Insights into the effects of surface/bulk defects on photocatalytic hydrogen evolution over TiO2 with exposed {001} facets. *Applied Catalysis B: Environmental* **2018,** *220*, 126-136.

185. Zou, X.; Liu, J.; Su, J.; Zuo, F.; Chen, J.; Feng, P., Facile Synthesis of Thermal- and Photostable Titania with Paramagnetic Oxygen Vacancies for Visible-Light Photocatalysis. *Chemistry – A European Journal* **2013,** *19* (8), 2866-2873.

186. Moya, A.; Cherevan, A.; Marchesan, S.; Gebhardt, P.; Prato, M.; Eder, D.; Vilatela, J. J., Oxygen vacancies and interfaces enhancing photocatalytic hydrogen production in mesoporous CNT/TiO2 hybrids. *Applied Catalysis B: Environmental* **2015,** *179*, 574-582.

187. Schaub, R.; Thostrup, P.; Lopez, N.; Lægsgaard, E.; Stensgaard, I.; Nørskov, J. K.; Besenbacher, F., Oxygen Vacancies as Active Sites for Water Dissociation on Rutile ${\mathrm{TiO}}_{2}(110)$. *Physical Review Letters* **2001,** *87* (26), 266104.

188. Bikondoa, O.; Pang, C. L.; Ithnin, R.; Muryn, C. A.; Onishi, H.; Thornton, G., Direct visualization of defect-mediated dissociation of water on TiO2(110). *Nature Materials* **2006,** *5*, 189.

189. Pan, X.; Yang, M.-Q.; Fu, X.; Zhang, N.; Xu, Y.-J., Defective TiO2 with oxygen vacancies: synthesis, properties and photocatalytic applications. *Nanoscale* **2013,** *5* (9), 3601-3614.

190. Spurr, R. A.; Myers, H., Quantitative Analysis of Anatase-Rutile Mixtures with an X-Ray Diffractometer. *Analytical Chemistry* **1957,** *29* (5), 760-762.

191. So, W. W.; Park, S. B.; Kim, K. J.; Shin, C. H.; Moon, S. J., The crystalline phase stability of titania particles prepared at room temperature by the sol-gel method. *Journal of Materials Science* **2001,** *36* (17), 4299-4305.

192. Gunatilleke, W. D. C. B.; Wei, K.; Niu, Z.; Wojtas, L.; Nolas, G.; Ma, S., Thermal conductivity of a perovskite-type metal–organic framework crystal. *Dalton Transactions* **2017,** *46* (39), 13342-13344.

193. Zhang, F.; Chen, C.; Xu, L.; Zhang, N., *Thermal Decomposition Investigation of Zn4O(NH2-BDC)(3) (IRMOF-3) and NH2-BDC by in situ DRIFTS*. 2013; Vol. 25, p 1937-1941.

194. Gagnon, K. J.; Beavers, C. M.; Clearfield, A., *J. Am. Chem. Soc.* **2013,** *135*, 1252.

195. Ocaña, M.; Garcia-Ramos, J. V.; Serna, C. J., Low-Temperature Nucleation of Rutile Observed by Raman Spectroscopy during Crystallization of TiO2. *Journal of the American Ceramic Society* **1992,** *75* (7), 2010-2012.

196. Karthik, P.; Vinoth, R.; Zhang, P.; Choi, W.; Balaraman, E.; Neppolian, B., π–π Interaction Between Metal–Organic Framework and Reduced Graphene Oxide for Visible-Light Photocatalytic H2 Production. *ACS Applied Energy Materials* **2018,** *1* (5), 1913-1923.

197. Bobb, J. A.; Ibrahim, A. A.; El-Shall, M. S., Laser Synthesis of Carbonaceous TiO2 from Metal–Organic Frameworks: Optimum Support for Pd Nanoparticles for C–C Cross-Coupling Reactions. *ACS Applied Nano Materials* **2018,** *1* (9), 4852-4862.

198. Nanda, S. S.; Yi, D. K.; Kim, K., Study of antibacterial mechanism of graphene oxide using Raman spectroscopy. *Scientific Reports* **2016,** *6*, 28443.

199. Zhang, J.; Li, M.; Feng, Z.; Chen, J.; Li, C., UV Raman Spectroscopic Study on TiO2. I. Phase Transformation at the Surface and in the Bulk. *The Journal of Physical Chemistry B* **2006,** *110* (2), 927-935.

200. Kojima, A.; Teshima, K.; Shirai, Y.; Miyasaka, T., Organometal Halide Perovskites as Visible-Light Sensitizers for Photovoltaic Cells. *Journal of the American Chemical Society* **2009,** *131* (17), 6050-6051.

201. Kim, B. J.; Lee, S.; Jung, H. S., Recent progressive efforts in perovskite solar cells toward commercialization. *Journal of Materials Chemistry A* **2018,** *6* (26), 12215-12236.

202. Husseini, T., New world record set for perovskite solar cell efficiency. *POWER TECHNOLOGY* **20018**.

203. Weber, D., *CH3NH3PbX3, ein Pb(II)-System mit kubischer Perowskitstruktur / CH3NH3PbX3, a Pb(II)-System with Cubic Perovskite Structure*. 1978; Vol. 33.

204. Kim, H.-S.; Im, S. H.; Park, N.-G., Organolead Halide Perovskite: New Horizons in Solar Cell Research. *The Journal of Physical Chemistry C* **2014,** *118* (11), 5615-5625.

205. Castelli, I. E.; García-Lastra, J. M.; Thygesen, K. S.; Jacobsen, K. W., Bandgap calculations and trends of organometal halide perovskites. *APL Materials* **2014,** *2* (8), 081514.

206. Gonzalez-Pedro, V.; Juarez-Perez, E. J.; Arsyad, W.-S.; Barea, E. M.; Fabregat-Santiago, F.; Mora-Sero, I.; Bisquert, J., General Working Principles of CH3NH3PbX3 Perovskite Solar Cells. *Nano Letters* **2014,** *14* (2), 888-893.

207. Lee, M. M.; Teuscher, J.; Miyasaka, T.; Murakami, T. N.; Snaith, H. J., Efficient Hybrid Solar Cells Based on Meso-Superstructured Organometal Halide Perovskites. *Science* **2012,** *338* (6107), 643.

208. Stranks, S. D.; Eperon, G. E.; Grancini, G.; Menelaou, C.; Alcocer, M. J. P.; Leijtens, T.; Herz, L. M.; Petrozza, A.; Snaith, H. J., Electron-Hole Diffusion Lengths Exceeding 1 Micrometer in an Organometal Trihalide Perovskite Absorber. *Science* **2013,** *342* (6156), 341.

209. Bi, D.; Moon, S.-J.; Häggman, L.; Boschloo, G.; Yang, L.; Johansson, E. M. J.; Nazeeruddin, M. K.; Grätzel, M.; Hagfeldt, A., Using a two-step deposition technique to prepare perovskite (CH3NH3PbI3) for thin film solar cells based on ZrO2 and TiO2 mesostructures. *RSC Advances* **2013,** *3* (41), 18762-18766.

210. Im, J.-H.; Jang, I.-H.; Pellet, N.; Grätzel, M.; Park, N.-G., Growth of CH3NH3PbI3 cuboids with controlled size for high-efficiency perovskite solar cells. *Nature Nanotechnology* **2014,** *9*, 927.

211. Xue, Q.; Hu, Z.; Sun, C.; Chen, Z.; Huang, F.; Yip, H.-L.; Cao, Y., Metallohalide perovskite–polymer composite film for hybrid planar heterojunction solar cells. *RSC Advances* **2015,** *5* (1), 775-783.

212. Lee, M.; Jo, Y.; Kim, D. S.; Jun, Y., Flexible organo-metal halide perovskite solar cells on a Ti metal substrate. *Journal of Materials Chemistry A* **2015,** *3* (8), 4129-4133.

213. Herz, L. M., Charge-Carrier Mobilities in Metal Halide Perovskites: Fundamental Mechanisms and Limits. *ACS Energy Letters* **2017,** *2* (7), 1539-1548.

214. Ito, S.; Murakami, T. N.; Comte, P.; Liska, P.; Grätzel, C.; Nazeeruddin, M. K.; Grätzel, M., Fabrication of thin film dye sensitized solar cells with solar to electric power conversion efficiency over 10%. *Thin Solid Films* **2008,** *516* (14), 4613-4619.

215. Sharma, M.; Pudasaini, P. R.; Ruiz-Zepeda, F.; Elam, D.; Ayon, A. A., Ultrathin, Flexible Organic–Inorganic Hybrid Solar Cells Based on Silicon Nanowires and PEDOT:PSS. *ACS Applied Materials & Interfaces* **2014,** *6* (6), 4356-4363.

216. Liang, Z.; Su, M.; Zhou, Y.; Gong, L.; Zhao, C.; Chen, K.; Xie, F.; Zhang, W.; Chen, J.; Liu, P.; Xie, W., Interaction at the silicon/transition metal oxide heterojunction interface and its effect on the photovoltaic performance. *Physical Chemistry Chemical Physics* **2015,** *17* (41), 27409-27413.

217. Eperon, G. E.; Burlakov, V. M.; Docampo, P.; Goriely, A.; Snaith, H. J., Morphological Control for High Performance, Solution-Processed Planar Heterojunction Perovskite Solar Cells. *Advanced Functional Materials* **2014,** *24* (1), 151-157.

218. Li, Z.; Yang, M.; Park, J.-S.; Wei, S.-H.; Berry, J. J.; Zhu, K., Stabilizing Perovskite Structures by Tuning Tolerance Factor: Formation of Formamidinium and Cesium Lead Iodide Solid-State Alloys. *Chemistry of Materials* **2016,** *28* (1), 284-292.

219. Saliba, M.; Matsui, T.; Seo, J.-Y.; Domanski, K.; Correa-Baena, J.-P.; Nazeeruddin, M. K.; Zakeeruddin, S. M.; Tress, W.; Abate, A.; Hagfeldt, A.; Grätzel, M., Cesium-containing triple cation perovskite solar cells: improved stability, reproducibility and high efficiency. *Energy & Environmental Science* **2016,** *9* (6), 1989-1997.

220. Kim, H.; Lee, Y. H.; Lyu, T.; Yoo, J. H.; Park, T.; Oh, J. H., Boosting the performance and stability of quasi-two-dimensional tin-based perovskite solar cells using the formamidinium thiocyanate additive. *Journal of Materials Chemistry A* **2018,** *6* (37), 18173-18182.

221. Seo, J.; Noh, J. H.; Seok, S. I., Rational Strategies for Efficient Perovskite Solar Cells. *Accounts of Chemical Research* **2016,** *49* (3), 562-572.

222. Ke, W.; Kanatzidis, M. G., Prospects for low-toxicity lead-free perovskite solar cells. *Nature Communications* **2019,** *10* (1), 965.

223. Kong, M.; Hu, H.; Wan, L.; Chen, M.; Gan, Y.; Wang, J.; Chen, F.; Dong, B.; Eder, D.; Wang, S., Nontoxic (CH3NH3)3Bi2I9 perovskite solar cells free of hole conductors with an alternative architectural design and a solution-processable approach. *RSC Advances* **2017,** *7* (56), 35549-35557.

224. Chen, M.; Wan, L.; Kong, M.; Hu, H.; Gan, Y.; Wang, J.; Chen, F.; Guo, Z.; Eder, D.; Wang, S., Influence of Rutile-TiO2 nanorod arrays on Pb-free (CH3NH3)3Bi2I9-based hybrid perovskite solar cells fabricated through two-step sequential solution process. *Journal of Alloys and Compounds* **2018,** *738*, 422-431.

Curriculum Vitae

Personal Details

Name	Jia WANG
Date of Birth	1989.02.07
Nationality	Chinese

Education

10/2015-present PhD student Technical University of Vienna Vienna, Austria

Institute of Materials Chemistry, Faculty of Technical Chemistry

11/2014-10/2015 PhD student Münster University Münster, Germany

Department of Physical Chemistry, Faculty of Chemistry

09/2011-04/2014 M.S Zhejiang University Hangzhou, China

Major in Materials Science & Engineering

09/2007-06/2011 B.S Qingdao University of Science and Technology Qingdao, China

Major in Inorganic Non-metal Materials

Research experience

Project assistant

11/2017- Titanium-based Metal Organic Framework as Photo-catalysts for Photocatalytic Water Splitting

Sponsored by Chinese Government Scholarship: CSC

11/2014-10/2017 PhD program – Pervskite Solar Cell

Sponsored by Chinese Government Scholarship: DFG

07/2017-08/2017 Visiting Student in the research group of Prof. Henry Snaith, Oxford, UK

Research assistant: Project supported by Zhejiang Provincial Natural Science Foundation of China (J20110056)

05/2012-06/2013 **Studied on the hydrothermal synthesis of nanorod anatase TiO_2 array on substrates**

06/2013-02/2014 **Experiment on the band gap tuning in TiO_2 with facile chemical route**

Lab Operator 09/2011-11/2013 **Master the operation of scanning electron microscope (SEM): HITCHI-4800 and Hitachi SU70.**

List of Publications

- M. Chen, Q. Zhang, L. Wan, Y. Gan, Z. Lui, Y. Wang, Y. Liu, **J. Wang**, F. Chen, D. Eder, S. Wang, High-efficiency hole-conductor-free rutile TiO_2 Nanorod/$CH_3NH_3PbI_3$ heterojunction solar cells with commercial carbon ink as counter-electrode, (Solar Energy, 170 (2018), S. 1087 - 1094.)
- M. Chen, L. Wan, M. Kong, H. Hanghu, Y. Gan, **J. Wang**, F. Chen, Z. Guo, D. Eder, S. Wang, Influence of Rutile-TiO_2 nanorod arrays on Pb-free $(CH_3NH_3)_3Bi_2I_9$-based hybrid perovskite solar cells fabricated through two-step sequential solution process. (Journal of Alloys and Compounds, 738 (2018), S. 422 – 431.)
- M. Kong, H. Hu, L. Wan, M. Chen, Y. Gan, **J. Wang**, F. Chen, B. Dong, D. Eder, S. Wang, Nontoxic $(CH_3NH_3)_3Bi_2I_9$ perovskite solar cells free of hole conductors with an alternative architectural design and a solution-processable approach. (RSC Advances, 7 (2017), 7; S. 35549 – 35557)
- **Jia Wang**, Zhimin Ren, Chenyao Fan, Guodong Qian, Zhiyu Wang, N-doped TiO_2/C nanocomposites and N-doped TiO_2 synthesised at different thermal treatment temperatures with the same hydrothermal precursor. (Dalton Transactions, 2014, 43, 13783-13791)
- Chao Chen, **Jia Wang**, Zhimin Ren, Guodong Qian and Zhiyu Wang, One-dimension TiO_2 nanostructures: oriented attachment and application in dye-sensitized solar cell (CrystEngComm, 2014, 16, 1681-1686.)
- **Jia Wang**, Chao Chen, Zhimin Ren, Zhiyu Wang, Seed-assisted hydrothermal synthesis of aligned single-crystalline anatase nanorods on FTO: synthesis and application. (Semiconductor Science and Technology, 2014, 29, 055006)
- **Jia Wang**, Rong Hu, Zhiyu Wang, UV-induced Synthesis of Ag-decorated TiO_2 Nanocrystals and Exploitation in Photocatalyst (材料科学工程学报, 2012, 31(4) 521-524)

List of Conferences

- 22nd International Conference on Photochemical Conversion and Storage of Solar Energy (IPS-22), 29. 07 – 03. 08. 2018, Hefei, China.

Oral presentation: “Bi-functional metal organic framework for photocatalytic H_2 production from water”. J. Wang, A. Leichner, S. P Nandam, T. Gupta, L. Deilmann, G. Haselmann, D. Eder.

- 32. Workshop Novel Materials and Superconductivity, 12. 02 – 18. 02. 2017, Obertraun, Austria.
  Poster: J. Wang, A. Cherevan, L. Deilmann, G.M. Haselmann, D. Eder: "Crystal-growth engineering of perovskite film via solvent tuning";

- 21st International Conference on Photochemical Conversion and Storage of Solar Energy (IPS-21), 25. 07 – 29. 07. 2016, St. Petersburg, Russia.
  Poster: J. Wang, A. Cherevan, L. Deilmann, G.M. Haselmann, D. Eder: "Crystal-growth engineering of perovskite film via solvent tuning"

- European Congress and Exhibition on Advanced Materials and Processes (EUROMAT 2015), 20. 09 – 24. 09. 2015, Warsaw, Poland.
  Oral Presentation: J. Wang, D. Eder: "Lower temperature and sovlent-assisted $CH_3NH_3PbI_3$ crystal growth control"

Acknowledgements

When I read PhD thesis written by other people, I have always been curious about their **Acknowledgements** section, and now finally the time comes to write my acknowledgements. When I was thinking what to write, I realized wow, I have been so lucky – I have met so many lovely people in my life, I have so many people to express my gratitude – life has been really nice to me.

First, I want to acknowledge my supervisor, Prof. Dominik Eder. Thank you for accepting me to work in your research group. During my PhD time, thank you very much for your supervision, and for those inspiring discussions we had. You have taught me a lot about how to deal with chemistry question using physical thinking, and how to extract information from the experimental data to the most extent. I do hope that I could acquire some of these skills and applied in this thesis. I also hope I will use them in my future life. Also, thank you very much for your time and patience during my writing period. I wish you all the best in the future.

I would also like to express my gratitude to Dr. Alexey Cherevan. You are the first person I met in this research group and I want to thank you for introducing me the group, the labs, Vienna... ah, also, the Onenote. Maybe I can never be so good at organizing as you, but I will keep trying my best. Thank you for those helpful discussions and thank you for being so nice all the time. Greta and Leonie, we are together since Münster. Greta, thank you for showing me around both Münster and Vienna, when I first arrived; that is so nice of you. Also, for introducing me to jogging and the sport world. Leo, thank you for your unique, kind, patient 'push' when we skied in Obertraun. Recently, this push showed up again, and it has helped me a lot with this thesis. Thinking of Münster, Nina, thank you for the SEM and ALD; Paul, old officemate, hope you are fine with the font choice and pity I have forgotten everything about juggling; Oliver, gentleman, tea master, I miss you especially when the lab rules need to be imposed.

Moving back to Vienna, Ari, thank you for being happy and for bring happiness to the group all the time; Paolo, thank you for the pasta, for the bier, for introducing me to Espresso and sharing your history and language knowledge; Tushar, thank you for the time we spent during the group retreat, your constant concern about my thesis and for the help with TEM; Sreejith, my kicker and swimming teammate, thank you for the help with XRD, we have to achieve the swimming goal ASAP; Shaghayegh, thank you for the help with BET and for sharing lovely Misha with me; Jasmin, thank you for the help with Coffee, which was of the same importance as were the

characterization data; Niusha, thank you for being so nice to everyone, for the help with DSL, for allowing me to join your piano session; Bernhard, thank you for the help with TEM and Raman.

Many more people contributed to to my work, just to name a few:Ralf (manufacturing), Nevzat (BET, TPO-MS), Christopher (ICP-MS), Mariana, Michael (2), Elias and Christian (FT-IR), Sven (Push)…

I would also like to thank the students whom I have worked with: Celine, an excellent master student, who has contributed a lot to the mix-ligand project in this thesis, I enjoyed a lot working with you; Andreas, worked bravely with incorporation of Cu into MOFs; Pablo, Igor and Max, though in shorter time periods, you all have done great job.

Here one more time thanks to Dominik, Alexey, Leonie, Paolo, Tushar. Sreejith, Bernhard and Ari for the generous help with proofreading.

There are also people who are not from my working circle, but have offered me great love and support during my PhD time, without them, things would have gotten more difficult. They are Qi Zhang and Chaona Li. Sladana and Flo, you have been so nice to me, I am grateful for having you as flatmates. Huiyu Wang, Zairong Liu, Huibiying Xiao, Mingjing Li, Hui Lv, it is my pleasure to get to know you during my PhD time.

Special thanks to Dr. Feifei, for the proofreading, but more for your daily cheering with odd jokes. I will remember those days when you greeted me with ‘are you still alive?’. Lucky you were there, all the time.

At last, I want to thank my family and brother for their constant love and support they give me. That is definitely one of the main motivations for this Thesis. Love you.

Grateful for all of you being there, wish you all the best.